DOCTOR OF PHILOSOPHY

Remote determination of bathymetric changes using ground based radar

Bell, Paul S.

Award date:
2005

Awarding institution:
Bangor University

Remote Determination of Bathymetric Changes Using Ground Based Radar

A thesis submitted in accordance with the requirements of the University of Wales for the degree of Doctor of Philosophy.

by

Paul S. Bell

2005

University of Wales Bangor
School of Ocean Sciences
Menai Bridge
Anglesey LL59 5EY
United Kingdom

Declaration

This work has not previously been accepted in substance for any degree and is not being concurrently submitted for any degree.

Signed …… (candidate)
Date ……

STATEMENT 1

This thesis is the result of my own investigations, except where otherwise stated. Other sources are acknowledged by footnotes giving explicit references. A bibliography is appended.

Signed …… (candidate)
Date ……

STATEMENT 2

I hereby give consent for my thesis, if accepted, to be available for photocopying and for inter-library loan, and for the title and summary to be made available to outside organizations.

Signed …… (candidate)
Date ……

Abstract

Remote Determination of Bathymetric Changes Using Ground Based Radar

Paul S. Bell

The determination of seabed bathymetry is a task commonly carried out by survey vessels using an echo sounder and satellite positioning systems. During the present study a method was developed to map the bathymetry of shallow water areas rapidly and remotely using radar image sequences of waves from two types of shore-based radar systems: an X-band marine radar (9.8 GHz) recording waves up to 2 km from the shore and a high resolution mm wave radar (77 GHz) with a range of approximately 200 m for measuring waves in the surf zone.

The physical properties of the wave field were determined from the radar images. Using wave theory, these properties were then used to determine the local water depth. Following investigation of several wave theories, a dispersion equation that approximates the effects of both frequency and amplitude dispersion was found to be the most appropriate. The wavelengths of the waves imaged by the radar were mapped over a range of wave frequencies using a Fourier transform based algorithm for determining the wavelength of 2D waveforms in short lengths of data. The results were used with the selected depth inversion algorithm to infer the water depth matching the observed wave behaviour.

Data from two sites were documented in detail: Faro in the Algarve region of Portugal, and Teignmouth in south west England. Radar data from these sites were processed to determine the bathymetry and the results compared with conventional surveys. The water depths derived from the short range mm wave radar data using the non-linear wave dispersion equation showed a mean offset of less than 0.1 m and the standard deviation of the scatter was of the order of 0.2 m. The water depths derived from the longer range X-band radar data again showed a mean offset of the order of 0.1 m and a slightly larger scatter standard deviation of 0.3 m for depths of up to 15 m. The water depths derived from the Teignmouth X-band radar data showed a similar pattern, with a mean offset of less than 0.1 m and a standard deviation of slightly over 0.2 m for water depths of up to 10 m.

Radar data obtained in 1999 and 2003 from a tidal inlet in the barrier island system near Faro, Portugal were analysed to obtain bathymetric maps. Comparison of these two bathymetries showed the natural migration of the inlet and the associated bathymetric changes recorded by other researchers using conventional survey methods. In addition, the bathymetric changes evident in the radar derived bathymetries identified deposition to depths exceeding 0.5 m over a wide area of the ebb delta. Further, the data revealed extensive down-drift erosion to a depth of more than 1.5 m. These new observations showed that the balance between accretion and erosion plays an important role in the mechanisms driving inlet migration. This had not been documented previously owing to the practical difficulties of surveying the site by conventional methods. The changes in sediment volume estimated from the two sets of radar data suggest that more than 85% of the sediment supplied by longshore transport is being sequestered in the flood and ebb deltas, resulting in the erosion of the down-drift barrier island and enhanced rates of inlet migration.

The techniques developed during this study are now firmly established for future use in coastal studies, and a number of projects are planned to include the use of X-band radar for this purpose.

Acknowledgements

I owe a great many people a debt of gratitude for supporting me through the various aspects of this study.

Firstly I would like to thank my supervisors Alan G. Davies and Judith Wolf for their invaluable guidance and patience.

To the Proudman Oceanographic Laboratory, who paid the majority of my tuition fees and gave me the opportunity to follow my nose.

To Roger Proctor, who encouraged me to use the radar work as the subject of my thesis.

To Peter Thorne, for adding the X-band radar into the COAST3D project at the last minute.

To Jon Williams, for seeing the benefits of repeat visits to Faro to monitor the tidal inlet with the radars, and for all his encouragement.

To Oscar Ferreira, for hosting us at the University of Algarve and all the help from the team there, especially Ana Vila-Concejo and Brad Morris who even came down to the beach at Praia de Faro in stormy weather on a Sunday to help me with the radar so I could record the waves.

And finally to my wife Karen, for her unwavering support in putting up with me while I was writing this thesis. I promised that I'd finish it before we got married – and I'm only a year, a wedding and a baby late.

I would like to acknowledge the following projects for funding various aspects of the data used within this thesis:

The Holderness Project was funded by the Ministry of Agriculture, Fisheries and Food under its Flood Protection Commission FD0306, and also by the European Union under the SCAWVEX (MAS2-CT94-0103) project.

The COAST3D project was funded by the Marine Science and Technology (MAST) RTD programme of the European Union under contract number MAS3-CT97-0086, and partly through national funding from the UK Ministry of Agriculture Fisheries and Food research project FD0803, the UK Environment Agency R&D Programme, the UK Environment Research Council and the Netherlands Rijkswaterstaat.

The INDIA project was funded by The Commission of the European Directorate General for Science, Research and Development under contract MAS3-CT97-0106, and also in part by the UK Environment Research Council and by the national governments and universities of the partners' institutes.

Thanks to the Parque Natural da Ria Formosa for their kind permission to carry out the fieldwork in Faro. And to the Portuguese FCT funded CROP project (PDCTM/MAR/15265/99) for supplying bathymetry/topography data and for funding Ana Vila-Concejo.

Paul S. Bell
August 2005

Table of Contents

Glossary of Terms

d	Water depth measured from the sea bed to the mean water level.
h	Water depth measured from the sea bed to the bottom of the wave trough, used primary in cnoidal wave theories.
η	Water surface profile, measured relative to mean water level.
L	Wavelength
L_0	Deep water wavelength, defined as $L_0 = \frac{gT^2}{2\pi}$
T	Wave period
f	Wave frequency, defined as $f = 1/T$
ω	Wave angular frequency, defined as $\omega = 2\pi f$
k	Wavenumber, defined as $k = 2\pi/L$
H	Wave height, defined as the vertical distance between the crest and trough of a wave.
a	Wave amplitude, defined as $a = H/2$
H_S	Significant wave height, defined as the average of the highest third of the wave heights in a given time series and corresponding originally to the wave height estimated by experienced observers by eye. $H_{1/3}$ and H_{m0} are often written as H_S.
$H_{1/3}$	Significant wave height calculated directly from a time series of water surface elevation by taking the average of the highest third of the waves.
H_{m0}	Significant wave height estimated from the zero-th moment of the wave spectrum. This is the most likely version of H_S to be quoted by wave measuring instruments.
H_b	The wave height at which a wave commences breaking.
T_P	Peak wave period, defined as the wave period of the highest peak in a wave spectrum.
T_Z	Zero crossing period, defined as the average time between the water surface elevation crossing the mean water level upwards (zero-upcrossing) or downwards (zero-downcrossing).

T_{m02} Equivalent to T_Z but calculated from the moments of a wave spectrum using the equation $T_{m02} = \sqrt{\frac{m_0}{m_2}}$

C Wave celerity or phase speed, defined as $C_0 = \frac{gT}{2\pi}$

C_0 Deep water wave celerity

Chapter 1: Background & Literature Review

Introduction

The major premise of this study is that given sufficient knowledge of the behaviour of waves in shallow water, it should be possible to infer the local water depths causing that wave behaviour. If a remote sensing system could be used to measure and map the wave properties, this should allow the remote mapping of shallow water coastal areas without the need for expensive survey vessels. Further, if such a technique proved successful, repeat measurements in areas of rapidly evolving bathymetry could allow changes to be mapped over wide areas and at low cost.

This chapter reviews the distinct topics that have been brought together within this thesis. Radar imaging of sea surface waves has been applied to the problem of remote mapping of shallow water coastal regions using wave dispersion equations to infer the water depths causing the wave behaviour observed on the radar images.

A brief history of the development of radio remote sensing begins in the late nineteenth century, culminating in the 1940s with the development of modern navigation radars as we know them today. Once these became widely available shortly after World War II, the oceanographic community became interested in their possibilities for ocean remote sensing, primarily for the measurement of wave spectra and more recently of currents. Almost in parallel with the development of radar but at that time unrelated, the requirement for covert mapping of enemy beaches during both world wars led to the development of a number of ingenious methods of remote mapping of shallow water areas.

A number of radar datasets have been collected by the author since the mid 1990s, only some of which are used directly in this study. A brief description of these various datasets is given in section 1.2, with a more detailed overview of those used directly in this work documented in Chapter 4.

The remote mapping of beaches and the use of radar images for oceanographic study of waves are based on relating the behaviour of waves to the underlying water depth. Section 1.3 presents a review of the wave theory that underpins the application of wave dispersion

equations. A detailed study of a selection of these dispersion equations and their applicability to shallow water bathymetric inversions is given in Chapter 2.

In Chapter 3 the practical aspects of using X-band marine radars and recording the radar images are discussed. In addition, a new 77GHz radar applied to oceanography for the first time by the author is introduced for short range, high resolution imaging.

The sequence of techniques that were developed to extract the required wave properties from the radar images are described in Chapter 5, from early pattern tracking algorithms to the development and application of the final wavelength measurement technique based on the Fourier transform.

The complete technique was tested on data collected by the author using two different radars deployed in Faro, Portugal. The results are presented in Chapter 6 and demonstrate that water depth maps can be derived from radar image sequences to an accuracy of better than 0.5m in areas of smoothly varying bathymetry.

The technique was tested on data from a second site at Teignmouth in the UK and the successful results presented in Chapter 7, thereby demonstrating that the technique is applicable at different sites.

Finally, in Chapter 8 two sets of radar data from Faro, recorded four years apart, are used to demonstrate and explain the bathymetric evolution of a tidal inlet through the barrier islands of the Ria Formosa in southern Portugal. The findings help to explain previous observations of tidal inlet evolution on that stretch of coast by other researchers.

1.1 Radar - History and Oceanographic Applications

1.1.1 The Development of Radar

Although the development of **RA**dio **D**etection **A**nd **R**anging (RADAR) did not mature until World War II, the concept of using radio waves to detect objects at a distance dates back to the late 19th century (Skolnick, 1981) when in 1886 Heinrich Hertz showed that radio waves with a wavelength of 66cm could be reflected from metallic and dielectric bodies.

By 1903 a German engineer, Christian Hulsmeyer was experimenting with the detection of radio waves reflected from ships, and in 1904 he obtained a patent in several countries including Britain for an obstacle detector and ships navigation device. His technique was demonstrated to the German Navy, but was dismissed on the grounds that at that stage of development the range was little better than that of visual observations. Marconi later recognised the potential of radio waves for this application and strongly urged their use in a speech to the Institute of Radio Engineers in 1922.

The first experimental radars demonstrated in 1922 in the USA used continuous wave (CW) transmissions and depended for detection upon the interference produced between the direct signal from the transmitter and the Doppler-frequency-shifted signal reflected by a moving target. The first application of a pulsed radar technique to the measurement of distance was in 1925 by Breit and Tuve who used it to measure the height of the ionosphere.

The first detection of aircraft using radar did not occur until 1930, and happened by accident when an engineer at the US Naval Research Laboratory working on direction finding equipment in a plane on the ground noticed that the strength of the radio beam was increased when an aircraft landing at a nearby airstrip passed through it. This led to further developments using the CW interference technique.

During the 1930s considerable effort was invested in radar developments by both the US and Germany. During the 1930s, Dr Hans Erich Hollmann working for the company Telefunken, and consulting for the Gesellschaft Fur Elektroakustische und Mechanische (GEMA) foundation, patented many developments in radar systems, including the multi-cavity magnetron (Hollmann, 1935). Many of the patents were filed both in Germany and in the US, possibly leading to the parallel set of developments on the two sides of the Atlantic. This

time the significance of this work was not missed by the German military, and in 1940, GEMA built the world's first Plan Position Indicator (PPI) scanning radar near Berlin on which the location of targets could be seen on a circular plan view. It was able to scan 360^{o} at a rate of 6 rpm and its range was 120km. With its operating wavelength of 50cm, the antenna was still far from portable, and it was the British who finally developed a magnetron of high enough frequency and small size to be practical for use on an aircraft.

The prospect of war spurred rapid British radar developments. In 1935 Sir Robert Watson-Watt was asked about the possibility of producing a "death ray" using radio waves. He concluded that this would require more power than was conceivably available, and instead recommended that it would be more promising to investigate techniques of radio detection rather than destruction. By June 1935, the British had demonstrated a 12MHz (25m wavelength) pulse technique to measure the range of an aircraft target. In March of 1936 the range of detection had reached 90 miles using 25MHz (12m wavelength) systems, and a series of Chain Home (CH) radar stations began 24 hour operation in September 1938 and continued until the end of the war.

It was realised that such low frequency radars did not have the accuracy to guide allied fighter aircraft to intercept enemy aircraft, so efforts were directed towards producing the developments required for a higher resolution 200MHz (1.5m wavelength) system of sufficient power to be useful. In 1939 Randell and Boot improved upon Hollmann's magnetron and patented their cavity magnetron power tube to fill this need. It operated at a frequency of 3GHz (10cm wavelength) and a power output of 1kW, a factor of 100 increase on all previous developments at this frequency and making an aircraft mounted radar a possibility at last. In 1940 the designs for the magnetron were supplied to the USA as part of the Tizard Mission when the research efforts of the two countries were combined for the war effort. It is one of the ironies of history that a technique originally developed in Germany but initially dismissed by their military as impractical, was used to such great effect by the British during World War II.

Radar systems have been developed across a wide range of frequencies, the various frequency bands being designated by letters. Although the purpose of these letter codes was originally to guard military secrecy, they have remained as convenient designations for the various frequency bands. The various frequency bands are listed in table 1.1.

Band designation	Nominal frequency range	Frequencies reserved for radar use
HF	3-30MHz	
VHF	30-300MHz	138-144MHz, 216-225MHz
UHF	300-1000MHz	420-450MHz, 890-942MHz
L	1-2GHz	1.215-1.400GHz
S	2-4GHz	2.3-2.5GHz, 2.7-3.7GHz
C	4-8GHz	5.250-5.925GHz
X	8-12GHz	8.50-10.68GHz
K_u	12-18GHz	13.4-14.0GHz, 15.7-17.7GHz
K	18-27GHz	24.05-24.25GHz
K_a	27-40GHz	33.4-36.0GHz
mm	40-300GHz	24GHz, 77GHz

Table 1.1 Standard radar frequency band designations

1.1.2 Applications of Radars to Oceanographic Remote Sensing

Attempts to use marine radars for oceanographic study began almost as soon as they became widely available. It was noticed that wave patterns were clearly visible on radar screens at high resolution, the crests of the waves reflecting the radar energy similar to the way a hard target would. This 'sea clutter' would normally be filtered out by anyone using radar for navigation purposes as it is considered as noise that could obscure the signals from real hard targets.

Oudshoorn (1961), working at the Rijkswaterstaat in the Netherlands documented a number of experiments using various radars at different frequencies to plot wave patterns and carry out float tracking to map current patterns. At this time all analyses had to be performed by hand and were very labour intensive.

Heathershaw et al. (1980) recorded single images from an X-band radar screen by using an automatic camera to photograph the PPI screen. They deployed this system in Start Bay in Devon from 1972-1974 and in Port Talbot in South Wales from 1976-1977. The data from Port Talbot were used to provide information on wave direction statistics, used in connection with beach erosion studies on the foreshore near Port Talbot (Carr et al., 1977). Their

analysis was also carried out by hand, and involved averaging the results from three researchers who each analysed the same images to obtain the wave directions.

With the introduction of more powerful computers in the early 1980s and the introduction of radar recording systems, recording of data and analyses of data could be carried out much more easily. Hoogeboom & Rosenthal (1982) presented the first attempts to extract wave spectra by digitising photographs of a radar screen, carrying out a Fourier transform analysis of the digitised images and applying the linear dispersion equation to the results. Hoogeboom et al. (1986) later showed developments of the analysis that fitted the linear dispersion equation to the frequency-wavenumber spectrum of a single cross-shore line of digitised radar data, recorded from a static, non-rotating antenna. The best fit of the mean depth to the frequency-wavenumber spectrum at a number of ranges from the radar were calculated and compared favorably to survey data. The best fit of the mean current was then also fitted. The two parameters preferentially affect slightly different parts of the wave spectrum, so they can in theory be resolved by the same method almost independently of each other. Long period waves are proportionally less affected by currents and more affected by water depth, while short period waves are more affected by currents and less so by water depth.

Young et al. (1985) demonstrated a method of carrying out a 3-D FFT of image sequences rather than the line of data used by Hoogeboom. The method of calibration was based on the signal to noise ratio of the spectrum. This approach has been refined a number of times by improving the algorithms for fitting a mean current to the dispersion shell (Senet et al. 1997) and identifying and including the aliased components of the wave spectrum in the calculations (Seeman et al., 1997). This method of extracting directional wave spectra was also used by researchers from Proudman Oceanographic Laboratory (POL) to obtain directional wave spectra from radar data recorded from the R.R.S. Challenger in the southern North Sea (Proctor & Wolf, 1990).

This method is now used in the commercially available WAMOS II radar recording and analysis system (Reichert et al., 1998), one of which is now installed on Hilbre Island in the POL Coastal Observatory. Wolf & Bell (2001) demonstrated a slightly different approach using spectral ratios at each frequency which led to an empirically derived transfer function relating the amplitude of the spectrum of the square of the radar backscatter images to frequency to the power 5.

There are other forms of non-imaging radar that can also be used for oceanographic study. In particular, ground based High Frequency (HF) Doppler radar systems are gaining popularity due to their ability to measure surface currents and wave spectra at ranges of 50km or more (Crombie, 1955) (Barrick et al., 1974) (Wyatt et al., 1999). These systems are beyond the scope of the present study and will not be discussed further.

1.1.3 Development of Bathymetric Inversion Techniques During World Wars I and II

Perhaps one of the earliest applications of the remote sensing of the ocean surface was during World War I. Aerial photographs of the Flanders coastline were taken at carefully recorded times over several tidal cycles. At the same time, the tidal level was observed from a submarine in that vicinity. The photographs were studied and the position of the waterline determined, while the tidal level provided the contour height of the waterline. The succession of the photographs at different tidal levels was used to build up a map of the intertidal areas of the beaches studied (Bacon, 1932).

This technique was re-used in World War II to map virtually all of the beaches used for amphibious landings. However, the ability to map only the intertidal areas was considered a severe limitation because knowledge of the sub-tidal areas was often also required to determine how far seaward of the beach amphibious landing vessels would ground. With the drafts of some of the vessels being up to 4m a new remote surveying approach was sought. A project that involved scientists on both sides of the Atlantic devised methods of using carefully timed aerial photographs to map wavelengths and celerities. These were then inverted using lookup tables calculated from linear wave theory to provide an estimate of the bathymetry of the Normandy beaches (Hart & Miskin, 1945; Williams, 1946) ready for the D-Day landings. Research aimed at the same purpose was also carried out in the USA as part of the Waves Project, and is described in some detail by Bascom (1964). The techniques demonstrated in this early work are equally applicable to radar images recorded today.

1.1.4 Modern Developments of Bathymetric Inversion Techniques

Although the idea of using radar images to obtain average depths over relatively large areas was demonstrated by Hoogeboom in 1986, detailed mapping of underwater topography using radar images of waves was not attempted until the present study (Bell, 1998, 1999). The details of this will be explored in later chapters. Hessner et al. (1999) followed with a similar approach.

As was apparent from the work done in the 1940s, photographic techniques are equally useful for providing the wave images required for bathymetric mapping. It is therefore not surprising that researchers have also focused on modern developments in this direction. Dugan et al. (2001a, 2001b, 2003) have demonstrated an evolution of the airborne photographic technique using a geo-referenced video imaging system. The data is analysed using a virtually identical method to that developed by the Young et al. (1984) using the 3-D FFT technique and the fitting of the linear dispersion equation. As such this suffers from the same limitation of requiring quite a large analysis area. Piotrowski & Dugan (2002) also published a comprehensive analysis of the accuracy of their system together with the sources of error.

Airborne systems are obviously ideal for military purposes, but are prohibitively expensive and impractical for routine monitoring. Ground based video imaging systems have gained a great deal of popularity, mostly due to the ARGUS video network initiated by Lippmann & Holman (1989, 1990). These systems need to be mounted as high as possible to obtain a good view of the sea, and have a resolution that deteriorates rapidly with range. Davidson at the University of Plymouth (unpublished work) has demonstrated bathymetric inversions using linear depth inversion over ranges of a few hundred metres on video image sequences recorded in shallow water areas.

1.2 Data Availability

Various radar datasets have been collected by the author using X-band and millimeter (mm) wave radars of which only some have contributed to this thesis. The brief chronology of these datasets below puts the data that has been used into the wider context of the radar work at POL More detailed discussions of the particular datasets that have been used for this work are given in Chapter 4.

1.2.1 Winter 1994-5 Holderness Project, United Kingdom

This was the first deployment of the X-band radar system from a land based station. The Holderness project was part of the Land Ocean Interaction Study (LOIS) (Prandle et al., 1996). The aim of the radar deployment was to collect radar data in order to obtain 2-D directional wave spectra close to the coast using the method of Young et al. (1985) for offshore wave spectra. It was while carrying out initial analyses to transform the 2-D wavenumber spectra generated by analysis of the radar image data into frequency spectra that the effects of variable water depth were noted. In order to transform the wavenumber spectra into frequency spectra, linear wave theory was used, requiring a value of the water depth. This was not a problem for offshore measurements where the water depth could be considered infinite (i.e. linear deep water approximation) for the purposes of the transformation of coordinates.

No accurate bathymetric survey of the area viewed by the radar was available, and the tidal variation was of similar order (3-4m) to the low resolution bathymetry shown by Admiralty charts of the area, so this lack of an accurate water depth was a problem. The data itself was recorded every 3 hours and 32 images per record were collected to a range of just over 1200m. The sea conditions during most of the deployment were below the threshold visible on the radar, except for one extreme storm during the New Year period that removed the majority of the sand from the beach and destroyed several pressure sensors that had been cabled into the beach.

1.2.2 Winter 1995-6 Holderness Project, United Kingdom

The radar was deployed again from the same site but with upgraded disk drives, allowing more images to be collected more frequently than during the first deployment. This time, 64 images in a row were collected during each record, and the records were taken every 1.5 hours. Again, no bathymetric survey of the area was made. The weather during this season

was unusually stormy, providing a number of events during which good quality radar data were recorded.

It was around this time that the author developed the idea of turning the problem of a lack of bathymetry data on its head and using the radar data to try and map the water depth using the wave transformation observed when trying to transform wavenumber spectra to frequency spectra. These data were used for the early part of this project in which the feasibility of the idea was investigated, with the results published in Bell (1999).

1.2.3 Winter 1998 EU COAST3D Project – Egmond aan Zee, The Netherlands

The European Union funded COAST3D project (Soulsby, 1998) was designed as a two site project to collect a suitable dataset for validating inshore hydrodynamic models. The Egmond site was chosen as an approximately 2D site, characterized by a long straight beach with a shore parallel double sand bar system. POL's original commitment to the project was for the deployment of acoustic instrumentation, but it also provided an excellent opportunity for collecting radar data in an area in which accurate bathymetric surveys and tidal records would be taken.

As a late addition to the project, a purpose built radar tower was constructed on one of the beach stations, and the radar deployed to record 64 images per record on an hourly basis. Unfortunately, during the initial setup of the equipment, the PC used to record the radar data ceased to function, so a replacement had to be obtained. This new PC proved to have an unexpectedly poor clock, leading to inaccuracies of up to 45 minutes in the logged time of each record over a two week deployment. By the time this was realised, it was too late to design a solution and hence temporally accurate comparisons between actual water levels and radar derived water levels could not be made, therefore data from this project will not be explored further here.

1.2.4 Spring 1999 EU INDIA Project – Ancao Tidal Inlet, Faro, Portugal

This EU funded project, the **IN**let **D**ynamics **I**nitiative **A**lgarve (INDIA), was designed to study the mechanisms involved in the evolution of an artificially opened but naturally evolving tidal inlet in a chain of barrier beaches in the Algarve region of Portugal using both experiments and modelling. The radar was deployed on a raised gantry on a jack-up barge (Williams et al., 2003a). The barge spent most of its time located in the inlet itself, but was moved about 200m behind the inlet at the end of the deployment, allowing an unobstructed

radar view of the inlet during a wave event. The clock problem discovered during the Egmond experiment was solved in time for this deployment by using a GPS system to correct the PC clock of the radar recorder on an hourly basis. These data have been used in Chapter 8 of this thesis to observe the evolution of the inlet and the surrounding beaches. All the data from the INDIA project are available to the public in line with EU funding policy.[1]

1.2.5 Winter 1999 EU COAST3D Project – Teignmouth, United Kingdom.

This was the second phase of the COAST3D project, the location being chosen as a challenging 3-D site for the modelling work. The Teignmouth study area included a rocky headland flanking the inlet to a river estuary, inside which is a working port. The ships operating in relation to the port have to navigate through a set of cyclically evolving sand banks at the mouth of the inlet, the outer edge of which is regularly dredged to maintain a navigable channel. The same multinational teams from the Egmond experiment combined forces to deploy a large suite of instruments including wave, current and tide monitors. High quality bathymetric surveys were also carried out, with all data being made available to all partners. Data from this experiment has been used in Chapter 7 to verify that the bathymetry inversion technique is applicable at more than one site. All the data from the COAST3D project are now available to the public in line with EU funding policy.[2]

1.2.6 Winter/Spring 2002 Faro Beach, Portugal

This was a follow-up to the INDIA project, funded by POL, to obtain further radar data and to test a new mm wave radar. Researchers from the University of Algarve were conducting experiments at a site approximately 2km alongshore of the inlet on a straight section of beach, so the opportunity was taken to deploy both X-band radar and mm wave radar overlooking the same area of beach. The researchers from the university of Algarve carried out a survey of several cross-shore transects out to a range of approximately 1.5km, and also performed a topographic survey of the beach itself, both of which were made available for this study. The experiment took place during a moderate wave event, allowing high quality radar pictures to be recorded to the maximum range of the instruments. This data has been used in Chapter 6 to verify the data analysis and depth inversion technique.

---

[1] Data from the INDIA project is available on request from the British Oceanographic Data Centre.

[2] Data from the COAST3D project is available on request from Delft Hydraulics in the Netherlands for the Egmond project and from Hydraulics Research Ltd in the UK for the Teignmouth project.

1.2.7 Winter/Spring 2003 Ancao Inlet, Portugal

This was a further visit to the Faro inlet, this time aimed specifically at collecting data covering the inlet, as it was not possible to collect the data required at the inlet during the 2002 visit. Several wave events were recorded using the X-band radar, providing excellent data for bathymetric inversions. No surveys were carried out this time. The age of the radar recording equipment started becoming a significant problem during this deployment as it became increasingly unreliable. This system has now been 'decommissioned' pending the design of a new radar recorder. The data recorded during this experiment have been used in Chapter 8 to infer bathymetric changes related to the inlet migration since the 1999 INDIA deployment.

1.3 An Introduction to Waves

The behaviour of waves on the ocean can be described mathematically using wave theory. The terminology and governing equations of wave theory are described below. There are various ways of solving these equations to allow parameters such as the wave length to be predicted for a given wave period, height and water depth. An investigation of a selection of these is given later in Chapter 2.

1.3.1 Definition of Coordinate System

The coordinate system and terminology used here to describe waves and their behaviour is illustrated in figure 1.3.1.

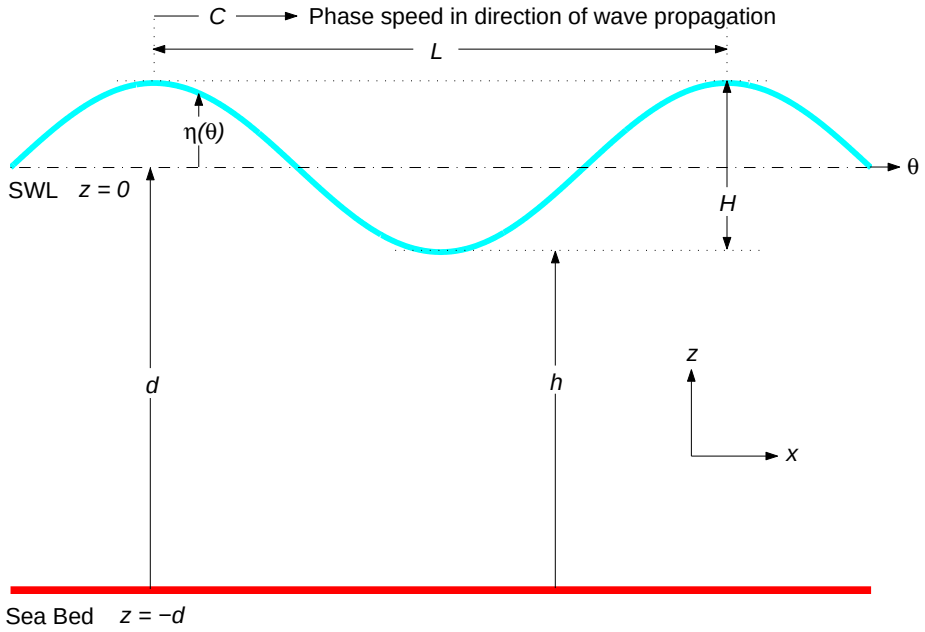

Figure 1.3.1. A sketch illustrating the definitions of various wave parameters.

The definitions are as follows:

Wave period	T
Wave height (peak-trough)	H
Wavelength (peak to peak, or trough to trough)	L
Water depth (undisturbed)	d
Water depth at the wave trough	h
Celerity or phase speed	C
Wave phase	θ
Wave profile or surface elevation	η
Still water level	SWL

1.3.2 The Development of Waves

Water waves have their origin in the wind. A small breeze is sufficient to roughen the surface of the water, generating small capillary waves with wavelengths of less than 1.73cm, rounded crests and v-shaped troughs (Kenyon, 1998). The capillary waves, whose restoring force is surface tension rather than gravity, give the breeze something to 'get hold of' and as the wind interacts with the capillary waves more energy is transferred from the wind to the sea and gravity waves form (Phillips, 1957; Miles, 1957). The mechanisms of energy transfer involve resonance with the turbulent wind eddies, but the details are still debated as experimental data by various researchers are not fully explained by theory (Janssen, 2004). As the wind continues to blow, energy continues to be transferred to the waves and their height increases to the point where their steepness – the ratio of height to length – reaches a critical value of about 1 in 7. At this point the wave cannot accept more energy and any further energy input results in white capping, whereby the crest of the wave becomes unstable i.e. the wave breaks. Longer waves can accept more energy, and so the sea state begins to grow, the waves becoming longer and higher as long as the action of the wind continues.

The waves propagate away from the generation region, undergoing a gradual transformation as they do so. Shorter period waves travel slower than longer waves and, as they propagate, spectral evolution occurs whereby the energy from the shorter waves is gradually transferred to the longer, faster moving waves. Thus there is rarely just one frequency of wave present, but rather a whole spectrum of different periods, heights and directions, combined, at least to first order, by superposition. A particularly good conceptual illustration of this was given by Bascom (1964), shown in Figure 1.3.2. It should be pointed out that linear superposition is not a perfect model to describe the combining of the different waves, as this could produce waves of unrealistic height and steepness if too many crests or troughs coincide.

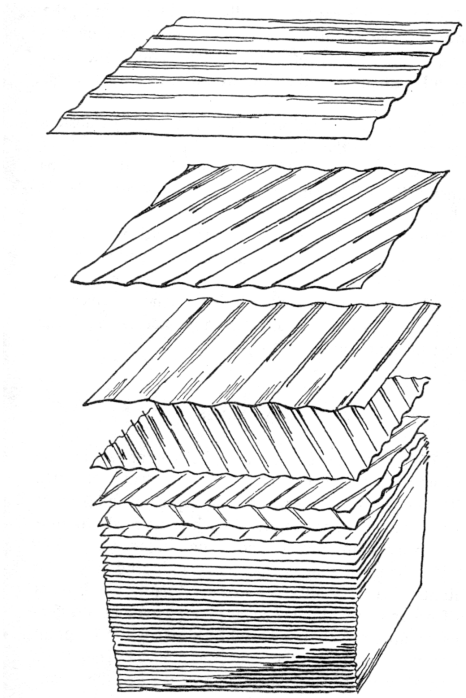

Figure 1.3.2 A conceptual diagram showing how the linear superposition of different wave trains makes a complete sea state (from Bascom 1964).

The gradual separation of waves of different wave periods as they travel from the area in which they were generated is known as frequency dispersion, and has been used in the past to determine the approximate location of the storm that generated them. Munk (1963) described how pressure records of waves recorded off the coast of southern California showed peaks in wave energy that moved up the frequency scale over several days. These peaks in wave energy started initially with long period faster travelling waves. Then during the following few days the peak in wave energy gradually changed to shorter period, slower moving waves. The rate of change of the peak in the wave frequency was used to estimate the distance travelled by the waves from their originating storm, and the angle of approach used to estimate their bearing. The range and bearing indicated that the waves measured at California had in that particular case originated from a storm located somewhere between New Zealand and Antarctica. The speed at which the wave energy travels is not the wave phase speed as might be expected, but rather the wave group velocity, which in deep water is half that of the phase speed, but tends to the phase speed in shallow water.

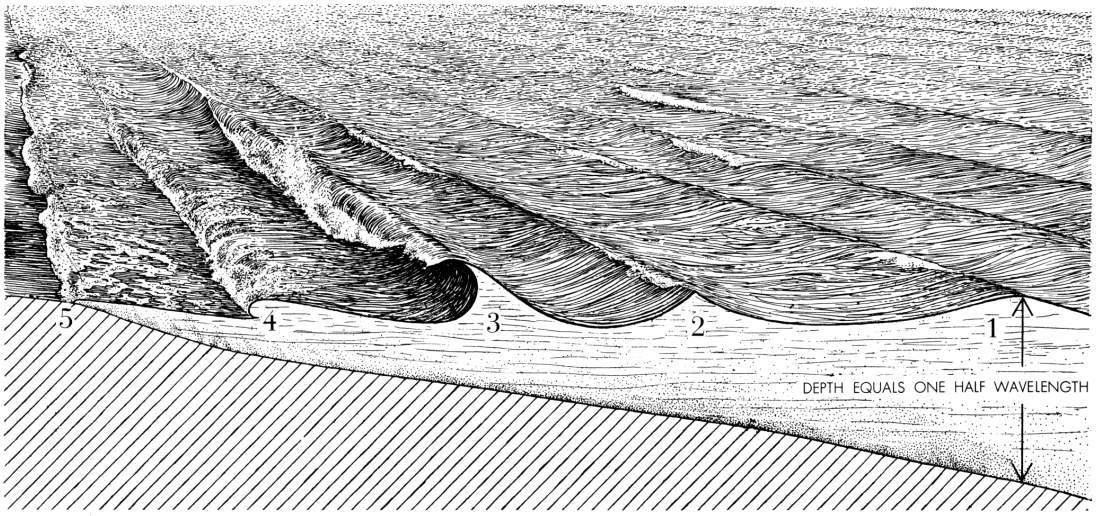

Figure 1.3.3 A conceptual diagram of wave transformation in shallow water on approaching a beach. (From Bascom - 1959).

For waves travelling in water depths of more than about half their wavelength the orbital excursions of the water particles at the sea bed due to the waves tend to zero; these so-called 'deep water' waves do not 'feel' the sea bottom. However, once they travel into water depths of less than half their wavelength, the orbital excursions of the water particles at the bed begin to increase and the waves feel the bottom and begin to slow down. Figure 1.3.3 illustrates the way the wave is transformed from that point onwards beginning with stage 1 as the wave just begins to feel the bottom. As a wave slows down, in the absence of currents its period remains constant and its wavelength is reduced; very little energy is lost, and so the wave height increases and the waves are transformed from a largely sinusoidal shape to one having shorter sharper crests and longer flatter troughs – stage 2 in Figure 1.3.3. In water depths of approximately 1.3 times the wave height, the propagation of this wave without significant energy loss is no longer sustainable. On relatively steep beaches since the wave is still slowing down, the crest ends up going faster than the rest of the wave, and it curls over and becomes a plunging breaker – stage 3. A foam line forms from the remains of the wave and the collapsed wave moves on in the form of a bore – stage 4. Finally the energy of the wave dissipates and the remaining swash runs up the beach face – stage 5. On less steep beaches, at stage 3 the crest merely spills down the front face of the wave; this is known as a spilling breaker. Spilling is also the dominant breaking mechanism in deeper water, amongst other things reducing the height of excessively steep waves generated by the superposition of different wave fields.

In order to allow the properties of waves to be predicted as they move through this sequence of transformations, numerous wave theories have been developed to describe the shape and properties of the waves. Some are applicable in only one stage of the above sequence, while others are applicable in more than one. All are approximations, and none are perfect. The key to the successful application of such theories is to use them only under the conditions for which they were developed. Many of the theories are mathematically rigorous solutions to the equations of motion defined for the water particles. However, these equations of motion are themselves based on assumptions, and hence an exact mathematical solution may not necessarily lead to a correct physical solution.

The equations relating wavelength, period, wave height and water depth are known generically as dispersion equations. Frequency dispersion describes the manner in which a field of propagating waves consisting of many frequencies would separate or ‘disperse’ due to the different wave speeds or celerities of the various frequency components, with longer period waves travelling faster than shorter period waves. Amplitude dispersion is a similar effect taken into account by higher order wave theories in which waves of larger wave-height have a higher celerity for a given wave frequency than those of lower wave-height.

1.3.3 Wave Theory Formulation

The formulation of all the wave theories discussed here uses a set of basic assumptions in order to solve the problem of wave motion (USACE Coastal Engineering Manual, 2002). Considering a wave progressing along a channel, at each point, (x,y,z) the fluid has a velocity:

$\mathbf{v}(x,z,t) = u(x,z,t)\mathbf{i} + v(x,z,t)\mathbf{j} + w(x,z,t)\mathbf{k}$.

although the v component in a channel could be neglected as it would be uniform across the channel.

- The water is to all intents and purposes incompressible and hence is assumed to have constant density. In an incompressible fluid, the equation of continuity (of mass) applies such that the velocity **v** of the water satisfies the equation:

  $$\frac{\partial u}{\partial x} + \frac{\partial w}{\partial z} = 0$$

- The fluid is considered irrotational, i.e. the water particles do not rotate. If the fluid is irrotational, the velocity may be expressed in terms of a velocity potential Φ such that

  $$u = \frac{\partial \Phi}{\partial x} \text{ and } w = \frac{\partial \Phi}{\partial z}$$

  This velocity potential is a scalar function whose gradient is the velocity vector.

- Introducing the velocity potential into the equation of continuity yields the Laplace equation which must be satisfied:

  $$\frac{\partial^2 \Phi}{\partial^2 x} + \frac{\partial^2 \Phi}{\partial^2 z} = 0$$

- For a two dimension flow, in an incompressible fluid, there is a stream function Ψ which is orthogonal to the velocity potential such that;

  $$\frac{\partial \Phi}{\partial x} = \frac{\partial \Psi}{\partial z} \text{ and } \frac{\partial \Phi}{\partial z} = -\frac{\partial \Psi}{\partial x}$$

  These equations are known as the Cauchy-Riemann conditions.

- The bed is a horizontal, fixed, impermeable boundary, which implies that the vertical velocity at the bed must be zero:

  $$\frac{\partial \Phi}{\partial z} = 0 \text{ at the bed.}$$

- The surface is always made up of the same fluid particles, i.e. the fluid particles on the surface stay on the surface, assuming the waveform is invariant, i.e. the waves are not breaking.

$$\frac{\partial \eta}{\partial t} + u\frac{\partial \eta}{\partial x} = w$$

This is known as the kinematic free surface boundary condition.

- The pressure in the fluid at the free surface is equal to the atmospheric pressure and is assumed to be constant:

$$\frac{\partial \Phi}{\partial t} + \frac{1}{2}(u^2 + w^2) + g\eta = 0$$

at the surface $z = \eta(x,t)$, known as the dynamic free surface boundary condition.

The solution of this combination of equations is the essence of the various wave theories discussed in the following sections. Linear theory assumes that the waves are of small amplitude and discards all but first order terms to simplify the problem. Stokes and Cnoidal theories make assumptions about the waves that hold only for certain combinations of wave height, wavelength and water depth in order to allow the use of their respective mathematical techniques to generate solutions to these equation but, outside these defined conditions, the solutions become unrealistic. Stream function theories use numerical methods to solve the equations without making additional assumptions, and are therefore the most accurate and widely applicable method of solving the problem, although a price is paid for this in computational effort.

1.3.4 Depth-limited Wave Breaking

The wave theories investigated below also involve one final and very important assumption – that the waves are not breaking. The wave dispersion equations reviewed in Chapter 2 can be split into two categories – ones that are solved analytically from the basic wave equations using a variety of techniques, and ones that are approximations to the curves produced by such solutions, developed for mathematical simplicity and ease of computation. The analytically derived equations that are applicable to intermediate to shallow water tend to become unstable and do not converge to a solution where the wave-height exceeds a presumed theoretical limit for that depth. For example, Borgman's (1986) DSFWAV routines for Dean's stream functions use the instability point in the equations to actually define the maximum possible wave height. Other researchers have used alternative methods. A brief review of a few definitions of the breaking point of a wave is given although this is not an exhaustive list as the identification of the exact breaking point is not necessary in the present study. The practical result of this instability point in the analytically derived equations is that they cannot be used to determine wave behaviour within the breaker zone,

while the approximation based equations can at least provide a realistic estimate because they are not constrained to solve the wave equations.

The highest possible depth limited solitary wave (to be discussed in the following section) has been determined theoretically by a number of researchers including Lenau (1966) and Hunter & Vanden-Broek (1983) to have a maximum height of:

$$H_b = 0.83 d_b \tag{1.3.4.1}$$

where the subscript $_b$ refers to the conditions at the break point.

Miche (1954) arrived at a theoretical breaking limit for monochromatic periodic waves of:

$$H_b = 0.142 L_b \tanh \frac{2\pi d_b}{L_b} \tag{1.3.4.2}$$

where L_b is the wavelength of a wave as it breaks.

Williams (1981) used very high order Stokes expansions to determine the maximum theoretical height for monochromatic periodic waves. Fenton (1990) neatly summarised the solitary wave limit and the results of Williams with an empirical equation, which he gave as:

$$H_b = \frac{0.141063 \frac{L_b}{d_b} + 0.0095721 \left(\frac{L_b}{d_b} \right)^2 + 0.0077829 \left(\frac{L_b}{d_b} \right)^3}{1 + 0.078834 \frac{L_b}{d_b} + 0.0317567 \left(\frac{L_b}{d_b} \right)^2 + 0.0093407 \left(\frac{L_b}{d_b} \right)^3} d_b \tag{1.3.4.3}$$

This definition of wave breaking will be used to illustrate graphically the limit of the analytically-solved equations in the following section.

Thornton and Guza (1982) observed from field data that spectral waves rarely reach the theoretical limits for monochromatic waves, but actually break at a somewhat lower level for which they determined the rms height to be:

$$H_{rms} = 0.42 d_b$$

which corresponds to

$$H_b = 0.6 d_b \tag{1.3.4.4}$$

Other more complicated expressions have been derived which also include the beach slope as a parameter, but they will not be explored here.

1.4 Wave Spectra

Waves are usually only of a single frequency in laboratory flume facilities. In the open sea a range of wave frequencies, heights and directions are normal and these are best represented by wave spectra. Waves can be measured by various types of instruments, the standard usually being tethered buoys containing accelerometers floating on the surface of the water, although Acoustic Doppler Current Profilers (ADCPs) are becoming a popular alternative, using measurements of wave orbital velocities to infer the wave spectra. Depending on the complexity of these instruments, either non-directional or directional wave spectra are produced. The surface movements of the buoy are measured as a proxy for the movement of the water surface, usually for a period of 1024 seconds. A spectrum of these time series are then produced using the Fast Fourier Transform algorithm (FFT) and instrument calibrations applied. The resulting wave spectra give a breakdown of the amount of energy in a number of frequency bands and, if the instrument has directional capability, a dominant wave direction for that frequency, a concept illustrated well by Figure 1.3.2. It is a general characteristic of these instruments that they assume a single wave direction at a particular wave frequency. Seas with waves at similar frequencies but from different directions are generally poorly represented by such data as the two wave fields are difficult to discriminate.

Wave spectra and various statistical parameters derived from them are used in various sections of this work, and so a brief review of their definitions and derivations is necessary. Prior to the invention of the FFT algorithm, many of these parameters were derived by wave train analysis in which a time series was analysed wave by wave. With the adoption of the FFT as a computationally efficient method of calculating spectra, statistical approximations to these parameters based on spectral moments were developed and have largely replaced those calculated from wave train analysis.

The moments of an energy spectrum $E(f)$ over a range of frequencies f are defined as:

$$m_i = \int_0^\infty f^i E(f) df \qquad 1.4.1$$

As an example with which to illustrate these parameters, a single wave energy spectrum from the INDIA experiment has been chosen and is shown in Figure 1.4.1. This was produced by a Triaxys directional wave buoy at 16:00 on the 3rd March 1999. The spectrum shows two distinct peaks, one with a frequency of 0.085 Hz or a period of 11.8 seconds corresponding to swell waves, and one at 0.225 Hz or 4.44 seconds, corresponding to locally generated wind waves.

The most easily determined parameter is the spectral peak period, indicated in Figure 1.4.1. This is generally referred to as T_p, or the period of the maximum energy in the spectrum, in this case 4.44 seconds.

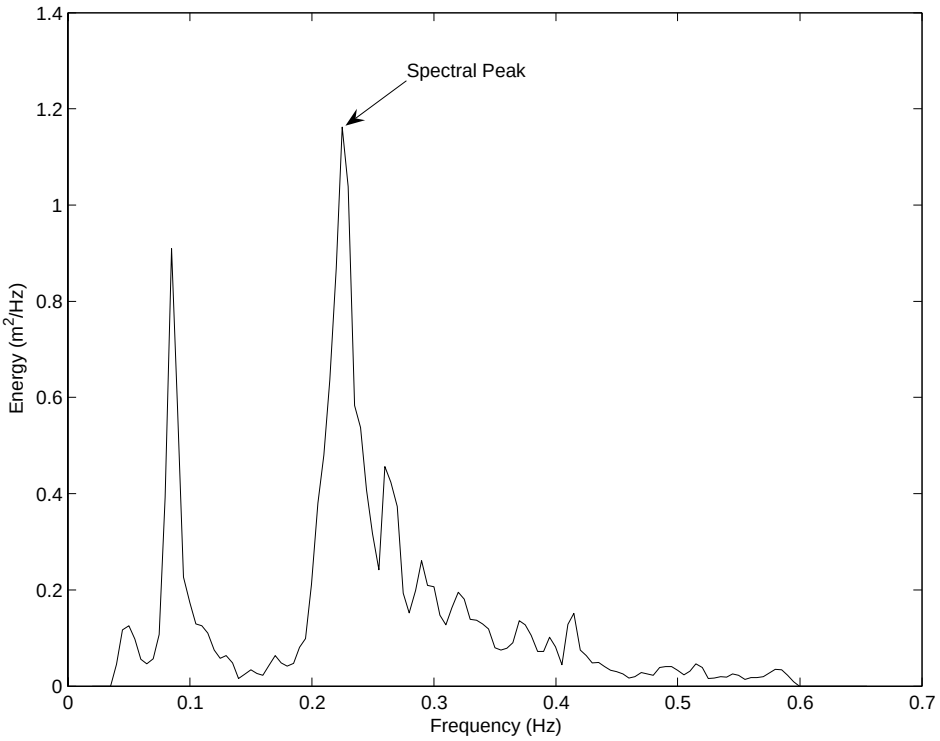

Figure 1.4.1 An example of a wave power spectrum from the INDIA experiment, recorded by a Triaxys wave buoy at 16:00 on 3rd March 1999.

The next parameter that is commonly quoted is the significant wave height, H_S. In the days before wave buoys, the significant wave height was the wave height estimated by observers of the ocean. From wave train analysis this was found to correspond to the mean of the highest third of waves in a given wave record, denoted $H_{1/3}$.

An approximation to this can be calculated from the zero-th moment of the spectrum m_0, using the equation:

$$H_{m0} = 4\sqrt{m_0} \qquad 1.4.2$$

which in physical terms is the area under the graph shown in Figure 1.4.1.

For this example, $H_{m0} = 1.11\,\mathrm{m}$

Another measure of the wave period that is commonly quoted is the zero crossing period T_Z. This is calculated using wave record analysis by taking the average of the times between successive zero up-crossings or zero down-crossings, and is approximated using spectral moments by the equation:

$$T_Z \approx \sqrt{\frac{m_0}{m_2}}, \text{ sometimes denoted } T_{02}. \qquad 1.4.3$$

For this example, $T_Z = 3.79$ seconds.

The maximum wave height can be estimated using the significant wave height and the zero crossing period, provided the length of the times series is known (Khandekar, 1989):

$$H_{\max} = H_S \sqrt{\frac{\ln N}{2}} \qquad 1.4.4$$

where N is the number of waves in the time series, calculated from the total record length of 1024 seconds:

$$N = \frac{1024}{T_z} = \frac{1024}{3.79} = 270 \text{ waves}$$

giving a maximum wave height of:

$$H_{\max} = 1.11\sqrt{\frac{\ln 270}{2}} = 1.86\,\text{m} \text{ for the example used here.}$$

This seems somewhat high, but the parameters calculated from spectral moments have been derived by making assumptions about the shape of the energy spectrum that do not necessarily hold for multimodal seas, and so should be treated with some caution.

Chapter 2: Wave Dispersion equations

A key element in the present study is the relationship between the period, wavelength and height of gravity waves, and the water depth in which they travel. The intention is to use this relationship inversely to determine water depth from the wave behaviour. During early stages of the present study linear wave theory, in which the relationship between wavelength, period and water depth does not depend on wave height, was used and found to provide acceptable results in most water depths, but was found to over predict the water depth in very shallow water. This is because waves with a height that is a significant proportion of the depth in which they travel do not conform to the assumptions of 'small' wave amplitude upon which linear theory is based. Therefore equations that more accurately describe this non-linear behaviour were sought. To this end a wide-ranging investigation of the subject has been carried out involving the testing of several types of wave dispersion equations to determine their suitability for this task, in terms of regions of applicability, accuracy, ease of use and computational effort. These wave dispersion equations can be grouped according to their method of derivation, usually in terms of the simplifications that have been made to reduce the complexity of the governing equations and hence their solutions, but which also limit the region of applicability of the resulting dispersion equations.

The standard against which the accuracy of the various theories is tested involves comparison with that of Fenton's stream functions, regarded as the most widely applicable and accurate method of solving the equations describing wave motion, and recommended in the USACE Coastal Engineering Manual (2002) for applications where accuracy is the principal requirement. Because of this, the review begins with stream function wave theories rather than the more usual linear theory.

Dimensionless plots comparing the predictions of the various wave dispersion equations are shown overlaid on those of Fenton's stream functions. These are generated for waves of period 4-14 seconds and 1m wave-height – typical of waves found in most European coastal waters. As a specific example, waveforms are plotted for waves having 8 second period and 1m wave-height propagating in 3m water depth, and these are compared with the stream function equivalents. During all of the experiments in which radar data have been collected, significant wave heights rarely exceeded 2m, and were most commonly observed at approximately 1m, so limiting the comparisons to the 1-2m wave height range was considered sufficient for this study. The best result would be for the predictions from other

dispersion equations to match those of Fenton's stream functions. If the predictions deviate from the stream function results by a sufficient amount to cross a stream function line corresponding to a different wave period, this would indicate a very poor prediction, as can be seen to happen in section 2.2 with long waves under linear theory.

The Matlab routines used in this chapter are supplied in the Technical Appendix on the CD accompanying this thesis.

2.1 Stream Function Wave Theories

Any periodic wave train can be approximated by a Fourier series of sine or cosine waves summed together to generate the final wave form. In the case of water waves, the task is to find the coefficients of each term in the series such that the hydrodynamic equations described above are satisfied. In 1961 Chappelear suggested the approach of solving a system of non-linear equations to determine these Fourier coefficients numerically. Similar methods have been published by Dean (1965), Chaplin (1980) and by Rieneker and Fenton (1981). These methods are now generally accepted to be the most accurate way of determining the properties of non-breaking waves.

Dean (1965) published perhaps the most widely applied stream function theory. The calculations necessary were so involved and laborious that, as well as publishing the approach, he also published tables of the solutions covering the range of possible wave conditions, from which desired parameters could be interpolated if not listed exactly. This allowed users to apply the technique without going through the entire analysis procedure.

Borgman and Petrakos (1986) produced a Matlab toolbox – DSFWAV [3](Dean's Stream Function Wave solutions) that interpolates across Dean's tables to give solutions for any wave condition. The wave heights in shallow water are limited to the maximum non-breaking height. This is determined by the software as the point beyond which the stream functions become unstable in the calculations.

In some cases, Dean's stream functions converge to solutions in which more than one crest per wave profile is observed. Dalrymple and Solana (1986) explored this phenomenon in some detail and concluded that the additional local maxima, while being mathematically

[3] This is available on the University of Wyoming web site, although one of the essential files was missing, but was kindly supplied by Prof. Borgman when contacted.

correct, are physically incorrect alternative solutions of the equations. They suggested several strategies for avoiding these solutions such as re-defining the initial estimate used to initialise the iterative procedure.

Another easily accessible method of using Dean's stream functions has been given by Dalrymple[4] (latest revision 2001) who has placed a Java applet allowing single calculations to be performed on his web site.

Rieneker and Fenton (1981) solved their system of equations more simply by using Newton's method of iteration, predictions from linear theory providing the initial solution. Fenton (1988) later published a modified version of the technique allowing for applications under more general wave conditions which could be extended to higher orders quite easily. In that paper he gave the complete listing of his FORTRAN program for determining wave properties[5]. One of the refinements included in that program was to approach the solutions for large waves in a number of height steps, each step supplying the initialisation for the next height iteration. This overcame a problem of the solution not converging for high waves and also long waves, for which the initial linear solution is not adequate, effectively guiding the course of the iteration to the correct solution – a similar problem to Dean's extra local maxima.

---

[4] Dalrymple's Java applet for calculating Dean's stream functions can be found at the University of Delaware website: http://www.coastal.udel.edu/faculty/rad/streamless.html

[5] For the purposes of the present review Fenton's FORTRAN program has been re-coded in Matlab by the author and modified to limit the wave-height to the maximum non-breaking height in order to prevent the solutions becoming unstable in very shallow water.

2.2 Linear Wave Theory

This is by far the most well known and widely used mathematical description of waves available. Developed by Airy in 1845, the principal assumption that characterises this theory is that the waves are of small amplitude; hence the effects of finite amplitude dispersion are neglected. Despite this limitation, the resulting equations have consistently proven sufficiently accurate for many applications. The linear dispersion equation is given by:

$$\omega^2 = gk \tanh kd \qquad (2.2.1)$$

This frequency dispersion relationship for transitional depths involves the tanh(x) function. Since this function has the property that for large x, $\tanh x \to 1$, and for small x, $\tanh x \to x$, simplifications can be made in the limits of deep and shallow water. These are tabulated below.

	Deep Water ($d/L > 0.5$)	Transitional Depths ($0.5 > d/L > 0.05$)	Shallow Water ($d/L < 0.05$)
Phase speed (C)	$C_0 = \frac{gT}{2\pi}$	$C_0 \tanh kd$	$\sqrt{gd}$
Wavelength (L)	$L_0 = \frac{gT^2}{2\pi}$	$L_0 \tanh kd$	$T\sqrt{gd}$

where the wavenumber $k = \frac{2\pi}{L}$ and the subscript '$_0$' denotes the deep water limit.

The predicted water surface profile at a particular instant is a sinusoid described by the equation

$$\eta = a \cos kx$$

The dimensionless plot in figure 2.2.1 demonstrates how linear wave theory breaks down when pushed outside its region of validity which requires small amplitudes. The wavelength of finite amplitude waves is underestimated by linear theory, with the problem increasing in severity near the breaking limit. The wave breaking limit is that of Fenton (1990) (equation 1.3.4.3). For the 1m wave height used in the example, the limit of validity for linear theory based on Figure 2.2.1 could be determined as waves of less than $H/d \approx 0.2$, i.e. a depth of approximately 5m. However, the validity of linear theory is actually related to the wave steepness *H/L* rather than *H/d*, but as *H* increases, *L* will not increase under linear theory, and the same ratio will approximately hold, making the depth limit of applicability double with doubling waveheight.

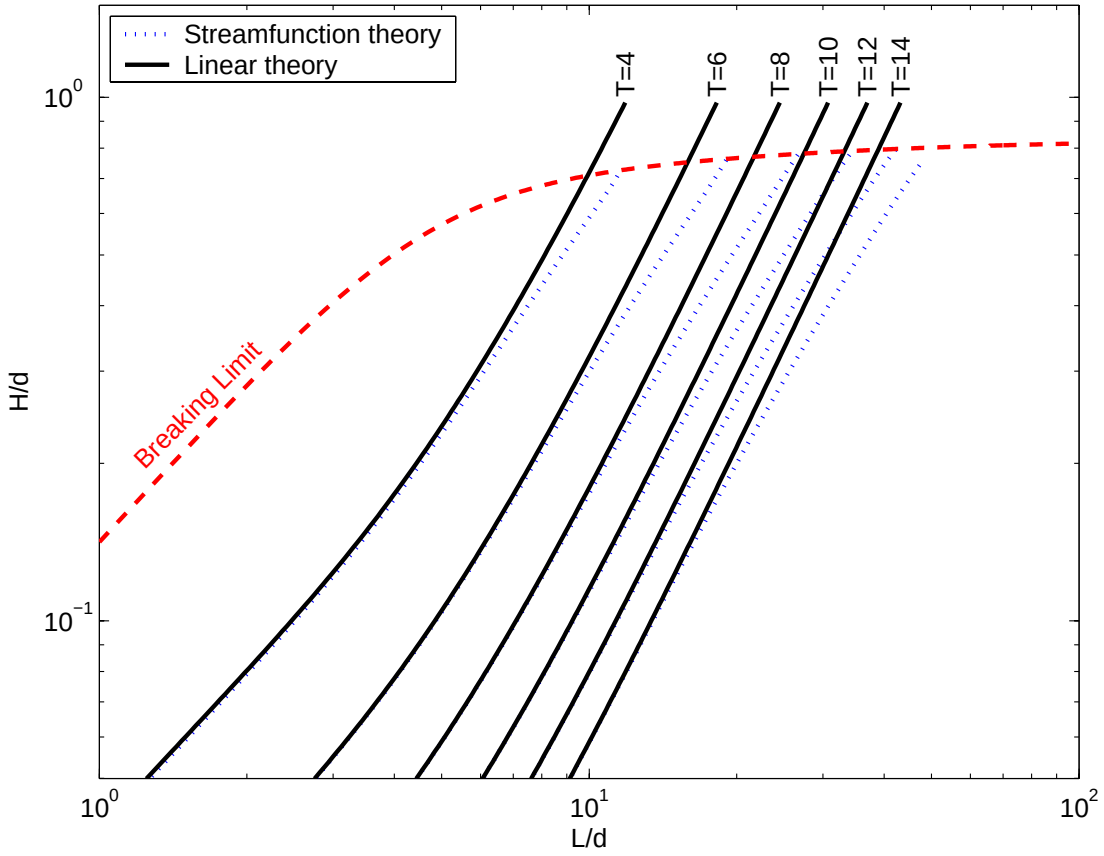

Figure 2.2.1 A comparison of linear theory predictions of wave behaviour compared with those of Fenton's stream function theory calculated for 1m high waves.

The plot of the sinusoidal wave form predicted by linear theory shows a considerable discrepancy from that of the corresponding stream function waveform for the 8 second, 1m wave in 3m depth, as shown in figure 2.2.2. The trough of the waveform based on stream function theory is considerably shallower, while the crest is higher than that of the linear wave, and the wavelength and hence celerity is larger.

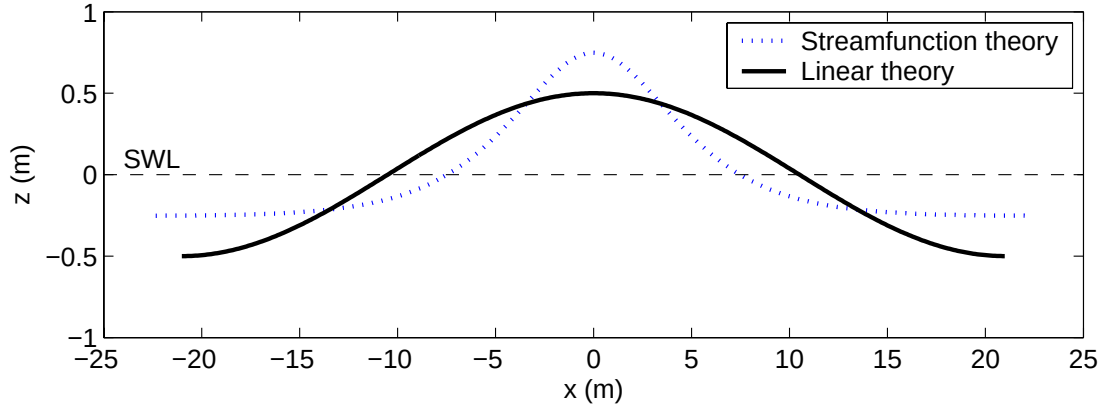

Figure 2.2.2 The sinusoidal wave profile described by linear wave theory for 8 second waves in 3m water depth and 1m wave height, compared to that of stream function theory.

2.3 Approximations to Linear Wave Theory

One of the difficulties with linear wave theory is that the dispersion equation is transcendental in the wavelength L, i.e. there is no way to explicitly solve for L. One therefore has to resort to iterative methods that converge to a value for L. In many instances a simpler method of calculation would be preferred that does not require iteration. As a result, numerous researchers have expended considerable effort in order to arrive at a variety of more user-friendly approximations to linear theory. Fenton (1990) summarised a number of these very well, whilst pointing out that "the ability of each formula to approximate linear wave theory is rather better than that of linear wave theory to approximate the actual problem".

While approximations to linear wave theory do not advance the accuracy of wave predictions, they are worthy of brief discussion as a computationally efficient method of determining the initial value for the iterative schemes that characterise some higher order theories. A number of these expressions are listed below, together with their accuracies relative to linear theory.

Eckart (1952) produced the following approximation for the wavelength

$$L = L_0 \tanh^{\frac{1}{2}}\left(\frac{2\pi d}{L_0}\right) \tag{2.3.1}$$

which tends to $L = L_0$ in deep water, and to $T\sqrt{gd}$ in shallow water, i.e. identical to linear theory in the limits. The maximum deviation from linear theory was determined as 5% for waves having $\frac{L}{d} \approx 7$.

Fenton & McKee (1990) generalised Eckart's 1952 equation and optimised it to give

$$L = L_0 \tanh^{\frac{1}{\nu}}\left(\frac{2\pi d}{L_0}\right)^{\frac{\nu}{2}} \tag{2.3.2}$$

where $\nu = \frac{3}{2}$ gave a maximum quoted deviation of 1.7% from linear theory.

Hunt (1979) published a ninth order polynomial expansion, with an accuracy of 0.01%, which he truncated and optimised to the following fifth order expression which has a maximum deviation from linear theory of 0.1%

$$L = \sqrt{\frac{2\pi d L_0}{y + \left(1 + 0.6522y + 0.4622y^2 + 0.0864y^4 + 0.0675y^5\right)^{-1}}} \qquad (2.3.3)$$

where $y = \frac{2\pi d}{L_0}$.

There are also a number of expressions developed by other researchers which serve the same purpose, most of which approximate only long or short waves, and hence are of little interest to this discussion.

2.4 Stokes Theories

Stokes (1847) developed a perturbation wave theory to which the solution is a converging power series (essentially another Fourier series) in terms of $\varepsilon = {}^{kH}\!/_{2}$, where ε is assumed to be small. The first order Stokes term reduces to linear theory, with higher order terms acting as successive corrections that allow for amplitude dispersion.

As with other wave theories, a number of researchers have produced a variety of wave equations based on Stokes' work, several of which are presented below.

Stokes (1847) original 3rd order equation for the wavelength is as follows

$$L = L_0\left(1 + \varepsilon^2 \frac{\cosh 4kd - 2\tanh^2 kd + 8}{8\sinh^4 kd}\right)\tanh kd \qquad (2.4.1)$$

Struik (1926) produced the following equation (Mason & Hall, 1941), which is very similar in form to Stokes 3rd order equation.

$$L = L_0\left(1 + \varepsilon^2 \frac{\cosh 4kd + 2\cosh 2kd + 6}{8\sinh^4 kd}\right)\tanh kd \qquad (2.4.2)$$

Brink-Kjaer (1974) produced a 3rd order equation for a closed channel (i.e. zero net mass flux):

$$L = L_0\left(1 + \varepsilon^2 \frac{8\cosh^4 kd - 8\cosh^2 kd + 9}{8\sinh^4 kd}\right)\tanh kd \qquad (2.4.3)$$

Fenton (1985) presented the following 5th order equation:

$$L = L_0\left(1+\varepsilon^2\frac{2+7S^2}{4(1-S)^2}+\varepsilon^4\frac{4+32S-116S^2-400S^3-71S^4+146S^5}{32(1-S)^5}\right)^2\tanh kd$$

where $S = \text{sech}\ 2kd$ (2.4.4)

The waveform in this case is given by[6]

$$\eta = d+\frac{1}{k}\sum_i\sum_j B_{ij}\left(\frac{kH}{2}\right)^i\cos jkx \qquad (2.4.5)$$

where the extensive table of coefficients B_{ij} can be found in Fenton's 1985 paper.

As $d \rightarrow 0$ it follows that $S \rightarrow 1\text{-}2(kd)^2$ and Fenton(1985) showed that the coefficients of the higher order terms behave like extra powers of $(kd)^{-3}$, hence the effective expansion parameter is $\varepsilon(kd)^{-3}$, i.e. the contributions of the higher order terms will tend to dominate in this limit. Therefore if the series is to converge, both ε and $\varepsilon(kd)^{-3}$ must be small or each successive term will increase in magnitude instead of decreasing as intended. Ursell (1953) pointed out that the so-called 'Ursell parameter' serves as a measure of whether Stokes or other higher order theories are appropriate to the wave conditions. This parameter is defined by:

$$U_R = \left(\frac{L}{d}\right)^2\frac{H}{d} = \frac{L^2H}{d^3} \qquad (2.4.6)$$

High values of U_R indicate large, finite amplitude long waves in shallow water. Values of U_R of less than about 40 are generally recommended for the applicability of Stokes type theories.

A plot comparing the predictions of Fenton's 5th order Stokes theory with the predictions from stream function theory is shown in figure 2.4.1. Since these wave theory formulations should be, by definition, a converging series, it follows that if each successive term in the power series is not smaller than the last then it is pushing the theory beyond its usable limits. This cut off based on the convergence of the series has been used for the present study as a computational tool to eliminate potentially invalid solutions on the comparison plots shown here, rather than using an arbitrarily chosen Ursell number. However, the fact that this cutoff criterion for the applicability of the theory correlates well with the Ursell number is a

[6] During the coding of these algorithms in Matlab the author found that the cosine term is printed incorrectly both in Fenton's original 1985 paper and also in the 1987 errata, with a different error in each.

pleasing result. In this case, Fenton's fifth order Stokes theory can be seen to break down for Ursell numbers exceeding about 40.

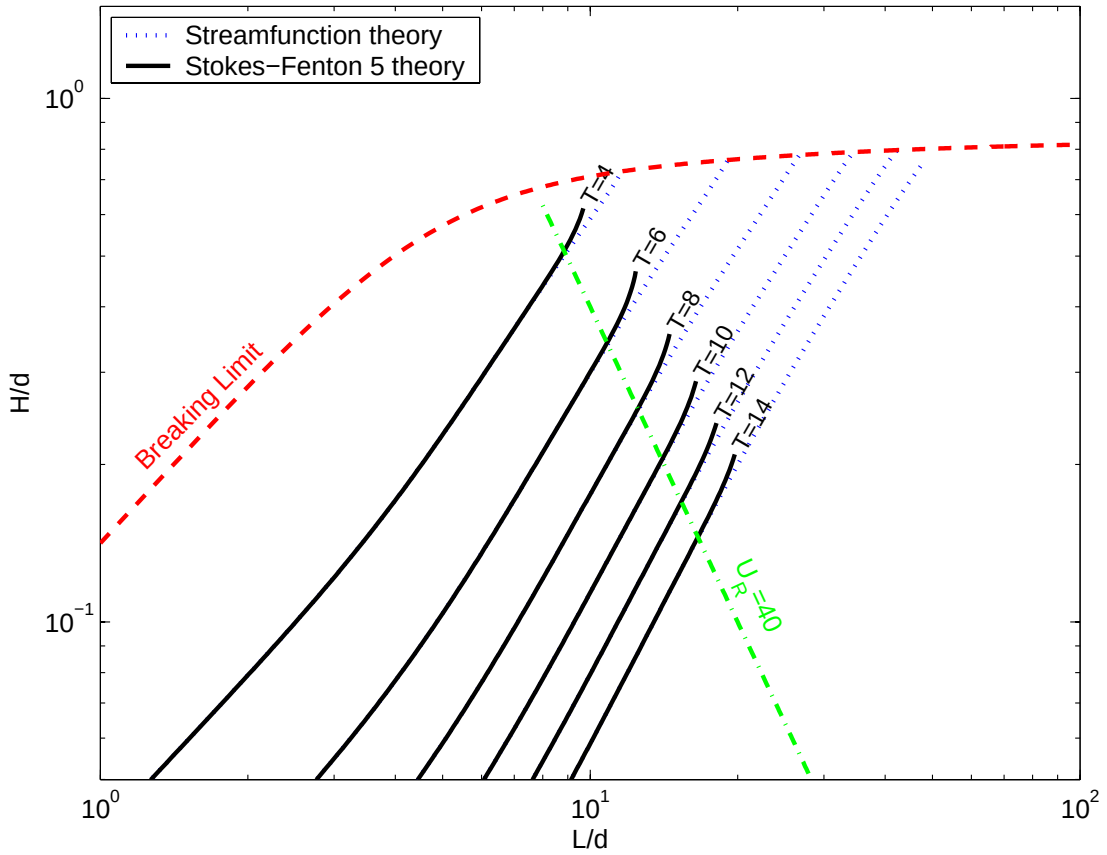

Figure 2.4.1 A comparison of Stokes-Fenton 5th order theory predictions of wave behaviour for H=1m waves with those of stream function theory. The line representing an Ursell number of 40 is shown as a suggested cut-off point for the applicability of Stokes-type theories.

The test wave of H=1m, d=3m and T=8seconds has an Ursell number of approximately 75, and as such is outside the limits of applicability for Stokes type theories. Plotting this waveform in Figure 2.4.2a as the solid line demonstrates how the waveform produced is no longer a physically realistic solution, the higher order terms being excessively large and causing multiple crests and troughs in the waveform. Reducing the wave-height to 0.5m in figure 2.4.2b brings the Ursell number to approximately 35, and hence to within the region of applicability. As a result, the waveform produced is very close to that produced by stream function theory. Provided the Stokes wave dispersion equations are used within their regions of applicability, it should be expected that the solutions should be very close to those of stream function formulations as the same basic governing equations are being satisfied, but by using a different mathematical approach.

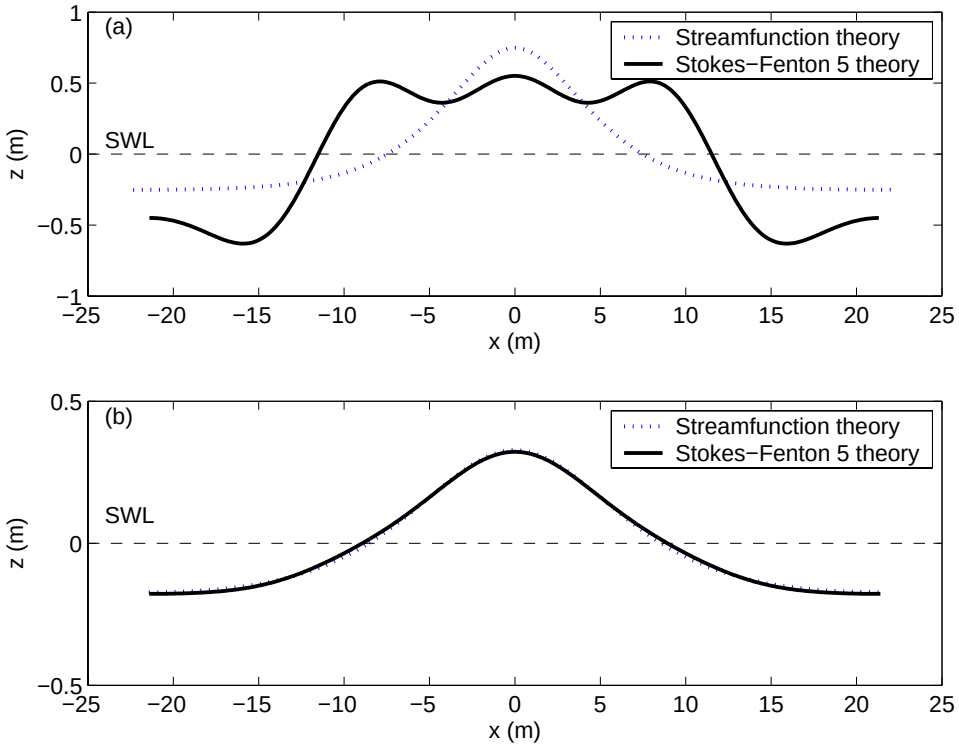

Figure 2.4.2 (a) The wave profile described by Fenton's 5th order Stokes theory for waves of period 8 seconds in 3m water depth and 1m wave height, compared to that given by stream function theory, showing how Stokes solutions break down when used outside their region of applicability. (b) The wave profile described by Fenton's 5th order Stokes theory for waves of period 8 seconds in 3m water depth and 0.5m wave height and within the region of applicability, compared to that given by stream function theory.

2.5 Cnoidal and Boussinesq Theories

Cnoidal and Boussinesq type wave theories are complementary to Stokes type equations in that they are most suited to waves in shallower water with large Ursell numbers, and behave poorly in deeper water. The essence of the Boussinesq approximation is that the wavelength is long in relation to the water depth. As such, the vertical variation in the horizontal oscillatory wave motion is considered small, and can be simplified, reducing the number of variables. Boussinesq (1871), in studying solitary waves in a rectangular canal, assumed no vertical variation in the horizontal component of the wave orbital velocity and set it to be that found at the bottom. Other approaches have been to use the velocity at the still water level, the velocity averaged over the depth, or assuming a linear variation in the velocity over depth. As a result, Boussinesq type equations break down in deeper water where the wavelength cannot be considered long in relation to the water depth. More recently, researchers have concentrated on trying to extend Boussinesq type theories into deeper water using various mathematical techniques (Witting, 1984), (Nwogu, 1993).

Cnoidal theories followed on from Boussinesq theories and were originally developed by Korteweg de Vries (1895) who showed that the first approximation to the surface profile of steadily progressing water waves in shallow water could be developed in terms of the Jacobian elliptic integral[7] cn, giving rise to the name 'cnoidal'.

While cnoidal theories are relatively complicated to implement, they work well in very shallow water. Since this region is of some importance to the present study, cnoidal waves will be explored here in some detail.

Russell (1844) initially determined that the wave celerity for the solitary waves that he first observed in a Scottish canal conformed to the equation

$$C = \sqrt{g(d+H)} \tag{2.5.1}$$

Generalising this to periodic waves, by substituting $C = \frac{L}{T}$ and the linear wave theory expression for deep water waves $L_0 = \frac{gT^2}{2\pi}$, gives:

$$L = L_0 k(d+H) \tag{2.5.2}$$

The development of the first cnoidal wave theory can be attributed to Korteweg and de Vries (1895) who identified the essential features of Russell's observations and produced what is now termed the Korteweg de Vries (KDV) equation, which balances the nonlinear and dispersive terms so that the solitary wave maintains its form instead of disintegrating. The KDV equation may be written:

$$\frac{\partial \eta}{\partial t} + C_0 \frac{\partial \eta}{\partial x} + \varepsilon \frac{\partial^3 \eta}{\partial x^3} + \gamma \eta \frac{\partial \eta}{\partial x} = 0 \tag{2.5.3}$$

where $\eta(x,t)$ describes the wave shape as a function of x and t

$C_0 = \sqrt{gd}$ is the speed of small amplitude waves in shallow water

---

[7] Many older texts refer the reader to the use of tables of elliptic functions and integrals; however, there are now various formulae available that approximate elliptic integrals and functions, such as those produced by Fenton and Gardiner-Garden (1982). Alternatively, the Matlab functions:

```
[K,E] = ellipke(m)
[Sn,Cn,Dn] = ellipj(U,m)
```

are extremely useful for present day use.

$\varepsilon = \frac{C_0 d^2}{6}$ is the dispersive parameter

$\gamma = \frac{3C_0}{2d}$ is the nonlinear parameter

Like the other wave theories described so far, numerous theories based on the KDV equation followed from other researchers. Despite their usefulness in shallow water, details of how to use these theories are rarely included in textbooks, perhaps due to their complexity and the need to deal with elliptic functions and integrals. In the limits of large waves in shallow water, cnoidal theory tends towards the equation for solitary waves.

Wiegel (1960) summarised the work of a number of researchers, including Korteweg & de Vries (1895), Keulegan & Patterson (1940), Keller (1948) and Littman (1957), who all produced similar first order cnoidal theories.

The basic equations for wavelength and celerity are given as

$$\text{Wavelength} = L = \sqrt{\frac{16d^3}{3H}} k_{cn} K(k_{cn}) \qquad (2.5.4)$$

where k_{cn} is the modulus of the elliptic function,
and $K(k_{cn})$ is the complete elliptic integral of the first kind.

The modulus k_{cn} is an unknown at this stage, and in most presentations of cnoidal theory the reader is directed to read the appropriate value from graphs. However, k_{cn} can be determined directly from the equation for celerity by iterative methods, setting the initial value of k_{cn} to its maximum value of 1:

$$\text{Celerity} = C = \sqrt{gd}\left(1 + \frac{H}{dk_{cn}^2}\left(\frac{1}{2} - \frac{E(k_{cn})}{K(k_{cn})}\right)\right) \qquad (2.5.5)$$

where $E(k_{cn})$ is the complete elliptic integral of the second kind.
To obtain the wave profile, the water depth below the trough of the wave h must be determined

$$h = 1 - \frac{H}{d} + \frac{16d^3}{3L^2}\left(K(k_{cn})\left[K(k_{cn}) - E(k_{cn})\right]\right) \qquad (2.5.6)$$

The surface profile can then be calculated from

$$\eta = h - d + Hcn^2\left(\frac{2K(k_{cn})x}{L}, k_{cn}\right) \tag{2.5.7}$$

In the limit as $k_{cn} \rightarrow 1$, the theory reduces to solitary wave theory in which a single wave 'crest' is dynamically isolated from any past or future crests.

Fenton (1979) gave a detailed description of a higher order cnoidal wave theory based on a converging power series, listing coefficients to 5th order[8]. The number of these coefficients is quite extensive, so in order to simplify its use, Fenton (1990) gave a considerably simplified version, which assumes that the parameter $m=k_{cn}^2$ is so close to 1 that it can be treated as 1 in many of the terms[9].

The coefficient tables in the following expressions refer to Fenton's 1979 paper. As with Wiegel's presentation of cnoidal theory, the first task is to find a value for the modulus of the elliptic integrals using iterative methods to solve the equation:

$$\sqrt{\frac{gT^2}{d}} = 4K\sqrt{\frac{dm}{3H}}\left(1 + \sum_{i=0}^{5}\left(\frac{H}{dm}\right)^i \sum_{j=0}^{i} m^j \sum_{k=0}^{i} e^k \tau_{ijk}\right) \tag{2.5.8}$$

where τ_{ijk} are the coefficients listed in Table A2 (in Fenton (1979)), and $e = \frac{E(m)}{K(m)}$

The iteration is again initialized with $m=1$.

Once m has been determined, the wavelength L can be calculated directly using the equation

$$L = 4dK(m)\sqrt{\frac{dm}{3H}}\left(1 + \sum_{i=0}^{5}\left(\frac{H}{dm}\right)^i \sum_{j=0}^{i} m^j \sum_{k=0}^{i} e^k \lambda_{ijk}\right) \tag{2.5.9}$$

where λ_{ijk} are the coefficients listed in Table A1 (in Fenton (1979)).

The depth at the trough h can be determined directly, using

$$h = d\left(1 + \sum_{i=1}^{5}\left(\frac{H}{dm}\right)^i \sum_{j=0}^{i} m^j \sum_{k=0}^{i} e^k h_{ijk}\right) \tag{2.5.10}$$

where h_{ijk} are the coefficients listed in Table A3 (in Fenton (1979)).

The determination of the wave profile requires the value of α to be determined first using

---

[8] The full fifth order solution was successfully coded in Matlab by the author based on Fenton's 1979 paper and used to generate the example plots below.

[9] Interestingly, the author was unable to obtain satisfactory wavelength estimates using Matlab routines coded to use the simplified version in Fenton's 1990 paper. The reason for this was not pursued since the full version based on his 1979 paper was successful.

$$\alpha = \sqrt{\frac{3H}{4mh}} \sum_{i=0}^{4} \left(\frac{H}{hm} \right)^i \sum_{j=0}^{i} m^j \alpha_{ij} \tag{2.5.11}$$

where α_{ij} are the coefficients listed in Table B1 (in Fenton (1979)).

Finally, the wave profile can be calculated as follows:

$$\eta = h\left(1 + \sum_{i=1}^{5} \left(\frac{H}{hm} \right)^i \sum_{j=1}^{i} m^j \sum_{k=1}^{j} cn^{2k}\left(\frac{\alpha x}{h}, m \right) \eta_{ijk} \right) - d \tag{2.5.12}$$

where η_{ijk} are the coefficients listed in Table B2 (in Fenton (1979)).

The dimensionless plots for Fenton's 5th order theory are shown in figure 2.5.1. A similar approach to that used for the Stokes formulations for eliminating invalid non-convergent solutions has been used here, and again the cutoff point following the trend of the Ursell number is a pleasing result. The cnoidal predictions can be seen to match those of stream function theory extremely well for Ursell numbers greater than 40 and right up to the breaking limit, while for Ursell numbers much less than 40 the solutions become unstable.

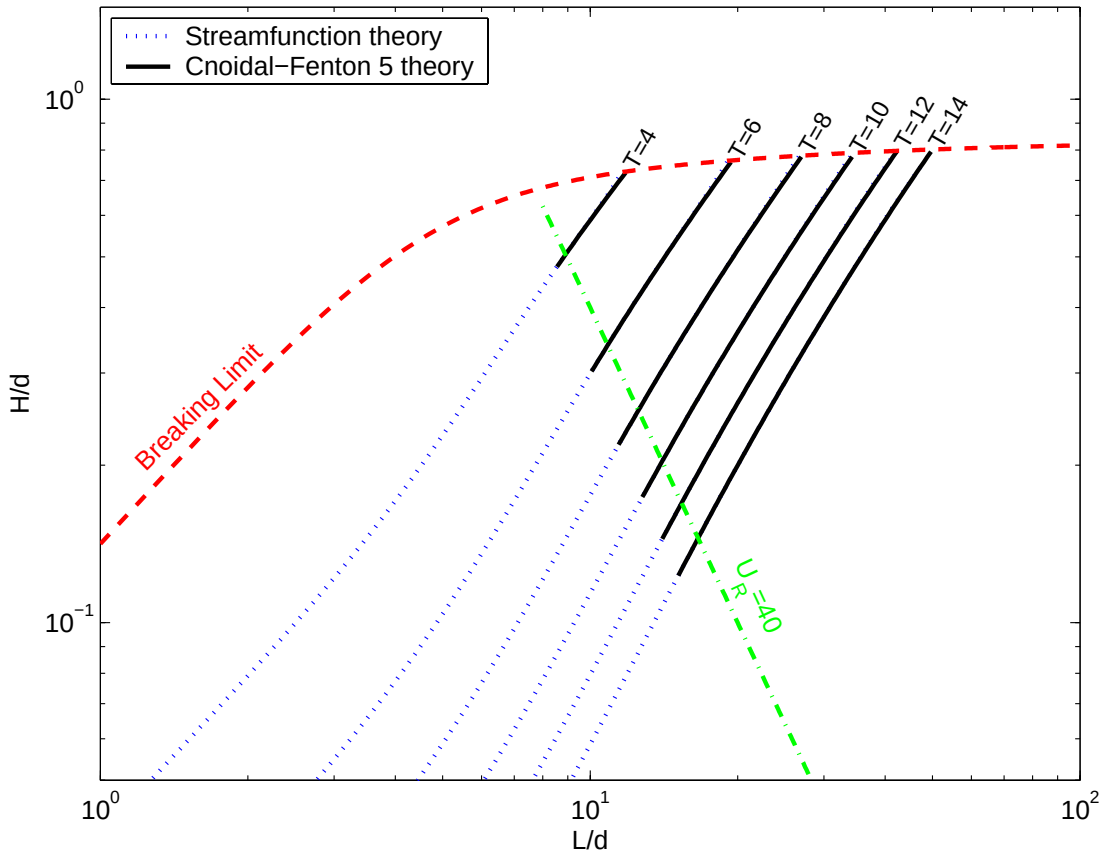

Figure 2.5.1 A comparison of Cnoidal-Fenton 5th order theory predictions of wave behaviour for H=1m waves with those of stream function theory. The line representing an Ursell number of 40 is shown as a suggested cut-off point for the applicability of Cnoidal-type theories.

The waveform for the H=1m, T=8seconds and d=3m test wave is shown in figure 2.5.2, and again it is almost identical to that predicted by stream function theory.

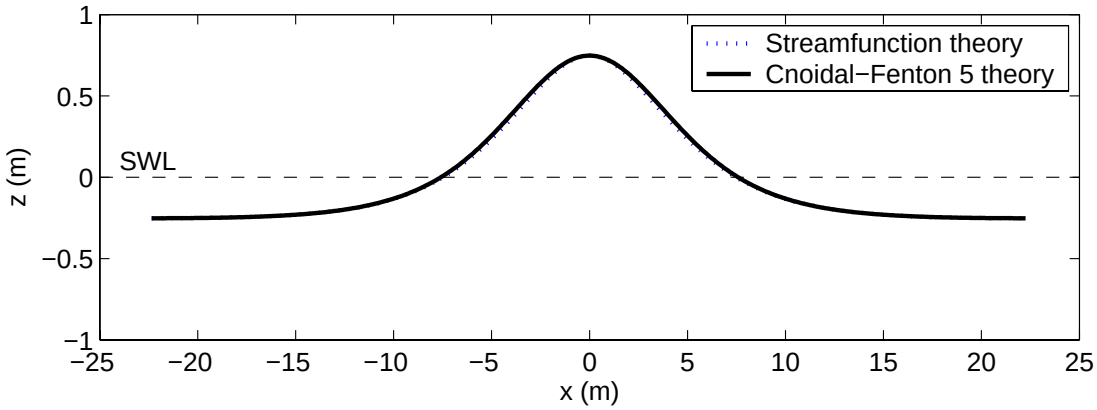

Figure 2.5.2 The wave profile described by Fenton's 5th order cnoidal theory for 8 second waves in 3m water depth 1m wave-height, compared with that of stream function theory.

2.6 Composite Approximations

The comparisons between stream function, linear, Stokes and cnoidal type wave theories have been illustrated in previous sections. Stream function theories, while accurate in the sense of solving the governing equations to a high order, are computationally slow. Cnoidal and Stokes theories are complementary and applicable in different wave regimes but suffer a similar computational overhead. If computation time was not an issue, stream function solutions would be the obvious choice for practical applications, although they would still fail close to the break point of the waves. In the absence of stream functions, Stokes and cnoidal, theories would make a complementary pair, together covering the whole range of possible wave conditions, but there would always be the risk of slight discontinuities in the solutions when swapping from one theory to the other.

Instead of obtaining exact solutions to the governing equations by the methods described so far, many researchers have overcome the computational overhead associated with the analytically solved equations by developing easily calculated approximations that combine the best aspects of the various theories. They are not rigorous mathematical solutions to the equations of motion, but rather engineering approximations based on the general form of the original theories. The most important aspect of them is that they are much simpler to use and more computationally efficient than the original theories that they approximate. As a result of their ready applicability, several have been used as the basis of the wave components of hydrodynamic models.

A second advantage of using these composite approximations is that predictions can be made in regions of wave breaking without the equations becoming unstable. Hence depth inversions may be carried out in the surf zone, even though strictly speaking the governing equations of the underlying theories may not be applicable.

Hedges (1976) combined linear theory with solitary wave theory, yielding an equation that tends towards linear theory in deep water and to solitary wave theory in shallow water.

$$L = L_0 \tanh k(d + Z) \qquad (2.6.1)$$

where Z is a function of the wave-height, and in his 1976 paper $Z=H$ was suggested;
hence for large d,

$$L \to L_0 \tanh kd \quad \text{i.e. linear theory}$$

and for small d,

$L \to L_0 k(d+H)$ i.e. solitary wave theory

A comparison between the predictions of wave behaviour for H=1m waves with those of stream function theory is shown in Figure 2.6.1. A noticeable discrepancy can be seen between the two sets of predictions in shallower water suggesting that the choice of Z may not be appropriate.

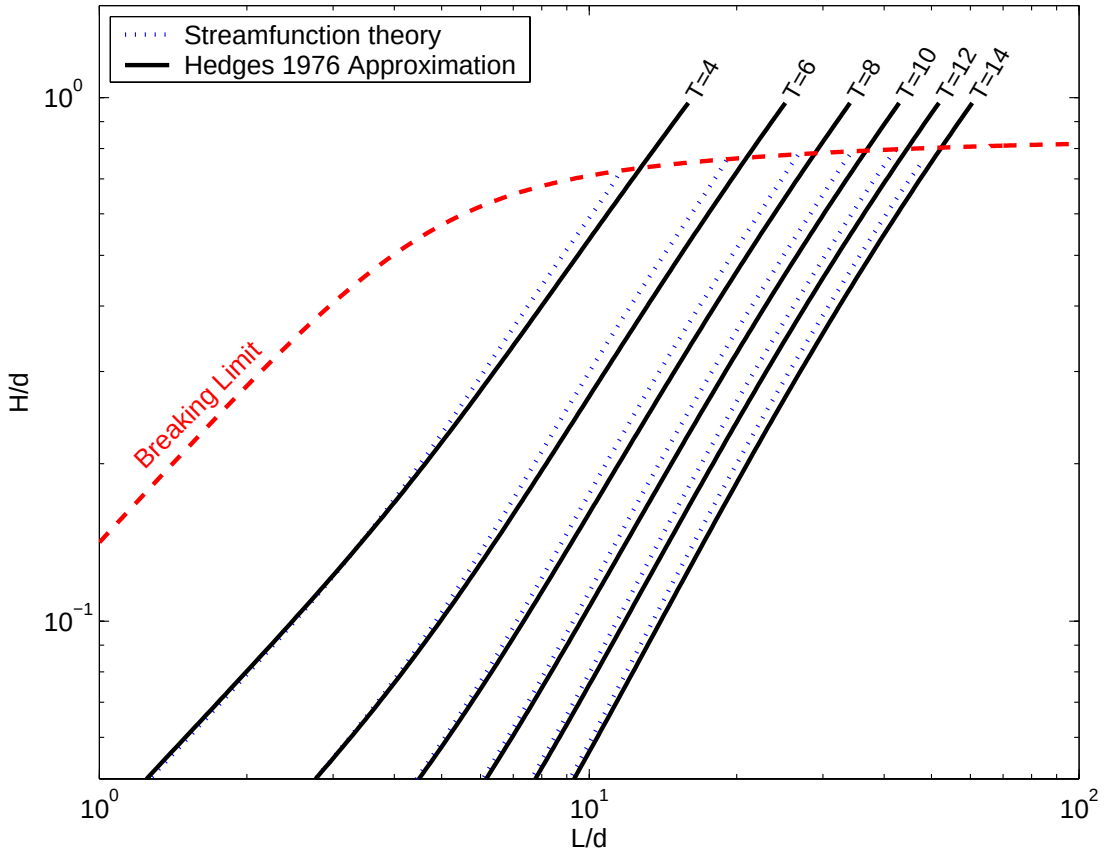

Figure 2.6.1 A comparison between Hedges' (1976) (Z=H) predictions of wave behaviour for H=1m waves with those of stream function theory. A noticeable discrepancy can be seen between the two sets of predictions in shallower water.

Booij (1981) later argued that based on work carried out by Walker (1976) where experimental data were compared with another approximate equation, $Z = \frac{H}{2}$ would be a better choice for the wave-height parameter[10], giving:

$$L = L_0 \tanh k(d + \frac{H}{2}) \qquad (2.6.2)$$

[10] Many thanks to Dr Terry Hedges at the University of Liverpool for his helpful comments clarifying the reason for the modification to the wave-height parameter in his equation, and his pointers to further references.

Re-calculating the predictions of wave behaviour using this version of Equation 2.6.1 gives much better agreement with the stream function predictions shown in Figure 2.6.2, reinforcing Booij's arguments, although there is still some disagreement, particularly near the breaking limit for large L/d values. This version of the equation was used in the Dutch parabolic wave model CREDIZ.

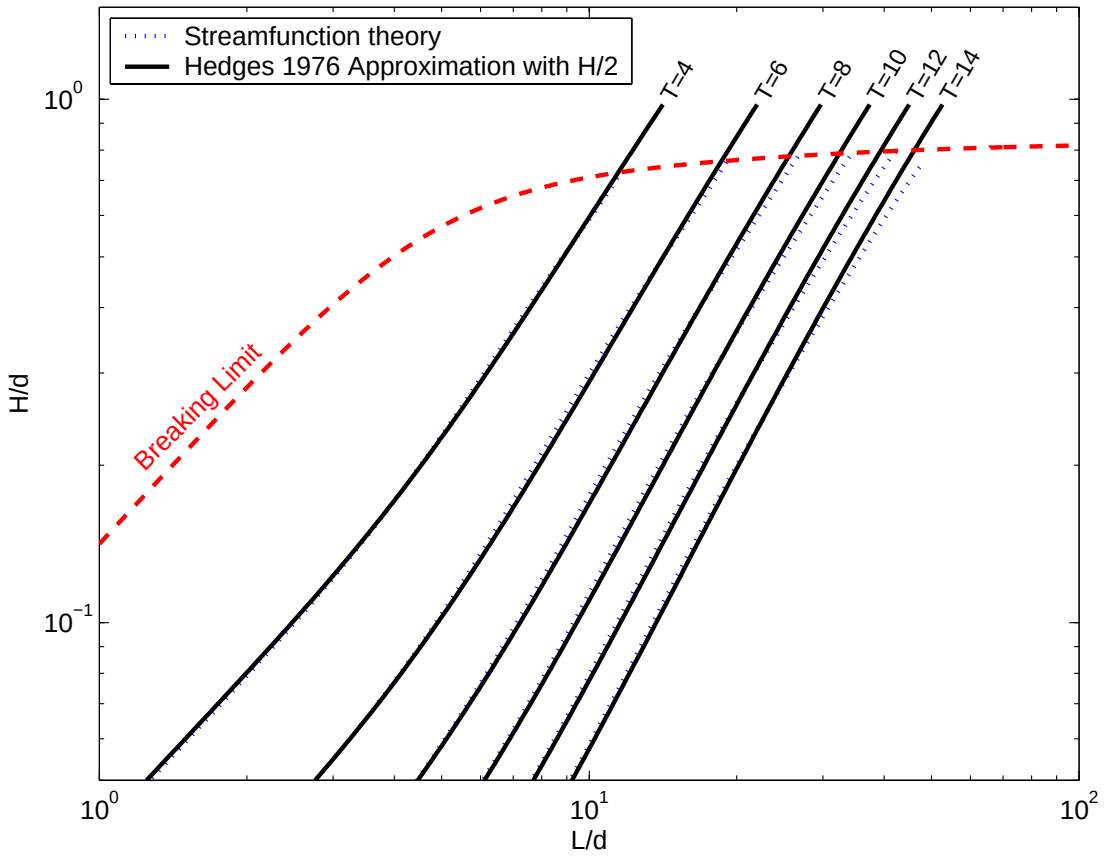

Figure 2.6.2 Predictions of wave behaviour using Hedges' (1976) equation with Booij's suggested modification of the wave-height parameter Z to H/2. Much better agreement with stream function predictions can now be seen.

Kirby and Dalrymple (1986) presented a composite approximation that tends towards Stokes theory in deep water and to cnoidal theory in shallow water. This equation was incorporated into the refraction/diffraction model REF/DIF 1 and is given as:

$$L = L_0\left(1 + f_1\varepsilon^2 D\right)\tanh\left(kd + f_2\varepsilon\right) \qquad (2.6.3)$$

where

$$D = \frac{\cosh 4kd - 2\tanh^2 kd + 8}{8\sinh^4 kd} \qquad \text{and} \qquad \varepsilon = \frac{kH}{2} \qquad \text{as in Stokes' equation.}$$

Hence in the limit of shallow water, the solution tends to that of solitary wave theory, and in deep water to that of Stokes. The functions f_1 and f_2 are somewhat arbitrary in nature

provided that f_1 tends to 1 in deep water and to 0 in shallow water, while f_2 tends to 0 in deep water and 1 in shallow water. In their 1986 paper, Kirby and Dalrymple chose:

$$f_1 = \tanh^5 kd \qquad \text{and} \qquad f_2 = \left(\frac{kd}{\sinh kd}\right)^4$$

Figure 2.6.3 shows the comparison between the predictions of Kirby & Dalrymple equation and those of stream function theory. At first glance they seem extremely close to those of Equation 2.6.1 in Figure 2.6.2, although there is slightly better agreement with stream function theory in intermediate values of *H/d*.

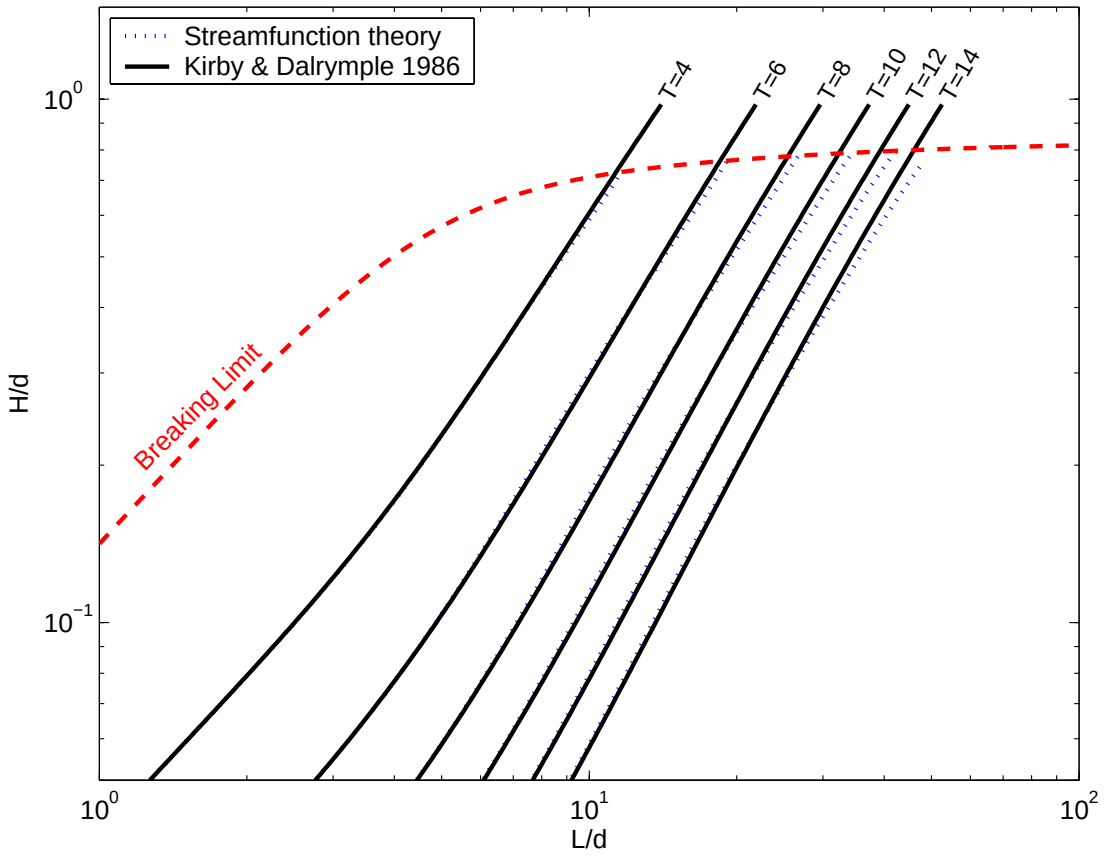

Figure 2.6.3 Predictions of wave behaviour using Kirby and Dalrymple's (1986) equation compared with those of stream function theory.

Hedges (1987) in a discussion of Kirby & Dalrymple's 1986 paper published a modified version of his equation to agree with Stokes 2nd order theory in deep water conditions, as opposed to tending to linear theory as in his 1976 equation:

$$L = L_0\left(1+\varepsilon^2\right)\tanh\left(\frac{kd+\varepsilon}{1+\varepsilon^2}\right) \qquad (2.6.4)$$

He pointed out that this equation better predicts the increase in wave celerity due to non-linearity in intermediate water depths than Kirby and Dalrymple's (1986) equation, in which

the excess celerity due to non-linearity does not increase monotonically from deep to shallow water but reaches a minimum in intermediate water depths. The predictions from this equation are illustrated in Figure 2.6.4, but actually show little difference from the previous versions for the 1m wave heights used as the example.

This new equation was subsequently adopted in CREDIZ, replacing Hedges' previous equation.

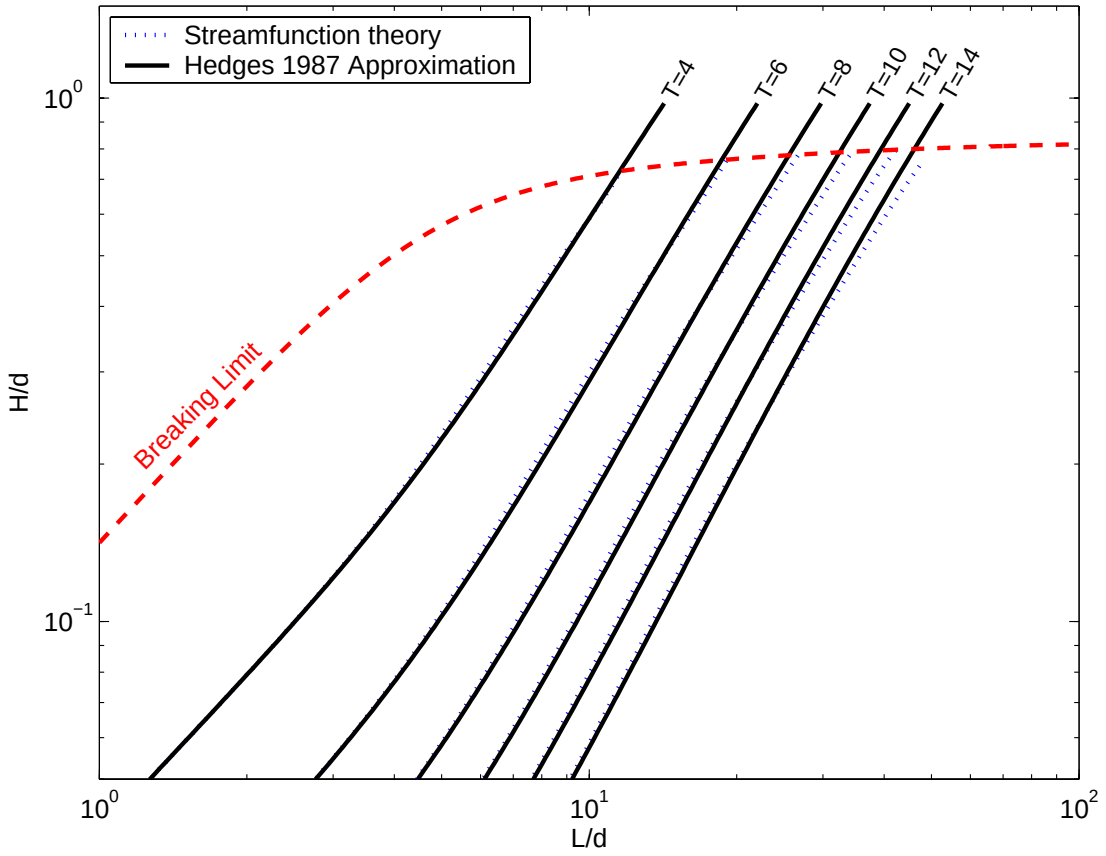

Figure 2.6.4 Predictions of wave behaviour using Hedges (1987) equation compared with those of stream function theory. Very little difference between the results of this equation and those of Kirby and Dalrymple's equation can be seen.

Kirby and Dalrymple (1987), in the reply immediately following Hedges 1987 discussion, published a further modification to their 1986 equation to correct the problem of the non-monotonic increase in non-linear correction observed by Hedges:

$$L = L_0 A \tanh\left(\frac{kd + f_2^{\frac{1}{4}}\varepsilon}{A}\right) \qquad \text{where} \qquad A = 1 + D\varepsilon^2\sqrt{f_1} \qquad (2.6.5)$$

and f_1 and f_2 and D remain the same as in their 1986 equation. While this is more theoretically satisfying, there can be seen in Figure 2.6.5 to be very little practical difference between this version and the previous one for the 1m example wave height.

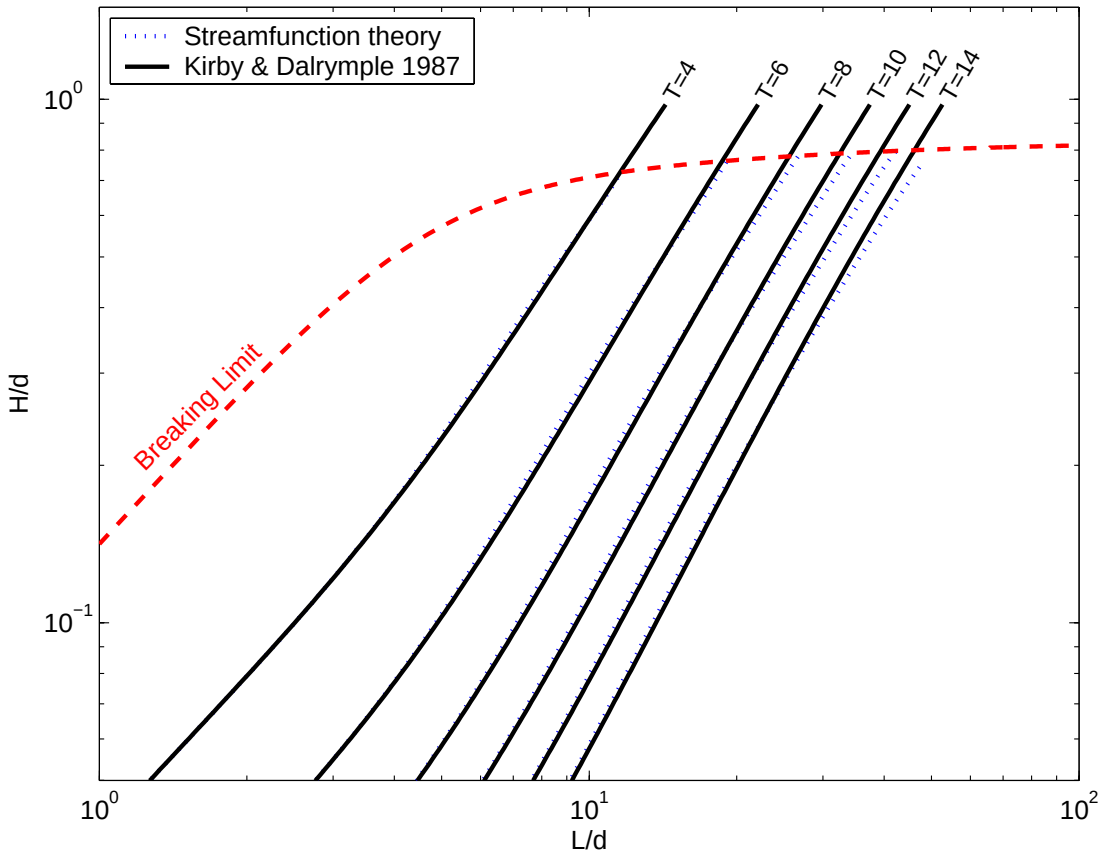

Figure 2.6.5 Predictions of wave behaviour using Kirby and Dalrymple's (1987) equation compared with those of stream function theory.

Holland (2001) used a simple shallow water correction for non-linearity to compensate for over-estimates in water depth by linear depth inversion. He applied this simple formula to invert wavelengths to water depths from wavelength data determined from video images. To overcome this specific problem in very shallow water, he combined shallow water simplification of linear theory with the equation for cnoidal celerity to give corrected depth estimates for water of depth less than 4m. In deeper water he used linear theory for the depth inversions. The shallow water depth inversion was given by:

$$d = \frac{\sigma^2}{gk^2} - \alpha H_S \qquad (2.6.6)$$

which rearranges to

$$L = L_0 k(d + \alpha H_S) \qquad (2.6.7)$$

i.e. very similar to Equation 2.6.1 for small d with Booij's modification using $Z=H/2$.

The value of wave height used was H_S since the data collected was for spectral waves. The value for α was determined empirically using experimental data collected from the SAMSON, DELILAH and Duck 94 experiments, and the best fit was found to be $\alpha = 0.40$ for those particular data. Examination of the plots demonstrating the results from applying this depth inversion show significant improvement over those that would be expected from linear theory. However, the need to swap from this equation to linear theory at the arbitrary cut-off point of 4m water depth may cause discontinuities in bathymetric contours if used for surveying purposes.

2.7 A Proposed Modification to Hedges 1976 Equation

The particular parameter range of interest in this work comprises depths from 0 to 20m. The need for a non-linear correction is particularly required in the shallowest depths, where it would be desirable to accurately mimic the behaviour of the stream function solutions up to the breaking limit and further to extrapolate these into the surf zone. The approximations discussed above appear to deviate from stream functions as they tend towards the breaking limit, which could cause an over-prediction of the water depth when used for depth inversions.

The principle of the approximate equations is that, in the limits, they tend towards the low order solutions of one of the analytically solved dispersion equations, while a proportion of both are used in the intermediate regions. For example, Hedges' 1976 equation tends towards linear theory for large water depth, to solitary wave theory for small water depth, and uses a combination of both for intermediate depths. It may be possible to more closely match the behaviour of stream function solutions by trying a different linkage between the two extremes of the approximate equations.

A possible modification of Hedges' 1976 equation (2.6.1) that changes the balance of the two extremes for intermediate depths is:

$$L = L_0 \tanh k\left(d + H \sin^3\left(\frac{\pi}{2}\left(1 - \frac{L}{L_0} \right) \right) \right) \qquad (2.7.1)$$

assuming H, L and T (and hence L_0) are measurable quantities.

The use of the sine function was chosen for the property that it goes from 0 to 1 over the spacing 0 to $\pi/2$, and the power of 3 by trial and error for the best fit to stream function predictions for 1m wave height.

In the limit of deep water, the equation still tends to that of linear theory, while in the limit of shallow water, it still tends to solitary wave theory as with Hedges' 1976 equation. The equation can be inverted directly for d with no iterative procedures necessary:

$$d = \frac{L}{2\pi}\tanh^{-1}\left(\frac{L}{L_0}\right) - H\sin^3\left(\frac{\pi}{2}\left(1-\frac{L}{L_0}\right)\right) \qquad (2.7.2)$$

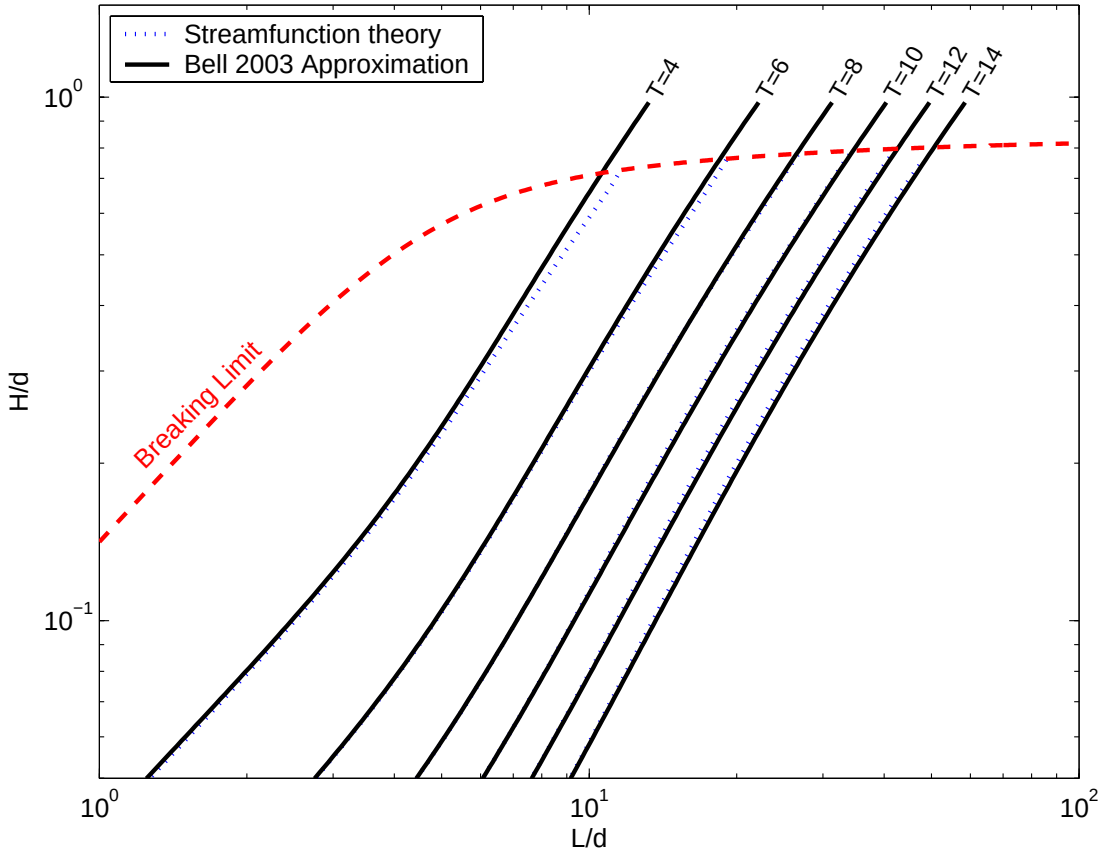

Figure 2.7.1 Predictions of wave behaviour using the proposed modification to Hedges (1976) equation. This shows closer agreement with stream function theory predictions near breaking than other equations discussed here.

In Figure 2.7.1 this dispersion equation can be seen to more closely approximate the stream function results, particularly near the breaking region. Some discrepancy is observed on the T=4 s line, but this is considered of minor importance compared with the close agreement for longer period waves used in the application of depth inversions. The is because waves of that short a period cease to feel the bottom in relatively shallow water and are of limited use in

deeper water depth inversions. However, the short period waves also have short wavelengths, and would allow finer bathymetric detail to be resolved if the measurement system had the resolution to image such short wavelength waves.

Unfortunately, when higher wave heights are tested, the predictions are not so favourable when set alongside Hedges' or Kirby and Dalrymple's equations. A more detailed study of the discrepancies between stream function solutions and those for linear and solitary waves may in future suggest a more robust mathematical linkage.

2.8 Choice of Dispersion Equation

Having explored a number of wave dispersion equations, the application of one of these to depth inversions for remotely sensed wave parameters must be considered.

The dimensionless plots presented in the previous section suggest that the effect of a Stokes correction in deeper water is of marginal value for the present application which is focussed on shallow coastal regions, at least for the 1m waves used to generate the plots. More important for the present application is accuracy in the shallowest water depths where the most active bathymetry is likely to be found. While stream function formulations are regarded as the benchmark for relating the various wave properties, they are too computationally intensive for serious consideration. Stokes and cnoidal theories are applicable exclusively in either shallow or deep water and are also computationally intensive. Composite approximations are already used for most modelling application, and so it seems reasonable to adopt one of these for the present use as a bathymetric inversion. The differences between the composite approximations detailed here appear to be marginal for waves of 1m significant wave height – a wave height into which most of the available data for this study falls. Hence it would seem appropriate to pick the simplest and most easily applied, i.e. Hedges' (1976) equation with $Z = H/2$.

2.9 The Interaction of Waves and Currents

2.9.1 Modification of the Linear Dispersion Equation to Allow for Currents

Having established an appropriate dispersion equation that adequately compensates for amplitude dispersion as well as frequency dispersion, the final physical property that should be considered is that of a mean current introducing a Doppler shift to the waves. In practical terms, a mean current moving in the same direction as the waves will Doppler shift the frequency of the waves to a higher frequency, keeping the wavelength the same (Krogstad, 2005; Dingemans, 1997). If the current opposes the waves, the frequency of the waves will be Doppler shifted down instead. The underlying wave frequency as it would be in frame of reference moving with the current is known as the intrinsic frequency, while the perceived wave frequency at a fixed geographical point (e.g. a wave recorder) in the presence of a current is known as the absolute frequency. The linear wave dispersion equation can be corrected for a mean current as follows:

$$\omega = \sqrt{gk \tanh kd} + \boldsymbol{k}.\boldsymbol{U}$$

where $\boldsymbol{k}$ is the wavenumber vector
and $\boldsymbol{U}$ is the current vector.

In cases where the current is strong, for example in a tidal inlet, an outflowing current speed may exceed the speed of higher frequency components of the wave spectrum, effectively barring the waves from entering the inlet. The precise criterion for this stopping velocity is related to the wave group velocity.

The ratio of the wave group velocity to the wave phase velocity is defined for linear waves in still water as:

$$\frac{c_{group}}{c_{phase}} = \frac{1}{2}\left(1 + \frac{2kd}{\sinh 2kd}\right)$$

hence for shallow water, $c_{group} \to c_{phase}$ and for deep water $c_{group} \to c_{phase}/2$.

Peregrine (1976) described the current required to stop an opposing wave train as when the stopping velocity U equals the opposing wave group velocity such that

$$U_{stopping} + c_{group} = 0$$

At the point where the group velocity equals the water velocity required to stop the waves, the wave phase speed is double the group velocity which in turn is double that predicted in still water, hence:

$$U_{stopping} = -\frac{1}{2} c_{phase\_at\_U\_stopping} = -\frac{1}{4} c_{phase\_still\_water}$$

This may have some application in future work looking at waves entering a tidal inlet.

2.9.2 Modifying Hedges Dispersion Equation to Allow for Currents

Hedges' dispersion equation may be modified to allow the Doppler shift of currents in the same way as the linear wave dispersion equation.

Hedges' dispersion equation without current:

$$\omega = \sqrt{gk \tanh k(d+Z)}$$

and with current:

$$\omega = \sqrt{gk \tanh k(d+Z)} + \boldsymbol{k}.\boldsymbol{U}$$

or re-arranged for the wavelength as:

$$L = \frac{2\pi g \tanh k(d+Z)}{(\omega - \boldsymbol{k}.\boldsymbol{U})^2}$$

It should be noted that this is a first order correction for current only – higher order effects have been neglected.

Chapter 3: Experimental Techniques

3.1 Collecting Data using Marine Radar

Standard marine radars have real time display systems designed for immediate ship-board use. No recording capability is currently built in as standard, although in the near future this might be expected to change as the technology becomes more straightforward. Early work such as that by Heathershaw et al. (1980) involved photographing the Plan Position Indicator (PPI) radar screen using an automatic camera and black and white film. The prints from this were then digitized for analysis. This was a laborious task that placed severe limitations on the size of datasets able to be collected.

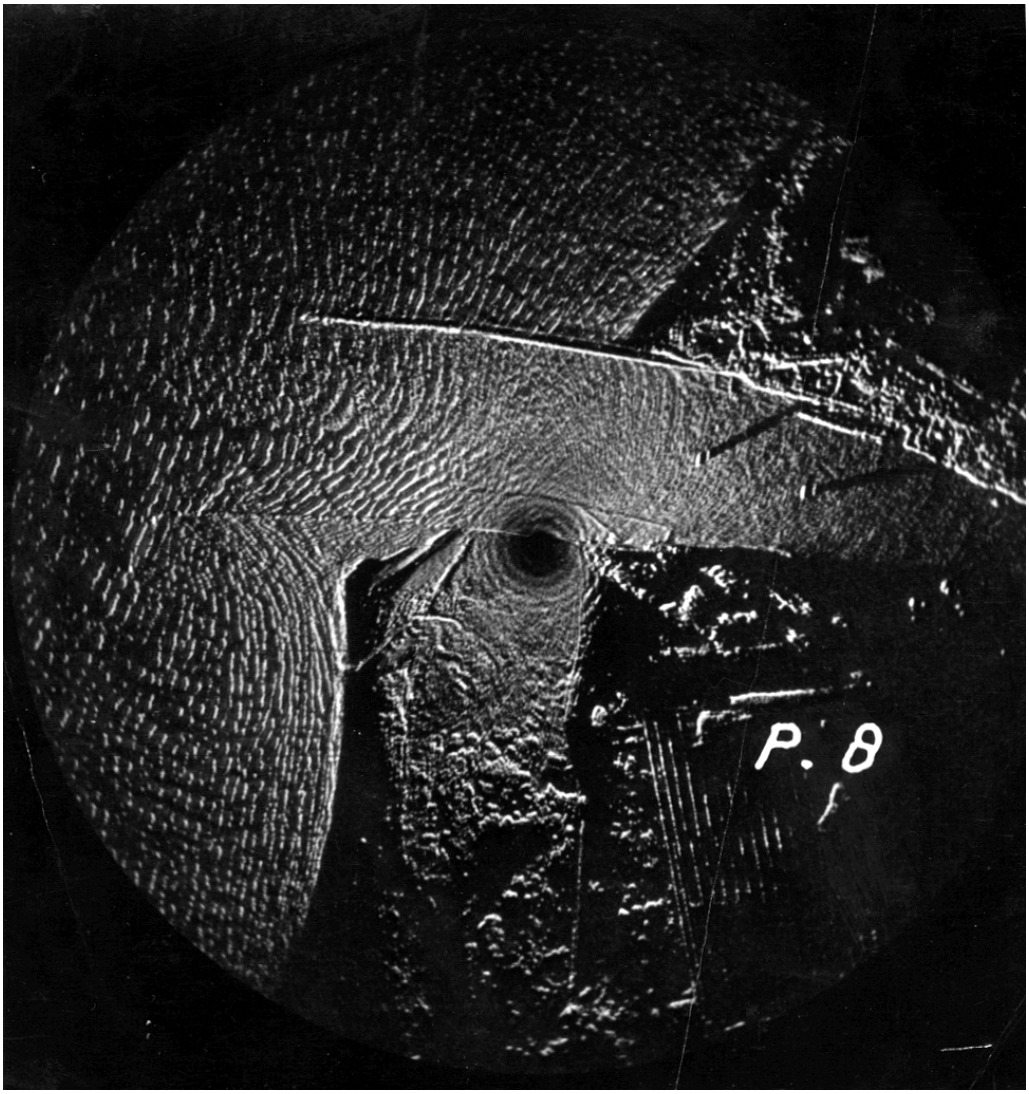

Figure 3.1.1 An old photograph of a radar PPI screen clearly showing wave patterns around the port of Hoek van Holland near Rotterdam.

A particularly fine example of an old photograph found in POL records of early radar work is of a radar PPI screen taken at the port of Hoek van Holland, shown in Figure 3.1.1. (Exact source unknown). The wave refraction patterns around the breakwaters are clearly visible, particularly around the breakwater in the centre-left of the picture. The radar shadows caused by two large structures are also evident in the centre-right of the image, demonstrating well that the radar, although capable of long range imaging, is still a line-of-sight instrument than cannot see through obstacles. The area in the lower part of the image has since been substantially enlarged and is now the site of Europort, although the breakwater in the upper part of the image is still a famous landmark in the area.

In the early 1990s a digitization system became available from Miros AS in Norway. Consisting of a pair of PC cards, the Wavex system was capable of digitizing the raw radar return signals at a rate of 20MHz, or a radial bin of 50ns length, corresponding to a radial bin length of 7.5m for radar signals travelling at the speed of light. This allowed sequences of radar images to be digitised directly rather than going through the laborious task of photographing the PPI screen. During the early 1990s, POL acquired a Wavex system, and it was the task of the author at that time to integrate this recorder with a separately purchased radar system. An example of an image recorded at Faro in 2002 using this system is shown in Figure 3.1.2. There are intertidal salt marshes with channels between them in the north-east half of the image behind the barrier beach of the Ancao peninsula; a clear sea-clutter signal to the south-west is visible, the radar being sited in the centre of the image on the barrier beach. The Ancao tidal inlet is located at the end of the barrier beach in the south east edge of the image but is not easily distinguished in the image other than by the lack of signal and the slight seaward breaking of the waves on the beginnings of the ebb delta, breaking waves presenting a considerably stronger radar reflection than non-breaking waves.

In this plot lighter shades represent stronger radar signals while darker areas represent weaker signal areas – matching the style of a conventional radar PPI screen. All future plots are shown with the colour scale reversed so that darker areas represent stronger signal areas – a convention adopted in the early stages of this work because it showed up weak signals more easily and used up less printer ink.

The interfacing of the recorder to the radar proved to be not nearly as straightforward as was initially expected, and various modifications and compromises had to be made before a working system could be demonstrated.

This chapter describes the basics of radar technology, the details of the recording system used in this study, and provides a brief guide to the interpretation of radar images. A new short range mm wave radar is also described that has been used in later chapters to study waves breaking on a beach at smaller spatial and temporal scales than is possible with standard marine radars.

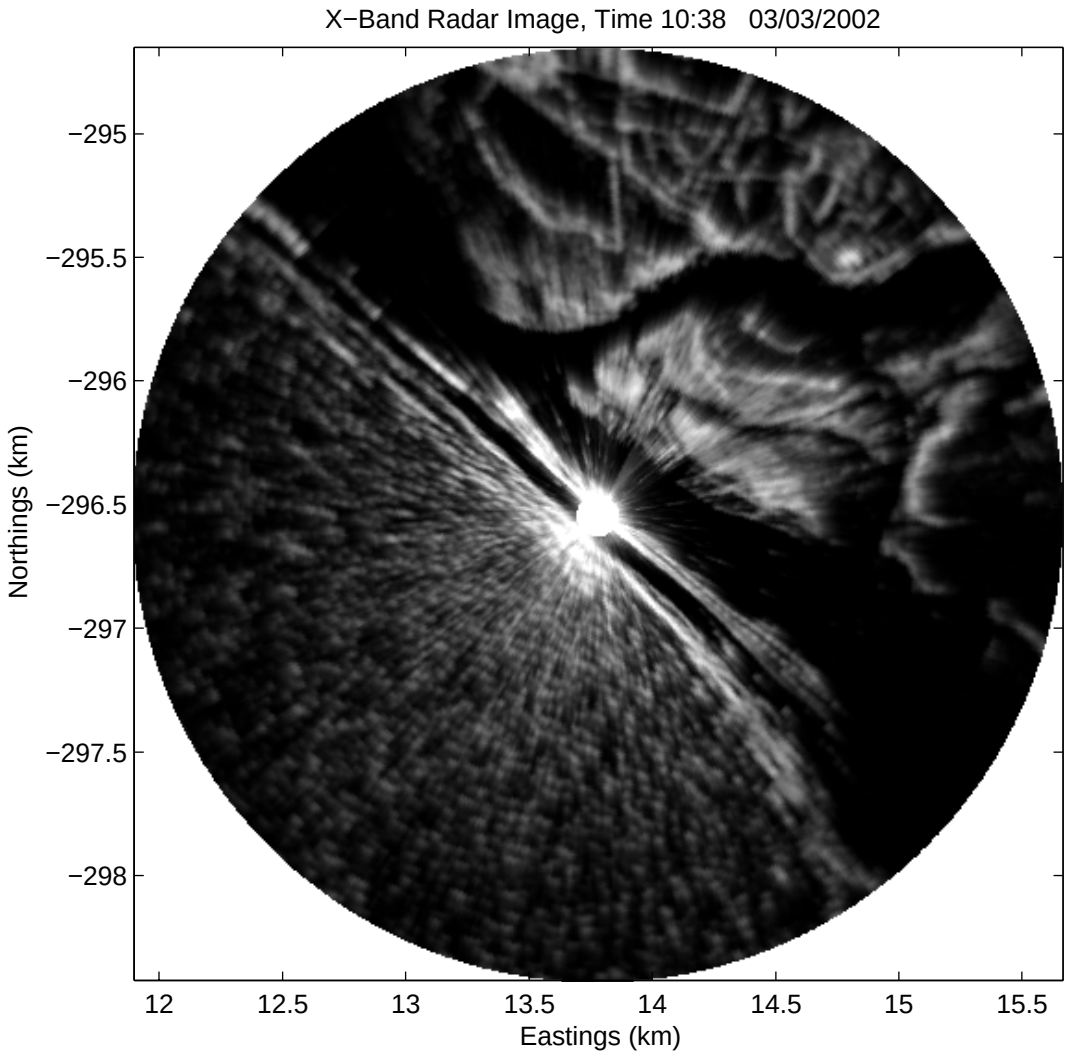

Figure 3.1.2 A radar image digitised using the Wavex digital recording system during a deployment in Faro during 2002.

3.1.1 X-Band Marine Radar

Early in the development of radar, letter codes such as S, X, L etc were employed to designate radar frequency bands. Although their original purpose was to guard military secrecy, the designations have been maintained out of habit, and the need for a convenient nomenclature. Today's X-band covers the region from 8GHz to 12GHz. Marine X-band radars normally used for ship navigation and of the type used in this study typically have an

operating frequency of 9.8GHz, giving a wavelength of 3cm. The transmitter consists of a 1.8m long antenna that rotates at approximately 2.4 second intervals, transmitting 60ns pulses at a rate of 1200Hz. The beam pattern generated by such an antenna is approximately 22^o in the vertical – deliberately wide to allow for pitch and roll of the ships on which they are intended to be mounted – and 1.2^o in the horizontal, giving very good angular resolution. The length of the sector traced out by the beamwidth increases with range and is illustrated in Figure 3.1.3. This demonstrates how, unlike the radial resolution, the resolution perpendicular to the radar beam decreases with range. The practical consequence of this is that short waves travelling perpendicular to the radar beam will not be resolved at the longer ranges.

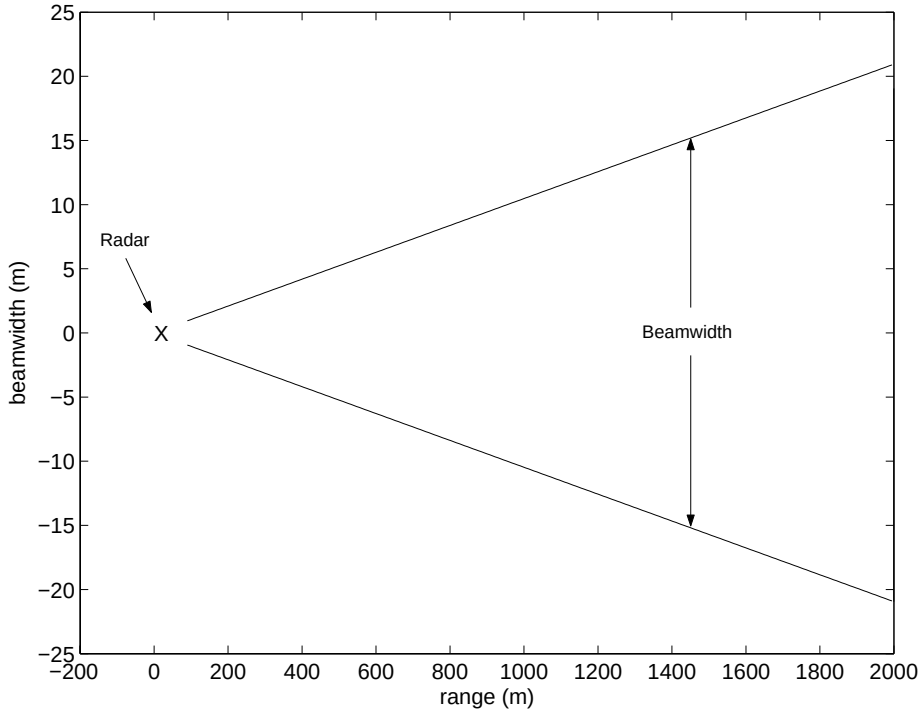

Figure 3.1.3 The sector length of the 1.2^o horizontal radar beamwidth plotted against range from the radar, showing that resolution perpendicular to the radar beam decreases with range.

The backscattered echoes from each transmitted pulse are plotted on a PPI screen in polar coordinates, the azimuth corresponding to the direction in which the antenna is pointing and the range being obtained from the time of travel of the radar pulse. This gives a two dimensional plan view of the area in view of the radar that refreshes at the rotation rate of the antenna. It should be pointed out that the signal being plotted on the screen corresponds to the envelope of the backscattered radar signal, generated by low-pass filtering the 10GHz radar signal to give a much lower bandwidth 18MHz signal for plotting, which roughly corresponds to the pulse length of the transmitted pulse.

If the radar is significantly above the mean water level, a correction for the slant range to the target compared to the horizontal distance might be required. However, all deployments for the present study have been at no more than 15m above sea level. The difference a slant range correction would make in the worst case for the nearest recorded backscatter echo at a range of 100m is of the order of 1m in range. For a system with a radial sampling interval of 7.5m, this is small enough to be neglected. With increasing range the slant range tends to the horizontal range and any correction becomes even less significant. Figure 3.1.4 illustrates the slant range difference.

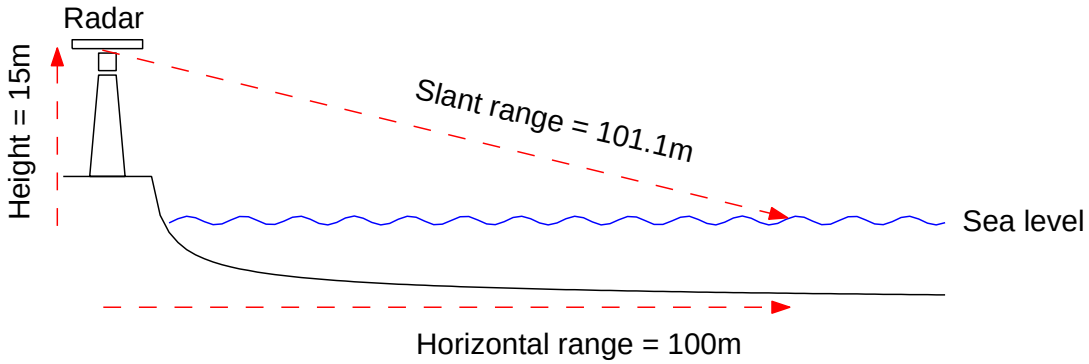

Figure 3.1.4 An illustration of the difference between horizontal range and the true slant range measured by the radar.

3.1.2 The Wavex Radar Recording System

The Wavex recording system was based on 1980's technology and only included the capability to record three out of the four signals required to fully capture radar images. Those three signals are:

- North marker – generated once per revolution of the antenna and used to orient the images relative to the forward looking direction of the radar.
- Synchronization (synch) pulse - which signals the start of the transmission of each radar pulse, and provides the start time for the time of travel measurements that give the range of the backscattered radar echoes.
- Video signal that actually carries the backscatter signal strength information, and it is this that is digitised at 20MHz.

The fourth signal that was not accounted for was the azimuth, a pulse generated every four degrees of rotation allowing the radar pulses to be accurately placed at the right angle relative to the north marker.

Early trials by the author with the Wavex system exposed a serious problem with using only three of the four signals to record radar images. The rate of revolution of the antenna was assumed by the Wavex system to be a constant that was measured once. This meant that the azimuth at which each pulse was plotted in the digitised data was assumed to be related to the number of synch pulses after the north marker. Unfortunately the motor control on the radar used was insufficiently precise to make this a valid assumption, particularly in windy weather. Hence, on successive images in a sequence, the uncertainty in azimuth caused fixed targets to have an azimuthal jitter of up to several degrees on the recorded images. The radar monitor itself has stabilization circuitry that uses the azimuth signal to correct this in the images displayed on the radar screen, but the Wavex recording system had no way of dealing with this.

There were three possible solutions to this problem:

1. Substantially improve the motor control so that the antenna rotation rate really was a constant.
2. Accurately digitise the azimuth signal separately and apply this to the radar data in post processing to stabilize the images.
3. Replace the 1200Hz trigger generation circuit with one that was locked to the antenna encoder using a phase locked loop circuit such that pulses were transmitted at fixed angular positions, rather than at fixed time intervals.

Option 3 was devised, and implemented by the author as it was considered a permanent solution to the problem and once done would not require extra data recording equipment or software post processing of the data.

A side effect of this solution that went unnoticed until late 1999 was that the average rotation rate of the antenna was also quite variable. This too had been assumed constant in the Wavex recording system. Unfortunately this will have had an adverse impact on quality of data presented in some already published work, specifically Bell (1995), Bell (1998), Bell (1999) and Wolf & Bell (2001). The reason for this is that frequency analysis was carried out on data recorded in 1994 and 1995 for these publications, and the variation in the elapsed time for each image sequence recorded will have varied, causing errors in the frequency values given by FFT analysis.

The problem, once identified, was relatively simple to correct to within acceptable accuracy. The start time of each record was known from the automatic recording software and timestamps at the start of each file. The last time of modification of each record, i.e. the end time, is part of the DOS file format. Hence by subtracting one from the other, the total time taken to record each image sequence could be determined to within one period of revolution of the antenna.

The effect of this problem can be illustrated as follows:

If 32 images are recorded in a sequence for a radar antenna that is assumed to be rotating at 2.25 second intervals, an FFT of a single pixel through time would give frequency bins calculated as follows:

$$F_n = \frac{n}{NOI * TPR}$$

where

NOI = Number Of Images in the sequence

TPR = Time Per Revolution of the antenna

n = index of FFT bin

Hence the frequency of bin 7 in the FFT would be

$$F_7 = \frac{7}{32 * 2.25} = 0.0972Hz$$ or a period of 10.28 seconds

If the antenna rotation rate was really 2.4 seconds, then FFT bin 7 would actually have a frequency of

$$F_7 = \frac{7}{32 * 2.4} = 0.0911Hz$$ or a period of 10.97 seconds

This is sufficient error to push the energy into a different Fourier bin, and have consequent effects of errors in any depth estimates made using depth inversion equations.

3.2 The Physics of Radar Sea Surface Imaging

The precise details of the imaging mechanism of marine radar have been the subject of study for numerous researchers throughout the world ever since marine radars came into common usage. The imaging mechanism is not linearly or exclusively related to the wave height of the waves seen on radar images, making the determination of wave height information significantly less straightforward than it might initially appear. Polarised radar scatterometers designed to allow separate measurements of horizontally and vertically polarised transmitted and received radar energy have given some insight into the various contributions to the backscatter signals imaged by marine radars (Keller et al., 1990; McLaughlin et al., 1995). There appear to be two main scattering mechanisms providing the backscatter signal in response to the transmitted radar pulses.

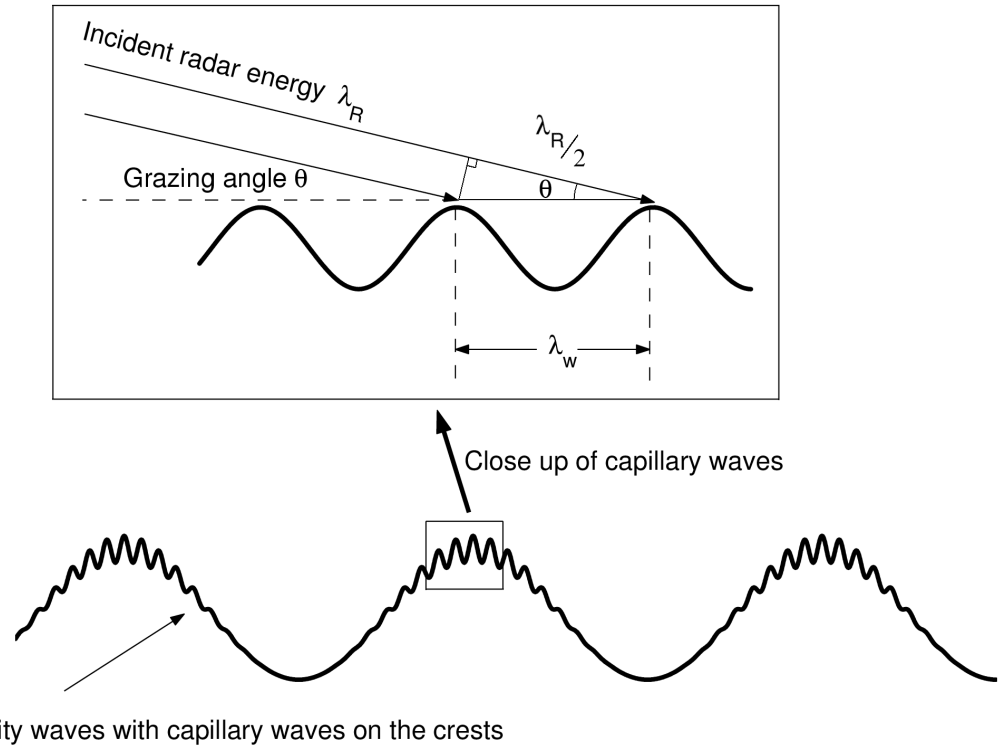

Figure 3.2.1 An illustration of the capillary waves on the crests of gravity waves that lead to the Bragg scattering of radar energy.

The first is a Bragg resonant scattering (Guinard et al., 1971), named after its similarity with X-ray scattering in crystals as observed by Bragg. This occurs when the wavelength of small wind induced capillary waves on the water surface have a wavelength component along the axis of the radar beam satisfying the Bragg condition $\lambda_w \cos\theta = \lambda_R/2$, where λ_w is the component of the capillary wavelength along the radar beam, λ_R is the wavelength of the

incident radar energy (3cm for X-Band Radar) and θ is the grazing angle between the incident radar beam and the sea surface, illustrated in Figure 3.2.1.

With ground based radars, θ is usually less than 10^{o} at close range and tends to zero at longer ranges. So for example, 1.5cm wavelength capillary waves with crests perpendicular to the radar beam would provide ideal conditions for Bragg resonant scattering. The fact that this is the principal scattering mechanism has the interesting and somewhat counter-intuitive side effect that a perfectly smooth sea surface undisturbed by local winds and hence having no capillary waves could have a significant smooth swell component that would give no signal on the radar. The minimum wind speed required to generate the capillary waves required for Bragg scattering and hence to produce an image on the radar is of the order of 3m/s (Nieto Borge & Reichert, 2005). Lee (1977) showed from laboratory work that the small capillary waves that lead to Bragg scattering tend to be localised at the crests of the waves, with almost none in the troughs. This would imply that the strong signals seen on radar images correspond to the wave crests as opposed to the front face of the wave as suggested in some literature. Heathershaw et al. (1980) agreed with this conclusion, having shown from field deployments that waves could be imaged just as successfully from behind as from the front.

Interestingly, the principal scattering mechanism of HF radar systems used for much longer range work such as CODAR, OSCR and WERA is also Bragg resonant scattering (Crombie, 1955), but in this case the radar frequencies used are of O(10MHz) which have an optimum Bragg scattering wavelength of the same order as the wavelengths of the gravity waves themselves, rather than the capillary waves on top of them.

The second contribution to the scattering mechanism is sea spikes, associated with steep and breaking waves (Kalmykov & Pustovoytenko, 1976). In horizontally polarised radars, which are the most common type used, these sea spikes cause backscattered signal levels considerably higher than Bragg scattering from non-breaking waves. Hence breaking waves stand out clearly on the radar images as much higher than normal backscatter levels. These strong backscatter levels from the sea spikes are thought to be generated by a combination of effects including specular (direct) and non-specular reflections.

In addition to the two main contributions to the imaging mechanism, the near 90-degree angle of incidence of the radar energy with the sea surface from most ship and coastal installations introduces the further complication of shadowing, where the rear faces of the

waves relative to the radar are shielded from the view of the radar. This effect means that not only are the rear face and troughs of the waves shielded from view, but any smaller waves behind larger waves may also be missed. To a ship's captain, this effect can cause the radar echo from a small boat to disappear when the boat is in the trough between two large waves.

3.3 Precipitation effects

The electromagnetic spectrum has regions within it that are relatively unaffected by precipitation. X-band is not one of them. The effect of steady rainfall on a radar image is to increase the background backscatter level. In heavy rain, this background can be sufficient to mask a wave signal completely. A good example of this can be seen in Figure 3.3.1 which was recorded at Egmond in the Netherlands during 1998. It shows a sequence of radar images at 10 second intervals as a heavy rain squall passed through the study area.

The squall can be seen as the dark pattern that moves from the middle-right of the images to the lower-right of the images. The orientation of the x-axis runs in the opposite direction to normal convention due to the choice of coordinate system chosen for that particular experiment by the Dutch hosts. Interestingly, there are windows in the electromagnetic spectrum in which precipitation has no effect - 77GHz being one that has been chosen for mm wave radar automotive applications partly because it is unaffected by rain and fog (described in section 3.7). Despite the rain signals on the images, waves of length 60m to 70m are still visible through the increased background signal, particularly over the sand bars parallel to the x-axis near the bottom of the image where the waves are breaking and consequently cause a significantly stronger return radar signal than non-breaking waves.

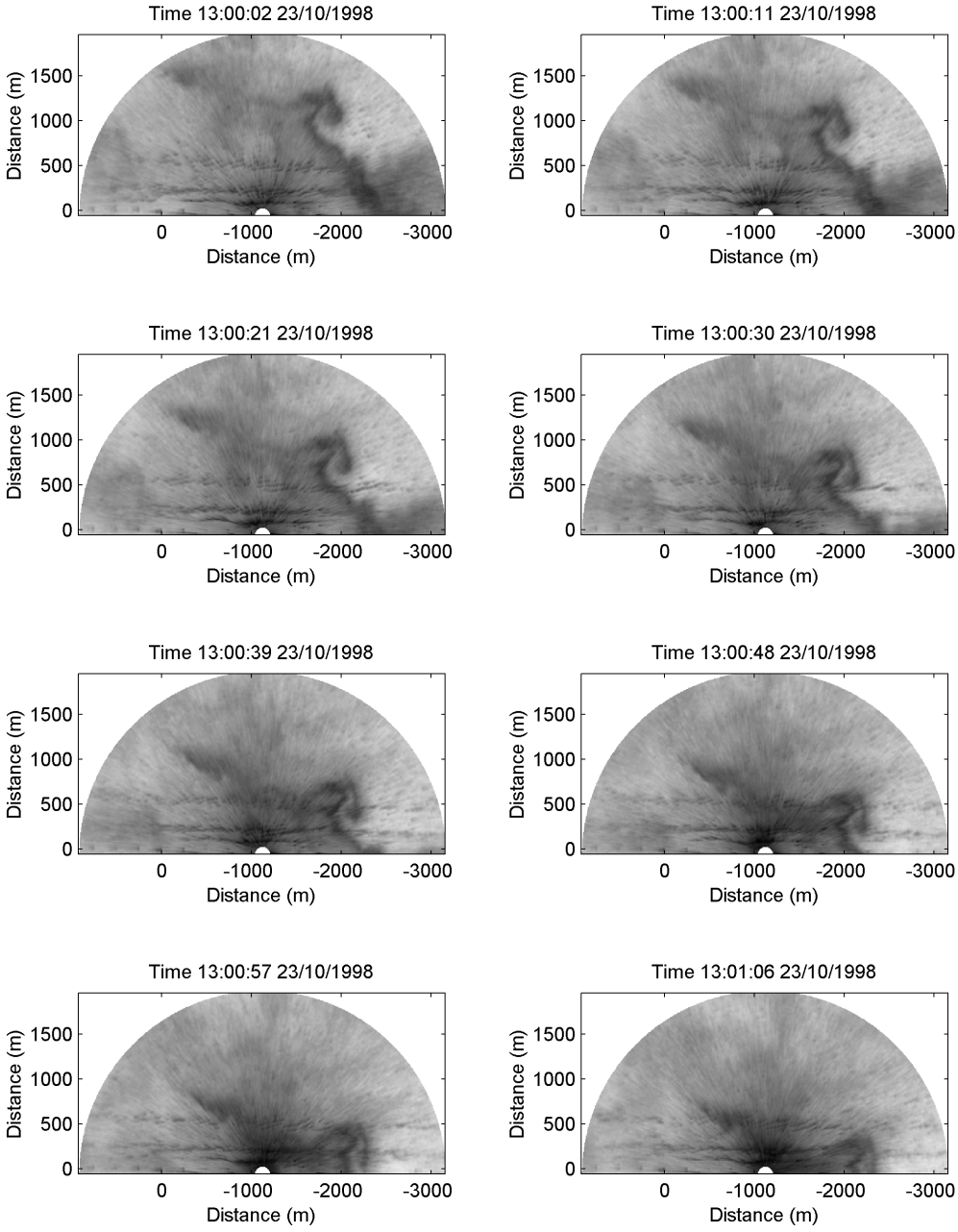

Figure 3.3.1 The passage of a rain squall across the study area during the Egmond COAST3D experiment in 1998. The rain squall is the dark swirl that moves from the middle right of the images to the bottom right.

3.4 Timing

The radar system at POL was developed with the intention of deploying it at a fixed location, setting it running automatically and leaving it to record data at preset intervals with no further intervention by the operator. Unfortunately this meant relying on the PC clock to trigger the recordings at the appropriate times. This proved to be a significant problem, as PC clocks are notoriously inaccurate and prone to drift. This problem was managed during early

work on the Holderness projects by estimating the average drift and making a correction to the PC clock of a few seconds following each recording. Unfortunately this procedure failed during the Egmond deployment during the COAST3D experiment when the PC failed during the experiment and the replacement PC proved to have a significantly worse clock drift than the old PC. This led to errors in determining the time of a recording of up to 30 minutes – a serious problem when trying to match radar derived water depths and tidal levels together.
To resolve this problem, during deployments after 1998 a GPS receiver was linked to the PC and the time automatically reset to GPS time following each recording.

3.5 Methods of Deployment

The normal method of deployment for the marine radar is to find a convenient flat roof overlooking the experiment area and negotiate with the owners for access and power. Ideally it should be deployed at least 10m above sea level and preferably 20-30m above sea level. Piers make relatively good deployment sites as there are often flat roofs with secure access available. Power is also usually present, as is somewhere dry to locate the recording PC. Three deployments have been carried out in this way - Teignmouth in 1999 and Great Yarmouth in 2003 and 2004. Figure 3.5.1 shows the radar mounted on Teignmouth Pier during the COAST3D experiment.

In more remote areas where no convenient flat roofs are present, a small scaffolding tower can be erected, preferably in a secure area on top of a low cliff. During the Holderness projects, just such a site was used, as shown in Figure 3.5.2.

Figure 3.5.1 The X-Band radar mounted on the roof of Teignmouth Pier during the 1999 COAST3D experiment.

Figure 3.5.2 The clifftop deployment location during the Holderness experiments.

Sometimes there are neither clifftops nor buildings, and the radar must simply be deployed from the top of the beach on a scaffolding tower. This was the method used during the Faro 2002 and 2003 experiments

One of the substantial advantages of radar over conventional in-situ oceanographic instruments is that it does not have to be deployed in the water. The risks of losing the equipment are therefore dramatically reduced and repairs and data retrieval are straightforward.

3.6 Other Useful Measurements

In order to use radar data for development of analyses as in the present study, it is helpful to have a range of other types of measurement besides the radar.

A Trustworthy Survey

Tests of the bathymetric inversion's ability to accurately pick out the correct water depth must be measured against ground truth measurements – in some experiments there were excellent surveys, in others there were none.

A Tide Gauge

To relate the water levels determined from the radar to chart depths, the tidal level must be known. A tide gauge within the area viewed by the radar is the ideal setup, however this is rarely possible. As a last resort tidal predictions may be used, but differences between the predicted and actual tide could easily be of the order of 0.5m at any instant in time due to surges caused by meteorological effects.

Wave Measurements

The ideal setup would be to have a wave gauge within the area viewed by the radar to determine the significant wave height and validate the frequency-direction spectrum.

3.7 The Navtech millimetre Wave Radar

This was a new development in 2001 based on an automotive radar used for obstacle avoidance on large opencast mining vehicles. The manufacturers modified it slightly for oceanographic use and added recording capability on a laptop. The operating frequency is far higher than the marine radar used for most of this work, and the radar operates on quite

different principles as a result. The transmission frequency is centred around 77GHz, or 4mm wavelength.

Figure 3.7.1 The Navtech mm wave radar deployed on an improvised mounting on the beach in Faro 2002.

The mini radar operates both at a different frequency and on a different principle to the X-band radar. Instead of transmitting discrete pulses, there is a continuous transmission of a 77 GHz baseband frequency. This frequency is the designated automotive frequency in Europe and the United States, chosen for its low atmospheric absorption (Skolnick, 1980). It is also license exempt in most parts of the world, eliminating the need to obtain a license to operate the system. The time between transmission and reception of the radar signal gives a measure of the distance to the reflecting surface as in the X-band radar. However given the limited maximum range, it is not practical to measure such small time intervals. Instead, transmitted and received mm wave signals are mixed and the frequency difference extracted, this intermediate frequency being a measure of the target distance.

The mm wave radar unit employs a 40db lens antenna yielding a beam divergence of approximately 2 degrees. This beam width is spoiled in elevation to approximately 4 degrees to create a fan beam effect. Spreading the beam reduces the signal power returned at a fixed range. For this reason, the maximum radar range in this system is 200 metres at present.

With such a narrow beamwidth, it is necessary to deploy the system only slightly above the water surface - the top of the beach berm being an ideal and easily accessible position as shown in Figure 3.7.1.

The radar images are transferred to a laptop computer via a CAN bus connection, allowing the continuous recording of radar images for hours at a time if necessary.

Recent developments on newer systems by the radar manufacturers have improved hardware design and the signal processing system, providing a range increase to 800m, whilst maintaining the high range resolution. An Ethernet interface can also be added to the radar to acquire the power spectra information at high rate. This would make it possible to acquire several measurements at each azimuth, improving the signal to noise performance of the sensor and allowing smaller waves and effects in the field of view to be extracted.

Early experiments showed that the signals that are detected using the mm wave radar are primarily breaking waves and swash bores running up the beach, rather than non-breaking waves. While this may seem to be a disadvantage, it can be considered an excellent method of studying the hydrodynamics of waves at or near the breaking point, since these are all that this radar sees. Datasets using this radar during the Faro 2002 experiments will be shown in Chapter 5 to validate depth inversions close to the shore.

Chapter 4: Data Collection

The data sets available for analysis vary considerably in content and quality, and since the quality of results of any analysis depend on the quality of the data, only the best quality data sets will be used rather than trying to extract useful information from datasets that have inherent problems. The Holderness data is discussed in some detail as these were the experiments that led to the present study and generated the data on which the early work was based. The experiments that stand out in terms of high quality additional measurements are INDIA (Faro 1999), Teignmouth and Faro 2002 and 2003.

Experiment	Num. Frames	Interval	Clock Accuracy	Survey Availability	Tide Gauge Availability	Wave Gauge Availability
Holderness 1 1994-5	32	3 hour	+/- 1 min	no	PMP pressure sensor	Directional Waverider
Holderness 2 1995-6	64	1.5 hour	+/- 1 min	no	PMP pressure sensor	Directional Waverider
Egmond 1998 (COAST3D)	64	1 hour	+/- 30 mins at worst	WESP for inshore bars, Ship survey offshore	Several pressure sensors on frames	Various available
Faro 1999 (INDIA)	64	1 hour	GPS +/- 1sec	Yes, but quality is suspect in certain areas due to poor tide correction	PMP pressure sensor outside inlet	Triaxys wave buoy
Teignmouth (COAST3D)	64	1 hour	GPS +/- 1sec	Yes, excellent quality	Yes, Gauge on Pier	Various available
Faro 2002	128	Opportunist when storms hit, then every 15 mins	GPS +/- 1sec	Yes, single mid beach RTK GPS + echo sounder transect to 1.5km offshore + beach surveys	No, Tide predictions only	Faro wave buoy graphs read off the web
Faro 2003	128	Opportunist when storms hit, then every 15 mins	GPS +/- 1sec	Beach surveys	No, Tide predictions only	No, Faro wave buoy not operational

Table 4.1 A summary of the various radar datasets in existence at POL up to early 2003, showing the associated conventional measurements available.

Full descriptions of the data are given and discussed before proceeding to the analyses in later chapters. Table 4.1 gives a full list of all available datasets to 2003.

4.1 Holderness I and II

The Holderness experiments were conducted with the funding and under the umbrella of a number of large programmes. Two large experiments were conducted through the winters of 1994-5 and 1995-6. A number of stations were instrumented along two cross-shore lines on the Holderness coast on the east coast of England. Stations along those lines were instrumented with bottom mounted frames, including POL Monitoring Packages (PMP), Sediment Transport And Boundary Layer Equipment (STABLE) and BLISS together with surface Waverider buoys for monitoring waves and meteorological data (Bell et al., 1997). The locations of these are shown in Figure 4.1.1.

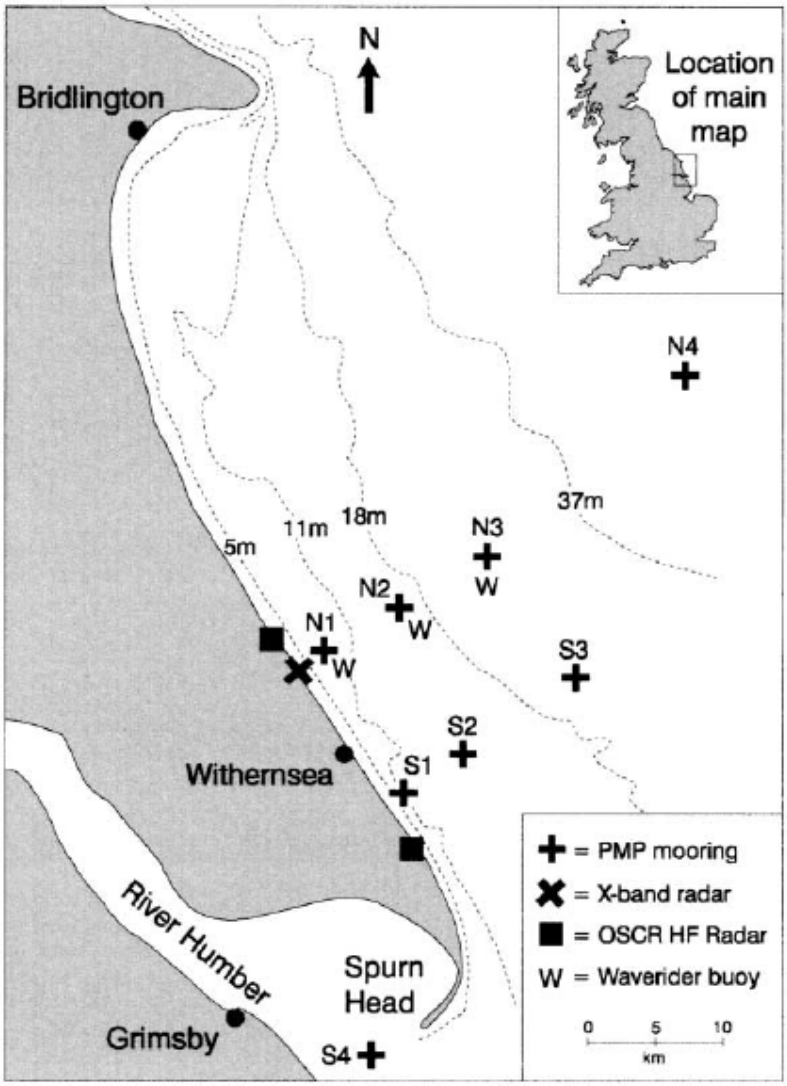

Figure 4.1.1 The instrument locations during the Holderness experiments.

The X-Band radar was deployed for the first time as a monitoring tool during the first winter, following two years of development, sorting out hardware and software compatibility problems. The radar was sited overlooking the beach at the shoreward end of the north line of instrument positions with the hope of obtaining 2-D directional wave spectra close to the shore. At the offshore sites, Waverider buoys monitored the waves and PMPs monitored the waves, currents, tides and suspended sediment conditions. Limitations on the size of discs in the PC controlling the radar kept the recording interval to 3 hours, and the number of images per record to 32, in line with the paper of Young et al. (1985). Apart from one extremely violent storm over New Year in 1994-5, the winter season was uneventful in terms of wave conditions. The second season was more interesting, with an unusually high number of storm events being recorded by the radar system. Unfortunately, despite a survey having been ordered, none was performed largely due to the lack of an appropriate weather window, so no direct bathymetric comparisons are possible with this data. However, it was used as the test case to develop the early versions of the bathymetric analysis as it was possible to compare variations in tidal water depth calculated from the radar data with those measured by pressure sensors on the PMP frames.

The radar was deployed on a small scaffold tower within a relatively secure bottled-gas storage compound at a caravan site near Tunstall, Figure 3.5.2. The compound was sited about 10-15 metres back from the cliff as a safety measure as that stretch of coastline is composed of easily eroded material and is retreating at a rate of several metres per year. As a result of being relatively far back from the cliff, the view of the beach was blocked, but the region seaward of the beach was in clear view. An example of a radar image from the Holderness II deployment is shown in Figure 4.1.2, overlaid on an aerial photograph of the area.

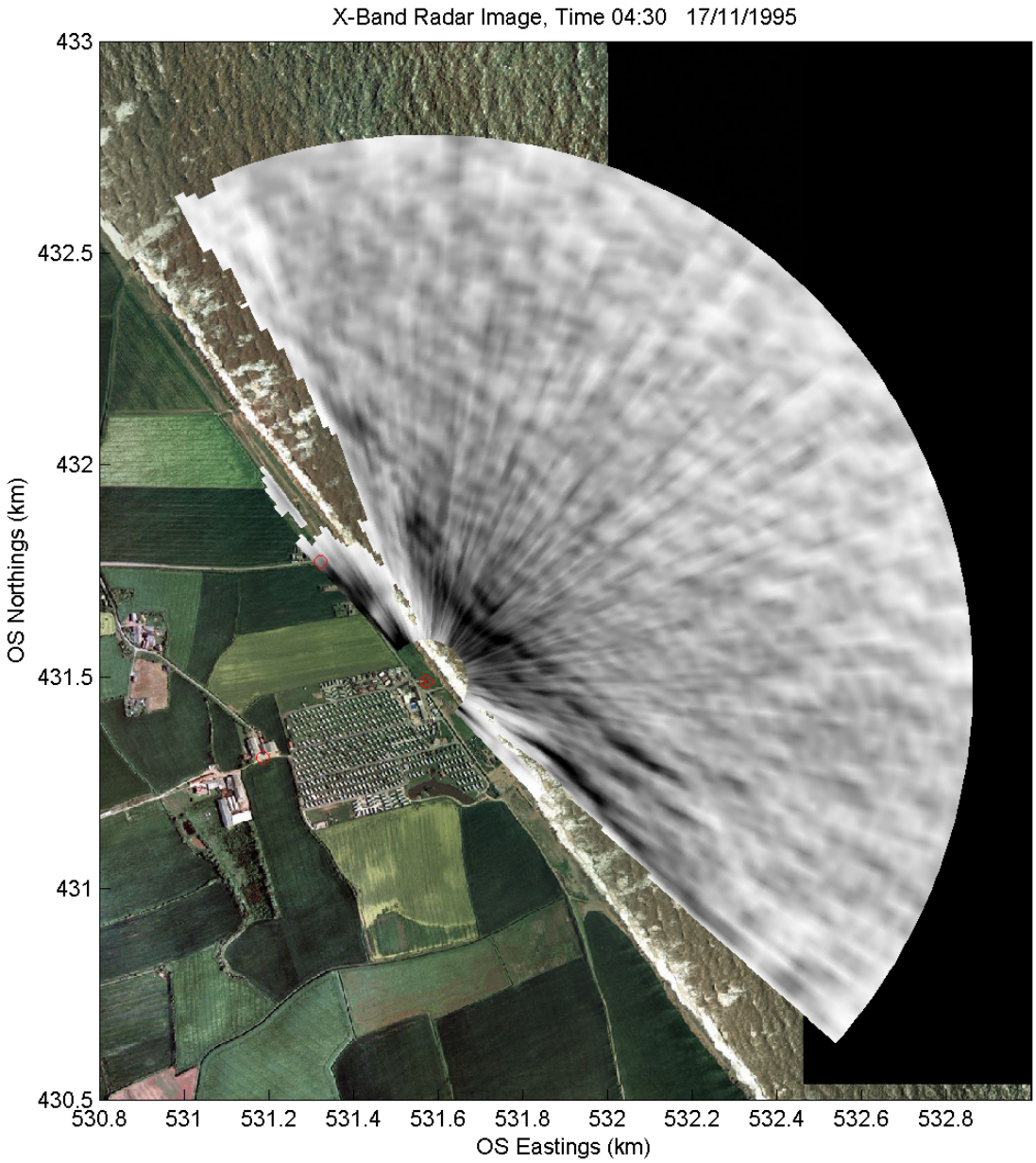

Figure 4.1.2 A raw X-band radar image from the Holderness II experiment overlaid on an aerial photo of Tunstall where the radar was deployed. Note that the time of the radar record does not match the time when the photo was taken.

For the purposes of computational efficiency, analyses of the Holderness radar data shown in later sections has been carried out on rotated radar images such that the coastline runs parallel to the x-axis.

4.2 INlet Dynamics Initiative Algarve (INDIA)

Faro beach and inlet was the site of the 1999 EU funded **IN**let **D**ynamics **I**nitiative **A**lgarve (INDIA) project (Williams et al., 2003), aimed at developing an understanding of the naturalisation of an artificially opened tidal inlet through a barrier beach, and its subsequent

natural migration. The location is shown in Figure 4.2.1. This EU funded project was a large collaborative effort by a number of international research groups. As such, a full description of the entire project is beyond the scope of the present work and only those measurements and observations that are of direct relevance will be described. The author's part in this project included all aspects of the radar deployment and data analysis as well as the day to day running of the other sediment process studies executed from on-board a barge in the tidal inlet.

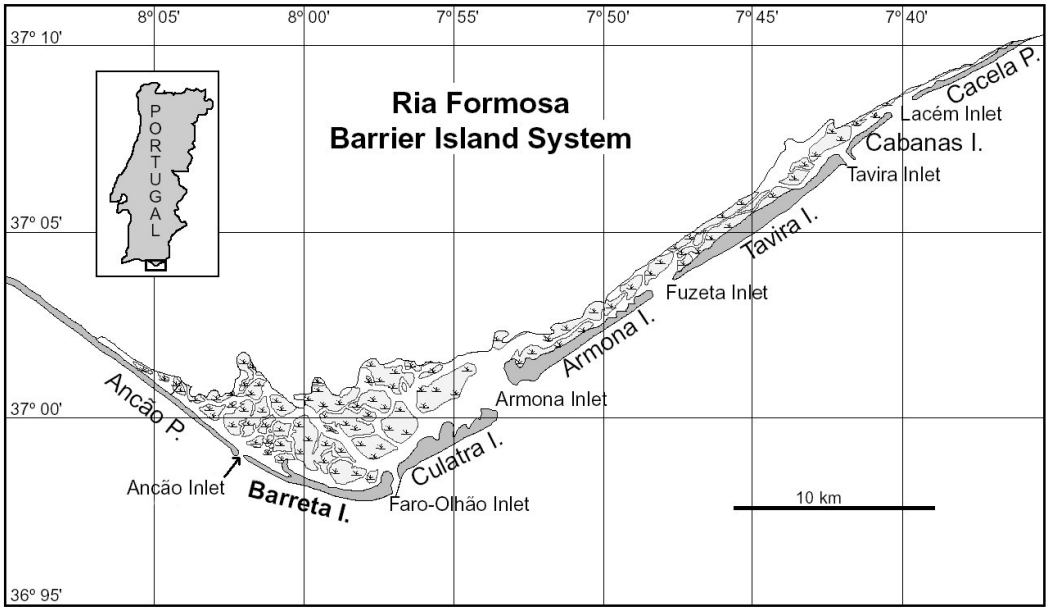

Figure 4.2.1 The location of the INDIA experiments in Faro, Portugal. The present Ancao Inlet is indicated to the bottom left of the map. (Map kindly provided by Brad Morris)

During the years leading up to 1997 the existing tidal inlet had migrated to the south east and become inefficient at exchanging water with the extensive salt marshes behind the barrier beach, a pattern of behaviour that repeats itself every 20-25 years. This inefficiency of the inlet led to water quality problems that were of serious concern to the local shell fishing industry, and in 1997 a new (Barra Nova) Ancao inlet was dredged through the barrier beach.

This situation was identified by researchers at the University of Algarve as an ideal opportunity to record, from the beginning, the evolution of an un-armoured naturally evolving tidal inlet, and the INDIA project built upon the foundation of this existing knowledge.

The X-band radar was deployed for a period of 38 days from a high level gantry on a Jack-up barge, the "Skate III", shown in Figure 4.2.2. Due to the isolation of the barge and its relative inaccessibility, it was possible to run the system continuously with minimal risk of interference from the general public. A regime of hourly records of 64 images each was implemented, leading to almost 5Gbytes of radar data being recorded during the project.

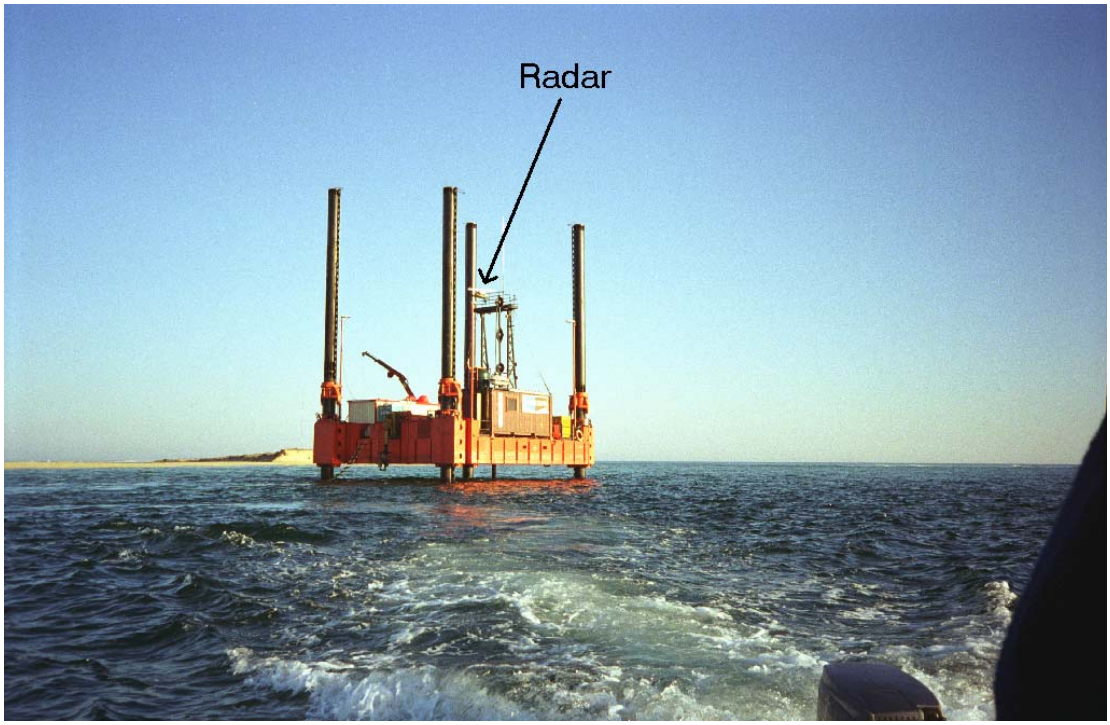

Figure 4.2.2 The "Skate III" barge jacked-up on its legs in the Ancao Inlet during the INDIA project in 1999.

While the height of the radar gave an excellent view from the gantry above the barge, the steel legs, upon which the barge was lifted out of the water, extended considerably above the radar position causing a number of problems with the radar images from the outset. The barge legs cast a radar shadow behind them, and also caused false radar echos at the azimuths corresponding to the leg positions, in essence leading to blind spots for the radar. The barge position was varied from day to day as the primary purpose of its presence was as a platform from which to carry out small scale sediment and hydrodynamic process studies (Williams et al., 2003b). This complicated matters for the radar work, as no precise positioning system was available on the barge, hence each time the barge was moved a new position and orientation had to be determined by manual alignment of the images with known landmarks.

In order to monitor the wave climate during the project, a Triaxys directional wave buoy was deployed on the 25m contour, approximately 4km offshore from the inlet. The significant wave height information and wave spectra measured by the Triaxys buoy are shown in Figure 4.2.3.

Data from the Faro wave buoy was also available but provided only wave statistics and not the full spectra. The statistics for the two wave buoys were almost identical so only the Triaxys data have been shown in order to keep Figure 4.2.3 simple. Both records have dropouts in the data at various times but, interestingly, both buoys failed to record a large event starting around March 8th that delayed the recovery cruise in port for several days. The Faro wave buoy is recorded via radio link, but the Triaxys buoy had its own internal data logger, so this was surprising.

The majority of this deployment was unfortunately of very low wave conditions as can be seen in Figure 4.2.3. The small wave events that did occur were primarily of locally generated wind sea of around 5 seconds period, such as that on the 10th February, and having a wavelength too short to be of use for depth inversions on their own. However, during the last two days of the deployment at the beginning of March, a small swell wave event ($H_S \approx 1$m) occurred and the barge was moved some distance behind the inlet for safety. The requirement for the barge to be in the inlet itself for the sediment studies had meant that much of the inlet was within the blanking distance of the radar recording system and could not be seen on the images. The movement of the barge to the inside of the inlet finally afforded the radar a good view of the Ancao Inlet under wave conditions just high enough to show up on the radar images, with a significant wave height of approximately 1m. The wave periods at that time were in the 10-15 second band and were ideal for use in a bathymetric inversion. These long period waves were particularly desirable for this site due to the rapid increase in depth with distance from the shore, 20m depths being reached within 2km of the inlet. Short period wind waves would not 'feel' the bottom in such deep water and would be unsuitable for determining the water depth, but even at depths of 20m the bed would still affect the longer period waves to a significant extent.

Tide levels during the experiment were monitored by a number of instruments, among them a POL Monitoring Package (PMP) that was deployed approximately 2km to the south of the Ancao Inlet in 18m water relative to chart datum (MSL-2m). This recorded water levels every 10 minutes for the duration of the project. The tidal record from this instrument is

shown in Figure 4.2.4 with a correction for atmospheric pressure recorded nearby at Faro Airport. The tide is semi-diurnal, with spring tide ranges of up to 3.5m and neap tide ranges of approximately 1m.

In addition to these in-situ recording systems, a video system was installed, in a joint effort by the University of Algarve and the University of Plymouth, on the island of Barreta (see Figure 4.2.1) on a 30m high tower to provide video images over a period of 14 months from July 1998 to January 2000 to monitor remotely the evolution of the inlet (Morris et al., 2001 & 2004). By January 2000, the island of Barreta had eroded to the point where the video tower was in danger of falling into the sea, so the system was dismantled.

Two black and white video cameras recorded snapshots and time-lapse images every daylight hour during that time. The time-lapse images average out the wave patterns and leave smoothed, lighter coloured areas where waves are breaking. These oblique angle snapshots and time-lapse images could then be rectified into x-y coordinates for comparison in true geographic coordinates using a standard photogrammetric technique described by Holland et al. (1997).

A photo of the video tower installed on Barreta Island in 1998 is shown in Figure 4.2.5. The cameras were mounted at the top of the tower and the entire system was solar powered as there was no mains power on the island.

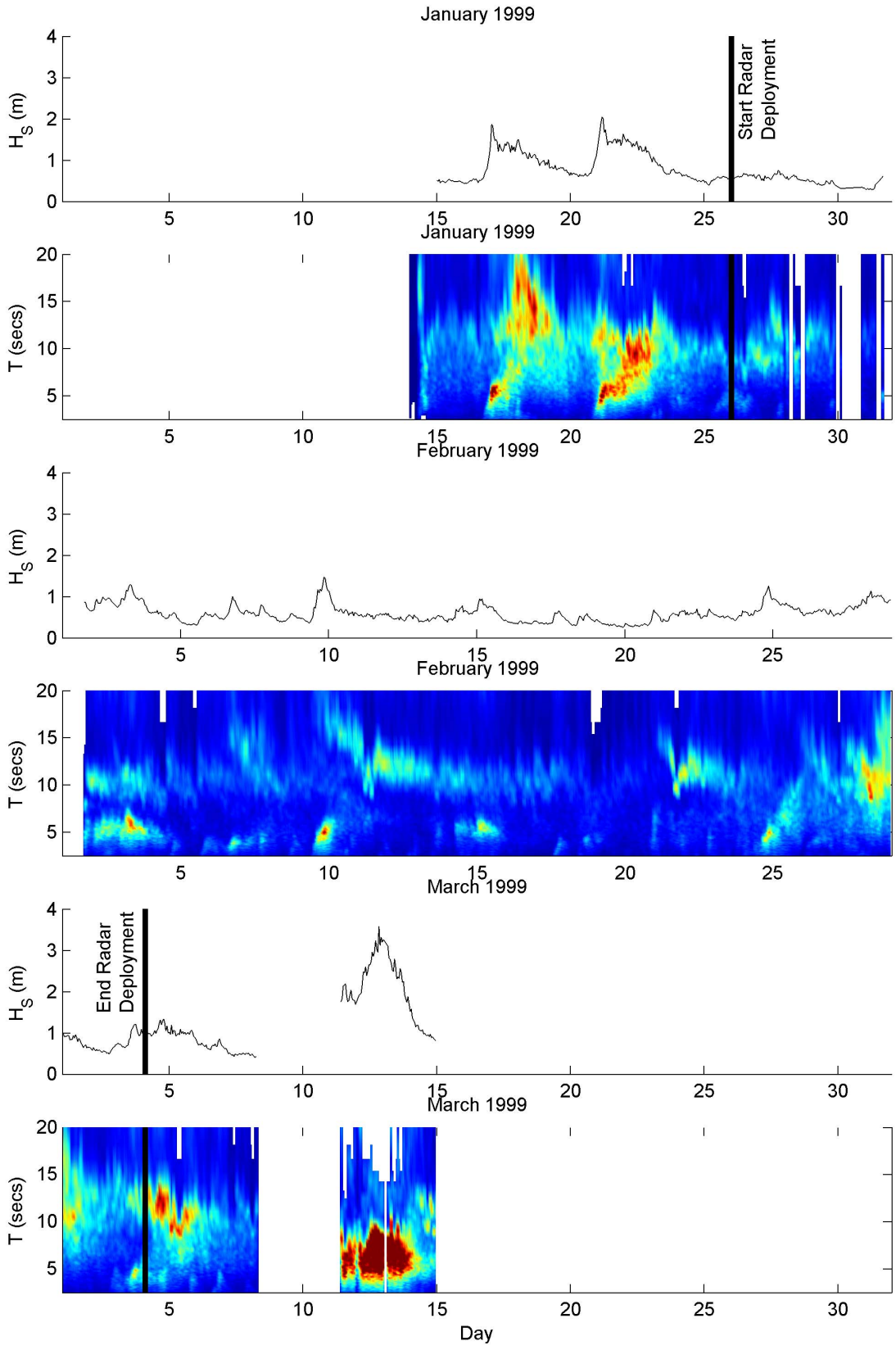

Figure 4.2.3 Wave data from a Triaxys directional wave buoy during the INDIA experiment. Significant wave height and the wave spectra are shown in alternate plots for the three months of the experiment. The colour scale in the spectra plots uses blues for low energy and reds for higher energy conditions. The start and end of the radar deployment are shown as the thick black lines.

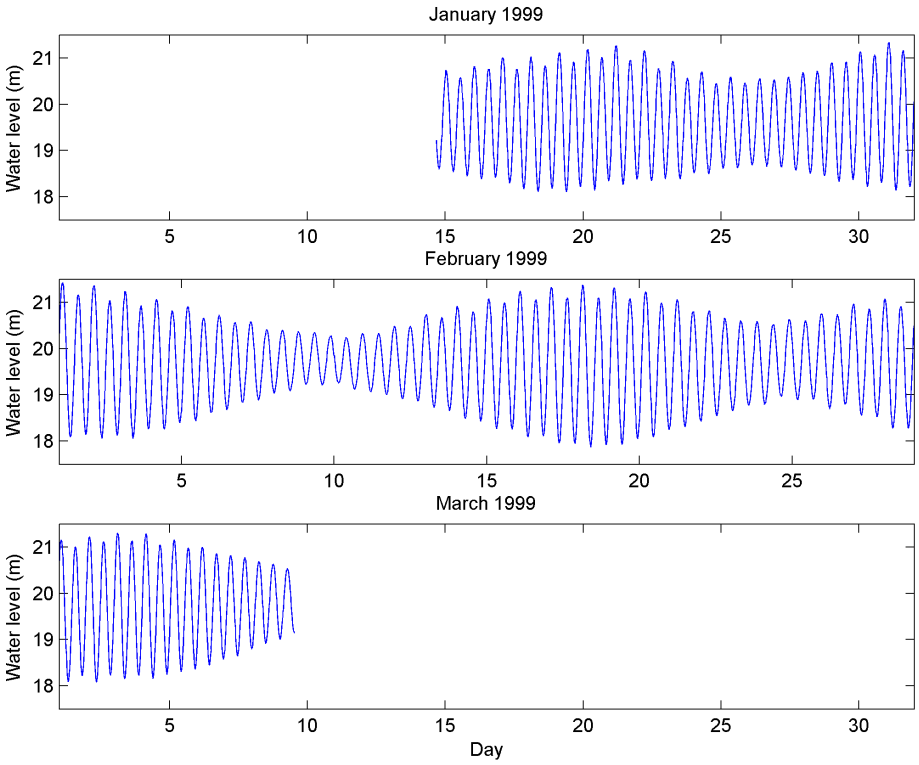

Figure 4.2.4 The water level recorded by an S4DW mounted on a PMP in approximately 18m of water relative to chart datum, 2km south of the Ancao Inlet during the INDIA project.

Figure 4.2.5 The video tower located on the Island of Barreta in 1998. (Photograph from the INDIA database)

Examples of the oblique snapshot images recorded by the video system at 15:00 on March 3rd 1999 are shown in Figure 4.2.6. In the left hand image, waves can be seen breaking over the ebb delta, with the shoreline of the Island of Barreta visible in the foreground. The right hand image shows the inlet itself, with the vegetated north-west tip of the Island of Barreta in the foreground, the inlet, and then the south-eastern tip of the Ancao peninsula at the top of the image. The two images overlap slightly and can be combined to provide one seamless image of the inlet and ebb delta when rectified using photogrammetry techniques.

These images were recorded at the time when the barge had been moved just inside the inlet and the radar was able to record wave images of sufficient quality to perform bathymetric inversions. The edge of the barge can just be seen in the top right of the right hand image.

Figure 4.2.6 Snapshot video images from the two cameras at 15:00 on 3rd March 1999. The left hand image shows the ebb delta seaward of Barreta, and the right hand image shows the inlet. The edge of the barge on which the radar was mounted behind the inlet can just be seen in the top right of this image.

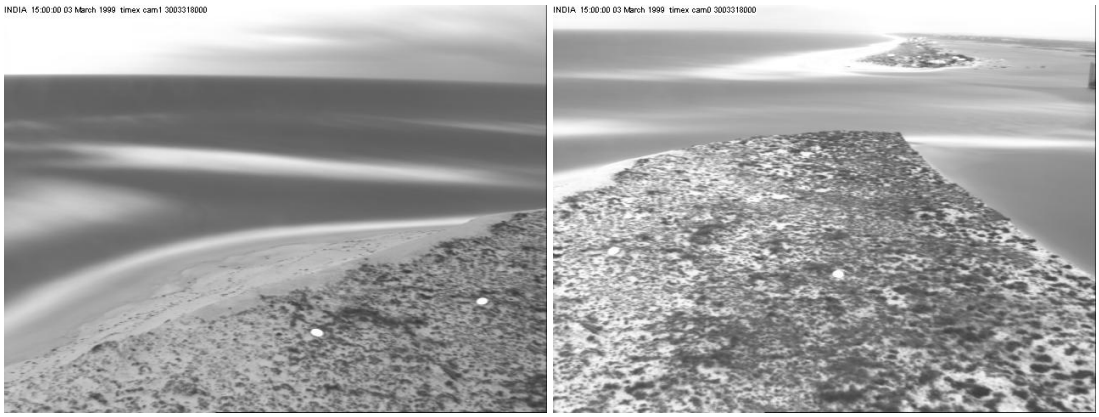

Figure 4.2.7 Time-lapse video images from the two cameras at 15:00 on 3rd March 1999. The wave patterns have been averaged out, revealing areas of consistent wave breaking as the lighter areas of the sea.

The corresponding time-lapse images are shown in Figure 4.2.7. The channel position could be inferred from the rectified time-lapse video images by identifying the darkest part of the image of the inlet, as documented in Morris et al. (2001).

4.3 Teignmouth COAST3D

This experiment was the second phase of the EU funded COAST3D project in 1999 aimed at collecting datasets designed specifically for model validations. The first phase took place at Egmond aan Zee in the Netherlands in the winter of 1998 and was originally intended to provide a more straightforward case for the models to simulate – a straight 2D coast with a double sand bar system. Unexpectedly, this provided greater challenges to the modelling systems due to the subtle variations in the 2D nature of the sand bar systems and the variable hydrodynamics associated with them. During that experiment there were serious problems with the clock on the radar system, leading to significant uncertainty in the exact time of recording of the radar data, and so that dataset is not used for verification of bathymetric inversions in the present study. Without an accurate fix on the time, the tidal level could not be identified in order to make water depth comparisons with survey data. As a result of this problem, the clock systems were upgraded in future experiments to regularly update the PC clock from a GPS receiver, and so the Teignmouth experiment in the winter of 1999 did not suffer from this flaw.

Teignmouth, on the south west coast of the UK, was intended to provide the more complex 3 dimensional case for the COAST3D project. The study area contains a rocky outcrop to the south, bounding a tidal inlet to an estuary and working port. A complex set of sand banks around the mouth of the inlet have a cyclic anticlockwise migration, leading to large variations in sand bar height and location during a 2-3 year cycle. The six-week duration of the main experiment could not hope to resolve the complete cycle of the sand bars, however the video monitoring system was planned as a permanent installation operated by Plymouth University and is still in operation at the time of writing as part of the US led ARGUS network of coastal video cameras[11].

To the north of the inlet is a groined straight beach that experiences significant changes in beach morphology in response to incident wave conditions. Numerous instrument packages were deployed around the experiment area to provide boundary conditions for the modelling studies; hence a number of wave and current measurements are available.

[11] The ARGUS video network is hosted by the Coastal Imaging Lab at Oregon State University in the USA, and can be found online at http://cil-www.oce.orst.edu:8080/

The radar was deployed on the shoreward end of Teignmouth Pier, approximately in the middle of the study area. A tide gauge was located on the same pier, and two surveys were carried out at the start and end of the experiment.

An aerial photograph of the area is shown in Figure 4.3.1. The same area with the survey carried out by the HR Wallingford survey vessel is shown in Figure 4.3.2. Depths are shown to Admiralty Chart Datum (ACD). The groins on the beach either side of the pier are not visible on the photograph in Figure 4.3.1, but are marked on the bathymetry plot in Figure 4.3.2.

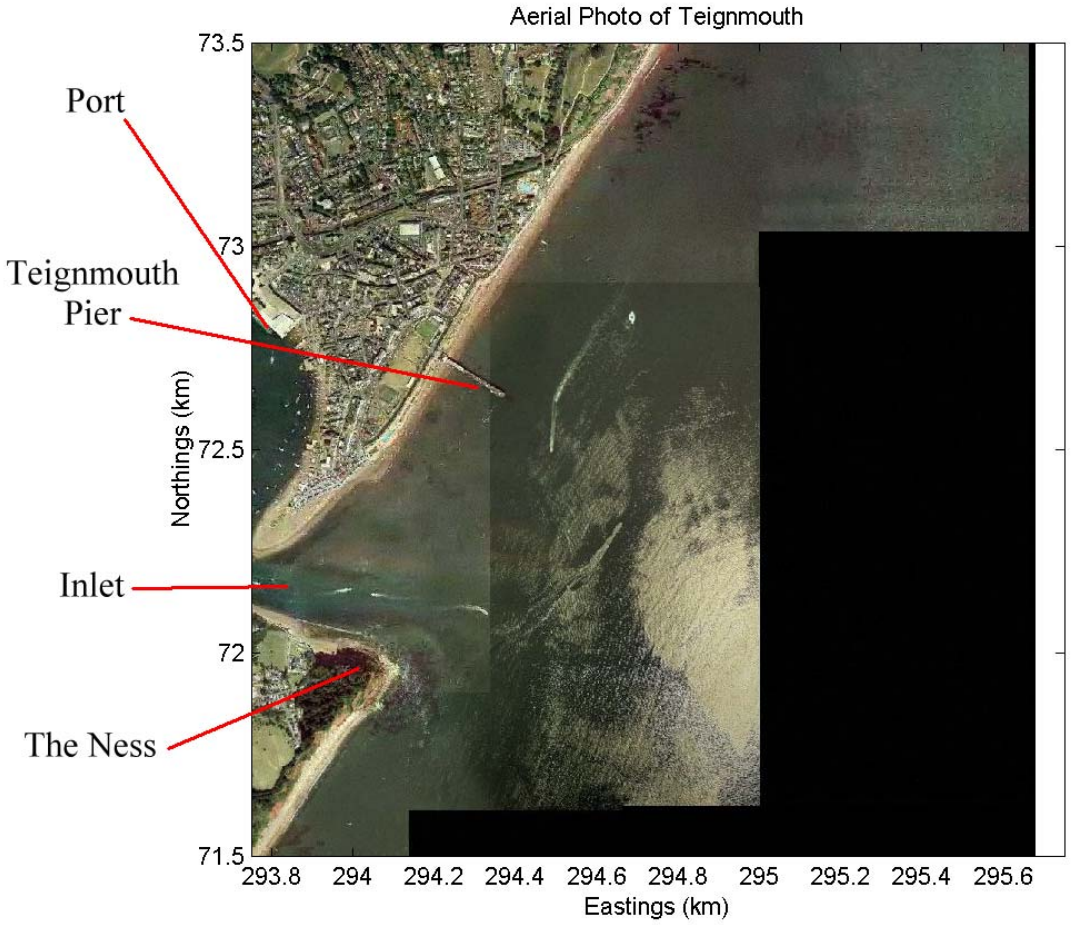

Figure 4.3.1 An aerial photograph of Teignmouth, showing the rocky outcrop known as the Ness to the south west, the tidal inlet to the north of the Ness, and the straight beach with Teignmouth Pier clearly visible.

The complex system of sand bars around the mouth of the inlet is clearly visible from the survey. The channel through the outer part of the system has a continuous tendency to infill, necessitating the almost daily dredging of the outer channel to allow the navigation of ships to and from the port inside the inlet. The maximum surveyed depth in the area is

approximately 8m, and the extent of the survey reflects the limits of the study area for the experiment. Another half kilometre range on the survey would have proven useful for comparisons with the radar, but this would have increased the offshore survey area from 1.5km^2 to approximately 4km^2, and the existing surveys already took several days to complete. The time taken and calm conditions required for surveying in a conventional manner emphasises the usefulness of a radar based bathymetric inversion that can produce a bathymetric map of almost double the range surveyed from only a few minutes of radar data, given a good set of waves.

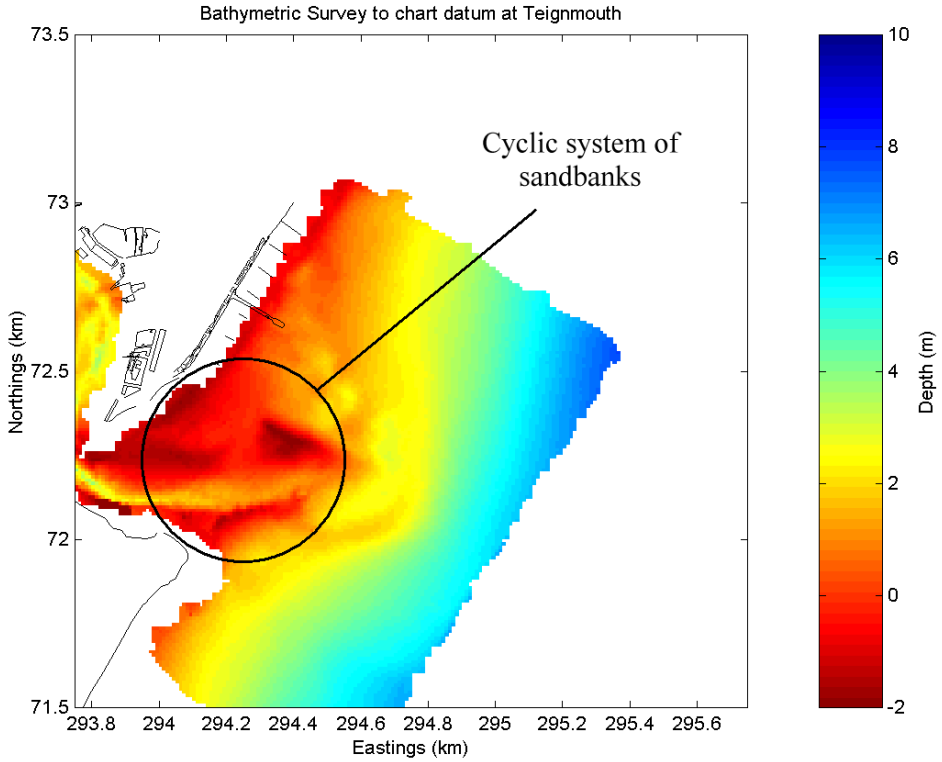

Figure 4.3.2 The HR Wallingford survey of the Teignmouth study area, plotted on the same scale as the aerial photo in Figure 4.1.1. Depths are to ACD.

The other background data collected can be illustrated by the plots in Figure 4.3.3. These show the wave conditions measured using a Datawell Directional Waverider (HR Wallingford, 2000) deployed in the north-east corner of the surveyed area and the tidal record from a tide gauge on the end of the pier. Several storm events were recorded during the experiment, providing an excellent dataset for both the planned modelling and also for the present study.

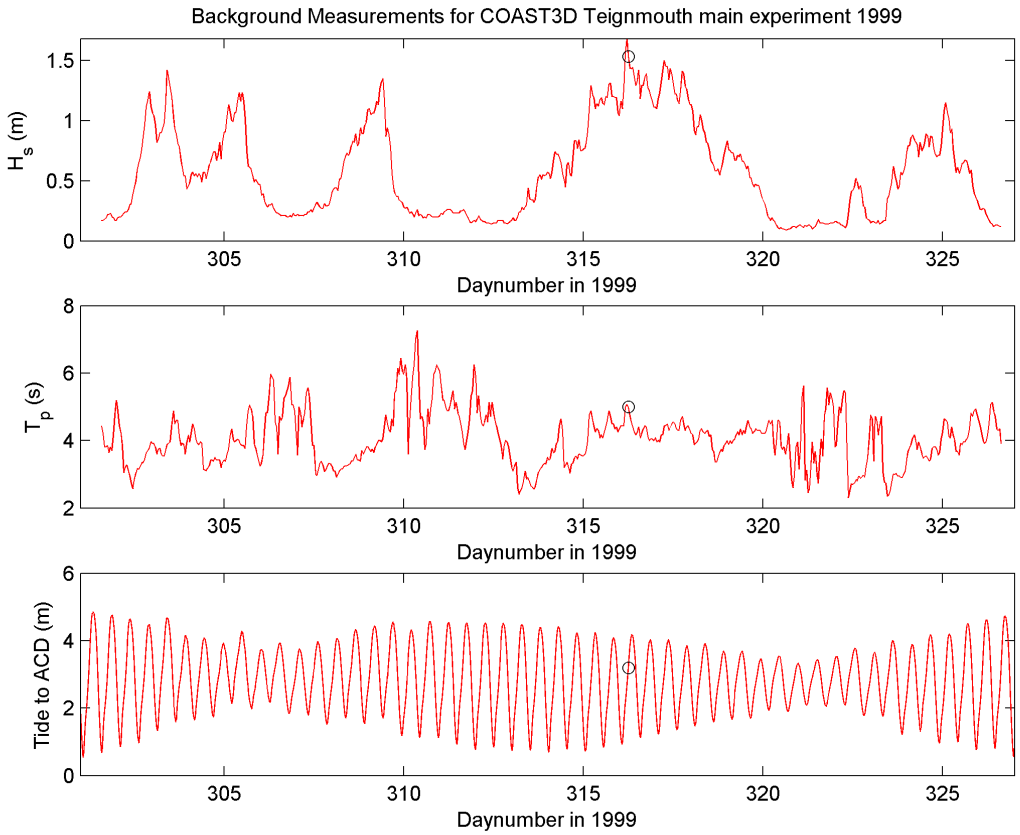

Figure 4.3.3 The wave and tide data recorded during the COAST3D Teignmouth main experiment. The black circles mark the conditions recorded at the time of the example radar record shown in Figures 4.3.4 and 4.3.5.

An example of one frame of radar data collected during this experiment is illustrated in Figure 4.3.4, recorded during one of the wave events on day 318 (Bell, 2001). The increased backscatter intensity shown by the waves in the region of the sandbanks demonstrates a nice example of breaking waves, and their refraction around the varying bathymetry. Although the peak period was 5s and rather short for depth inversion purposes due to the limited depth at which the waves would feel the bottom, there was significant wave energy in periods up to 8s, allowing depth inversions to be performed from the shallowest depths to the deepest areas viewed by the radar (approximately 10m).

The corresponding average image – the mean of the 64 images in that record is shown in Figure 4.3.5, in which the areas of breaking waves are clearly associated with the shallow areas of the sand banks and beach. Various notable features are highlighted in this figure, such as the sand banks themselves, the Ness and the wave staff array installed by Plymouth University.

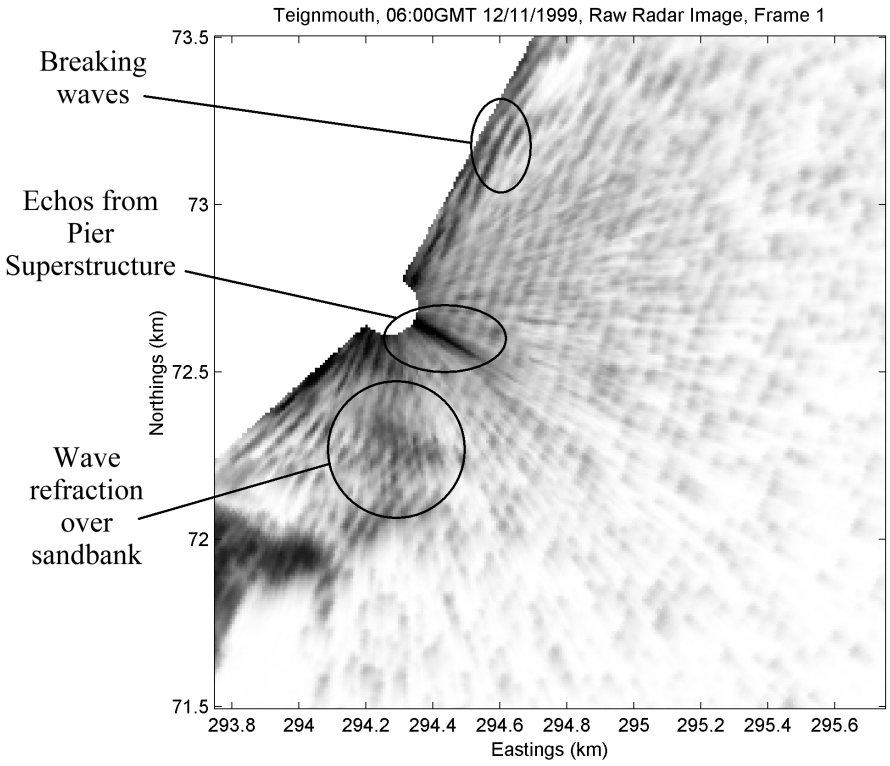

Figure 4.3.4 A frame from the Teignmouth radar deployment during a storm on day 316.

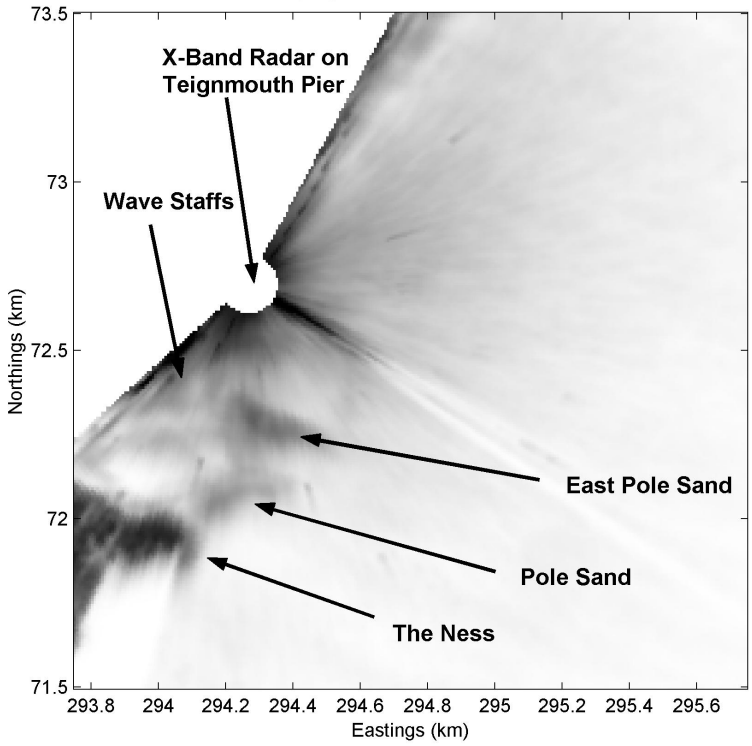

Figure 4.3.5 The mean image associated with the record from day 316 shown in Figure 4.3.3, illustrating the increased backscatter around various bathymetric features and hard targets.

4.4 Faro 2002 Nested Radar Experiment

This experiment is highlighted due to the unique deployment of two imaging radars of different resolutions to monitor the same area of sea simultaneously (Bell, 2005).

In 2002 the author returned to the site of the INDIA experiment in Faro to deploy the radar for another winter season in the hope of recording a more interesting series of wave conditions than those experienced during the INDIA project. This coincided with the University of Algarve group continuing their monitoring efforts to document the beach and inlet evolution, and carry out swash experiments on the beach.

Figure 4.4.1 The two radars deployed simultaneously during a storm on Faro beach in 2002. The mm wave radar can be seen on the left, and the X-band radar on the right, the photograph being taken looking approximately inshore.

The X-Band marine radar was deployed from the top of the beach on a low scaffold tower only at times when appreciable waves were present, largely because the site was not considered secure enough to leave equipment unattended. During one wave event, a joint experiment with the University of Algarve group took place in which detailed beach surveys were carried out at low water, and both the X-Band radar and the Navtech mm wave radar were deployed on the same area of beach. The two radars are shown together in Figure 4.4.1 during that experiment. Data were recorded through a rising tide every 15 minutes. Unfortunately, it was not possible to deploy a tide gauge or wave gauge during the experiment, but it was possible to download plots of wave data from the Faro wave buoy, located a few miles away. The significant wave height and period graphs for the week including this experiment are shown in Figure 4.4.2 and 4.4.3. The experiment itself took

place on the 4th March, towards the end of the time series. The significant period (*T02)* line in Figure 4.4.3 refers to T_z calculated from *m0* and *m2* of the wave spectrum. The T_{max} values are significantly above the T_z values for the majority of the record, consistent with the presence of long period swell visible on the radar and originating from the Atlantic.

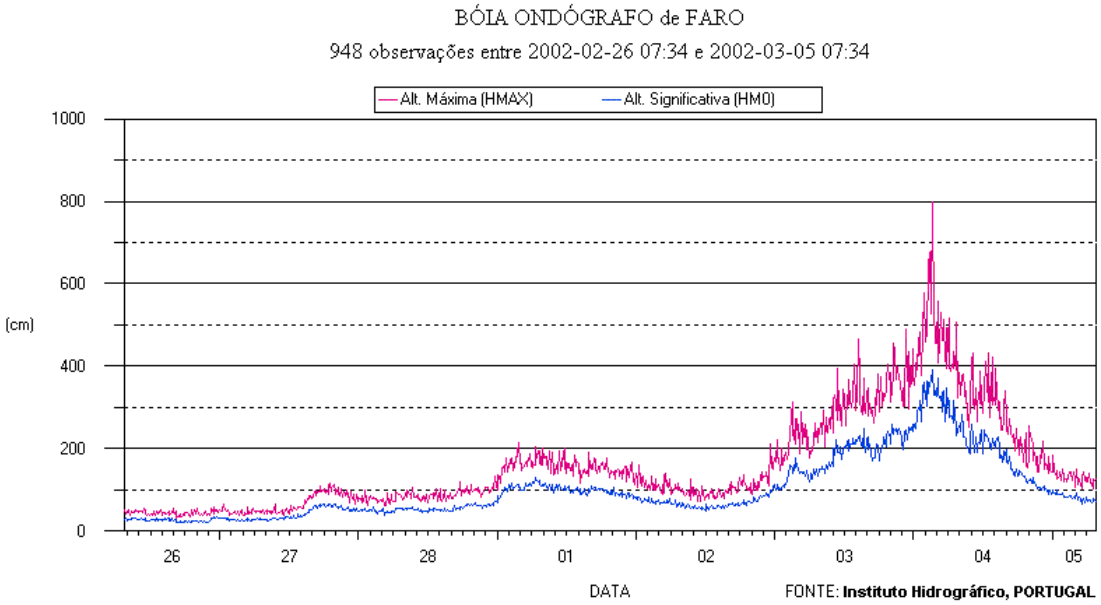

Figure 4.4.2 The Faro wave buoy weekly wave height data covering the time of the nested radar experiment on 4th March 2002.

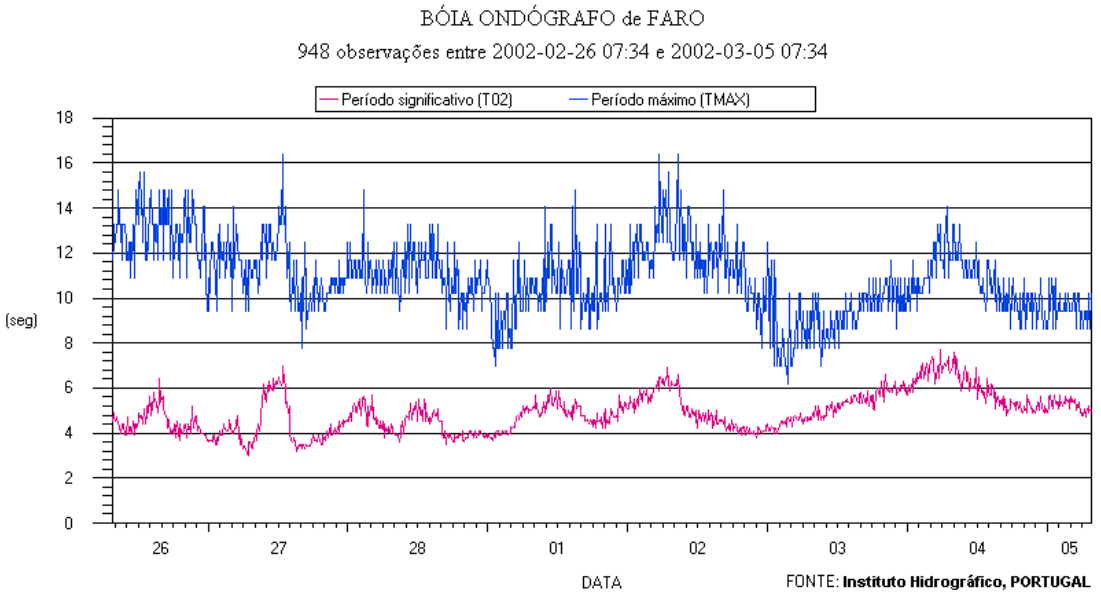

Figure 4.4.3 The Faro wave buoy weekly wave period data covering the time of the nested radar experiment on 4th March 2002.

The *HMAX* values were approximately double those of the significant wave height and are consistent with those that can be estimated from H_s and T_z. The maximum waveheight can be

estimated from H_s multiplied by a factor based on the number of waves in the record, using equation 1.4.4.

Hence if we assume that the data is derived from records of length 1024 seconds as would normally be the case, T_z at the time of the experiment around midday on the 4th March is approximately 6 seconds, while T_p was approximately 11 seconds. H_s is approximately 2m and H_{max} is approximately 3.2m. This would give a value for N according to the equation as:

$$N = \frac{1024}{T_z} = \frac{1024}{6} = 170 \text{ waves}$$

and

$$H_{\max} = H_S \sqrt{\frac{\ln N}{2}} = H_S \sqrt{\frac{\ln 170}{2}} = 1.6 H_S = 3.2 \text{ m}$$

So the H_{max} values plotted in Figure 4.4.2, while on the large side are in line with the T_z values in plotted in Figure 4.4.3.

The experiment took place largely in the afternoon of the 4th March, the morning being occupied transporting and setting the equipment up at the site. During this time the significant wave height recorded by the Faro wave buoy was relatively stable at approximately 2m.

It would also have been useful to have had an accurate tidal record, but none was available. However, during the 1999 INDIA campaign, a POL Monitoring Package (PMP) was deployed not far from the inlet, and a pressure record was obtained (shown in Figure 4.2.4), from which tidal constituents were extracted. These were then used in the commercially available POLTIPS tidal prediction software to generate tidal predictions for all subsequent experiments at that site[12].

The tidal predictions for this period are shown in Figure 4.4.4, with the thick red line indicating the duration of the nested radar experiment from 11am to 3pm. The experiment was terminated at 3pm due to the approach of rain, for which the temporary nature of the installation was unsuitable.

[12] Many thanks to David Blackman at POL for carrying out the tidal analysis, and to Colin Bell at POL for supplying a customised version of POLTIPS tidal prediction software including these tidal constituents.

It is likely that the actual tidal level would not exactly match the predictions during a storm. However, it has been observed from previous experiments that deviations from the predictions due to meteorological effects are usually no more than 30cm in that area, and so the use of predictions in the absence of measurements was considered unlikely to be a major source of error.

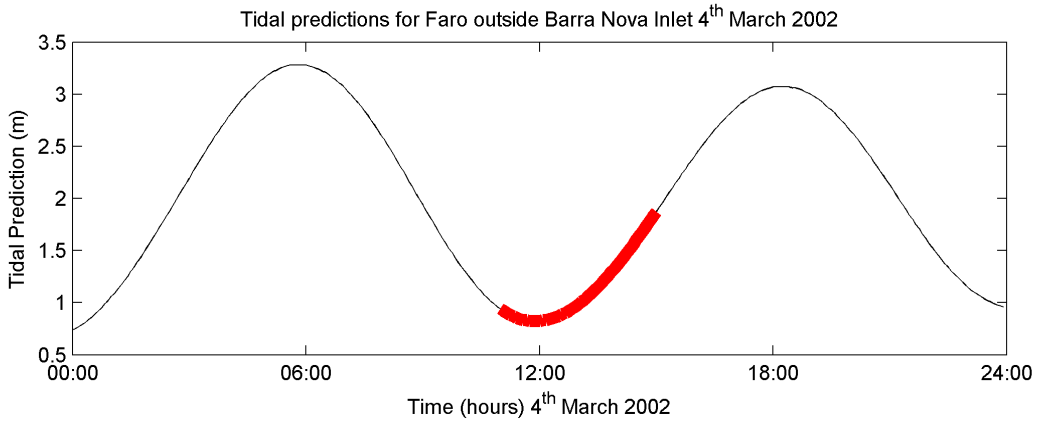

Figure 4.4.4 The tidal predictions for Faro beach during the 4th March 2002. The thick red line indicates the duration of the nested radar experiment.

A complete survey of the area was not available. However the University of Algarve group carried out both a topographic survey of the beach in the immediate area of the experiment and a bathymetric survey a few days previously along a number of cross shore transects up to 1.5km from the shore. These were kindly made available to the author for use in this work.

4.5 Faro 2003 X-Band Radar Deployment

The site was visited again during February – March 2003 in particular to collect radar data covering the Ancao Inlet area, as the 2002 deployment failed to obtain good quality data for that part of the coast. A number of wave events occurred during that deployment, although wave statistics are not available for that time due to a fault with the Faro wave buoy. The wave conditions recorded on the radar during these periods were of high quality, providing excellent wave images on which to perform the bathymetric inversion, the results of which are presented in chapter 7. In addition, a number of mm wave radar records were made by the author during some of the wave events, including one overnight deployment on Barreta Island to study wave overwash processes in collaboration with the University of Algarve. The radar data from these mm wave radar experiments has not been used in this work so will not be discussed further, although photographs taken on Barreta Island following the overwash experiment proved serendipitous in light of results presented in chapter 7. A photo of the X-band radar set up at the end of the Ancao peninsula overlooking the inlet is shown in Figure 4.5.1. It is interesting to note that the area of sand on which the radar is shown in this image was, four years previously, in the middle of the inlet and not far from the barge position shown in Figure 4.2.2 during the INDIA project in 1999. The barrier beach had re-formed as the inlet migrated to the south east in the intervening years, with vegetation starting to re-establish itself.

Figure 4.5.1 The X-band radar set up at the end of the Ancao peninsula overlooking the inlet during the Faro 2003 deployment.

Chapter 5: Data Analyses

The derivation of water depth maps from image sequences of waves requires an analysis that is capable of extracting either the precise wavelength or the celerity of the waves. Following the realisation by the author that relatively detailed water depth information was contained within the X-band radar image sequences of waves, a number of different approaches to this problem were attempted. Each successive approach generated new insights that led to the next approach, until the final algorithm as described in section 5.6 was developed. This method of mapping the wavelengths of the waves was used in the later chapters of this thesis to establish the validity of the technique and to study the bathymetric changes associated with a tidal inlet through a barrier beach.

Fourier theory has played an important part in the following sections, so the chapter begins with a short review of Fourier theory and the Fast Fourier Transform (FFT). A brief review of the methods used by other researchers to extract wave information from radar images puts the developments achieved in the present study into context. The various approaches taken by the author to extract the required wave information are then described in chronological order, finishing with the final version of the analysis that has been used in the later chapters.

5.1 Fourier Theory and the Fast Fourier Transform

Fourier theory states that if *h(t)* is a periodic function in the time domain, then it can be represented in the frequency domain by a function *H(f),* where $-\infty < f < \infty$, by the equations:

$$\text{Fourier transform } H(f) = \int_{-\infty}^{\infty} h(t) e^{-2\pi i f t}\, dt \qquad 5.1.1$$

$$\text{time series } h(t) = \int_{-\infty}^{\infty} H(f) e^{2\pi i f t}\, df \qquad 5.1.2$$

known as the Fourier transform equations.

The form of these equations for a time series of discretely sampled data with N data points sampled with an interval of Δt seconds such as would be produced by any oceanographic instrument are:

discrete Fourier transform $$H(k) = \sum_{n=0}^{N-1} h(n) e^{-2\pi i k n / N} \qquad 5.1.3$$

and

discrete time series $$h(n) = \frac{1}{N} \sum_{n=0}^{N-1} H(k) e^{2\pi i k n / N} \qquad 5.1.4$$

where

$$k = -\frac{N}{2}, \ldots, \frac{N}{2}$$

The Fast Fourier Transform (FFT) carries out this process in an extremely efficient manner in computational terms, provided N is an integer power of 2, and so tends to be the algorithm of choice for most applications.

In practical terms, if the FFT algorithm is applied to a time series (or a series of measurements in space) of N points, it is broken down into a series of frequency components ranging in integer steps from 1 cycle per $N\Delta t$ seconds to $N/2$ cycles per $N\Delta t$ seconds. The complex coefficients *H(k)* of these components indicate their phase and magnitude. The integer steps are a requirement of the Discrete Fourier Transform for the mean value of a Fourier component to be zero over the data length.

When operating on a time series of N real data points, the standard FFT algorithm outputs a series of N complex values. The first value represents the mean of the real input data. The next $N/2$ values represent the *H(k)* coefficients representing 1 cycle per N data points to $N/2$ cycles per N data points. Where the input data are real, the remaining $N/2-1$ values are the complex conjugates of the first $N/2-1$ *H(k)* values and can be ignored. However, where the input data are complex, these last $N/2-1$ *H(k)* values represent negative frequencies, or in practical terms, waveforms that are moving backwards.

This is an established analysis technique for time series in which the signals of interest have significantly shorter period than the overall length of the time series. A good example would be the analysis of a wave record in which 1024 seconds of data would usually be recorded at

a rate of 2Hz. The signals of interest, i.e. the waves, have periods of up to approximately 20seconds, so the wave record will contain at least 50 cycles of even the longest waves. Hence for waves with a period of approximately 20 seconds, the nearest components produced by the FFT are 19.69s, 20.08s and 20.48s corresponding to 52, 51 and 50 cycles per 1024s respectively, a frequency resolution that is sufficient for most purposes.

The FFT is not so useful for time series in which the signals of interest approach the overall length of the data. For example, consider an image of the sea surface with 2m square pixels and draw a line perpendicular to a set of wave crests over a distance of 128 pixels or 256m. If the waves had a period of 7s and the water depth was 10m, linear wave theory would predict waves with a wavelength of 60m. If the FFT algorithm was performed on this line to measure the wavelength from the image, the nearest FFT components or bins would be 51.2m and 64.0m, corresponding to 5 and 4 wavelengths per 256m respectively. If a depth inversion based on linear theory were then used to infer the water depth based on these wavelength measurements, the nearest FFT components would indicate water depths of 6.6m and 12.3m respectively. This level of accuracy in water depth measurement would be of little benefit for any shallow water mapping application.

Zero padding the ends of a short length of data and then applying the FFT could increase the frequency resolution by a factor of two with each doubling of the padded data length, but this would only be practical for 1D data. Using the above example, zero padding the original 128 pixels to 8192 pixels would achieve a final wavelength spacing in the resulting FFT of the order of +/-10cm. If used in a depth inversion, this would be sufficient for a depth accuracy of the order of +/-5cm. Matlab running on the PC used for the latter part of this work is capable of executing approximately 400 FFTs of that length of data per second. However, the problem being addressed here is to determine the wavelength contained in a 2D matrix. A single 2D FFT executed on a 4096 pixels square matrix took 17 seconds to execute, and the PC had insufficient memory to create a matrix of 8192 pixels square, but would have taken in excess of a minute to execute had it been possible. This would not be an efficient method of achieving the accuracy required for depth inversions.

5.2 Existing Methods of Data Analysis

From the earliest days of radar research it has been observed that waves can be seen on radar images. When well defined wave patterns are visible, the wavelengths and directions of the waves can be measured by hand if so desired (Hart & Miskin, 1945; Heathershaw et al., 1980). This approach is both time consuming and subjective, being dependent on the individual making the measurements. For example, the wave direction measurements generated by Heathershaw et al. (1980) from photographs of a radar screen were repeated by three different operators and the results of the three then averaged. The automatic and objective measurement of wave parameters is a necessity if the image analysis of radar data is to be adopted widely. Given a recorded sequence of radar or video images of the sea surface the problem, like much of oceanographic research, becomes one of basic physics and signal analysis.

Early work from offshore installations by Young et al. (1985) made use of 3-dimensional Fast Fourier Transforms (FFTs) of 500m square areas of the image sequences, generating a mean image spectrum in wavenumber-frequency space. Energy in this spectrum that is attributable to wave action lies on a funnel shaped surface in this 3-dimensional wavenumber-frequency space. The equation for this surface is that of the wave dispersion relationship, and in this case the linear dispersion equation was used as a suitable approximation to this. This is a reasonable wave theory to use in relatively deep water where the wave behaviour can be considered homogeneous over the area viewed by the radar. A least squares fit of the linear dispersion equation was carried out to the wave energy surface in the 3-D spectra, and this was used to estimate the mean water depth and current in the area under analysis. Once the water depth and current were estimated, the wavenumber spectra were inverted to the more commonly used wave frequency spectra and integrated to give a 2-D wave frequency spectrum, the inversion from wavenumber to frequency being done using linear wave theory. In these deep water cases, the effects of tidal variation in the water depth could be neglected as they represented an extremely small variation in wave behaviour in deeper water. A version of this analysis is now used in the commercially available WaMoS system (Reichert et al., 1998).

While this approach is reasonable in waters where the wave behaviour is homogeneous, it has drawbacks in more complicated situations such as areas of shoaling waves near the shore. In such areas, the waves in one part of the radar image sequence may have different

directions and wavelengths from those in another; hence the mean values generated by the FFT approach will be an amalgam of these different wave types, and possibly not an accurate representation of any of them.

This variation was observed in the Holderness II radar dataset (Bell, 1998 & 1999) where the water depth was known to vary considerably within the size of area required for the FFT analysis. This variation in water depth, the lack of a recent bathymetric survey and a 3-4m tidal range made the determination of the water depth parameter needed by the inversion from wavenumber spectra to frequency spectra virtually impossible, and led directly to this present study.

The underlying concepts of Fourier transforms were re-visited in an effort to finds a more efficient algorithm for determining wavelength and direction. An algorithm was developed that homed in on the dominant wave signal in the data by maximising the result of the Fourier transform equation in the x and y directions and allowing accurate determination of wavelength without the integer limitation of the FFT.

5.3 Time Domain Motion Tracking

Early work to investigate the variation in wave behaviour close to the shore, captured in the Holderness dataset, used the most obvious method of obtaining the average wave celerity of the wave patterns recorded on the radar data, namely motion tracking of the wave patterns. A motion tracking algorithm would rely on a certain level of coherence in the wave pattern from one image to the next, allowing the wave celerity to be determined by following small sub-sections of the image with a size chosen to include two or three wavelengths. By repeating this process throughout the area viewed by the radar, a map of wave celerities could be assembled, and the depth estimated using a simple re-arrangement of the linear dispersion equation in the absence of a mean current:

Water depth $$d = \frac{L_0}{2\pi}\frac{C}{C_0}\tanh^{-1}\frac{C}{C_0}$$

where C is the celerity of the wave pattern determined from a motion tracking analysis, C_0 and L_0 are the deep water celerity and wavelength given as:

Deep water celerity $C_0 = \frac{gT}{2\pi}$

Deep water wavelength $L_0 = \frac{gT^2}{2\pi}$

where T is the wave period of the spectral peak identified from the FFT of the wave patterns in the radar images through time.

As d tends to 0, i.e. the shallow water case of the linear dispersion equation, the equation for celerity becomes independent of the wave period T and dependent only on d:

Shallow water celerity $C \to \sqrt{gd}$ as $d \to 0$.

This can be illustrated by the graph of celerity vs. depth in Figure 5.3.1

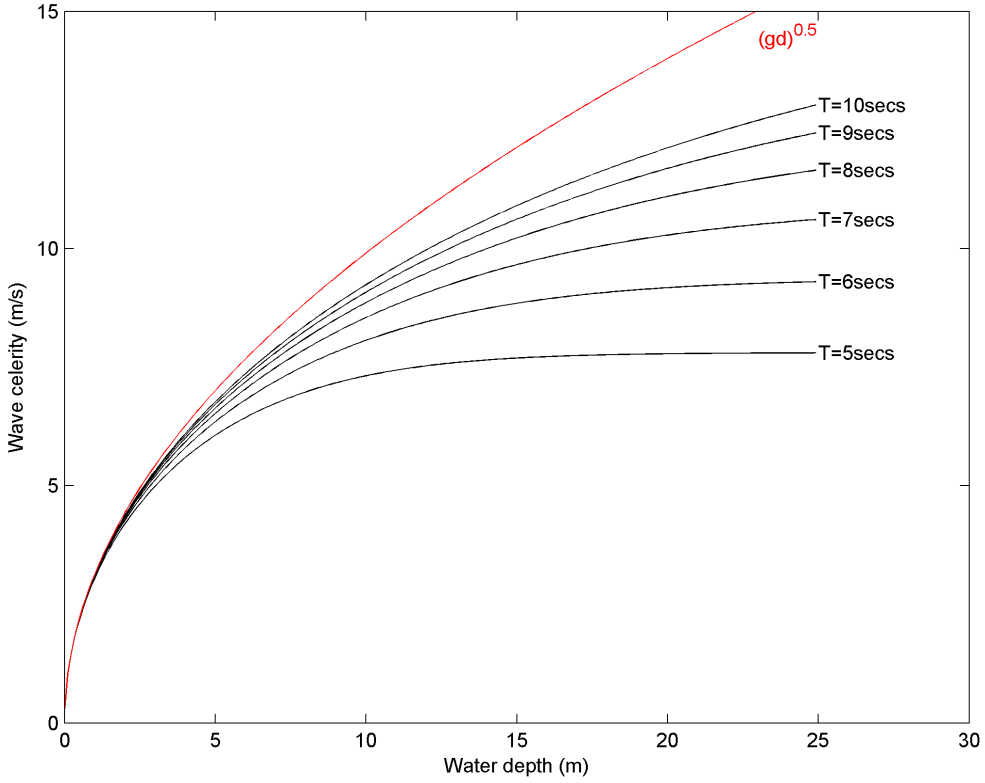

Figure 5.3.1 A plot of the wave celerities for wave periods of 5-10 seconds water depths of 0-25m according to linear wave theory. The shallow water approximation is shown in red.

The early version of this motion tracking analysis operated on successive image pairs through the radar image sequence (Bell, 1998). The best method of implementing motion

tracking between image pairs is to start by choosing a small subsection of the first image, for example a square of 32x32 pixels, corresponding to a 240m square area. The size of this area is a compromise between the desire to pick out as much detail as possible, and the need to have an area large enough to contain a distinctive section of wave pattern to be identified in the following image. The image subsection from the first image can then be compared with the same area in the following image and moved around by a few pixels in each direction to find where that subsection of wave pattern has moved to. It can be seen from Figure 5.3.1 that the maximum wave celerity of waves in a water depth of 20m would not exceed 14m/s. The X-band radar has an interval between images of approximately 2.25 seconds, hence the maximum distance that a wave could move between images is 14x2.25=31.5m, which corresponds to approximately 4 pixels (assuming 7.5m square pixels). Therefore, the algorithm compared the image subsection from the first image with all those within +/- 4 pixels in the following image. It was assumed that the wave properties would be homogeneous through time at a particular point in the image so this search method was then extended to operate on each successive pair of images through the image sequences simultaneously, so that instead of comparing two dimensional images, three dimensional blocks of data were tracked.

The actual comparison between image sub-sections can be performed using a variety of algorithms, and a number of such methods was investigated.

One of the simplest approaches looks for the least-squares difference by subtracting all of the pixels in one image from those in the next then squaring and summing the result. However, this would lead to very different magnitudes of results depending on the sea conditions, making any form of automatic quality control based on the numerical result of the comparison algorithm difficult.

An algorithm that standardises the results of a comparison is the linear cross-correlation (Press et al., 1992), which compares two sets of data x and y containing n points and outputs a correlation coefficient r between -1 and 1, with 1 indicating a perfect match and zero indicating no match:

$$r = \frac{\sum_n \left(x_n - \bar{x}\right)\left(y_n - \bar{y}\right)}{\sqrt{\sum_n \left(x_n - \bar{x}\right)^2} \sqrt{\sum_n \left(y_n - \bar{y}\right)^2}} \qquad (5.3.1)$$

There is also an FFT based cross correlation algorithm. However the standard library functions that calculate cross correlations using such methods are inherently unsuitable for highly detailed work using short data lengths. The reason for this can be illustrated by the example of a pair of radar images. If a 16x16 pixel area were to be extracted from both images and passed through the FFT based cross correlation, the statistics of the comparison between the image sub-sections would change for each increase in offset. At zero offset, all of the pixels contribute to the comparison. By the time a 3 pixel offset in the x and y direction is compared by the algorithm, the overlap area of the two image sub-sections would be reduced to only 13x13 pixels, i.e. the number of pixels used for the comparison would have fallen from 256 to 169, and by a 4 pixel offset, the number of pixels actually being compared by the algorithm would have fallen by almost a half. This means that the confidence of the motion offset estimates using this algorithm would deteriorate with increasing offset. A simple, but more robust algorithm was developed to allow the comparison of image sub-sections of the same size, regardless of the offset.

The operation of the motion tracking algorithm that was coded in Matlab can be illustrated using a pair of sequential radar image sub-sections shown in Figures 5.3.2 and 5.3.3. These show a 32x32 pixel area of a radar image from two sequential radar images representing an area of 240m square. The darker areas represent stronger radar backscatter and the lighter areas lower backscatter. A 12x12 pixel area has been outlined as an example in Figure 5.3.2 and the new position of that area wave pattern in the following image outlined in Figure 5.3.3. This new position has been determined using the search routine outlined above together with the linear cross correlation method in equation 5.3.1 as the measure of similarity. Each offset in the search routine generates a correlation coefficient, allowing a matrix of correlation coefficients to be assembled in which the highest value relates to the best match. This process is repeated through each successive pair of images in the sequence and a single correlation coefficient for each spatial offset calculated from all of the image pairs. A map of these correlation coefficients relating to the strength of similarity of the image sub-sections for the various offsets is shown in Figure 5.3.4. The darker areas in this plot represent higher values of correlation coefficient, and a distinct ridge can be seen in the result that represents the position to which the 12x12 pixel area has moved to from one image to the next. A number of points have been identified along this ridge by the fitting of quadratic curves through the peaks in each column of the correlation matrix using the Matlab polyfit command. Calculation of the derivatives of these quadratic curves allows the location

of the peak of each curve to sub-pixel accuracy. These points are marked using white crosses in Figure 5.3.4. This process is made possible by the assumption of a smoothly varying matrix of correlation coefficients. The peak of the ridge is located by determining the derivative, i.e. the gradient, of the quadratic and simply finding where it equals zero.

A straight line was then automatically fitted through this set of points from which the motion vector was determined. The motion vector is defined as a line passing through the zero offset position with a gradient that is the reciprocal of that fitted through the peaks of the ridge in the correlation matrix, and is therefore perpendicular to that line. The length and direction of this line, denoted by the arrow in Figure 5.3.4, represent the motion vector of the image subsection and hence the wave motion vector from one radar image to the next.

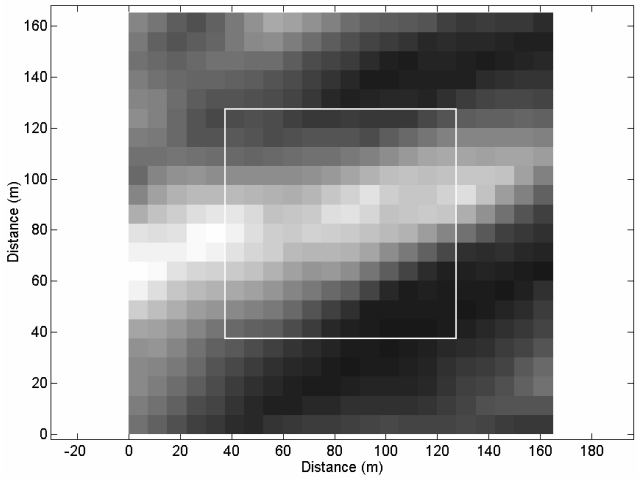

Figure 5.3.2 shows a small section of a radar image with the selected fragment of 12 pixels (90m) square outlined.

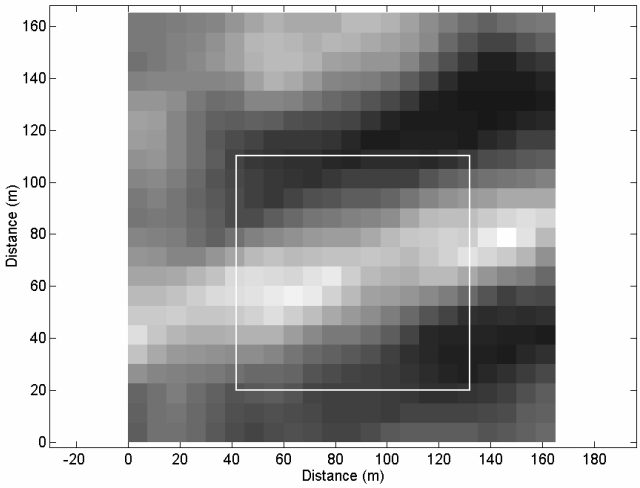

Figure 5.3.3 shows the same area within the subsequent image, with the new position of the selected image fragment as determined by the 2-D cross-correlation algorithm.

This process is repeated throughout the radar image area to build up a map of motion vectors and hence wave celerities by dividing by the time interval between images.

A number of other motion tracking algorithms were also tested, including that used by MPEG video compression, but none was found to approach the accuracy of the cross correlation technique described above.

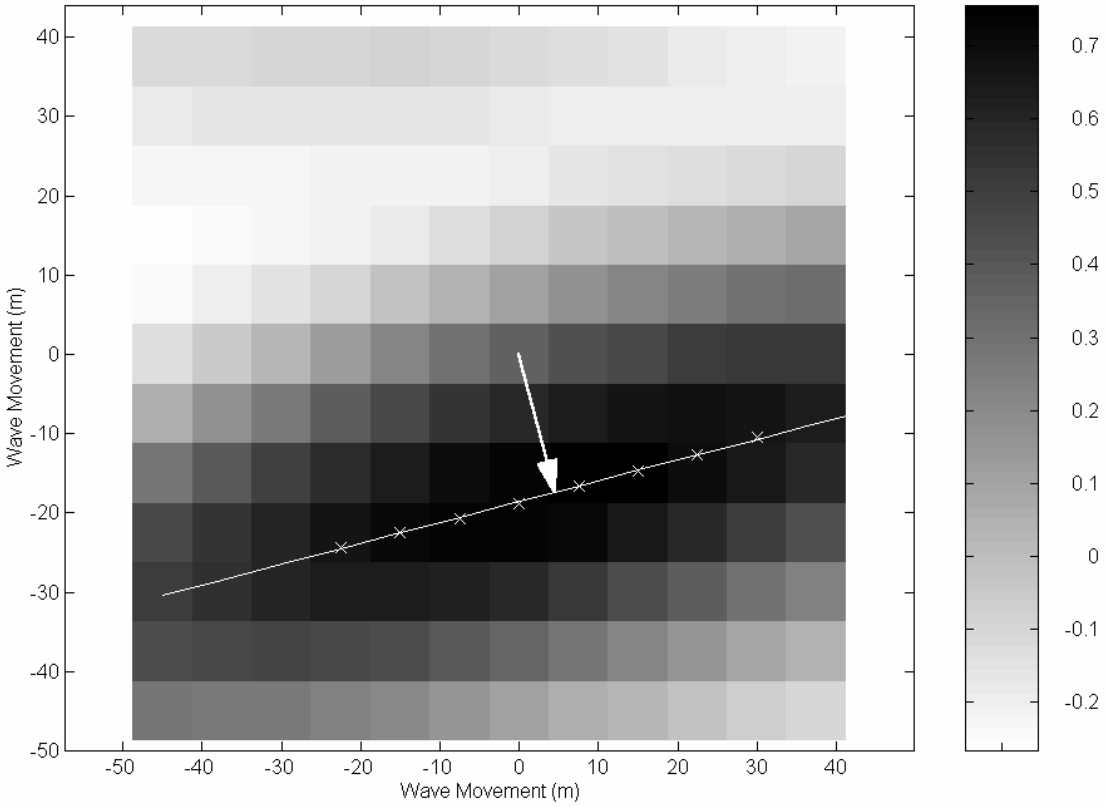

Figure 5.3.4 A plot of the cross correlation matrix from the image fragments, showing the expected linear ridge picked out by the white line. The white arrow represents the displacement of the pattern fragments shown in figures 5.3.2 and 5.3.3. The greyscale corresponds to the correlation coefficient.

As an example, a raw image from the Holderness experiment is given in Figure 5.3.5, rotated from its true orientation as shown in Figure 3.1.3 so that the coastline is parallel to the x-axis. The mean wave celerities calculated by the cross correlation approach on the raw images are shown in Figure 5.3.6. The celerities are represented by the colour scale with 1m/s contours shown as the black lines. The arrows illustrate the calculated wave direction with the length of each arrow being related to the celerity. The water depth map derived from the wave celerities is shown in Figure 5.3.7 with depth contours at 2m intervals.

As expected, the wave celerities get larger with distance offshore and hence deeper water, and the water depth calculated from the celerities using linear theory show depths of less than 2m close to the coast and deeper areas of up to 12m water depth at a distance of 1km offshore – values that are quite reasonable in the absence of a corroborating survey.

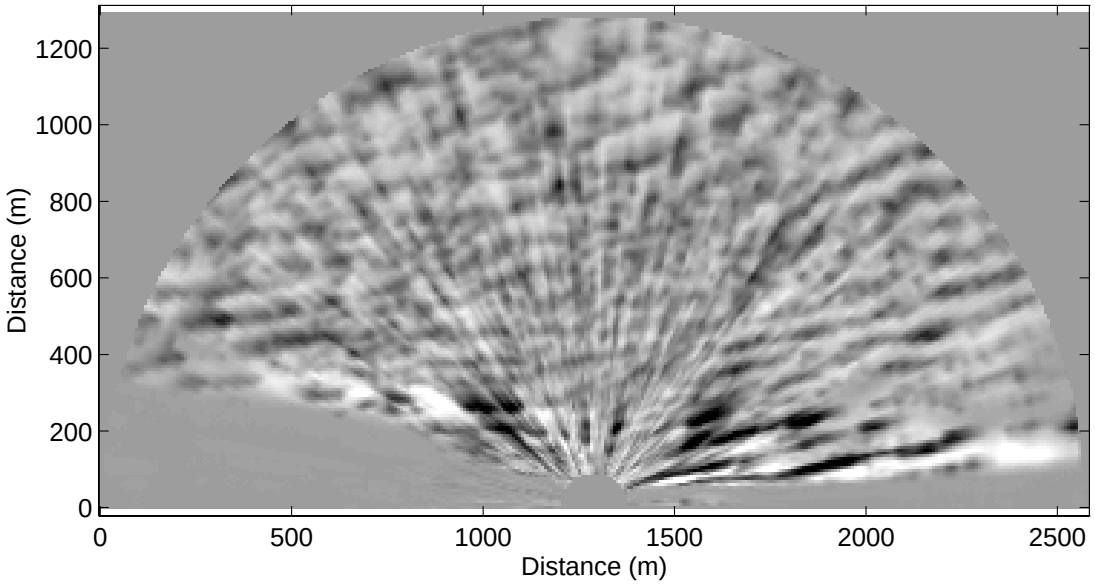

Figure 5.3.5 A snapshot of a single radar image from a sequence of 64, recorded at Holderness at 16:30, 17/11/1995 with the mean signal level subtracted. The darker areas correspond to regions of high radar backscatter from the waves. The larger signals in the lower part of the image relate to regions of breaking waves.

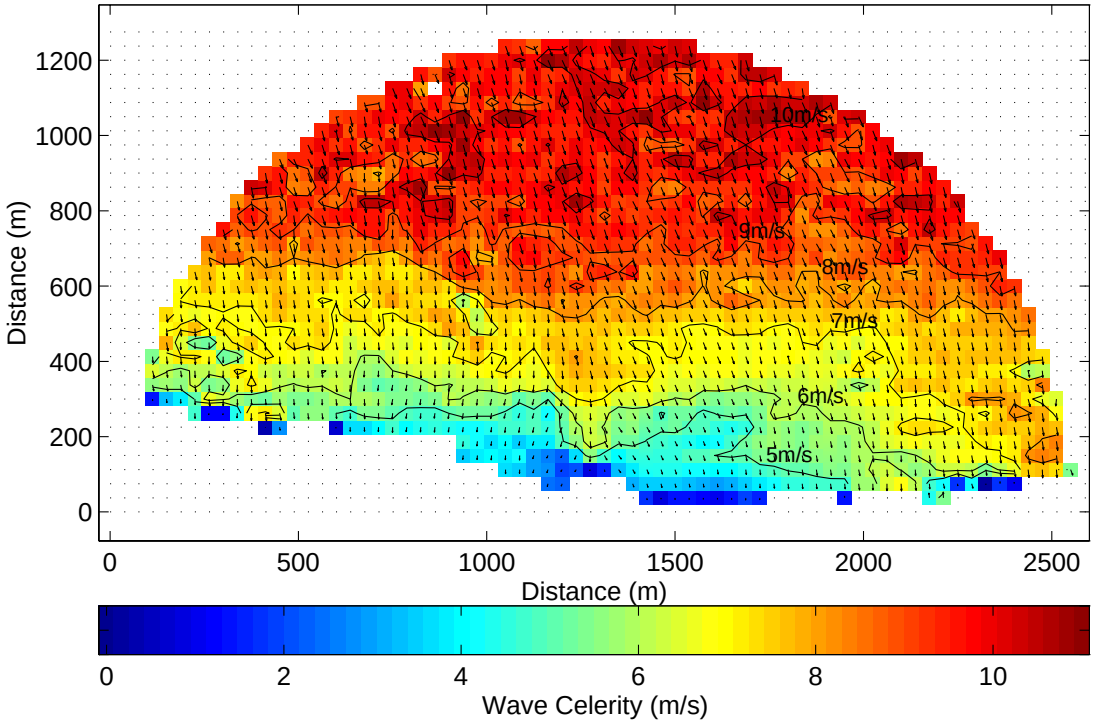

Figure 5.3.6 A plot of the wave celerity for 16:30, 17/11/1995, illustrating the variations in celerity calculated using the cross correlation technique. Contours show celerity intervals of 1m/s and arrows show the wave celerity vector.

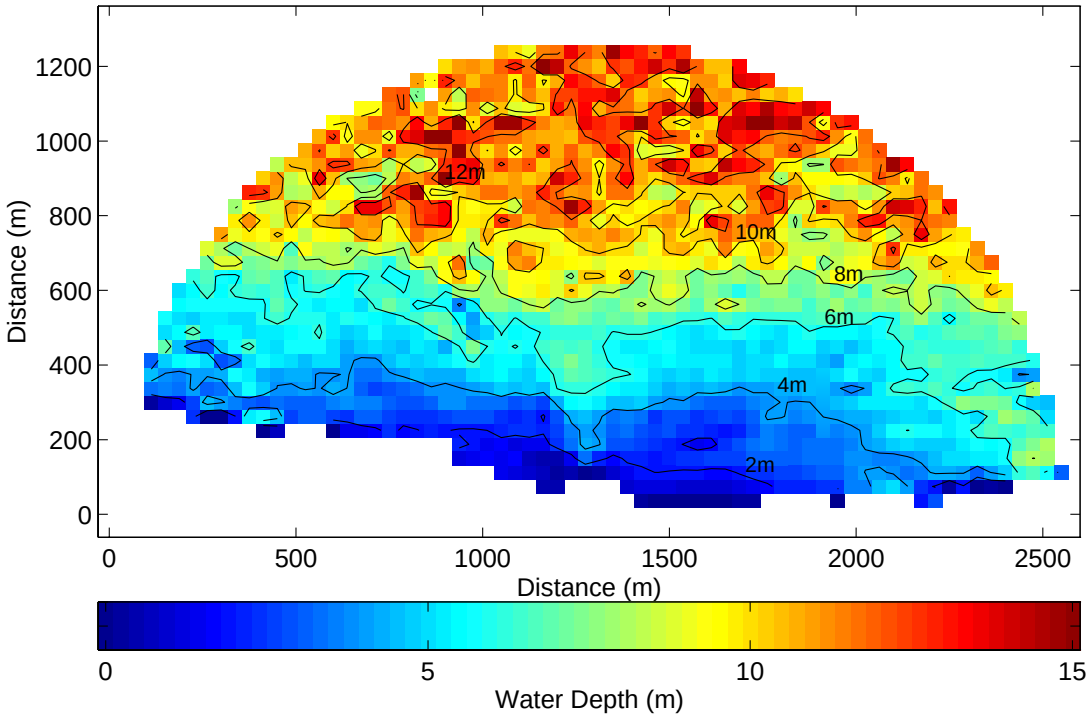

Figure 5.3.7 A plot of the calculated bathymetry derived from the wave celerities shown in Figure 5.3.6 using the linear dispersion equation. Water depth contours derived from the data are shown at 2m intervals.

It is interesting to note what appears to be a cross-shore channel of deeper water at the alongshore position of 1300m in Figure 5.3.7, running from the beach out to approximately 500m offshore. The wave direction vectors in Figure 5.3.6 can be also be seen to veer to the edges of this channel as might be expected. Again, without a survey for verification, it is difficult to confirm the presence of this feature. However, during the fieldwork in which this data was collected, the author observed local fishermen regularly launch their small boats from this position, despite the slipway for beach access being some distance from that point. This was presumably because they knew that the waves curved to the outside of the channel, leaving a passage of relatively calm water through which to safely launch their boats.

Three days of radar data from the Holderness II experiment in late 1995 were analysed using this technique, and the results published by Bell (1999). Unfortunately, without a conventional bathymetric survey it was difficult to verify the results of the depth inversions calculated by this method. However, a pressure sensor on an S4DW mounted on an offshore POL benthic frame was used to generate a tidal signal for that part of the coast. The availability of this tidal record made possible the comparison of variations in water level

determined from the radar data from record to record, providing at least some indication of the quality of the results.

To this end, the water depths determined using the radar data along an along-shore transect located 300m offshore were compared with the tidal record. This transect shows a mean water depth of approximately 4m and includes the deeper cross-shore channel mentioned above. The water depths calculated from each record are plotted in Figure 5.3.8a, with the colour representing water depth. Figure 5.3.8b shows the average water depth along the transect for that record, and a clear semidiurnal tidal signal can be seen. Figure 5.3.8c shows the water depth variation at the offshore benthic frame in a mean water depth of 14.5m. A strong correlation can be seen between the tidal signals from the offshore instrument and the radar derived water depths, giving confidence in this early attempt at bathymetric mapping using the radar data. The significant waveheight during this period is shown in Figure 5.3.8d, again measured by the offshore frame. Figure 5.3.8e plots the peak wave period from the offshore site as the solid line, together with the peak period of the radar image spectra as the asterisks. The peak period of the radar image spectra is consistently larger than that measured by the S4DW. This is probably due to the frequency dependence in the radar imaging mechanism (Wolf, 2001) which causes long period waves to be imaged more strongly than short period waves of equal magnitude. This would manifest as a shift in the spectral peak from its true period to a slightly longer period, as is seen here.

An uncertainty in this process is the issue of whether the average motion of the waves determined by motion tracking of the wave patterns in the raw radar images can be attributed to the peak wave period determined by FFT of the image sequence. This uncertainty in knowing exactly what wave period relates to the radar derived wave celerities could lead to significant depth errors, increasing in severity with depth as the wave celerity becomes more variable with the wave period as the water gets deeper. Despite this, the motion tracking technique may be of use in future for determining the wave angles of incidence on beaches with a view to predicting longshore transport, and perhaps for high resolution two dimensional tracking of swash on beaches.

The next development aimed to resolve this uncertainty by using Fourier methods to separate the different wave periods and allow them to be treated individually rather than as the amalgamation represented by the raw radar images.

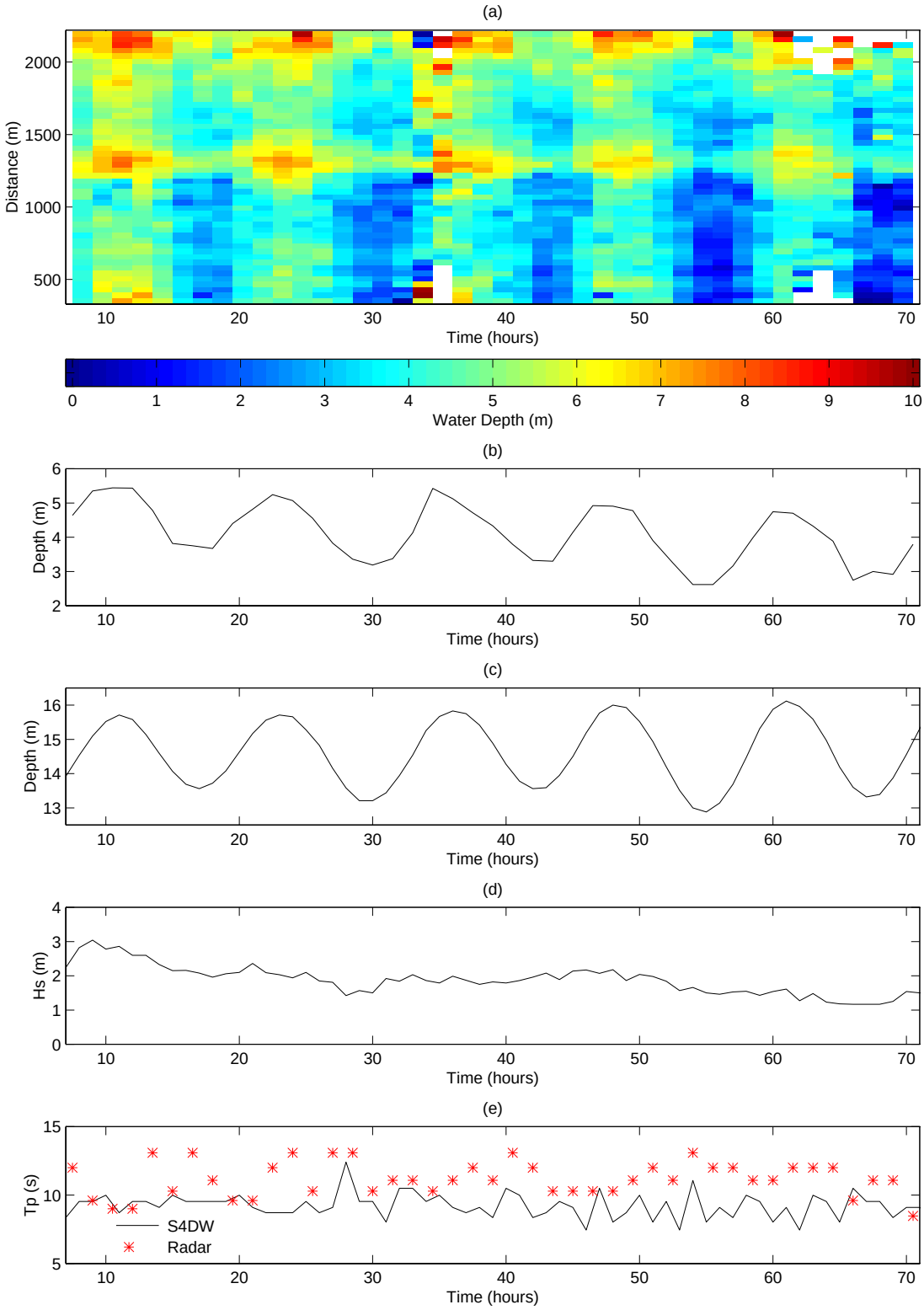

Figure 5.3.8 (a) A plot of the water depth 300 m offshore along a 1500 m line, (b) averaged to give a mean water depth along that line showing the tidal signal, (c) compared with the water depth measured by an S4DW further offshore, again showing the tidal signal, (d) the significant wave height during that period and (e) the peak period values derived from the S4DW and the radar.

5.4 Moving the Analysis into the Frequency Domain

An approach that was suggested and illustrated by Bell (1999) was to use the FFT to break down the radar image sequence into individual wave frequencies and analyse each of these in turn using the cross correlation motion tracking, thereby overcoming the problem of not knowing exactly what period waves are being tracked. The frequency breakdown is carried out by applying an FFT to the time series of each pixel, yielding for each pixel a spectrum of complex coefficients *H(k)* (c.f. equation 5.1.4) the modulus and argument of each complex coefficient representing the magnitude and phase respectively of the wave signal at the corresponding period. The result of this process is a 3-D matrix with *N* layers, in which the first layer corresponds to the map of the mean of the image sequence, analogous to a time lapse photograph. Each of the following $N/2$ layers contains a map of the respective Fourier coefficient *H(k)*, i.e. a map of complex coefficients that relate to the phase and magnitude of the waves at a particular wave frequency.

Having obtained the spectrum of *H(k)* values for each pixel through time using equation 5.1.3, an image sequence containing only one wave frequency can be reconstructed using the inverse FFT represented by equation 5.1.4 by nulling all but the *H(k)* values on the positive and negative side of the spectrum that relate to the desired frequency component. Such a single frequency image sequence will have the same image interval, i.e. 2.25s as the original image sequence, but with waves of only the specified wave period present, thus eliminating the uncertainty in wave period identified in section 5.3.

To illustrate this, the wave patterns from each spectral frequency or "bin" produced by the FFT can be visualised by plotting either the real or the imaginary parts of one *H(k)* value out of the spectra of each pixel through time. Plots generated in this manner are effectively a snapshot of any coherent wave patterns present at each wave frequency in the FFT, and if a greyscale colour palette is used, the crests and troughs appear as extremes in light and dark respectively. One such frequency breakdown has been illustrated using the radar image sequence for the Holderness example used in section 5.3, and is shown in Figures 5.4.1a and 5.4.1b. The original radar image sequence contained $N = 64$ images at 2.38s intervals spanning 152.5s, yielding the 32 single frequencies generated by the FFT algorithm. These clearly show a coherent long crested swell starting to appear in the 16.9 second image and becoming very clear in the 13.9 second image. From that period down to the shortest period

resolvable by the radar there are identifiable coherent wave patterns in the images, reducing in wavelength with reducing period as would be expected.

While the images of gravity waves are the point of interest to this study, there appear to be large scale coherent patterns in the two longest period bins, close to the shore at the bottom of the images. A possible explanation of this could be the long period modulation of wave breaking over several minutes linked to wave groups or possibly edge waves. Ideally, longer time series should be collected to resolve the details of these long period signals for study in future work.

Having produced the set of filtered single frequency wave image sequences, the same cross-correlation motion tracking procedure could be carried out on each. The wave celerities calculated for each known wave period could then be inverted to a water depth using linear theory, providing a number of estimates of water depth at each point in the image. Finally the depth estimates calculated for each wave frequency could be averaged to reduce noise and a final water depth map produced.

This approach was abandoned as too computationally inefficient when it was realised that all the information contained in the reconstructed single frequency wave sequences could be accessed directly in the frequency domain without reconstructing a new image sequence for each Fourier component, and thereby reducing the computational overhead.

What was now required was a method of mapping the precise wavelength directly from the complex $H(k)$ images as illustrated in Figures 5.4.1a and 5.4.1b, rather than cross correlation motion tracking in the time domain. Ideally, with a perfect sinusoidal noiseless signal, this would be a straightforward task for which any number of approaches could be used - simple zero crossing analysis for example. Unfortunately, the wave patterns visible in the Fourier breakdown of the radar images can be very noisy, have interference patterns on them and sometimes waves from more than one direction. Zero crossing analysis can be unreliable under these circumstances and was quickly discarded. FFT analysis was also discarded as the small size of area being analysed may contain only one or two wavelengths, and as described in section 5.1, FFT analysis can only provide answers to the nearest integer number of wavelengths in the analysis area. It is possible to extend the limits of the FFT by padding the ends of the data with zeros to create an artificially longer set of data, doubling the wavelength resolution with each doubling of the zero padded data length. However, this

would still not give the precise answers required for this application unless the data were zero padded to many times its original size, resulting in unacceptably large computation times for 2D FFTs.

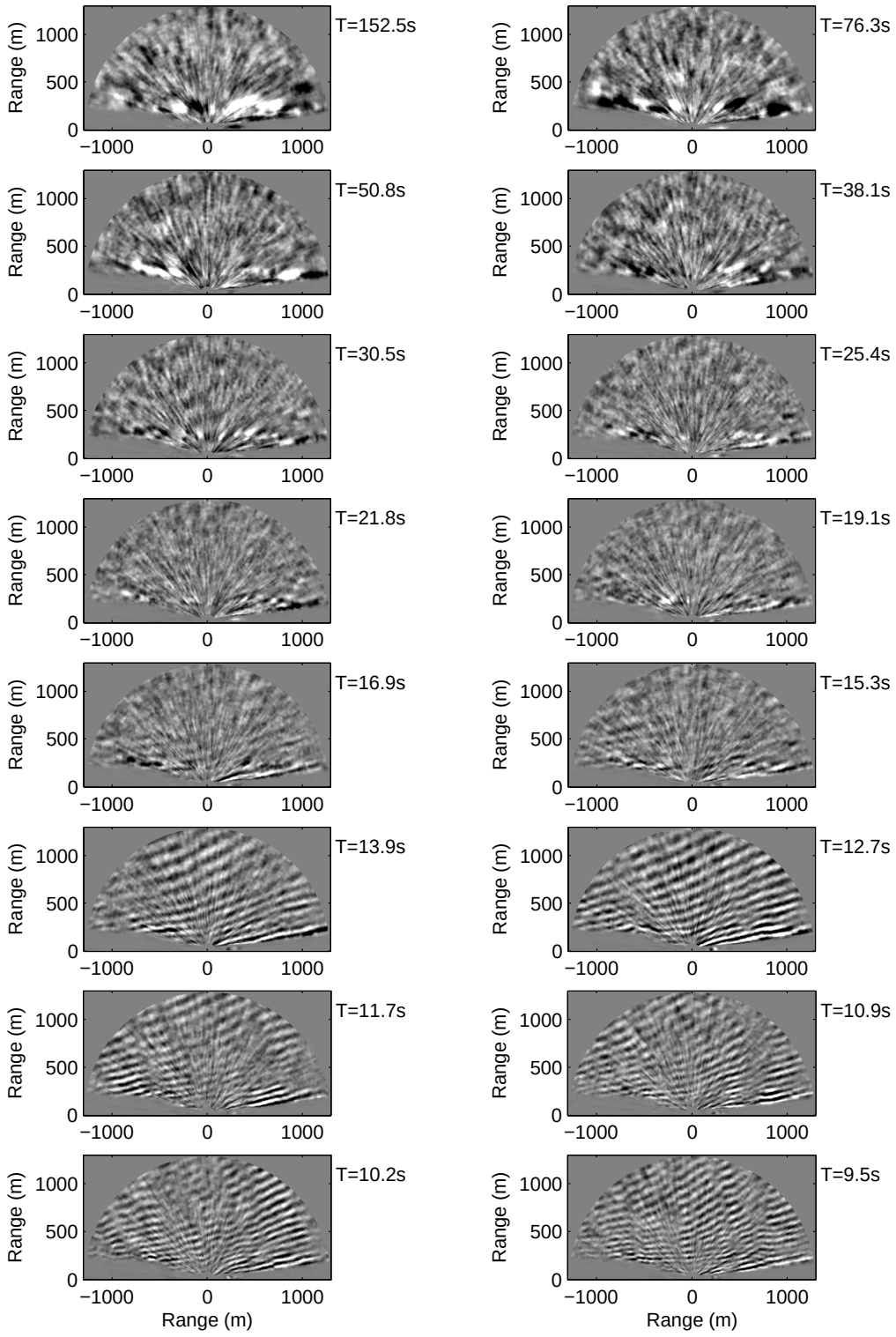

Figure 5.4.1a. The real parts of complex Fourier components 1-16 of the FFT of the Holderness radar image sequence from 16:30GMT, 17th November 1995. These represent snapshots of individual wave frequencies, showing any coherent wave patterns present. In these images long crested swell can clearly be seen.

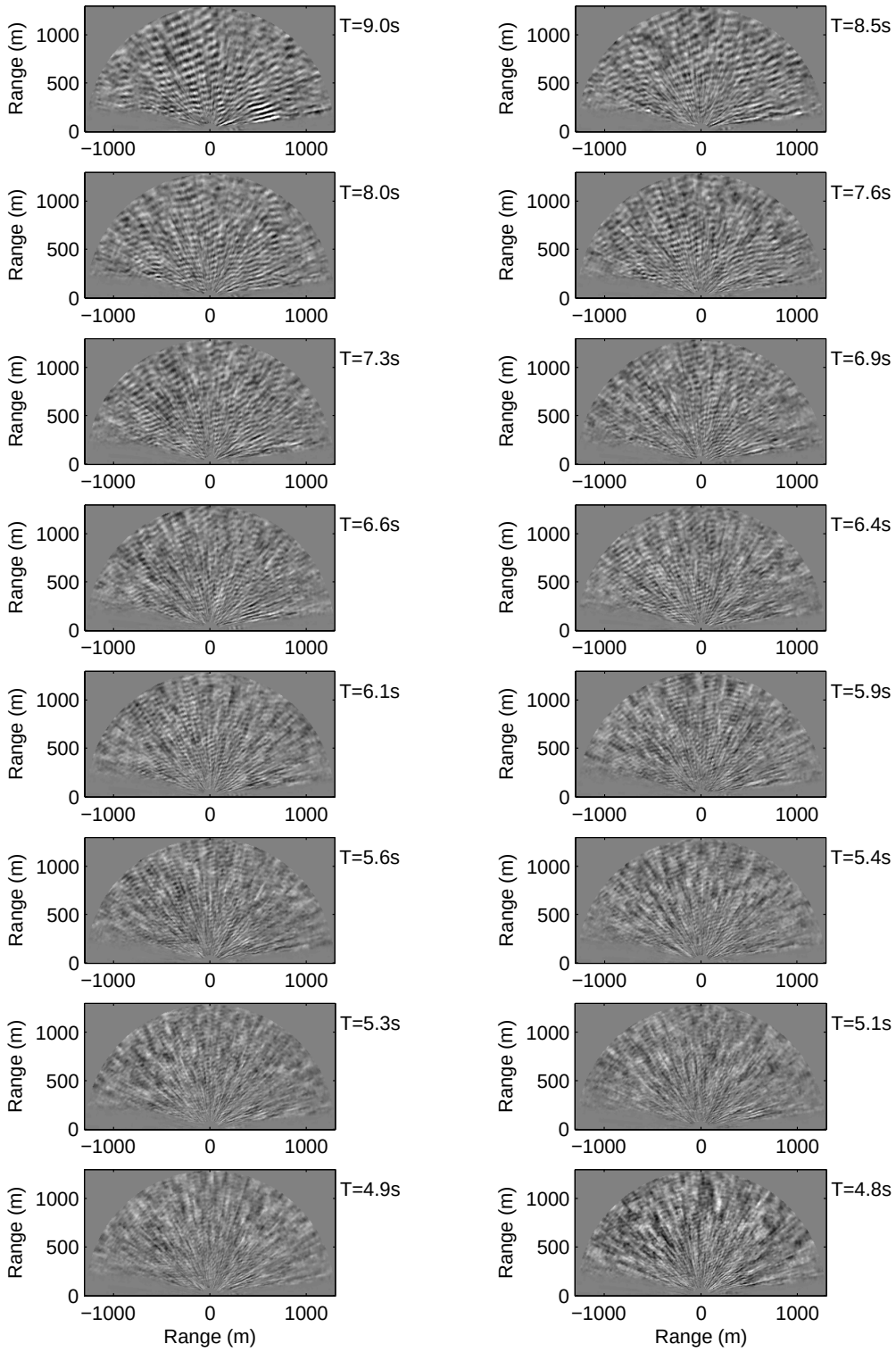

Figure 5.4.1b. The real parts of Fourier components 17-32 of the FFT of the Holderness radar image sequence from 16:30GMT, 17th November 1995 These represent snapshots of individual wave frequencies, showing any coherent wave patterns present. In these images the more confused, but still identifiable, patterns of wind sea can be seen.

5.5 The Radon Transform

A technique gaining popularity in oceanography, for example in the detection of ship wakes in synthetic aperture radar images (Copeland et al., 1995), and having been borrowed from medical tomography is that of the radon transform (Srinivasa et al., 1987). This technique is generally used as a way of picking out the presence of straight lines in noisy image data. For example, a noise filled image with two faint straight lines within it is shown in figure 5.5.1.

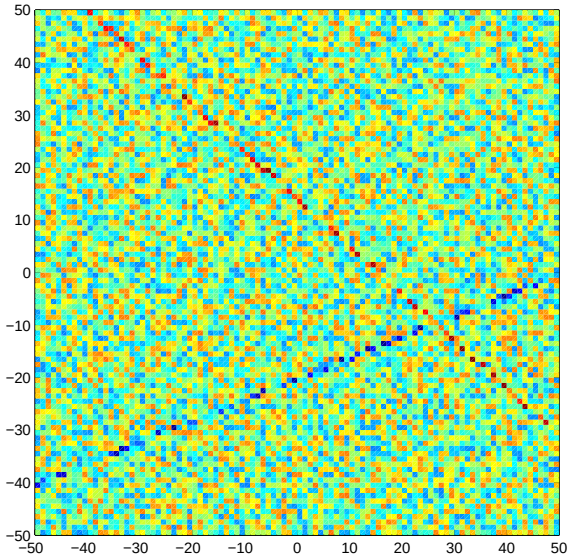

Figure 5.5.1 A noise filled image with two faint straight lines within it, one red one blue.

This image is rotated at small angular intervals and at each angular interval the sum of the columns in the image matrix is taken – effectively the projection of the image onto a 1-D line. The result generated by such an analysis is a new image in which the lines have been reduced to points, the location of which represent the angle and offset of the line within the original image (Figure 5.5.2).

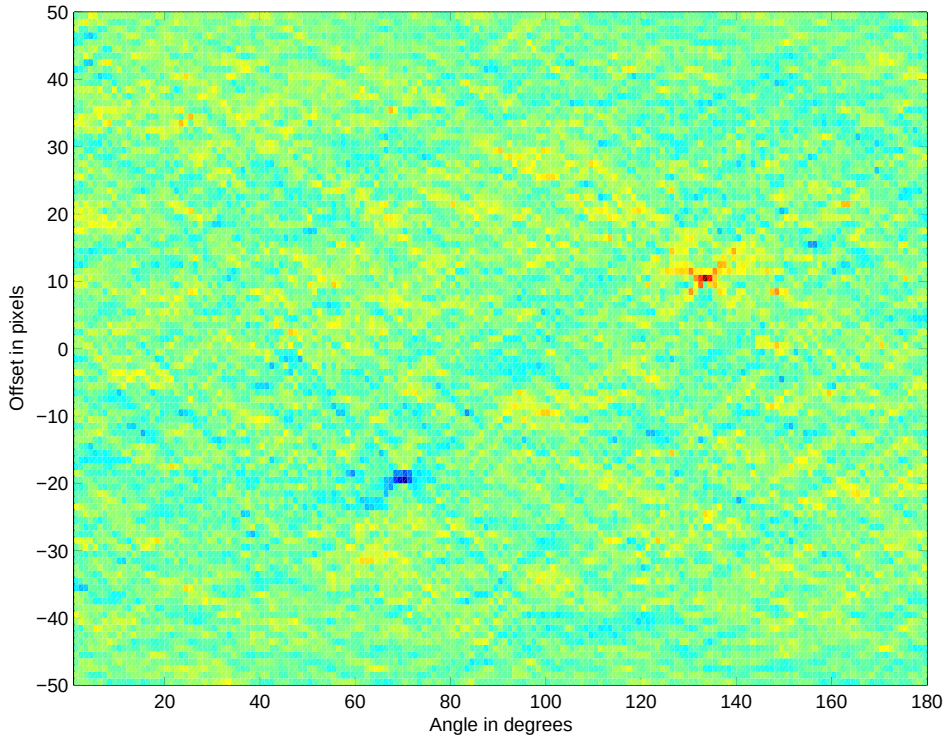

Figure 5.5.2 The radon transform of the image in figure 5.5.1, the red line and blue line having been reduced to points in the matrix instead of a line, blue at (offset -20, angle 70^o) and red at (offset 10, angle 130^o).

The locations of these points within the transform are relatively straightforward to determine, unlike trying to determine the location of the lines directly from the source image. However, lines are not the same as a sinusoidal signal, but with the radon transform a sinusoidal signal can still be identified and located more easily than from the original image.

The 2-D rotation is the key element of this process and can be represented in matrix terms by a standard 2-D rotation matrix operation:

$$\begin{pmatrix} x_1 & \dots & x_N \\ y_1 & \dots & y_N \end{pmatrix}_{rotated} = \begin{pmatrix} \cos\theta & -\sin\theta \\ \sin\theta & \cos\theta \end{pmatrix} \begin{pmatrix} x_1 & \dots & x_N \\ y_1 & \dots & y_N \end{pmatrix} \qquad 5.5.1$$

This operation rotates a set of N 2-D coordinates (x_1,y_1), (x_2,y_2) … (x_N,y_N) clockwise by angle θ about the co-ordinate origin in the middle of the image subsection.

The 2-D input coordinates are the locations of the image pixels, specified with the origin being the centre of the image subsection. The new positions of these pixels are determined

using equation 5.5.1, and a standard 2-D interpolation library function then used to determine the pixel intensities at these new coordinates.

The rows and columns of the new image matrix can then be summed and placed in a matrix relating the angle of rotation and the projection of the image at that rotation. By summing both rows and columns of the image at each rotation angle, the number of rotations needed can be reduced to those covering a quarter of a revolution.

As an example, an image subsection similar to that from the radar system in form and size is shown in Figure 5.5.3 with an image size of 20 pixels, corresponding to an area of approximately 150m square, with a noisy wave signal of approximately 9 pixels, or 70m wavelength.

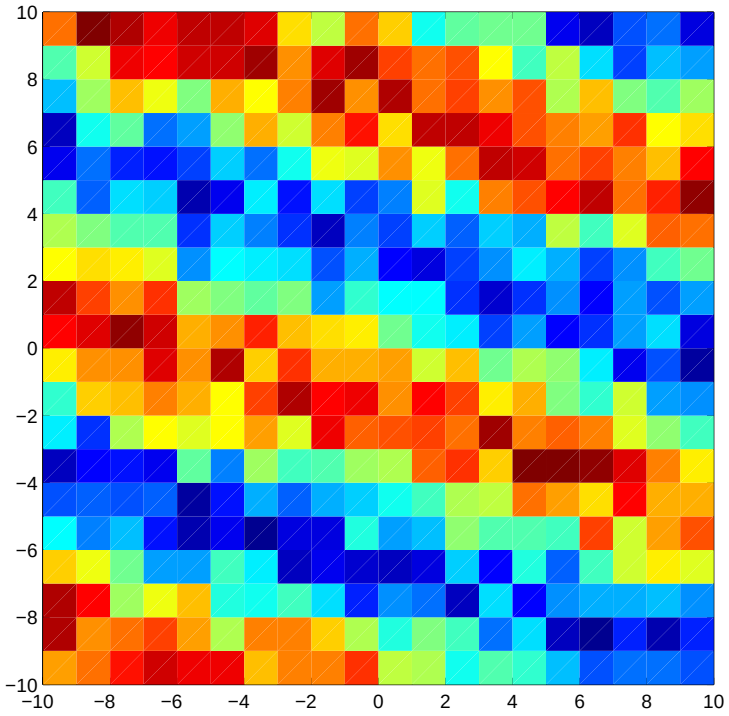

Figure 5.5.3 A test image of 20 pixels square with a sine wave signal within it, similar to the image fragments within the radar data.

The radon transform of the image containing the wave pattern, instead of reducing it to a point, reduces the wave pattern in any given direction from a 2-D signal to a 1-D signal, the maximum variance of which can be found at the orientation of the along crest direction.

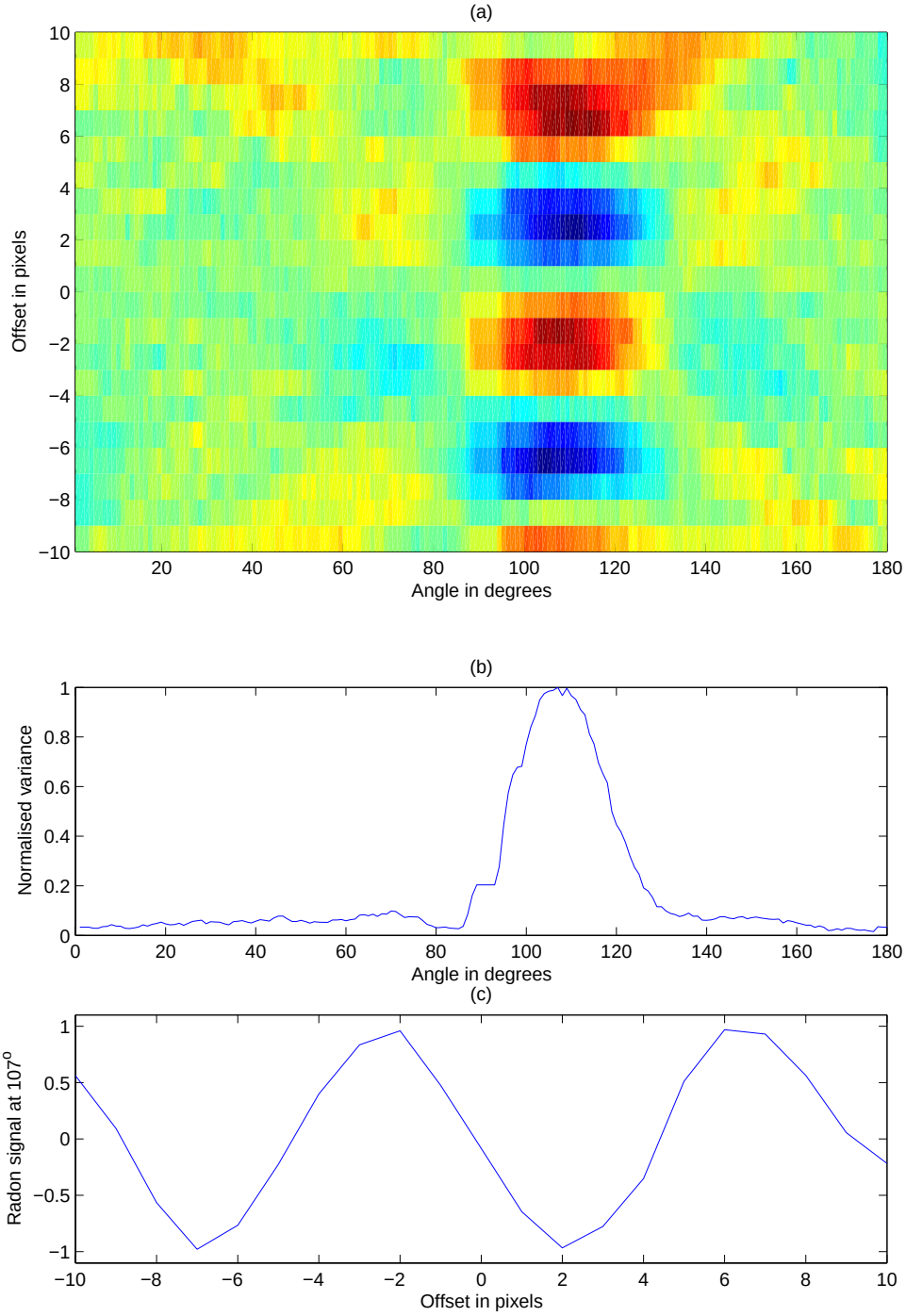

Figure 5.5.4 (a) The radon transform of the noisy 2-D waveform shown in figure 5.5.3; (b) the normalised variance of the transform by angle and (c) the mean waveform at the angle of greatest signal variance.

Figure 5.5.4a shows this radon transform, and below it the variance of the transform plotted with angle in 5.5.4b. The line in the transform corresponding to this angle has been extracted and plotted in figure 5.5.4c, showing clearly the sine wave used to generate the original image. In order for this algorithm to correctly identify the 2-D waveform, the assumption is made that the waves are homogeneous within the small image subsection under analysis. In practical terms, the small image sub-sections used would contain between 1 and 3 wavelengths, and so would require the crests to stretch the width of the image subsection area for the algorithms to work best.

The example shown in Figures 5.5.3 and 5.5.4 represents the operation of the radon transform on a waveform of real data. The 2-D image sub-sections extracted from the FFT of the radar image sequences are of course made up of complex numbers. However, by taking the real and imaginary components and treating them separately, the same principles apply, and the results from the real and imaginary components can be combined at each stage of the analysis to increase the ability of the analysis to extract an accurate wavelength measurement.

Having identified the rotation angle of the waveform by locating the peak in the variance of the projections at that rotation angle, as shown in Figure 5.5.4b, the wavelength can then be determined from the 1-D signal in Figure 5.5.4c.

In order to identify the wavelength from this signal, a crest is first located to sub-pixel accuracy by fitting a quadratic equation to the first peak found in the signal and the values immediately either side of it, and then using a similar method to that used in section 5.3 to identify the exact peak location from the derivative of the quadratic equation. At this point, one could then use the same method to simply identify the next trough and use the locations of the crest and trough to infer a quarter wavelength. If the signal was a clean sine wave then this would be a simple and computationally efficient approach, but radar data rarely provides such an ideal signal. Instead an approach was sought to make use of the full 1-D signal to increase confidence in the wavelength determination.

A 1-D FFT was performed on the signal to identify, to the nearest integer, the number n_w of waves present. A cosine wave was then centred on the first crest that was identified as above. A range of wavelengths of cosine wave from n_w -1 to n_w +1 were compared with the signal using the correlation coefficient method (equation 5.3.1) and the cosine wave producing the

highest correlation coefficient taken to represent the wavelength L of the waves in the image subsection. The use of the correlation coefficient allows a certain degree of quality control to be implemented, and a process of trial and error indicated that if the correlation coefficient r falls below 0.3, then the wave pattern in the image subsection has not been of sufficient clarity to identify a wavelength with any certainty.

The wavelength L determined for that small image subsection can then be used to provide an estimate of the water depth d, calculated using a simple re-arrangement of the linear dispersion equation:

$$d = \frac{L}{2\pi}\tanh^{-1}\left(\frac{L}{L_0}\right) \qquad 5.5.1$$

This is repeated at intervals of a few pixels across the area viewed by the radar, hence building up a map of wavelengths, directions and hence water depths. This process is performed on each Fourier layer in turn, allowing a number of independent estimates of water depth to be made at each point in space but at the different wave periods associated with the FFT. This set of water depth maps can then be averaged to provide a final water depth map representative of all the wave periods containing coherent wave patterns. The water depths associated with each wave period are weighted by the associated correlation coefficient in the averaging process such that:

$$d_{averaged} = \frac{1}{\sum r_n}\sum_{n=1}^{N/2} d_n r_n$$

In practical terms, this enhances the contribution of depth estimates generated from clearly defined wave patterns, while reducing the contribution of depth estimates where the correlation coefficient indicates a lower quality wave pattern.

This analysis was applied to radar data collected at Teignmouth during the second phase of the COAST3D project. A wave event on the 12th November 1999 provided a particularly clear set of wave patterns with which to test the combination of the radon transform and the use of the FFT to isolate particular wave frequencies.

The wavelength and direction mapping results for the 7.6s wave period Fourier layer associated with the spectral peak of the image data from 06:00GMT Teignmouth on the 12th

November 1999 are shown in Figure 5.5.5. The wave directions can be seen to align well with the single frequency wave pattern on which they are overlaid, showing that the radon transform algorithm has determined the wave directions correctly, although there are a few spurious points. In particular, the wave refraction patterns over the sand banks in the lower left corner of the image demonstrate the ability of the technique to pick out relatively small scale variations in wave behaviour.

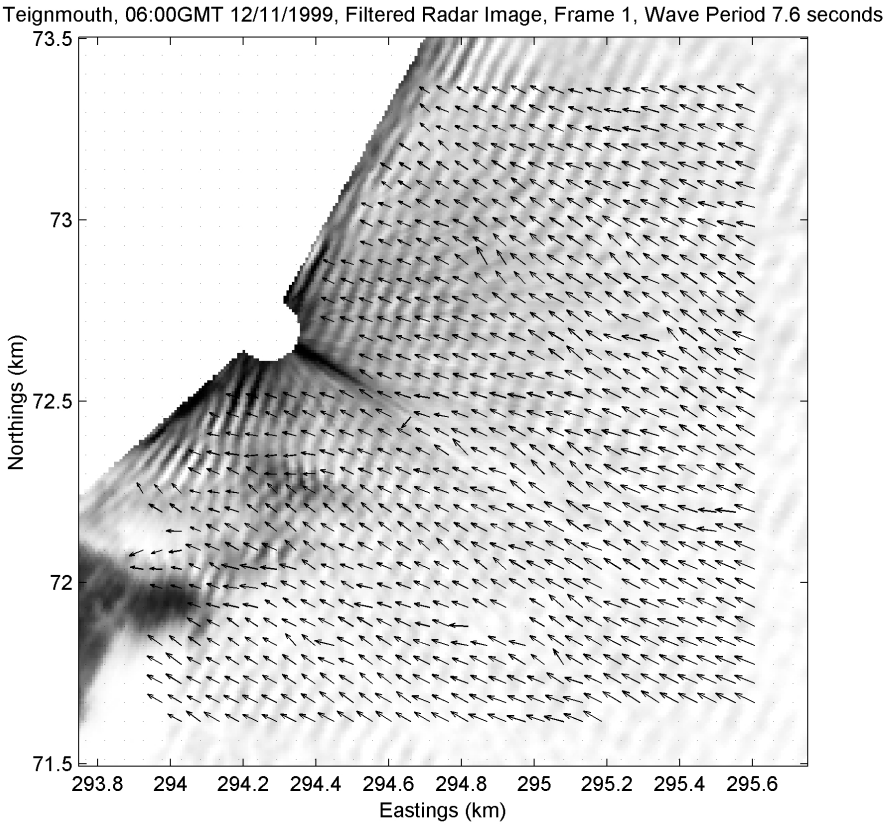

Figure 5.5.5 The wavelength vectors from a single Fourier layer overlaid on a plot of the real part of the layer. The length and direction of the arrows corresponds to the wavelength vectors.

Tests of this method of analysis on the COAST3D Teignmouth radar data showed that the water depths determined using this algorithm contained a considerable number of outliers and noise, particularly in areas of weak signal strength. As a result of this noise, the bathymetric maps generated from individual radar sequences were quite unconvincing. In the longer term, longer time series would almost certainly improve the ability of the FFT to isolate coherent wave patterns from the radar image sequences, but poor recording system reliability and insufficient disk space precluded lengthening the sequences during this experiment.

To overcome this problem, the water depth maps determined from 24 hourly radar sequences spanning two tidal cycles were combined into a single bathymetric map. The tidal water levels measured at a tide gauge on Teignmouth pier close to the radar system were subtracted from the depth estimates calculated from each hourly record, thereby adjusting the calculated depths to be relative to Admiralty Chart Datum – the water level of lowest astronomical tide. These were then averaged at each point, with outliers of more than 2 standard deviations from the mean being discarded. The resulting bathymetric map, shown in Figure 5.5.6, shows striking similarities to the conventional ship survey with regard to the large scale topography, but does not compare so favourably on the small scale features such as the sand banks and shipping channel. The survey carried out for the project by a conventional survey vessel is shown in Figure 5.5.7 for comparison.

The depth inversion used for this analysis was still a rearrangement of the linear dispersion equation, and so no correction for non-linear wave behaviour was applied. As a result of this, the water depths over the sand banks and close to the shore would have been systematically overestimated. This effect is particularly obvious when the depths from the ship echo sounder survey and the radar analysis are plotted against each other as shown in Figure 5.5.8. The ideal case would be for the points of the scatter plot to lie on the line x = y. For the range of wave periods experienced while this data was being recorded (little wave energy above T = 8 seconds, T_p = 5 seconds) there is little bias and scatter for depths over about 4m, but an increasing bias to overestimating the depths can be seen in the radar as the water depth becomes smaller.

This analysis approach inherently involves a degree of spatial averaging, with the assumption being made that the wave behaviour is homogeneous over an area encompassing two to three wavelengths. As a result, rapid changes in bathymetry cannot be resolved, a factor that may also lead to inaccuracies in the depth estimates in shallow, rapidly varying areas of topography such as would be found around sand banks and channels. However, the author is of the opinion that the ultimate limit of resolution of such depth inversion techniques is the wavelength of the waves that are effectively ‘illuminating’ the bathymetry, in the same way that the ultimate limit of resolution of an optical microscope is the wavelength of the light used to illuminate the object being viewed. Hence bathymetric features that are substantially smaller in scale than the wavelength of the waves, such as the concrete block of a tank trap will not affect the behaviour of the waves passing over them.

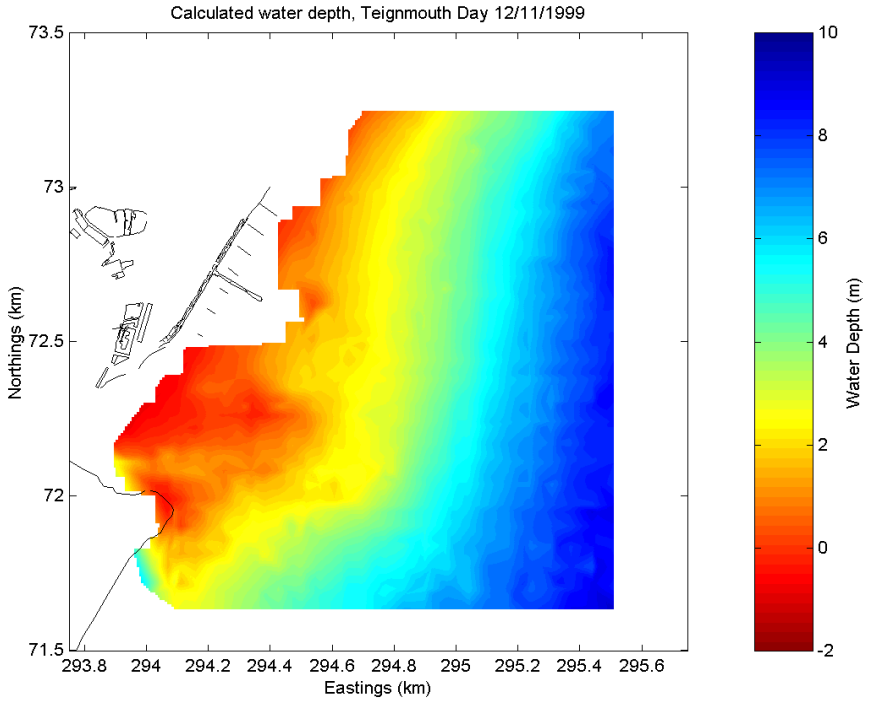

Figure 5.5.6 The bathymetric map generated by combining the analysis of 24 hourly radar records for 12th November 1999 during the Teignmouth COAST3D experiment.

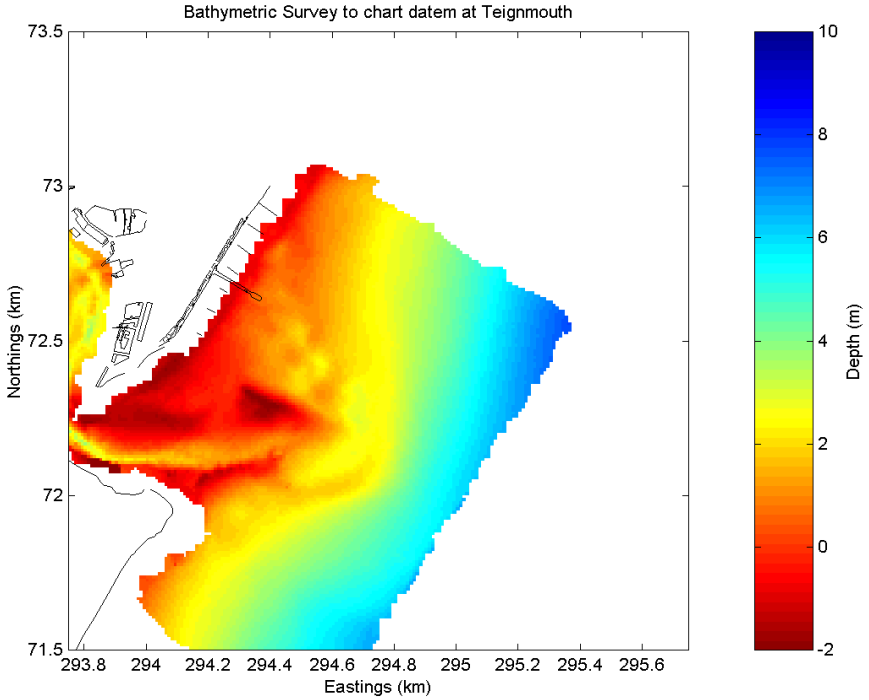

Figure 5.5.7 The bathymetric ship survey carried out at Teignmouth during the 1999 COAST3D experiment.

No correction has been made for the Doppler shift due to currents, which may also cause some deviation from the true depths, particularly in the fast flowing main tidal channel. It is suspected that errors due to the Doppler shift of waves by currents should largely cancel out when results are averaged over a tidal cycle.

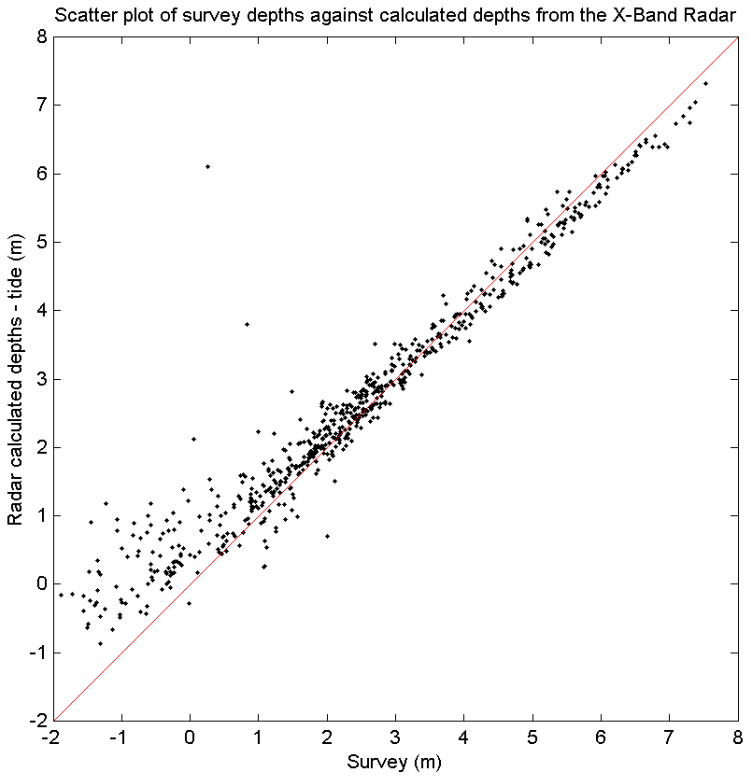

Figure 5.5.8 A comparison of the bathymetric survey carried out by a survey vessel and the bathymetry derived from radar data.

Some of the differences between the radar derived and the surveyed bathymetries may also be attributable to changes in the sandbanks between the time of the survey and the time of the radar recordings, but based on a comparison between the surveys carried out at the start and end of the project, such changes are considerably smaller than the differences found between the radar derived maps and the survey.

These results were presented at the Waves 2001 conference, together with similar results from an analysis of Egmond COAST3D radar data (Bell, 2001).

Although this technique performed adequately on good quality data, the noise in individual depth inversions continued to cause problems, leading to spurious results in weaker signal

areas in particular. The software code needed to support this approach was also overly cumbersome and slow to execute. In order to derive meaningful bathymetric maps using this technique, a more elegant and efficient method of wavelength determination was required and so the radon transform approach was abandoned.

Fast Fourier Transforms had already been discarded due to their inability to resolve non-integer wavenumbers in a data sample. However, the strength of a 2-D FFT is that it takes full advantage of the available data, and so Fourier techniques were re-visited.

5.6 Fourier Based Wavelength Measurement

The popularity of the Fast Fourier Transform (FFT) algorithm in computational mathematics makes it easy to forget that this is not the only way of calculating the discrete Fourier transform of a signal. The FFT algorithm is ideal for relatively large lengths of data where the wavelengths of the desired signals are significantly less than the sample length. This is because, as described in section 5.1, the FFT provides a Fourier component for integer numbers of wavelengths within the data from 1 cycle per length of data to $N/2$ cycles per length of data, where N is the number of samples in the dataset. It does this very quickly in a computationally efficient manner.

The integer wavelength restriction creates a problem for analysing short lengths of data, as has been stated before. So if the requirement for integer components were to be relaxed, the principle behind equations 5.1.3 and 5.1.4 could be used to identify any wavelength from a short length of data. In order to test this, a set of routines were written to calculate integer and non-integer wavenumber Fourier components by following equation 5.1.3, but allowing n to be non-integer numbers as well as integers.

Recall that the discrete Fourier transform H of a waveform h is calculated using equation :

$$H(k) = \sum_{n=0}^{N-1} h(n) e^{-2\pi i k n / N} \qquad 5.1.3$$

In practical terms this equation means that the complex coefficient representing the phase and magnitude of a particular frequency in a time series of N points can be determined by multiplying that time series, on a point by point basis, by an array containing a pure complex waveform of that frequency and then summing the resulting values.

Hence, if the spectrum from an FFT of a complex time series is used to identify the nearest integer number of waves in that time series from the spectral peak, this equation could then be used to fill in the coefficients for non-integer wavenumbers around the FFT spectral peak, and more accurately pinpoint the true spectral peak.

A 1-D analysis was initially developed to test this idea and was found to identify the wavelengths in short sections of complex data precisely. The same technique was tested on short sections of real data, but was found to introduce small errors in the wavelength

measurements, although these errors were small compared to those generated by assuming integer wave numbers in conventional FFT analysis, the wavelength estimates determined using this new procedure varying by only a few percent of a wavelength from the original signal.

A number of methods can be used to converge on the peak in the spectrum once the nearest integer wavenumber has been identified using the FFT. For example, the method of bisection could be used to gradually home in on the spectral peak. A more computationally efficient method is to fit a curve through the points around the spectral peak and obtain a new estimate for its location, assuming a smooth spectral peak.

A parabola is fitted to the magnitude of the spectral peak in the FFT and the adjacent coefficients, the peak of which represents the next estimate of the location of the spectral peak from which a new complex coefficient is calculated using equation 5.1.3. This process is repeated in an iterative process, with each successive iteration using the three coefficients in the spectrum with the largest magnitudes to fit a new parabola until the locations of the peaks of each successive parabola converge on the true spectral peak. This of course assumes that if there are multiple spectral peaks present then they are sufficiently separated in either angle or frequency to be resolved using such a small area of data.

For example, a complex time series of 32 points containing 1.4 cycles of a waveform is shown in Figure 5.6.1a. The real part of the signal is shown as the solid line and the imaginary as the dashed line, representing a progressive wave. This signal could be processed using an FFT, and the resulting spectrum of complex coefficients would represent the strength of signals with -16 to 16 cycles within the 32 data points, so the nearest integer wavelength coefficients would be for 1 and 2 wavelengths, with 1 wavelength emerging as the spectral peak in the FFT, with a corresponding signal as shown in Figure 5.6.1b. The wavelength of this waveform is evidently not an accurate representation of the true waveform in Figure 6.6.1a. However, by homing in on the true spectral peak using the iterative process described above, the signal can be identified as 1.41 wavelengths after 2 iterations, i.e. to within 1% of its true value and exactly 1.4 wavelengths after 5 iterations. The waveform identified by the iterative process is shown in Figure 5.6.1c and is an exact match to the original waveform in Figure 5.6.1a.

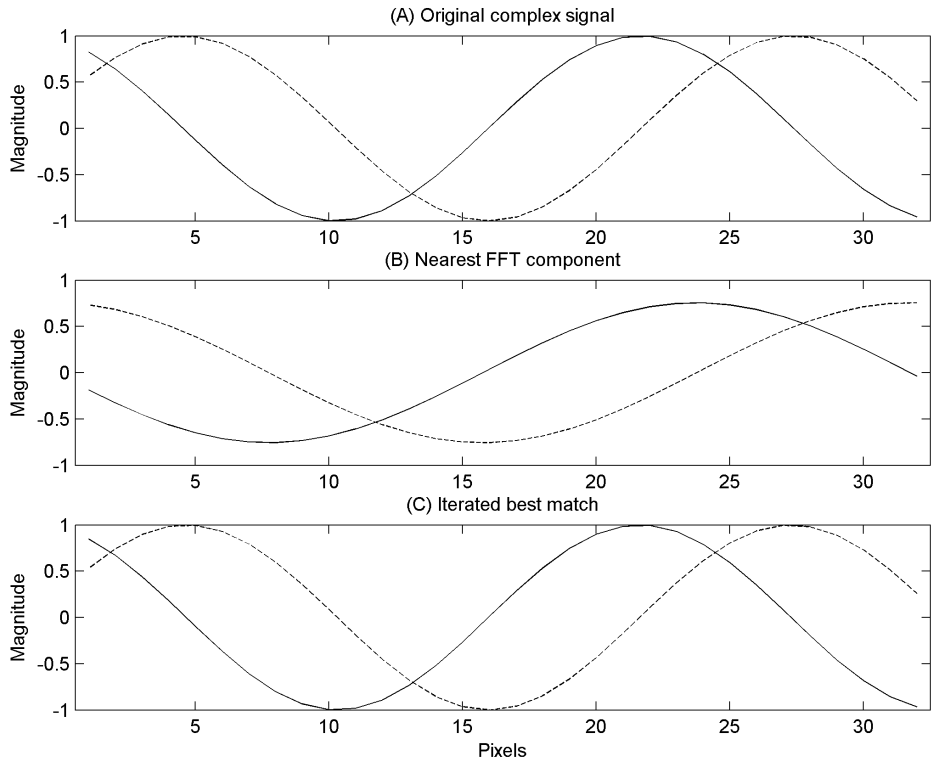

Figure 5.6.1 (a) The original complex waveform with 1.4 wavelengths in 32 data points or pixels. The solid line represents the real part of the signal and the dashed line represents the imaginary part; (b) The nearest FFT component of 1 cycle per 32 pixels; (c) The signal correctly identified by the iterative procedure as 1.4 cycles per 32 pixels.

The magnitudes of the spectral components are shown in Figure 5.6.2. The integer cycle magnitudes determined using the FFT are shown as 'x' with the peaks estimated using the curve fitting process at each stage of the iteration shown as '+'. The points at 0, 1 and 2 cycles, used to initialise the iteration, are plotted with both symbols.

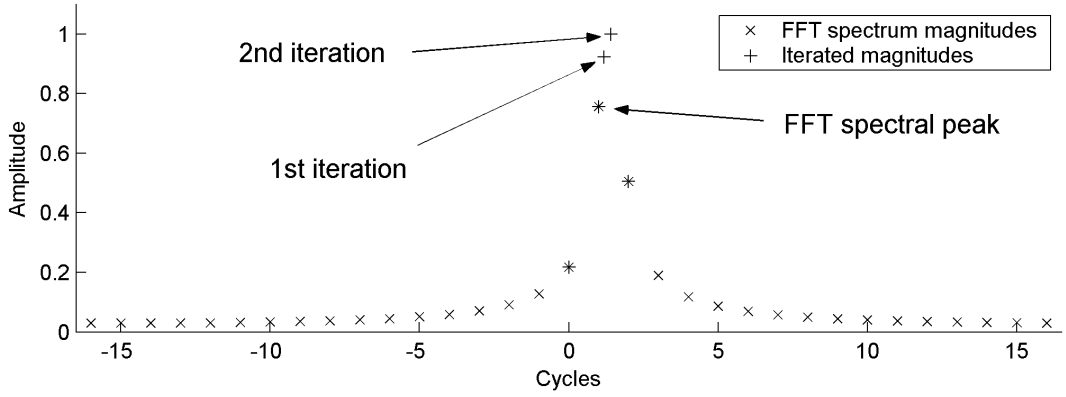

Figure 5.6.2 The amplitude spectrum calculated using an FFT, shown as 'x' with the iterated amplitudes of non-integer numbers of cycles shown as '+'. The three FFT derived points at 0, 1 and 2 cycles, used to initialise the peak detection iteration, are marked using both symbols.

The extension of this 1-D analysis to the identification of a noisy 2-D waveform needed to extract the wavelength from data such as that shown in Figure 5.6.3a is relatively straightforward. A 16 x 16 pixel complex image is used as an example this time, equivalent to a 120m square area of X-band radar data. A complex signal of amplitude 1 unit representing a progressive wave with 1.4 waves in the x-direction and 0.75 waves in the y-direction has been generated within the image matrix. The real and imaginary components of the 2-D waveform are plotted in the two columns of Figure 5.6.3a.

A similar analysis as the 1-D version described above is performed on each row of the matrix, except that at each iteration, the magnitudes of the spectral coefficients produced by each row in the matrix are summed to produce a single amplitude spectrum for the whole matrix, rather than a spectrum for each row. This results in the identification of the average number of waves in the x-direction, i.e. 1.4 cycles, corresponding to a wavelength in the x-direction of $L_x = 16/1.4 = 11.43$ pixels.

The complex coefficients resulting from the 1-D analysis of each individual row in the 2-D matrix using the x-direction spectral peak of 1.4 cycles then yields a further 1-D complex waveform that corresponds to the average waveform in the y-direction. This is identified using the 1-D analysis as the expected 0.75 cycles, corresponding to a wavelength in the y-direction of $L_y = 16/0.75 = 21.33$ pixels.

Having identified the 2-D waveform as having 1.4 cycles in the x-direction and hence a wavelength component of 11.43 pixels and 0.75 cycles in the y-direction or a wavelength of 21.33 pixels, it is then straightforward to calculate that the 2-D waveform has a wavelength of:

$$L = \left(\frac{1}{L_x^2} + \frac{1}{L_y^2} \right)^{-\frac{1}{2}} = 10.07 \text{ pixels}$$

The best fit to the 2-D complex waveform has now been identified and can even be reconstructed if desired, offering the possibility of generating ‘cleaned up’ versions of the original radar images.

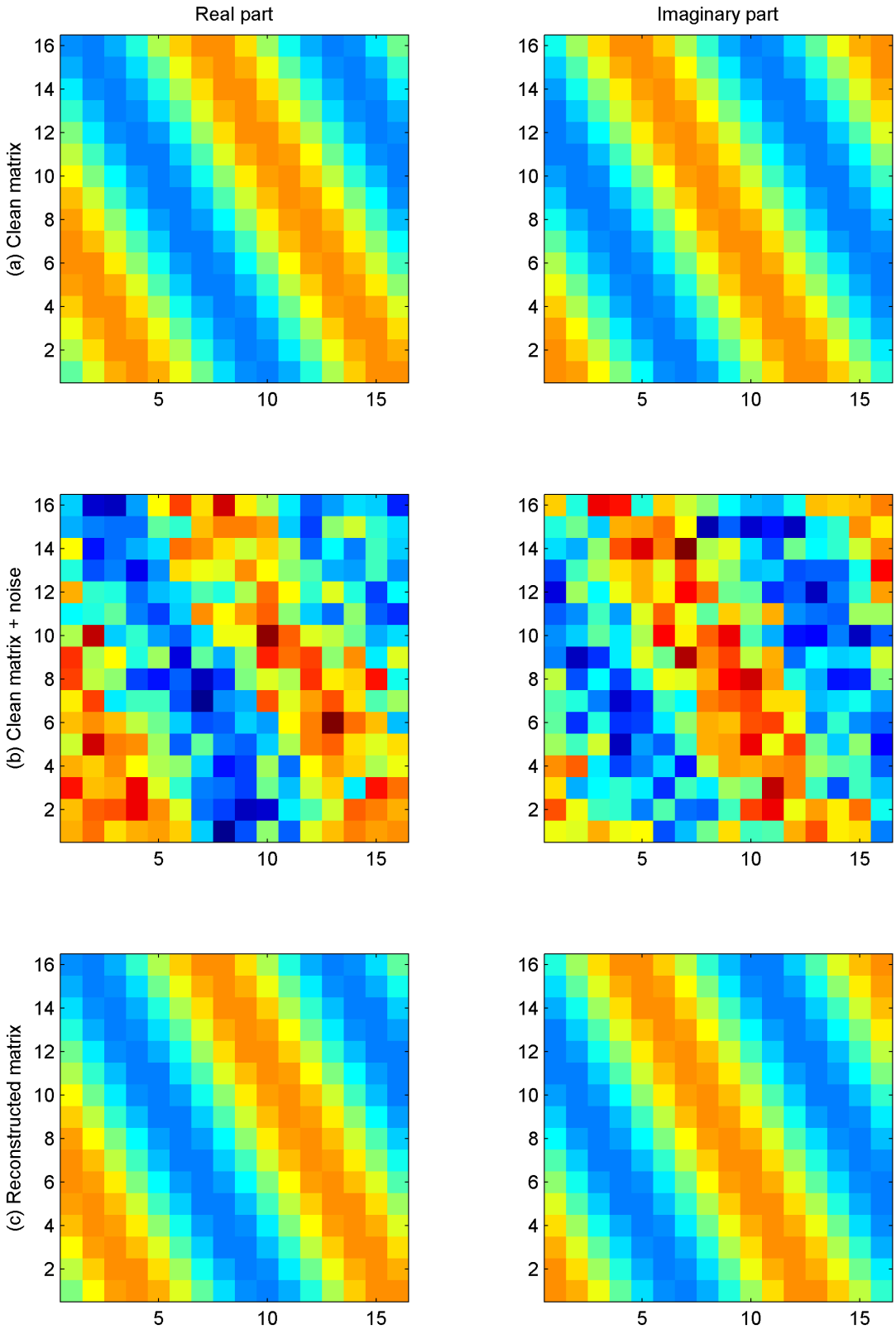

Figure 5.6.3 A demonstration of the ability of the Fourier transform based algorithm described above to pick out and reconstruct a sine wave signal from noisy 2-D data. The real and imaginary parts are plotted side by side and (a) shows the original test signal; (b) shows the test signal with added random noise and (c) shows the best fit to the noisy signal, which is not an exact match to the original, but is indistinguishable by eye.

Noise can be added to the waveform to deliberately degrade the complex image and demonstrate the effect of poor quality image data. Figure 5.6.3b shows the example waveform with added random noise up to 0.5 units in amplitude. Figure 5.6.3c shows the best fit to the noisy data, which in this case was 1.38 wavelengths in the x direction and 0.74 wavelengths in the y direction, giving a calculated wavelength of 10.25 pixels. At this resolution of image, this is indistinguishable from the original clean matrix. The less noise that is added to the signal, the more accurate are the estimates of the best fit signal.

No reference to such a technique has been found in the literature, so it appears to be a new method for locating the spectral peak of short complex time series.

In real terms, with pixel sizes of 7.5m, the original signal corresponds to a wavelength of 75.53m, while the measured signal corresponds to a wavelength of 76.88m, a difference of 1.35m. If these were 8 second waves, linear theory would indicate a depth of 11.86m for the true wavelength in the clean signal, and a depth of 12.47m for the measured wavelength in the noisy signal, an overestimate of 0.61m. If this were the only depth estimate, it might be considered a problem that the accuracy in water depth measurement is more than 0.5m in error. This example serves as demonstration of the dependence of this technique on good quality data. However in most cases a water depth measurement is possible at a number of wave frequencies, and in practice such errors will balance out over a number of wave frequencies.

The size of image subsection used to determine wavelengths in the final version of the analysis adjusts automatically to the data. It is initially set to 32 pixels, or 240m square. This size was chosen to ensure that at least one complete wavelength should fit within the image subsection even for long period swell in deep water. If more than four wavelengths are detected, the image subsection size automatically reduces to a size that maintains between two and four wavelengths, thus ensuring that a recognizable signal is present, but minimizing the spatial averaging that is inherent in this technique. If it becomes desirable to try to obtain water depth estimates from poorer quality data, such as that recorded during the INDIA project in 1999, it may be necessary to increase the size of the image sub-sections to ensure reliable mapping of wavelengths.

In the final version of the data analysis, this technique is used to map the wavelengths across a number of frequency layers, each layer providing an independent measurement of water

depth at a particular point in the radar image. Some of these depth estimates will be more reliable than others, depending on the quality of the wave patterns at a particular wave frequency. Figure 5.4.1 illustrates this point well, with clear and easily defined long crested swell patterns that should present this wavelength measurement algorithm with no problems, compared with the more confused wave patterns in the plots corresponding to higher wave frequencies in which the wavelengths may not be so well defined.

The final estimate of the water depth at a particular point is calculated using a least squares fit to the wave dispersion equation (equation 2.6.2). The contribution from each wave frequency is weighted by the amplitude of the spectral peak coefficient identified by the wavelength measurement algorithm. That means that wave frequencies from which a clear wavelength has been identified will contribute to the final result more than those in which the waveform is less clearly defined. Hence to obtain the final estimate of the water depth the following error function is minimized:

$$\text{Wavelength error function } L_{error} = \sum_{n=1}^{N/2} |H_n| \left(L_{n\_dispersion} - L_{n\_measured} \right)^2$$

where $L_{n\_dispersion}$ is the wavelength calculated using the wave dispersion equation at the particular frequency; $L_{n\_measured}$ is the wavelength measured from the complex image subsection using the analysis described above; $|H_n|$ is the magnitude of the spectral peak coefficient.

5.7 Image Distortion Due to a Rotating Antenna

An unquantified effect that has been raised a number of times in the past has been that of image distortion due to the rotating antenna, and what effect this would have on the use of the radar as an imaging tool. Unlike a camera, that takes an instantaneous image, when a rotating antenna is used to build up an image of an area, the signal from one azimuth is recorded at a different time to that from another azimuth, the time difference being dependent on the rotation rate of the antenna.

To illustrate this and try to quantify any problem this might cause, an example can be used. In the following example which has been deliberately chosen to be a worst case scenario, a uniform water depth of 5m is assumed, and a set of waves with a wave period of 5 seconds and a wavelength of 31.1m is generated that travels from left to right, defined by Hedges' dispersion equation (with $Z = 0.4H$) with a wave height of 1m. A radar is sited at the coordinate origin (0,0) and has a rotation rate of 2.25 seconds in the clockwise direction – approximately the specification of the marine X-band radar used in this study. Figure 5.7.1 shows the true instantaneous image of the simulated waves, while Figure 5.7.2 shows the image that would be produced by the rotating antenna.

As can be seen from Figures 5.7.1 and 5.7.2, the wave image generated from the simulated rotating antenna is distorted from the true instantaneous image, the waves in the top right of the image having been 'recorded' half an antenna rotation or 1.125 seconds later than those in the bottom right. When a wavelength mapping routine is performed on this image, the difference between the true wavelength and the distorted wavelength can be quantified. Where the radar beam is scanning against the direction of motion of the waves, the perceived wavelength will be slightly shorter than reality, and slightly longer than reality if the beam is scanning in the same direction as the wave direction – effectively a slight Doppler shift.

The difference caused by this is most noticeable at the join between the start and end of the rotation of the antenna where the 2.25 second rotation leads to an almost 180^{o} phase mismatch for the 5 second waves used in the example. This effect will be most noticeable for short period waves, as the rotation time as a proportion of a wave period becomes less significant as the wave period increases.

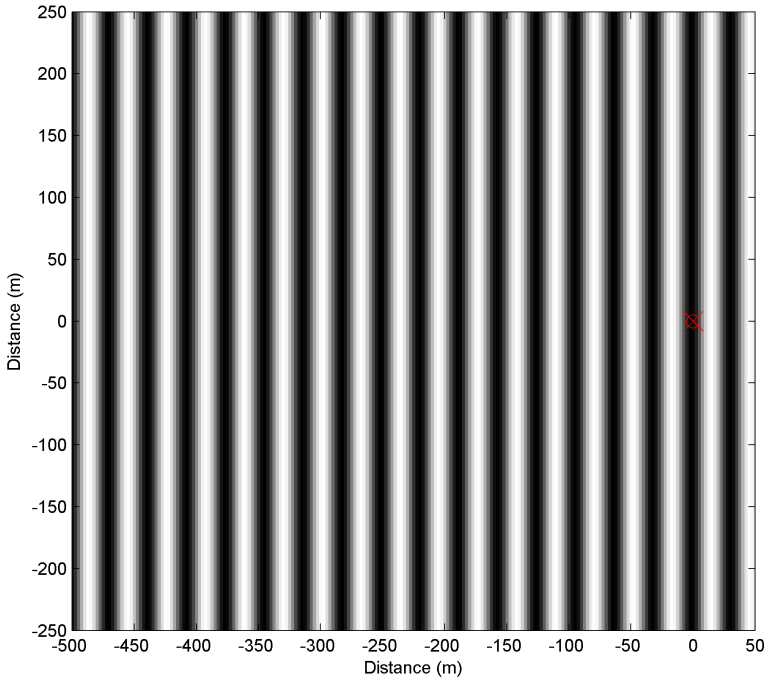

Figure 5.7.1 A simulated wave image for 5 second period waves in 5 metres of water 'recorded' instantaneously.

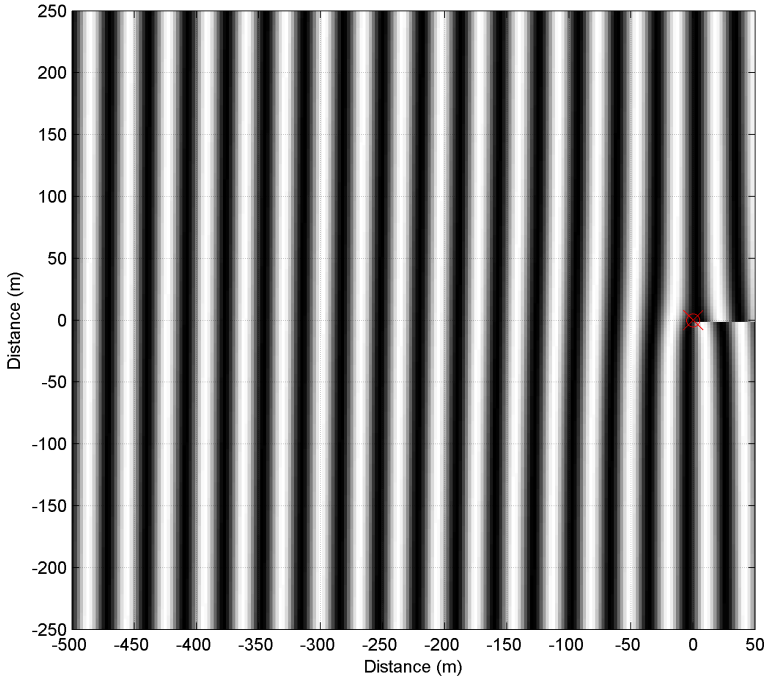

Figure 5.7.2 A simulated wave image for 5 second period waves in 5 metres of water 'recorded' using a rotating antenna located at the coordinate origin with a rotation time of 2.25 seconds.

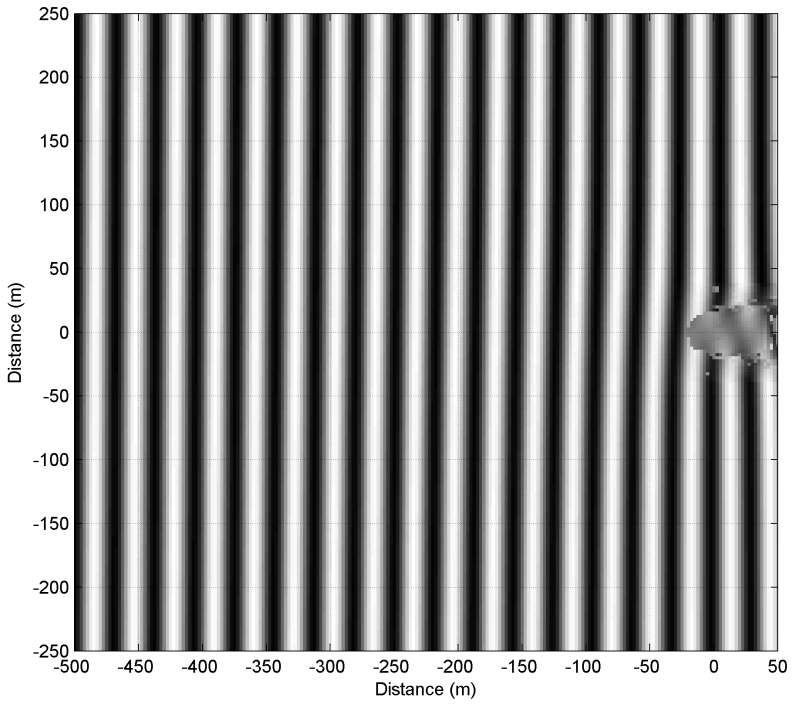

Figure 5.7.3 The reconstructed wave image resulting from the wavelength mapping algorithm performed on the distorted wave image simulating a rotating antenna.

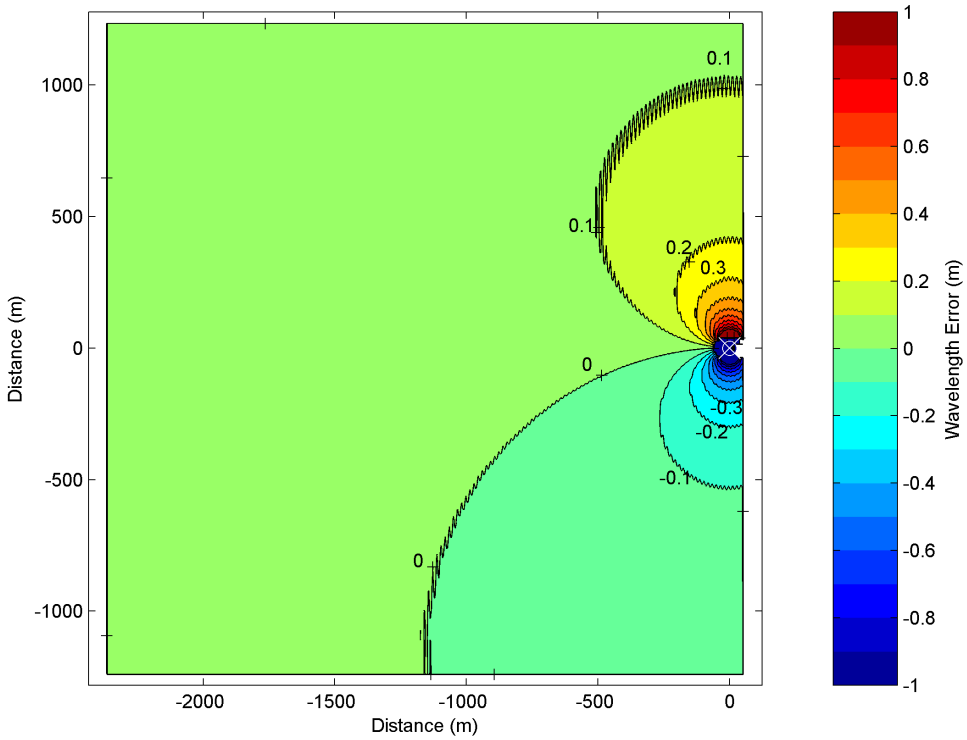

Figure 5.7.4 The results of a wavelength-mapping analysis on a wave image of 5 second period waves in 5 metres of water distorted by antenna rotation. The greatest deviations are located closest to the antenna, but become insignificant with range from the radar. The colour scale refers to the deviation from the true wavelength.

Figure 5.7.3 is the reconstructed wave image produced using the wavelength mapping technique for single images discussed in the previous section, in this case using a sub-image area of 80m square to determine the wavelength at each pixel. The wave pattern is measured and reconstructed well over most of the image, but the smeared region near the origin causes problems as there are two distinct wave phases present side by side with a discontinuity between them. With two different strong signals within that region, the algorithm has tried to fit a single sine wave to both signals with limited success.

Figure 5.7.4 shows the difference between the actual and the 'recorded' wavelengths determined using the wavelength mapping algorithm. To illustrate the significance this might have on a depth inversion, a plot of wavelength against water depth has been generated in Figure 5.7.5. As can be seen in this plot, a wavelength error of, for example, 0.2m due to antenna rotation distortion could lead to a predicted depth error of the order of 10cm in 5m of water. An error of this magnitude is unlikely to be of concern in most applications.

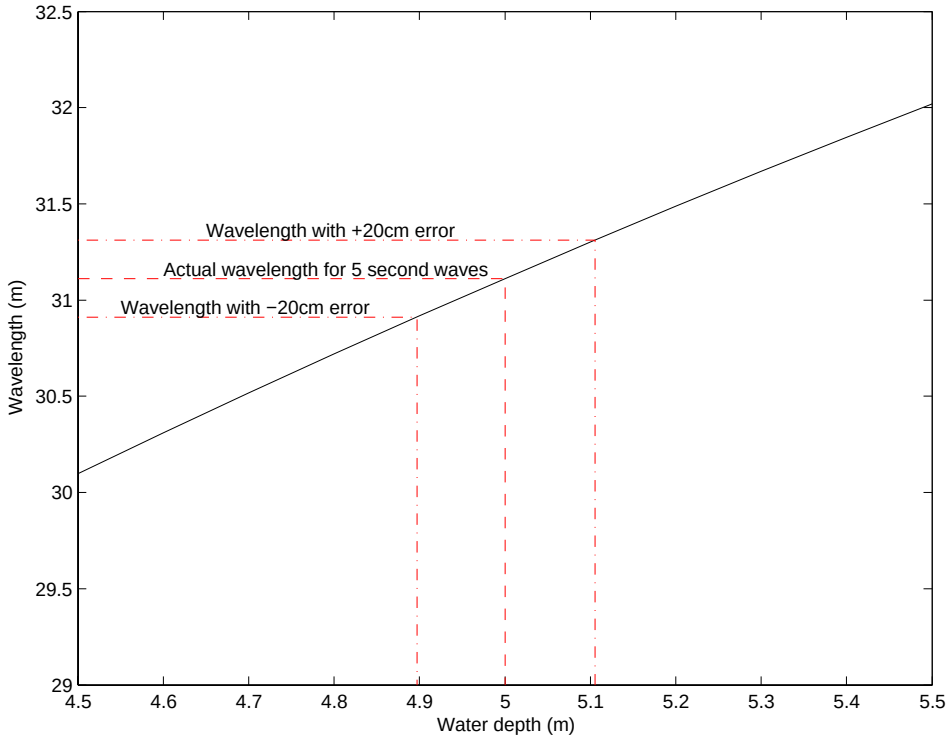

Figure 5.7.5 The wavelengths of 5 second waves for depths around that of the test case used for the antenna rotation image distortion. The dashed line shows the wavelength-water depth relationship for waves in 5m water depth with a 1m wave height, while the dot-dashed lines show the effect of a 20cm wavelength measurement error on the inferred water depth, i.e. about 10cm error in water depth either way.

In normal deployment situations where the radar is mounted on a coast with approximately 180^o view of the sea, the effects of antenna rotation have been shown to be relatively insignificant except in the regions closest to the antenna. However, since they are also relatively straightforward to correct, a routine has been implemented to remove this as a source of error. When the initial Fourier breakdown of the image sequence is performed, the phase of the Fourier components of each pixel f_n is adjusted in line with the rotation rate of the antenna, effectively reversing the time shift introduced across the image by the antenna rotation using the following equation:

$$f_{n\_corrected} = \frac{f_n}{\exp\left(\frac{-2\pi i t_{delay}}{T}\right)} \qquad 5.7.1$$

where t_{delay} is the time difference at a particular pixel between the start of the radar scan and the time the pixel was recorded, and T is the period of the waves for that Fourier component. The sign within the exponential term controls whether the phase is shifted forward or back, depending on the direction of rotation of the radar antenna.

This operation adjusts the image "recorded" by the rotating antenna in Figure 5.7.2 to that of the instantaneous snapshot image shown in Figure 5.7.1.

5.8 Summary

A range of image analysis techniques have been explored for the application of mapping the celerity and wavelength of waves in the radar images. The initial motion tracking approach operated on raw image sequences provided sufficiently interesting results to warrant continued effort in algorithm development, and may be of future use in the study of wave approach angles on beaches and their contribution to longshore drift.

The radon transform provided a tool for accurately determining the angle of waveforms in small areas of complex data extracted from FFTs of pixel time series. However this technique proved insufficiently robust for continued use, and was considered by the author to be too slow for processing large quantities of data.

The extension of the FFT mathematics to allow non-integer wave numbers within the small areas of complex data has provided the ideal tool for accurately mapping the variation in wavelength found over slowly varying bathymetry. This technique still involves a certain

amount of spatial averaging to allow the determination of the wavelength from finite sized sub-sections of the radar images, and so it is expected that rapidly varying bathymetry will not be well resolved using this technique. However, it is a very fast and accurate algorithm for determining a 2D waveform. This is the algorithm that has been used throughout the following chapters to measure the wave lengths of the waves visible in the radar image sequences, and thereby to infer the water depth maps.

A set of comparison tests were run on a simple case of a 16x16 pixel complex matrix containing an artificially generated complex waveform of wavelength 10 pixels. For the X-band radar this would relate to a 75m wavelength in a 120m square area such as might be found in a section of one of the Fourier layers illustrated in Figure 5.4.1a. Table 5.8.1 shows the execution times of the various analysis algorithms for 1000 cycles of the three algorithms tested. The algorithm described in section 5.6 is almost three orders of magnitude faster than using a zero padded 2D FFT, while retaining the mathematical properties of the FFT.

Algorithm	**Execution time (1000 cycles)**
2D FFT zero padded to 2048x2048 pixels, giving an approximate wavelength resolution of 40cm	6383 seconds
Radon transform based approach (section 5.5)	480 seconds
Bell Fourier based algorithm (section 5.6)	9.8 seconds

Table 5.8.1 A comparison of execution times under Matlab 6.5 on a 2GHz Pentium 4 for determining the wavelength of a waveform embedded within a 16x16 pixel array containing a complex waveform with a wavelength of 10 pixels.

Chapter 6: Verification of Bathymetric Inversions - Faro

Early work for this study focused on linear wave theory due to its simplicity. In chapter 1, a number of non-linear corrections to linear theory were explored, out of which Hedges' 1976 equation was selected, again for its simplicity, and also for its good agreement with stream function calculated wave properties. In order to study the effect of switching from linear to non-linear wave dispersion equations, a suitable set of field data was needed, against which the equations could be tested. As was described in Chapter 3, the Faro 2002 experiment deployed two radars of different resolutions overlooking the same area of beach at the same time. This permitted the study of wave transformation from the deepest water, 2km offshore, right up to the waves breaking on the beach. The use of the mini radar to study the breaking waves ensured that there could be no question of resolution problems influencing the results in the shallowest areas. Hedges' 1976 dispersion equation was applied to the data derived from the radars initially using $Z = 0.5H_S$, where the value of H_S measured by the Faro wave buoy was used. The data from the mm wave radar showed that $Z = 0.4H_S$ gave a better fit to the data, and so was applied to the X-band radar data. The analyses of data from both radars demonstrate that the depth inversion using this dispersion equation at this site can be used to obtain the water depths from the beach out to 15m water depth with accuracy considerably better than 0.5m.

6.1 Analysis of the Faro 2002 Nested Radar Experiment

The data from both radars were converted from polar to Cartesian grids and then analysed using the Fourier based wavelength mapping routine described in Section 5.6. The various statistics describing the two datasets are listed in Table 6.1. The wavelengths determined using this technique were then used in a least squares fitting routine to find the best fit to the water depth at each point in the area imaged using both linear and non-linear wave dispersion equations, the non-linear equation using the significant wave height measured by the Faro wave buoy. Doppler shifts due to currents were neglected as the direction of travel of the waves was approximately perpendicular to the shore, while tidal currents would be largely parallel to the shore and have a minimal component in the direction of wave propagation.

Radar	Range	Image interval	Number of Images in sequence	Duration of each record	Grid spacing	Analysis sub-image size
X-Band Marine	2km	~2.4 seconds	128	307 seconds	7.5m	32/16/8 pixels square =240/120/60 metres square
77GHz mini-radar	200m	~1 second	512	512 seconds	2m	16/8 pixels square =32/16 metres square

Table 6.1 The details of the two radar datasets from the Faro 2002 experiment.

The water depth maps calculated from the two sets of radar data were compared to the combined bathymetric and topographic survey with the predicted tidal level added.

Although the two radars have slightly different imaging mechanisms, they both use properties of the waves to produce images of them. It should therefore be possible to take simultaneous image sequences from the two radars and overlay them such that the wave patterns match. The clearest way to do this was to use single frequency images from the initial frequency breakdown of the time series. The results are shown in Figure 6.1, with a single frequency image with wave period 8.9 seconds from the X-band radar as the background, and the corresponding single frequency image from the mm wave radar overlaid. The difference between the resolutions of the two radars is apparent by virtue of the smaller area and higher resolution of the mm wave radar, which yields much smoother and more detailed images of the waves than the X-band radar. The locations of the two radars on the beach at Faro are shown as the cross for the X-band radar and the circle for the mm wave radar.

As expected, the wave patterns match precisely, and so the results from the two radars should be comparable if processed in a similar fashion.

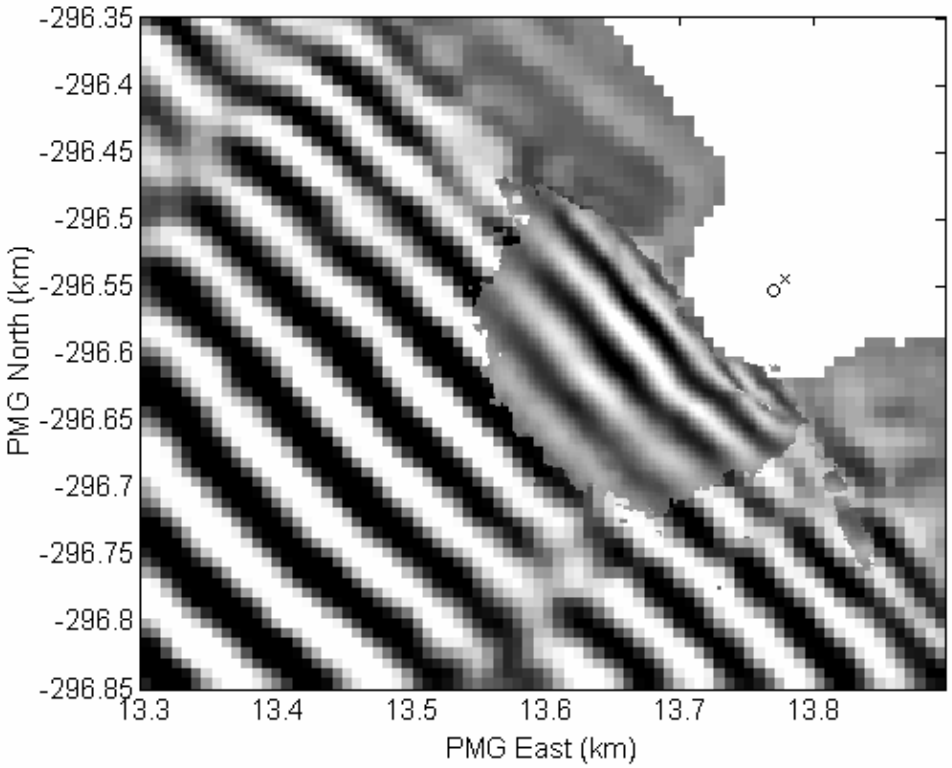

Figure 6.1 A single frequency image of 8.9 second waves recorded using the X-band radar from the beach at Faro in 2002; the location of the radar is marked with a 'x'. The corresponding single frequency wave image from the mm wave radar recorded simultaneously has been overlaid, and the location of that radar marked with a 'o'.

6.2 The Faro 2002 Nested Radar MM Wave Radar Results

The X-band radar was only half of the nested radar experiment, and did not provide sufficient resolution to prove or disprove the practical application of Hedges wave dispersion equation over linear theory. The use of the new mm wave radar (often referred to in practice as the mini-radar) provided much higher resolution and duration of records, and for the first time allowed the techniques developed for the X-band radar to be extended through the surf zone and right up to the shore.

The considerably higher resolution and longer record duration possible with the mm wave radar yielded excellent quality single frequency wave patterns in the Fourier breakdown of the image sequences. Examples of these for wave periods of 3-14 seconds are shown in Figures 6.2.1a and 6.2.1b, generated by plotting the real component of the complex Fourier layer corresponding to the particular wave period. These plots demonstrate the excellent resolution achievable using the mm wave radar, particularly for the plots of short period waves in which waves with lengths of less than 10m are clearly resolved.

The survey carried out by the University of Algarve was confined approximately to one particular cross-shore section of the beach that was the subject of a regular re-survey programme, rather than a wide area survey. Within that section a number of cross-shore transects were surveyed by boat at 20m intervals, spanning an alongshore distance of 100m in total. It should be noted that the subtidal part of the survey was carried out from the boat during calm conditions approximately 1 week prior to the storm during which the nested radar experiment was carried out. As such one could easily expect some changes to the nearshore bathymetry between the survey and the experiment, for instance in the location of nearshore sand bars, an uncertainty that applies equally to the data inferred from both radars.

The boat survey was matched by a similar one, carried out on foot, of the intertidal region and up to the dune base. The long-shore width of this area corresponds to approximately one third of the long-shore length viewed by the mm wave radar, while the cross-shore range of the survey extended offshore to around 1500m, compared to the maximum range of 200m for the radar.

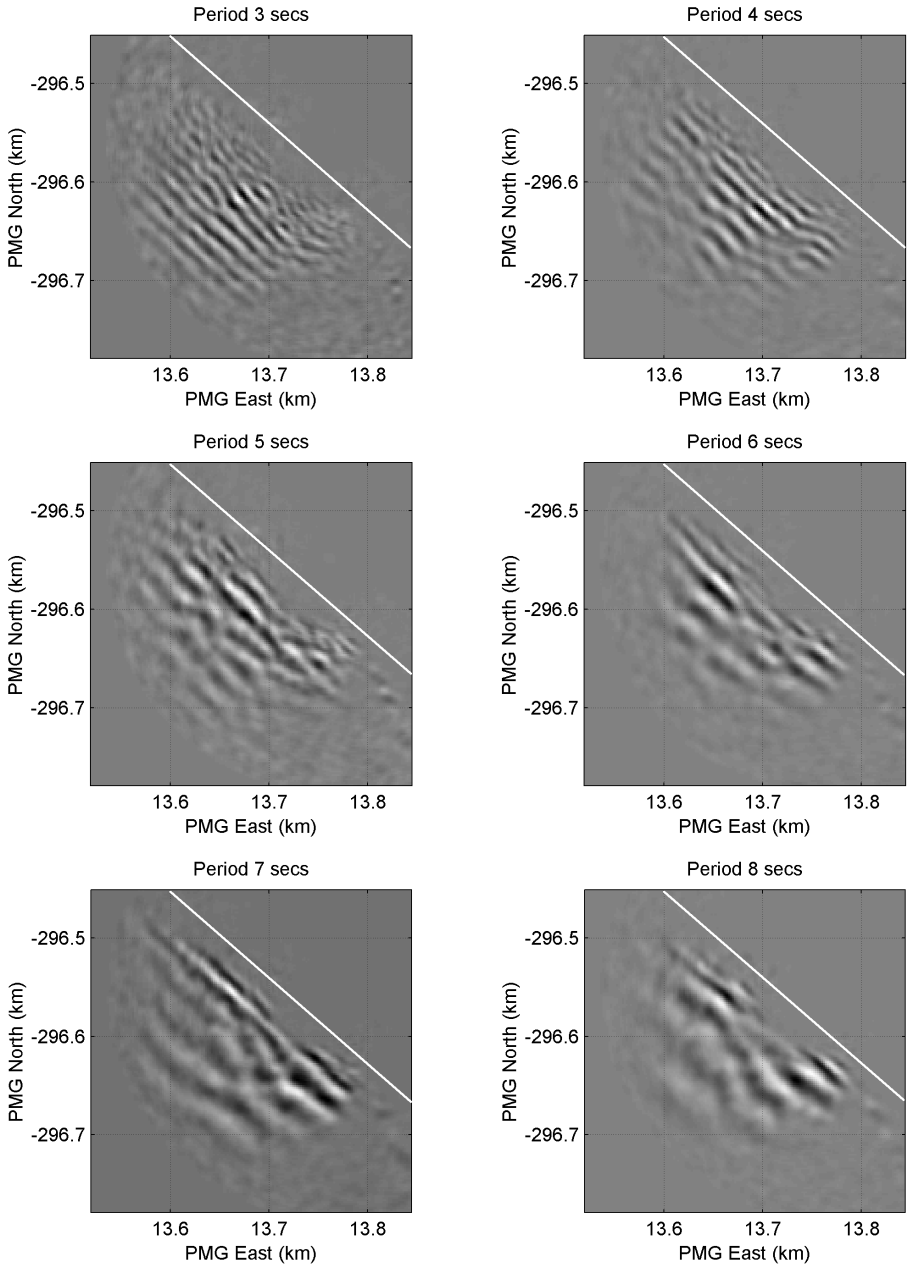

Figure 6.2.1a Plots of the real component of single frequency wave layers from a Fourier breakdown of a 10 minute mm wave radar sequence. Wave images for periods of 3-8 seconds are shown. The white line denotes the approximate location of the waterline.

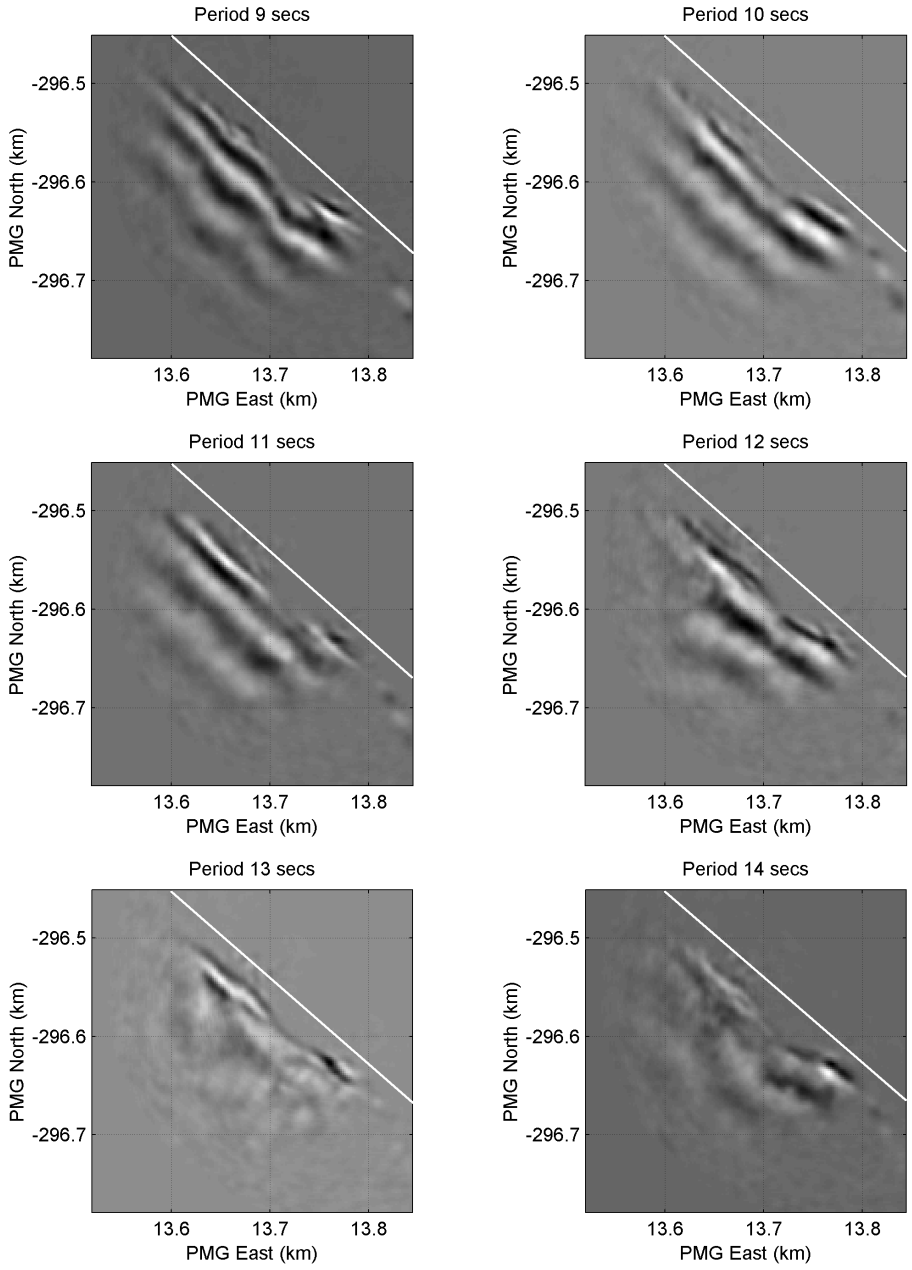

Figure 6.2.1b Plots of the real component of single frequency wave layers from a Fourier breakdown of a 10 minute mm wave radar sequence. Wave images for periods of 9-14 seconds are shown. The white line denotes the approximate location of the waterline.

Figure 6.2.2 shows the results from five different times during this nested-radar experiment, each row of plots representing the results at hourly intervals starting at 11am and finishing at 3pm. It would have been useful to continue the experiment for a full tidal cycle, but conditions on the beach, safety and manpower precluded this possibility. Records were

actually taken every 15 minutes, but those illustrated by the results in Figure 6.2.2 are considered sufficiently representative of this dataset.

The first column in Figure 6.2.2 shows a single cross-shore transect passing through the area viewed by the radar and within the survey area. The solid black line represents the bathymetry according to the survey, with the predicted tide level added to give the water depth at that time. The red line shows the water depths determined using Hedges' 1976 dispersion equation using $Z = 0.5H_S$ applied to the wavelengths and periods determined from the mm wave radar data. The significant wave height, H_S, was that measured by the Faro wave buoy, taken to be 2m based on the graph shown in Figure 4.4.2. The blue horizontal line at the top of each plot shows the water level predicted at that time. The second column of plots shows the tidal predictions for that day with a circle marking the state of the tide at the time of each record. The final column shows scatter plots of the radar derived water depths for linear theory (in red) and non-linear theory (black) against the survey plus predicted tide for the whole area of overlap of the radar and survey. The blue line represents the target result of the radar derived depths being equal to those of the survey plus tide.

The results from the mm wave radar as shown in Figure 6.2.2 column 3 demonstrate how, as expected, linear theory is over predicting the water depth based on the measured wavelengths and periods. The non-linear Hedges (1976) dispersion equation using $Z = 0.5H_S$ shows considerably better correlation to the surveyed bathymetry with the predicted tide added.

The bathymetry calculated by analysing individual radar records yields a reasonable approximation to the overall bathymetry of the scanned area, but by averaging a number of records, subtle variations of the sea floor emerge from the low level noise on the individual records. The predicted tide level was subtracted from each of the water depth maps calculated from the radar data and the resulting depths averaged for each pixel to give a mean bathymetric map referenced to the survey datum. A scatter plot showing the comparison between the amalgamated radar derived depths and the survey is shown in Figure 6.2.3.

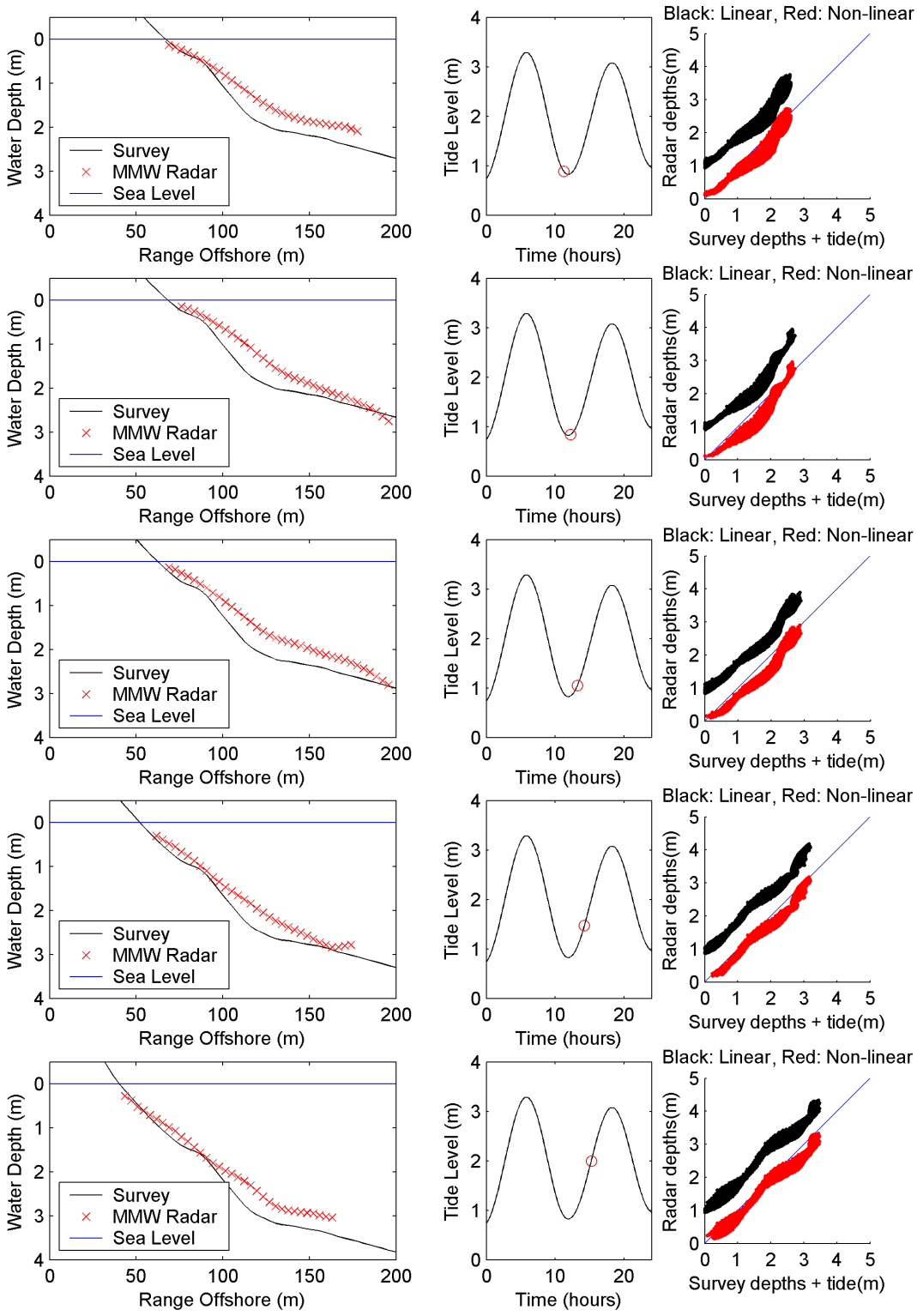

Figure 6.2.2 Mm wave radar derived water depths at 1 hour intervals through the nested radar deployment. The first column shows comparisons between the non-linear theory radar derived water depths with the survey transect to a cross shore distance of 200m. The second column shows the state of the predicted tide at that time, and the third shows a scatter plot of the radar derived depths using linear (black) and non-linear (red) dispersion against the survey depths with predicted tide added. The value of $Z=0.5H_S$ was used in the dispersion equation.

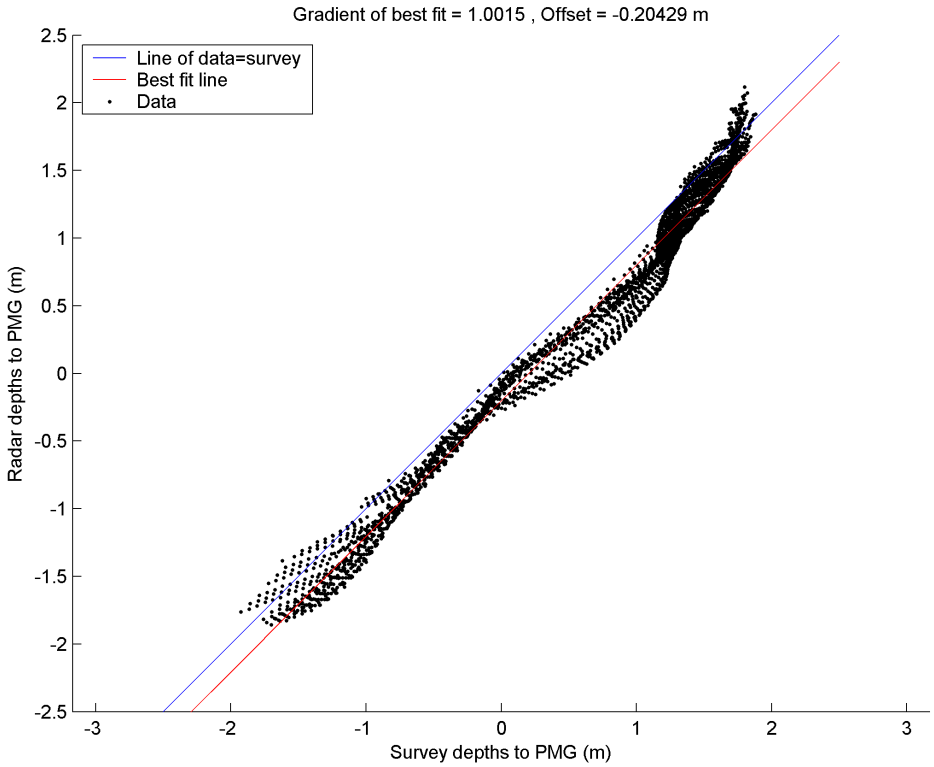

Figure 6.2.3 A comparison between the amalgamated mm wave radar derived depths and the survey. The line of equality is shown in blue, while the best fit to the data is shown in red. The parameter Z=0.5Hs was used for this set of results.

A best fit to the scatter has been plotted as the red line and the gradient of that best fit of 1.0015 is an excellent result. However, the offset shows an underestimate of the water depth by the radar of slightly more than 20cm. This is considered a significant improvement over linear theory, which over predicts the water depths by approximately 1m. The results can be brought into near perfect agreement by setting the parameter Z=0.4H_S and recalculating the results, effectively shifting the data up by approximately 20cm as shown in Figure 6.2.4. This is more in line with the findings of Holland (2001) who found that a value of $\alpha = 0.40$ in equation 2.6.7, in which αH_S is equivalent to Z in equation 2.6.1, gave the best fit to experimental data.

Table 6.2.1 gives the mean offset and standard deviation values for the five records illustrated by figures 6.2.2 and 6.2.4. The values are given for linear theory, i.e. Z=0, Z=0.5H_S and Z=0.4H_S. The linear theory offsets are all between 0.7m and 0.8m above the survey measurements, but with Z=0.5H_S the offsets are over corrected to between -0.19m and -0.28m. The offsets corresponding to Z=0.4H_S are reduced to between -0.01m and -

0.11m. The standard deviations are slightly lower for the non-linear processing compared with linear theory but the differences are very slight, the average standard deviation for linear theory being 0.19m, and 0.16m and 0.18m for Z=0.5H_S and Z=0.4H_S respectively.

	Linear (Z = 0)		**Z = 0.5H_S**		**Z = 0.4H_S**	
Time	**Offset**	**Standard deviation**	**Offset**	**Standard deviation**	**Offset**	**Standard deviation**
11:00	0.81 m	0.18 m	-0.19 m	0.18 m	-0.01 m	0.17 m
12:00	0.80 m	0.20 m	-0.19 m	0.18 m	-0.02 m	0.19 m
13:00	0.71 m	0.19 m	-0.28 m	0.15 m	-0.11 m	0.17 m
14:00	0.73 m	0.16 m	-0.23 m	0.14 m	-0.09 m	0.14 m
15:00	0.73 m	0.23 m	-0.25 m	0.15 m	-0.07 m	0.23 m

Table 6.2.1 The offsets and standard deviations for the depth inversions carried out on the Faro 2002 mm wave radar data. Values correspond to Z = 0, Z = 0.5H_S and Z = 0.4H_S.

Alternatively, one could suggest that the use of the measurement of Hs=2m by the somewhat distant Faro wave buoy could be larger than might be measured closer to the shore and nearer to the experiment site, although this is speculation.

These results demonstrate generally excellent agreement between the radar derived water depths and the surveyed bathymetry. However, there are small discrepancies, such as the apparent underestimate of the water depth by up to 0.5m along the transect in the first column of Figure 6.2.4, between 100m and 150m offshore. Unfortunately, it is impossible to determine whether this discrepancy is a result of the inability of the analysis to detect the dip in the bathymetry or whether it was caused by a genuine change in bathymetry between the time of the radar recordings and the time of the survey a few days earlier. However, changes of this magnitude such as the movement of a sand bar would not be an unreasonable consequence of the high wave conditions observed in the days prior to the radar recordings.

The re-calculated results using Z=0.4H_S were adjusted to be relative to chart datum (MSL-2m) by subtracting the predicted tide levels and averaged to yield a bathymetric map. The final bathymetric map determined from the radar data has been plotted in Figure 6.2.5 and the rectangular survey region has been overlaid and delineated by the white lines to allow a visual comparison of the join between the two sets of data. The colour scale represents a range of 4m in height, with the upper limit of -2m representing the maximum tidal height achieved during the experiment.

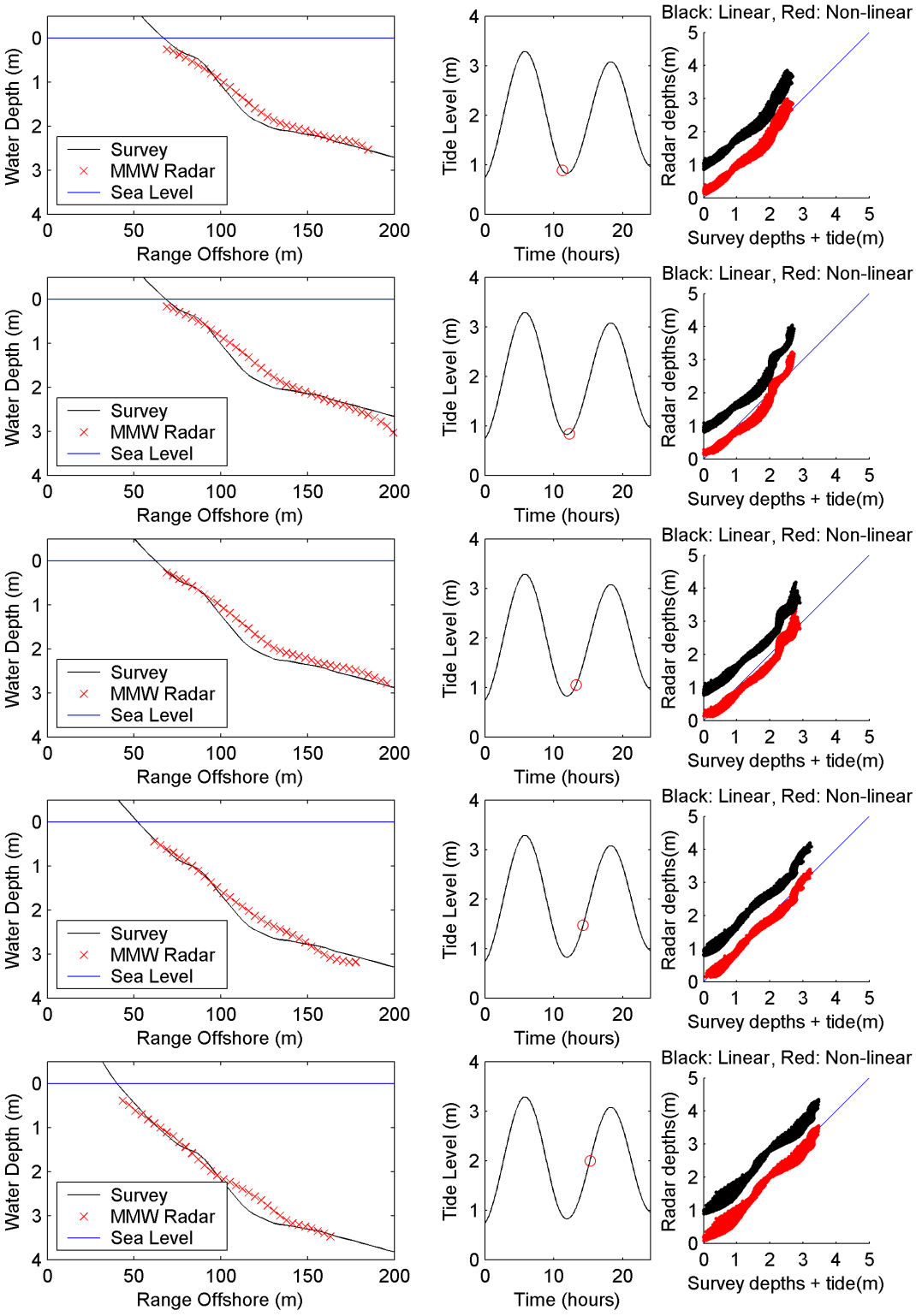

Figure 6.2.4 Data from Figure 6.2.2 recalculated for $Z=0.4H_S$, showing mm wave radar derived water depths at 1 hour intervals through the nested radar deployment. The first column shows comparisons between the non-linear theory radar derived water depths with the survey transect to a cross shore distance of 200m. The second column shows the state of the predicted tide at that time, and the third shows a scatter plot of the radar derived depths using linear (black) and non-linear (red) dispersion against the survey depths with predicted tide added.

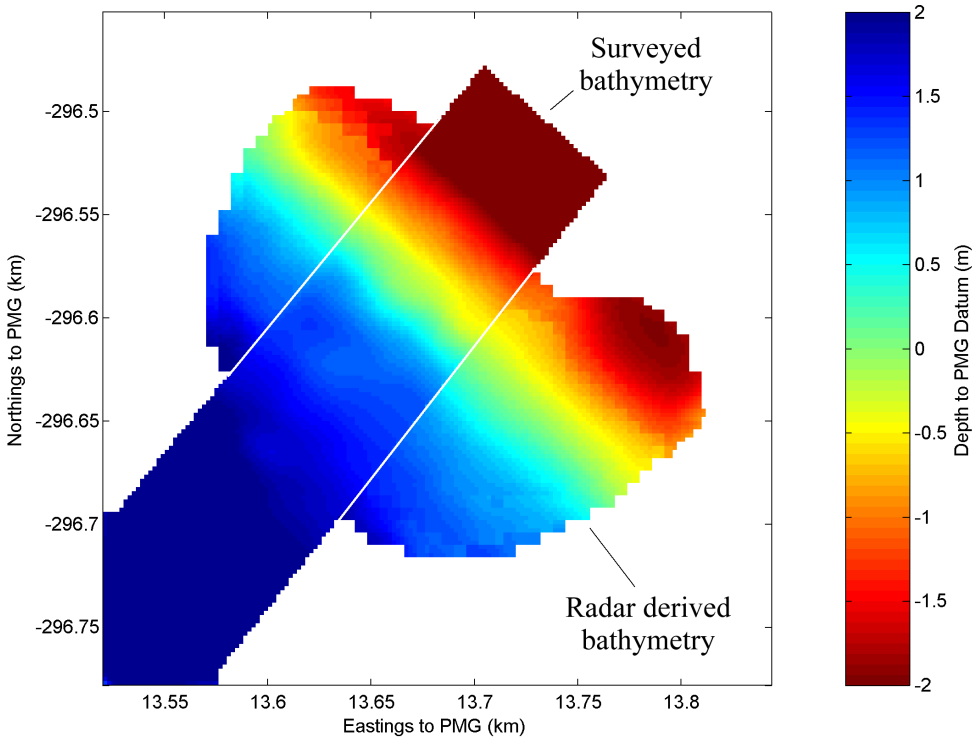

Figure 6.2.5 The amalgamated bathymetric map generated from the five records illustrated in Figure 6.2.4 using Z=0.4Hs. The rectangular bathymetric survey has been overlaid for comparison.

Scrutiny of the boundary between the radar derived bathymetry and the survey shows how well the two sets of data match although the discrepancy between the heights found between 100m and 150m offshore that was discussed earlier is evident. As was stated before, the survey and radar derived bathymetry are separated in time by several days, during which a wave event occurred, so it is impossible to prove whether this discrepancy is due to the inability of the radar technique to resolve small features such as a short bar or trough, or whether there was a real bathymetric change caused by the wave event.

6.3 The Faro 2002 Nested Radar X-Band Radar Results

The X-band radar was set up to record at exactly the same time as the mm wave radar during the nested-radar experiment. Every 15 minutes 128 sequential images were recorded, spanning 5 minutes in contrast to the 512 images over 10 minutes for the mini radar. It would have been better to try to match the recording durations of the two instruments, but the old X-band radar recorder was unable to record more than 128 images in a row for reasons that were never fully explained.

The same analysis as used on the mm wave radar was carried out on the X-band radar image sequences, this time using $Z = 0.4H_S$ in Hedges' non-linear dispersion equation, based on the results from the mm wave radar in section 6.2. Longer wavelengths were anticipated from the longer range achievable by the X-band radar, so the maximum size of the image sub-sections used for the analysis was increased from the 32m square used for the mm wave radar to 240m, thus ensuring the long wavelength swell waves detected further offshore would fit at least one wavelength within the sub-image area. Again, the plots of the results from the analyses of the radar sequences shown in Figure 6.3.1 are limited to those recorded on the hour, considered as representative of the complete dataset.

As before, the first column in Figure 6.3.1 shows a single cross-shore transect passing through the area viewed by the radar and within the survey area. The solid black line represents the bathymetry according to the survey, with the predicted tide level added to give the water depth at that time. The red line shows the water depths determined using Hedges' 1976 dispersion equation using $Z = 0.4H_S$ applied to the wavelengths and periods determined from the X-band radar data. The significant wave height, H_S, was that measured by the Faro wave buoy, taken to be 2m based on the graph shown in Figure 3.4.2. The blue horizontal line at the top of each plot shows the water level predicted at that time. The second column of plots shows the tidal predictions for that day with a circle marking the state of the tide at the time of each record. The final column shows scatter plots of the radar derived water depths for linear theory (in black) and non-linear theory (red) against the survey plus predicted tide for the whole area of overlap of the radar and survey. The blue line represents the target result of the radar derived depths being equal to those of the survey plus tide.

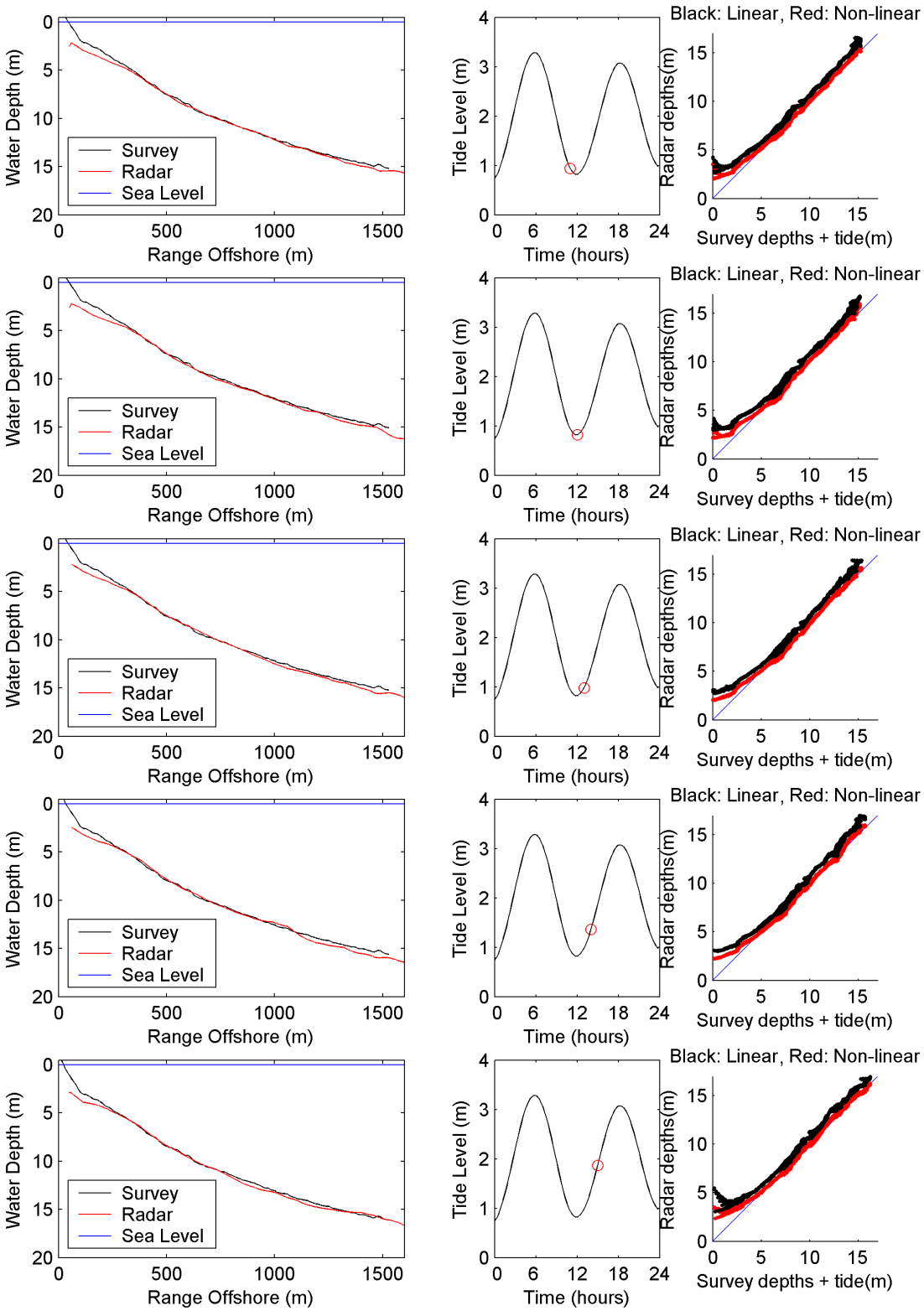

Figure 6.3.1 X-Band radar derived water depths at 1 hour intervals through the nested radar deployment. The first column shows comparisons with the survey transects to a cross shore distance of about 1500m. The second column shows the state of the predicted tide at that time, and the third shows a scatter plot of the radar derived depths using linear (in black) and Hedges' (in red) dispersion equations against the survey depths with predicted tide added

	Linear ($Z = 0$)		Non-linear ($Z = 0.4H_S$)	
Time	**Offset**	**Standard Deviation**	**Offset**	**Standard deviation**
11:00	0.60 m	0.39 m	-0.16 m	0.32 m
12:00	0.73 m	0.39 m	-0.04 m	0.33 m
13:00	0.60 m	0.42 m	-0.08 m	0.34 m
14:00	0.65 m	0.34 m	-0.07 m	0.34 m
15:00	0.55 m	0.40 m	-0.12 m	0.26 m

Table 6.3.1 The offsets and standard deviations for the depth inversions carried out on the Faro 2002 Day 63 X-band radar data. Values correspond to Z=0 and Z=0.4H_S.

As with the mm wave radar results, and as expected, the water depths calculated by the non-linear equation match the survey better than those from linear theory, with linear theory over predicting the water depths again. The non-linear equation performs well except in the region closer than 250m to the shore or in less than 5m of water. In this region, the radar derived depths overestimate the water depth to a greater extent as the shore is approached with a maximum error of the order of 1m. The mean offsets shown in table 6.3.1 are reduced to between -0.4mm and -0.16, i.e. a slight under prediction, but considering that the tidal level is a prediction and not a measurement, offsets of this order can be considered to be within experimental error. The standard deviations are slightly smaller using the non-linear correction, but the difference is marginal, being of the order of a few centimeters. When the five records illustrated above are combined into one map and compared to the survey, the mean offset is calculated as -0.1m and the standard deviation as 0.30m.

The accuracy of the mm wave radar results suggest that the problem does not lie with the equation used for the depth inversion, but rather something related to the X-band radar imaging system. There are at least two possible explanations for this overestimate of depth close to the shore, both of which may contribute to this effect to some degree.

The first is a problem of resolution. The analysis technique requires a finite area of the sea from which to derive accurate wavelengths and hence water depths. This area has been set as a maximum of 240m square in order to accurately obtain wavelengths in the deeper regions of the scanned area where the swell waves have wavelengths in excess of 100m. The water depth calculated can be considered as the average wavelength in this 240m square. Close to the shore, this means that the depth calculated for a point, for example 10m offshore, could be calculated from waves located up to 150m from the shore on one side of the 32

pixel/240m square image subsection which would have a strong signal, but have no signal from the dry beach area on the other side of the image subsection where there would be no waves, hence some overestimate on the water depths could be expected. In essence the 'centre of mass' of the data within the sub-image area would be offset seawards from the centre of the sub-image area, placing the depth estimate derived from it in the wrong location. Ideally the size of the sub-image area would reduce in this region to try and offset this effect, and this is already part of the analysis as described in section 5.7, but the quality of the X-Band radar images may be insufficient to obtain clean wavelength measurements in areas small enough to resolve the rapid change in bathymetry in this nearshore area. This problem could potentially be alleviated in future analyses by determining the 'centre of mass' of the data in each sub-image area and applying the calculated water depth to that location rather than the exact centre of the sub-image.

Another possible contribution to this overestimate of water depth close to the shore is the change from non-breaking waves to breaking waves. Depth induced wave breaking is usually characterised by the crest of the wave moving faster than the rest of the wave, leading to the crest being further forward in the wave profile than in a symmetric non-breaking wave. This asymmetry develops precisely in the region in which the X-band radar data analysis shows overestimates in water depth, resulting from overestimates in wavelength from the radar images. The change from symmetric to asymmetric waves could introduce a localised error, overestimating the wavelengths at the onset of breaking, as the radar imaging changes from seeing the wave crests at the centre of the wave profile to seeing the maximum signal at the breaking front of the waves somewhat forward of the centre of the wave profile. This change from symmetric to slightly asymmetric waves need only be of the order of a few meters in waves with a length of tens of metres to fully account for the overestimate in depth of approximately 1m found here. At the present time, there is no way of verifying this second hypothesis.

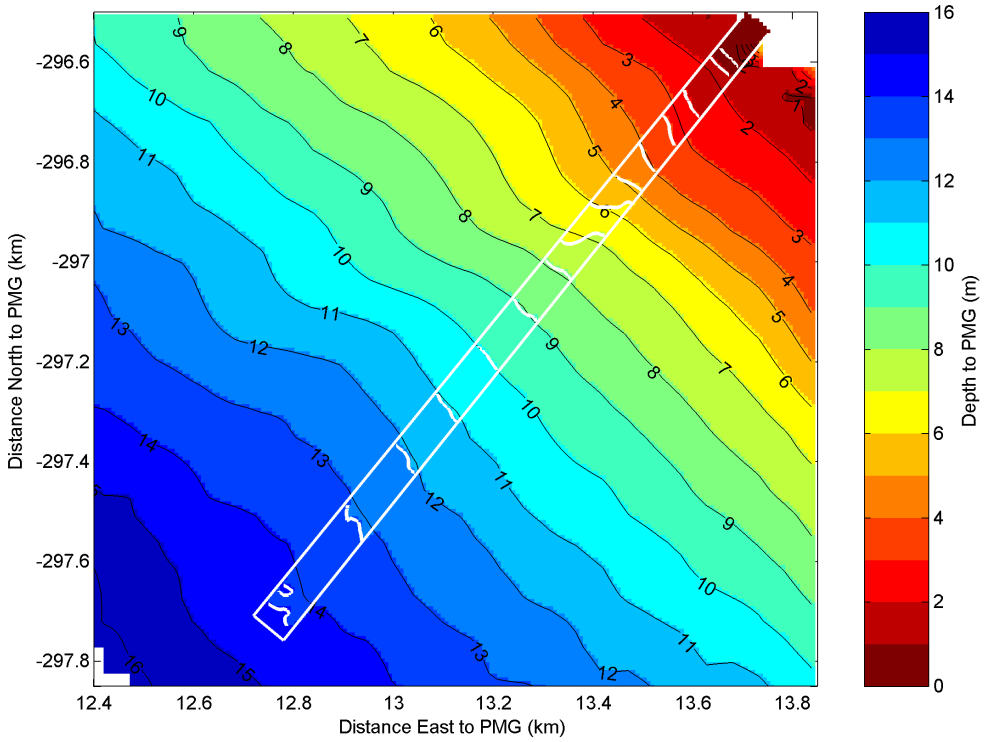

Figure 6.3.2 The amalgamated bathymetric map calculated from nine half-hourly radar records, including those shown in Figure 6.3.1, with the survey overlaid in the area outlined in white. The contours are at 1m intervals and are shown for both the radar derived depths (in black) and the narrow strip of the survey (in white). The water depths are shown relative to the local datum which is defined as 2m below mean sea level.

The predicted tidal level was subtracted from each record, and the mean of the depth estimates taken at each pixel. The resulting bathymetric map produced by averaging the five sets of results represented by Figure 6.3.1 together with those recorded on the half hour, totalling 9 records in all, is presented in Figure 6.3.2. The conventional survey has been interposed in the white-bordered area for comparison, but is almost indistinguishable except by comparing the detail of the 1m spaced contours of each set of data. It is interesting to note the transverse ridge stretching roughly east-south-east in the radar derived bathymetry, the contours of which are mirrored in the survey data in the 4m-7m contours. The ridge covers such a large area that an extensive and very expensive survey would be required to resolve its extent in a manner to match that provided by the short set of hourly radar records of five minutes duration shown here. In terms of accuracy, beyond 200m (approximately the 4m contour) from the shore the radar contours are all within 25cm of the survey contours as far as the limit of the survey at the 14m contour to chart datum.

6.4 Testing of the Limited Resolution Hypothesis

In section 6.3 it was suggested that the over-prediction of the water depth close to the shore using the X-band radar data was due to the finite size of the area needed to pick out the wavelengths, i.e. a resolution problem. It would be difficult to reduce the analysis area size and maintain the quality of the results sufficiently to test this hypothesis using X-band radar data. However, it is possible to increase the size of the area used for the wavelength determination with the mm wave radar, hence degrading the results to more closely mimic the resolution used for the X-band radar data.

This test was carried out by increasing the area used for wavelength determination from the maximum 32m square used in section 6.2 to 64m – still only about one quarter of the scale used in the X-band radar analysis. The results are presented in Figure 6.4.1 and clearly show the beginnings of a consistent overestimate of the water depth in the region closest to the shore that was not present in the results shown in Figure 6.2.4. This suggests that the overestimates in water depth produced in this region by the analysis of the X-band radar data could be at least partly due to need for larger analysis areas for the wavelength determination than is used for the mm wave radar. This is a direct consequence of the lower resolution and increased noise in the X-band radar data compared to the mm wave radar. The improvement in resolution and image clarity of the X-band radar images could be an area for future work. Perhaps the collection of more images in each sequence would reduce the noise in the FFT frequency breakdown and allow smaller image sub-sections to be used in the analysis.

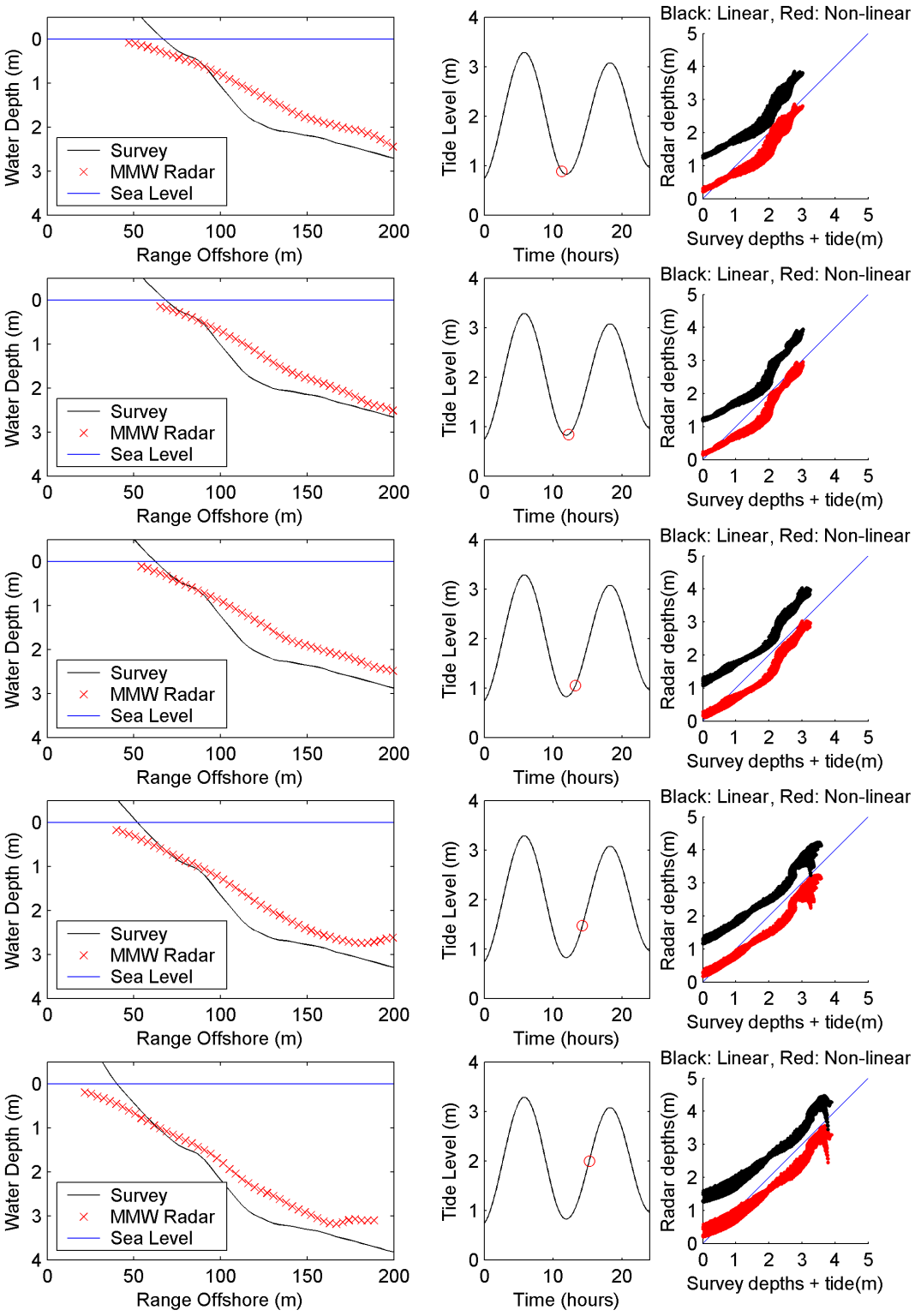

Figure 6.4.1 The results of the mm wave radar bathymetry analysis using an analysis area of 64m square rather than 32m square showing a consistent overestimate in the water depths closest to the shore in the first column of plots.

Chapter 7: Verification of Bathymetric Inversions – Teignmouth

The results from the Faro 2002 nested radar experiments in Chapter 5 demonstrated the accuracy of the bathymetric inversion technique at one site. In order to have confidence in such a technique it was worth carrying out the same type of comparisons at a different site with a different wave climate. The radar data recorded during the COAST3D Teignmouth project represented a very different site to that of Faro. The wave climate in Faro is dominated by long period swell waves, while at Teignmouth the waves are generally more locally generated with shorter periods and rarely extend into the swell region. The presence of a high quality survey and tidal records made it ideal to study as a second test site.

7.1 Analysis of Teignmouth X-Band Radar Data

The data collected at Teignmouth during the 1999 COAST3D experiment was of sufficiently high quality for bathymetric inversions, although the image sequences collected were of only 64 images in length, rather than the 128 collected at Faro. The more images collected in a sequence, the greater the ability of the FFT frequency analysis to pick out the wave patterns. Initial analysis of the Teignmouth data showed that although sub-image sizes of 240m could yield a believable bathymetry close to the shore, the depth estimates degraded rapidly with range due to noisy wave patterns and low radar backscatter levels. Two effects contributed to this. First and most important, the wave climate experienced at Teignmouth during the COAST3D deployment showed that most of the incident wave energy was concentrated in the sub 8 second band. This was a significant contrast to Faro in which the waves were dominated by long period swell of greater than 10 seconds. The practical result of this was considerably shorter wavelengths at Teignmouth than at Faro, leading to problems in resolving individual waves at a range from the radar considerably closer than at Faro. The second effect was statistical in nature, the FFT having only 64 images in a row with which to separate the wave signals, rather than 128 at Faro, leading to more noise on the resulting single frequency Fourier layers, and hence poorer quality wavelength measurements. In order to overcome this, the sub-image area was increased to 480m square, substantially improving the quality of the results, although the image quality and resulting water depths were still poor in the southern half of the area. As with the Faro data, a number of hourly records were processed at different states of the tide.

The measurements of significant wave height used in the bathymetric inversion are those described in section 4.3, and plotted in Figure 4.3.3, measured approximately in the centre of

the surveyed area. The significant wave height during the records analysed here varied between 1.25m and 1.5m. The value of Z was dropped to $Z = 0.3H_s$ compared with $Z = 0.4H_s$ for the Faro data, because using $Z = 0.4H_s$ consistently led to a significant underestimate of the water depths based on the Teignmouth radar data. It would seem that the function Z may need slight tuning for different sites – an issue that will need addressing in future work, but possibly related to the distance offshore that the measurement of significant wave height was recorded. For the present study it has been accepted that Z needs slight tuning.

The statistics for a series of records are shown in Table 7.1.1. The records run from 02:00 on the 12th October 1999 to 11:00 on the same day. During this time the wave signal was reasonably clear on the radar images. The times in the table which are marked with asterisks correspond to the results illustrated in Figure 7.1.1. Linear theory is over predicting the water depth by approximately 0.5m, but setting $Z = 0.3H_s$ in the non-linear dispersion equation reduces this to approximately -0.08m i.e. a slight under-prediction in water depth. Interestingly, the standard deviations in the results are reduced from an average of 0.32m for linear theory to 0.23m, suggesting that the non-linear equation is not only reducing the offset but also the scatter in the data.

	Linear ($Z = 0$)		**Non-linear ($Z = 0.3H_S$)**	
Time	**Offset**	**Standard Deviation**	**Offset**	**Standard Deviation**
02:00 *	0.47 m	0.50 m	-0.08 m	0.34 m
03:00	0.46 m	0.31 m	0.03 m	0.28 m
04:00 *	0.40 m	0.26 m	-0.14 m	0.23 m
05:00	0.56 m	0.31 m	-0.06 m	0.23 m
06:00 *	0.65 m	0.43 m	-0.16 m	0.21 m
07:00	0.61 m	0.29 m	0.07 m	0.21 m
09:00 *	0.53 m	0.25 m	-0.04 m	0.17 m
10:00	0.26 m	0.25 m	-0.21 m	0.19 m
11:00 *	0.37 m	0.25 m	-0.12 m	0.22 m

Table 7.1.1 The offsets and standard deviations for the depth inversions carried out on the Teignmouth X-band radar data. Values correspond to Z=0, Z=0.3H_S. The asterisks in the time column indicate those records that correspond to those shown in Figure 7.1.1.

A selection of results from different states of the tide are shown in Figure 7.1.1, as in Chapter 6 with cross-shore transect plots in the first column, tide level plots in the second column and scatter plots of the radar derived depths compared to the survey plus tide depths in the third column. The transects plotted in the first column represent the northern cross-shore boundary of the survey area.

The overall results mimic those obtained for the Faro data, with linear theory consistently over predicting the water depth and non-linear theory providing a much better match to the surveyed water depths. This discrepancy is less marked than was found in the Faro data due mostly to the lower wave height leading to less non-linear behaviour. Again, the radar derived water depths do not provide a good representation of the bathymetry close to the shore due to the limited resolution of the analysis and the edge effect of being close to the shore.

The bathymetry calculated from averaging the radar derived bathymetric maps from all the records represented by table 7.1.1 and with the tide level subtracted is shown in Figure 7.1.2. By averaging the individual maps generated from these 9 records the resulting mean offset is -0.07m i.e. a slight under prediction overall, with the standard deviation being 0.21m. This amalgamated bathymetric map reproduces the shape of the ebb delta of the tidal inlet very well and shows its influence on the bathymetry extending considerably beyond the area surveyed for the COAST3D project. The bathymetric contours determined from the radar are shown in black, with the corresponding surveyed contours shown in white. The bathymetric contours derived from the radar and the survey can be seen to match very well in the northern part of the area where the image quality was good, but to the south the contours diverge by up to 1m in places due to the poor quality of the image data. Low quality raw images, i.e. poorly defined wave patterns visible in the images, tend to lead to low quality results from the frequency separation of the pixel time series, and hence to unreliable wave length measurements.

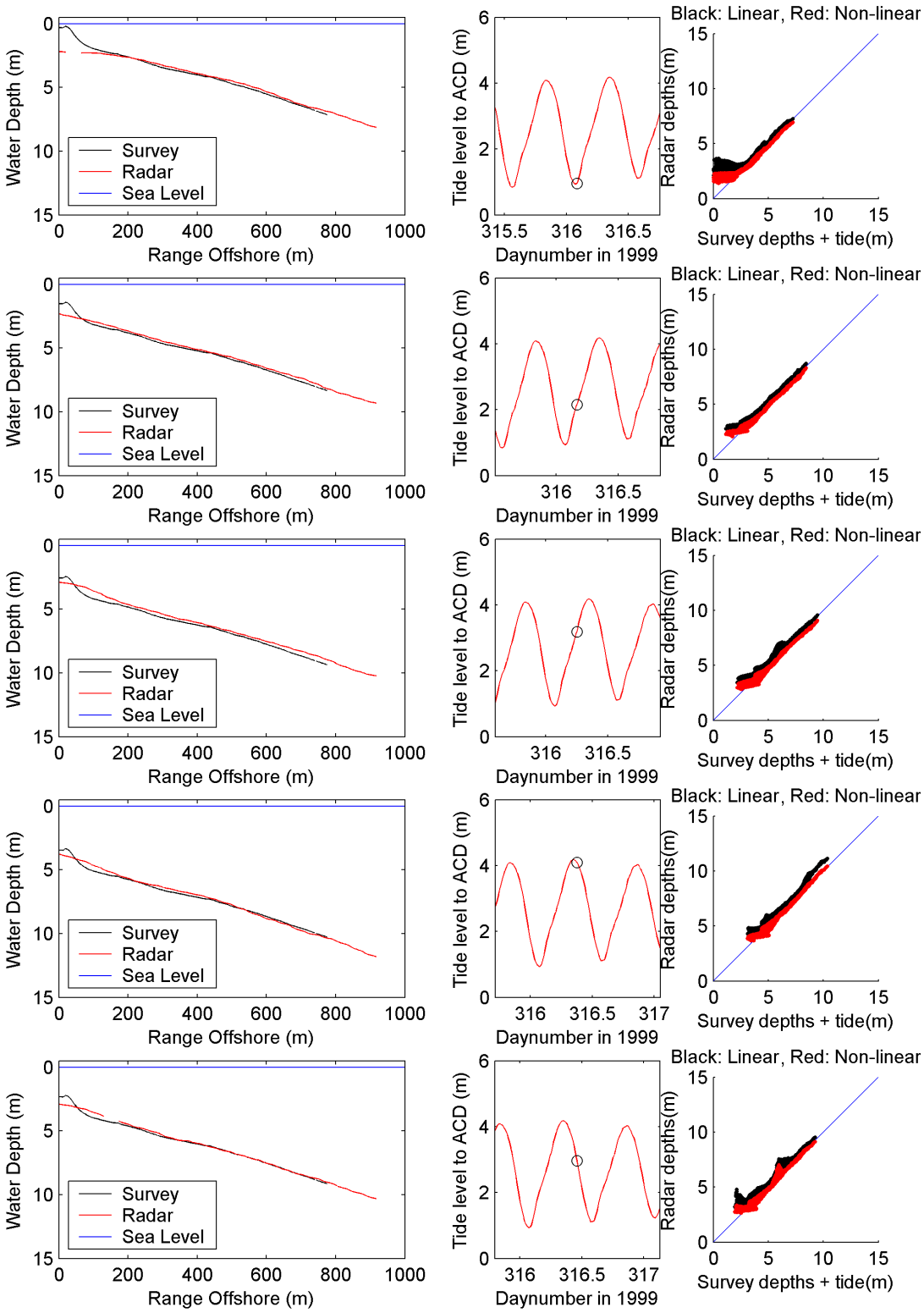

Figure 7.1.1 A selection of results of bathymetric inversion during day 316 in 1999 at different stages of the tide.

Longer image sequences would have been of considerable help in cleaning up this part of the data. This lower signal strength in the southern part of the radar images can be seen in the example shown in Figures 4.3.4 and 4.3.5 in Chapter 4. Unfortunately, the met station on the

pier was not in operation at the time these data were recorded, but data supplied by the U.K. Met. Office to the COAST3D project from the meteorological station nearby in Portland showed a wind direction of 50 degrees, i.e. from the north east. This would tend to produce wind-induced capillary waves oriented approximately NW-SE, leading to the radar looking into the capillary waves in the north easterly direction, and along the line of the capillary waves when looking to the south east. This introduces an angular dependence to the strength of the radar signal returned from the capillary waves on the sea surface by the Bragg scattering mechanism, with a maximum signal when the radar looks into the capillary waves, and a minimum when the radar looks along the line of the capillary waves (Young & Moore, 1977).

The area chosen in what follows for direct comparison of the radar derived bathymetry with the survey has been confined to the northern part of the surveyed area as the image quality has been shown to be of good quality in this area thus providing a more valid test of the technique than using the poorer quality parts of the radar data to the south from which accurate wavelengths would be difficult to determine. The comparison area was also chosen to exclude complex sandbanks which would be poorly resolved due to the large radar sub-image analysis area used.

In Figure 7.1.3 the surveyed bathymetry is overlaid on the radar derived bathymetry in the area outlined in white. The area used for the comparison is outlined by the black dashed line. The agreement between the depth contours of the radar derived bathymetry and the survey is excellent in the northern part of Figure 7.1.3, with differences being of the order of centimeters. The southern part of the study area shows larger discrepancies between the two sets of contours, with the radar derived contours overestimating the water depth by approximately 0.5m, due to the poorer quality of the wave images in that area.

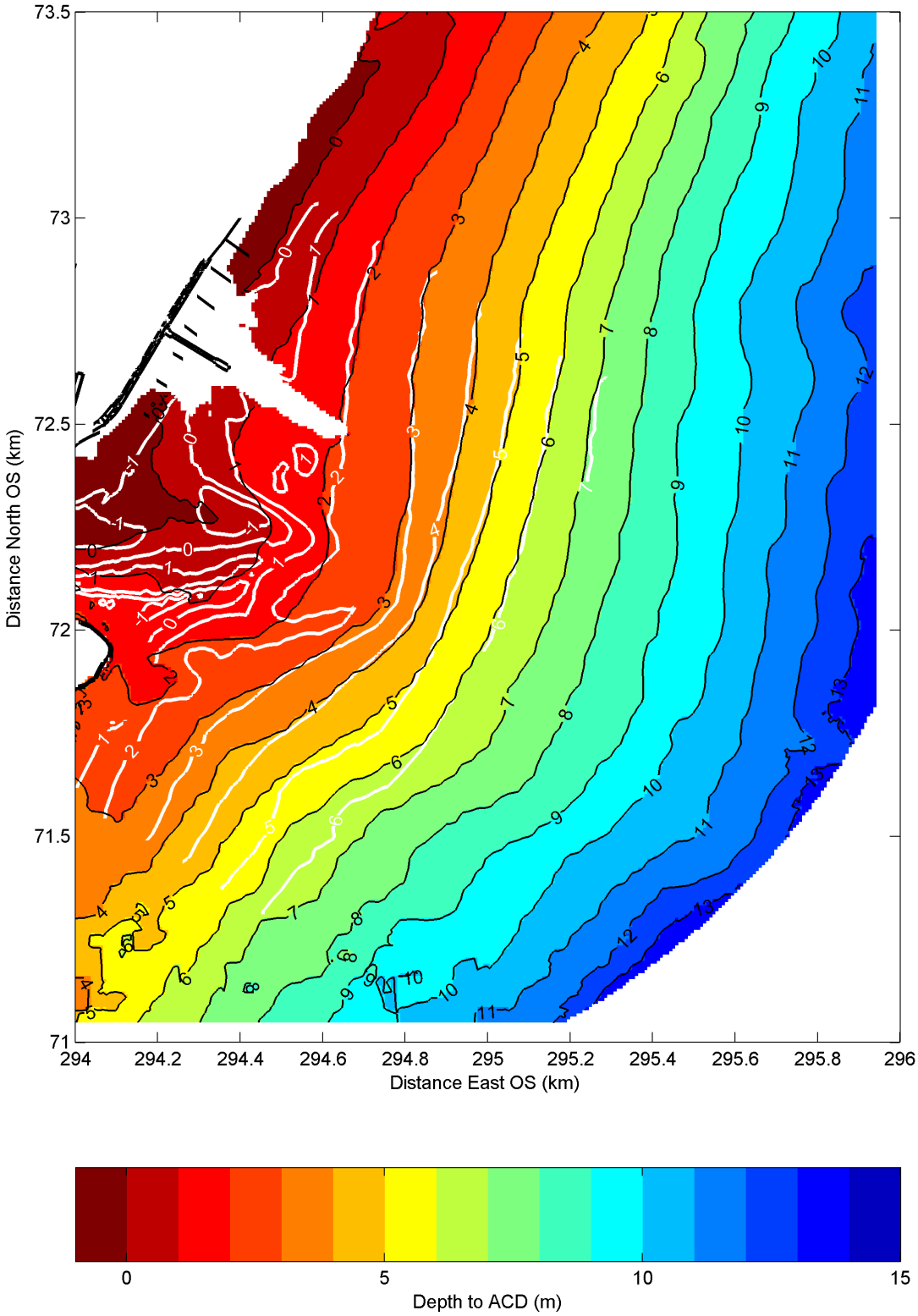

Figure 7.1.2 The amalgamated bathymetry data for Teignmouth using the radar records summarised in Table 7.1.1. Radar derived bathymetric contours are shown in black, with the contours from the surveyed area shown in white for comparison. Depths are to Admiralty Chart Datum.

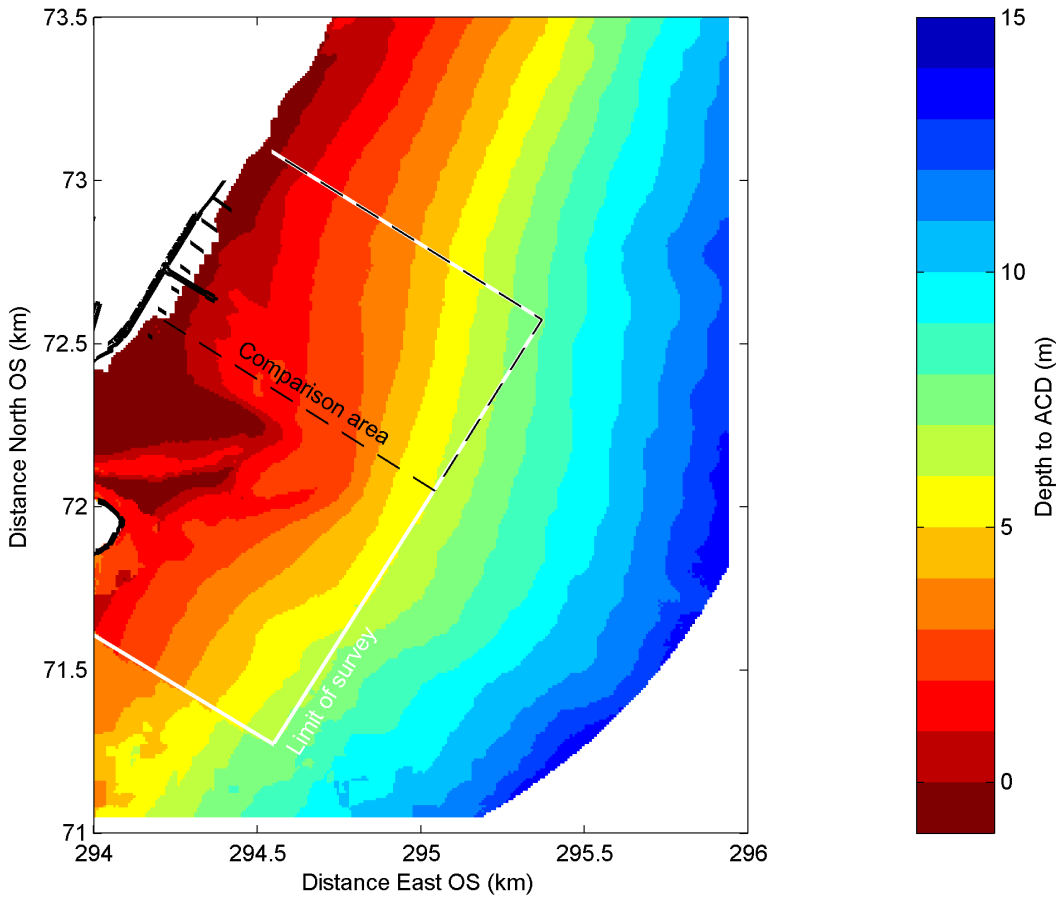

Figure 7.1.3 The same bathymetry as shown in Figure 7.1.2, but with the conventional survey overlaid and outlined in white with the box used for direct comparison with the survey outlined in black.

A scatter plot of the radar derived depths in the area chosen for comparison and outlined in black in Figure 7.1.3 is shown in figure 7.1.4. This plot shows an excellent correlation between the survey and the radar derived bathymetry, with problems only being evident in the shallowest water close to the shore, as with the Faro data.

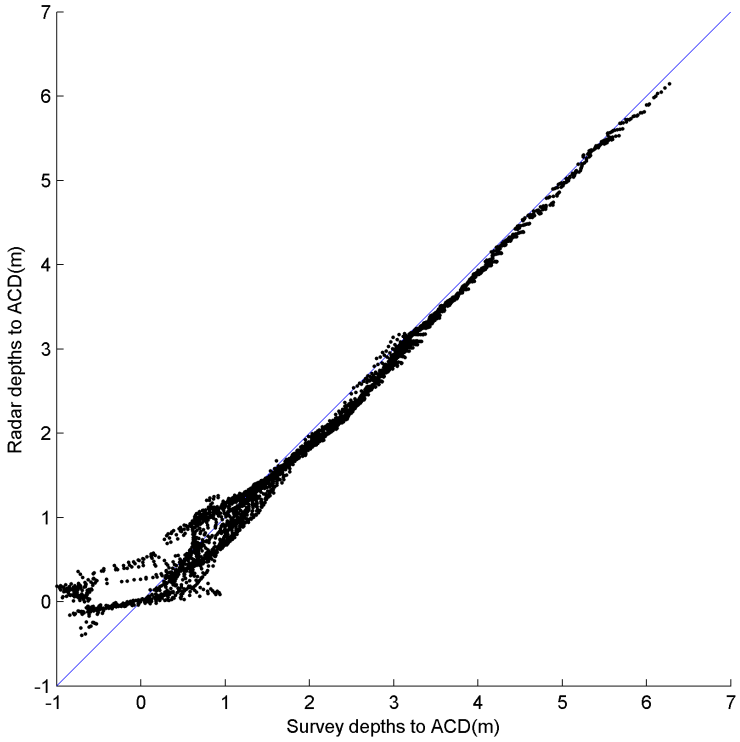

Figure 7.1.4 A scatter plot of the amalgamated radar derived depths compared to the conventional survey. The line of equality is shown in blue.

It can be concluded from the results obtained from Faro and Teignmouth that the bathymetric inversion technique works extremely well when the original radar images show well defined wave patterns, and the bathymetry varies gradually. The non-linear depth inversion gives a better estimate of the water depths than linear theory in all cases. The edge effects and spatial averaging of the analysis, related to the need for a finite analysis area for wavelength measurement can cause problems in the area adjacent to the shore and also in regions where the bathymetry changes on spatial scales of similar size or smaller than that of the analysis sub-image area.

Provided these issues are not forgotten when interpreting the bathymetry derived from radar images, it should be possible to measure large scale bathymetric changes from such data recorded in morphologically active shallow water areas. Work in the following chapter illustrates just such an application, based on visits to the Faro field site over a number of years.

Chapter 8: Movement of the Ancao Inlet observed using depth inversions of radar data from 1999 & 2003

The culmination of this study, and an example of the value the radar measurements and the bathymetric maps derived from them has been found in two sets of radar data from Faro, recorded 4 years apart. While there was a possible 0.5m change in bathymetry due perhaps to the movement of a sand bar between the time of a survey and the time of the mm wave radar recordings during the Faro 2002 experiment described in section 6.2, it was not a change that could be verified with independent data. The Faro field site presented a more large scale and verifiable phenomenon than this in the form of the movement of the tidal inlet.

8.1 Radar Derived Bathymetric Maps from 1999 and 2003

Part of the reason for repeated visits to this particular field site was to attempt the remote monitoring of the natural along-shore migration of the Ancao inlet towards the south-east using X-band radar. Radar data were available from the original INDIA deployment in 1999 (described in section 3.2), the 2002 experiments (section 3.4 & Chapter 5) and also from a deployment in 2003 (described in section 3.5).

The natural behaviour of inlets on this stretch of coast is for there to be a single inlet that migrates from the point of opening towards the south east where they eventually close, driven by the dominant wave conditions of Atlantic swell. The present inlet has also been observed to migrate to the northwest for short periods of time under occasional wave conditions originating from the south east, known as “Levante” conditions. The behaviour of the present inlet during its first two years from August 1997 to July 1999 was summarised by Vila-Concejo et al. (2003a), while the historical behaviour of earlier inlets was studied in detail by Vila-Concejo et al. (2002). In addition, Pilkey et al. (1989) described, in some detail, the whole Ria Formosa barrier island system, consisting of a number of barrier islands and tidal inlets. This work showed a cyclic behaviour of inlets in that part of the barrier island chain from opening in a position that promoted efficient water exchange to eventual closure due to inefficient water exchange once the inlets had migrated approximately 2.5km alongshore to the south east from their point of opening. Historical data show that the inlets move little in the first few years after opening, perhaps as they are stabilising after initial opening. After this initial period of relative stability, the inlets migrate with increasing speed towards their final closure location, developing a smaller cross sectional area with less efficient water exchange as they go. The opening of previous inlets has been a natural

process that was temporally linked to the increasing inefficiency of the existing inlets as they migrated to the south east. The present inlet was dredged artificially, before a new inlet had a chance to open naturally.

Vila-Concejo (2003a) documented surveys that indicated little movement in the two years after the present new inlet was created. During this first two years, the new inlet widened considerably and evolved to an equilibrium state with fully developed flood and ebb deltas. Considering that the position of the channel was largely unchanged from 1997 to 1999, radar derived bathymetric maps based on the 1999 INDIA data should give a good representation of the initial position of the inlet, with subsequent years providing data to track the migration from this point together with the offshore changes associated with the inlet migration.

Unfortunately, there was little in the way of wave action during the period of radar operation in the INDIA project, the major wave events of the season occurring shortly before and shortly after the end of the radar deployment. However, the few wave events available have been processed and amalgamated into a useable bathymetric map. The best conditions for mapping were just before the barge, on which the radar was mounted, returned to port. The barge was moored between the two barrier islands at various sites towards the south-eastern side of the inlet channel for the majority of the INDIA experiment; hence no images could be taken of the inlet itself. However, on the day prior to return to port, the wave conditions became sufficient to warrant moving the barge a short distance behind the barrier islands and onto the flood delta for safety reasons, finally allowing a good view of the inlet using the radar.

Data from the afternoon high water on March 3rd 1999 were analysed to generate the bathymetric map shown in Figure 8.1.1. The maximum size of the sub-image area was set at 240m (32 pixels square) to keep at least one wavelength of the swell waves within the size of area used for wavelength determination, and to provide the best chance of resolving the tidal inlet.

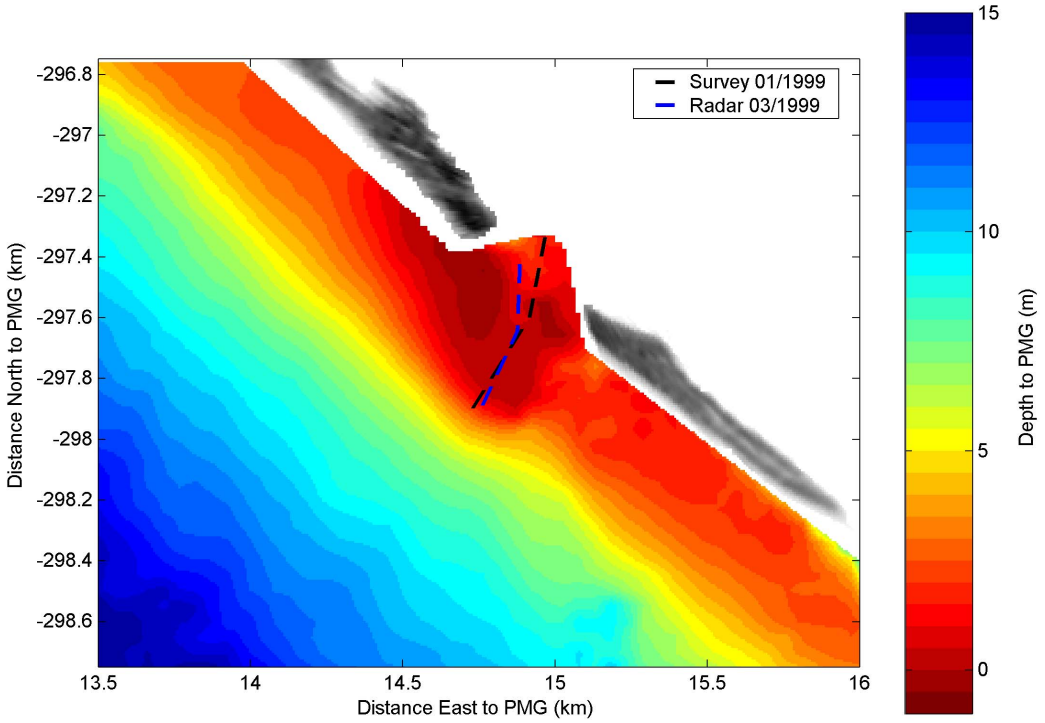

Figure 8.1.1 The radar derived bathymetry from March 3rd 1999 with the centre of the channel determined from the radar bathymetry (in blue) and from the video camera system (labelled as Survey and in black). The dunes of the two islands either side of the inlet are shown in greyscale.

Additionally, in order to put the bathymetry from both years into context, the component of the raw radar images corresponding to non-moving targets (i.e. dune vegetation and cliffs) has been isolated and plotted to show the positions of the barrier islands in greyscale.

A line[13] representing the deepest part of the channel in January 1999 has been plotted as the black dashed line, and was determined from video images by the University of Algarve. A corresponding line determined by hand from the radar bathymetry has been plotted in blue. The radar derived channel line does not exactly match the line determined from the video images, but this was not surprising since the channel was known to have moved during this time in response to different wave conditions (Morris et al., 2004). In particular, at the time the channel line was determined from the video images, the outer part of the channel was in the orientation corresponding to low energy 'Levante' conditions, and emerged from the ebb delta in a south westerly direction. Following storm conditions with the dominant waves

[13] Many thanks to Brad Morris at CIRCOMAR, University of Algarve for the coordinates of the channel lines from 1999 and 2003.

originating from the Atlantic, the channel was known to have been pushed more to the south east as is seen by the radar during these conditions.

The 2002 deployment was confined largely to a mid-beach site 2km north-west from the inlet and was detailed in section 4.4. The radar was placed at the inlet for a short period of a few days, however only low wave conditions were experienced during this time and the data were of insufficient quality for bathymetric inversions.

The 2003 deployment concentrated solely on the inlet and was considerably more successful, in particular, two days of significant wave conditions were experienced on February 20th and 26th 2003. These showed significant wave signals on the radar images from 5-16 second periods, and allowed complete bathymetric maps to be generated using sub-image areas of 240m square. Figure 8.1.2 shows the bathymetry calculated from the radar data from those two days. A line representing the January 2003 position of the channel has been plotted as the black dashed line; this was determined from unpublished surveys by the University of Algarve and the Portuguese Port Authority, recorded prior to the storms during which the radar data was collected. The corresponding line determined by hand from the radar derived bathymetry is shown in blue and is angled almost due south, compared to the survey which shows the channel line to be angled almost cross-shore to the south-west. This would be consistent with previous findings by Morris et al. (2004) who showed that following a period of calm conditions, such as when the survey was carried out, the channel will tend to be aligned approximately cross-shore. However, they also showed that following a period of storm conditions, dominated by waves off the Atlantic, the channel veers to the south as is seen in the radar data recorded following a storm.

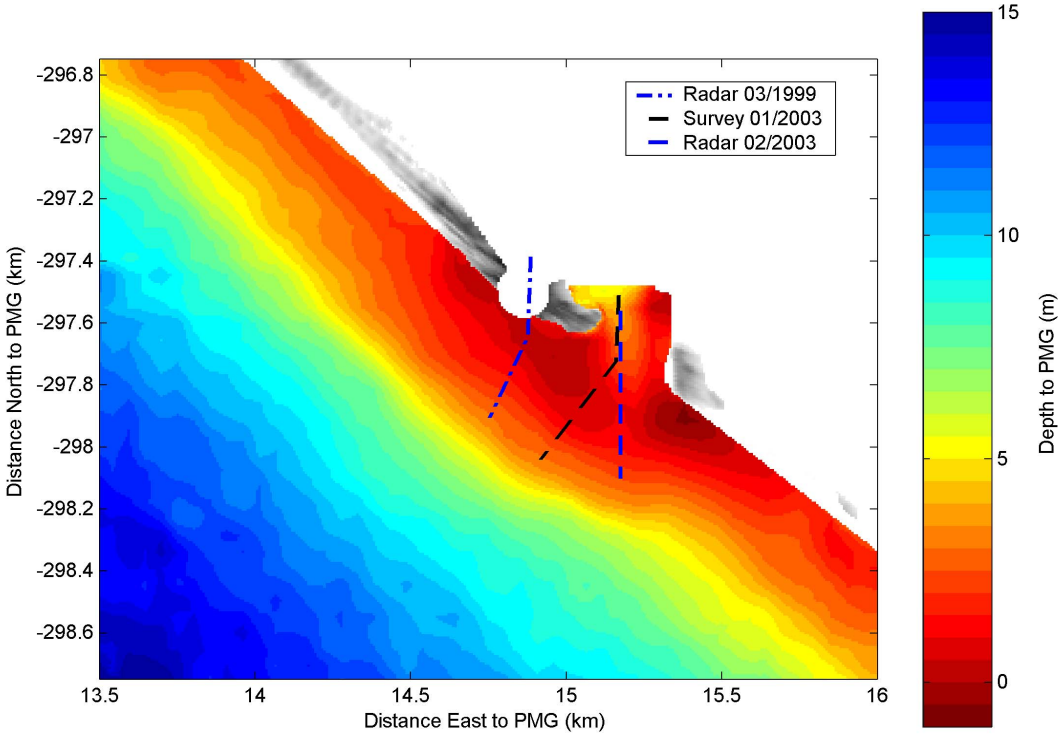

Figure 8.1.2 The radar derived bathymetry from February 2003 with the centre of the channel determined from the radar bathymetry (in blue dashed) and determined from surveys in black. The channel line from 1999 is shown as the dot-dashed blue line for comparison. The dunes of the two islands either side of the inlet are shown in greyscale, with Barreta Island (to the south-east) showing significant reduction in dunes compared to 1999.

The line representing the deepest part of the channel in January 1999 as shown in Figure 8.1.1 has also been plotted as the black dot-dashed line in Figure 8.1.2 to demonstrate the extent of the inlet migration during the 4 years separating the radar measurements – a distance of approximately 300m alongshore to the south-east.

8.2 Radar and Photographic Evidence of the Erosion of Barreta

There are more subtle changes evident in this data that may form a wider picture of the inlet behaviour in this part of the barrier island system than just the inlet migration.

The radar images from 1999 show a considerable signal from dune vegetation on the Barreta island, stretching almost 1km south-east from the inlet. However, the 2003 radar images appear to show that this has all but disappeared, although some of this lack of signal from dunes is likely to be due to the lower vantage point in 2003 compared to 1999. A lower vantage point for the radar means that the front face of the dunes may be shielding large

areas of the Barreta dunes from line of sight view of the radar. However, photographic confirmation of the loss of dunes can be found in a set of aerial photographs of the inlet and surrounding area contained in the INDIA database from 1999. These have been assembled into a photo mosaic of the area and are presented in Figure 8.2.1 to approximately the same scale as the bathymetry plots in Figures 8.1.1 and 8.1.2. These clearly show a wide area of vegetation covered dunes on Barreta Island in 1999.

The particular area in question has been enlarged in Figure 8.2.2 and clearly shows a relatively wide strip of vegetated dune on Barreta, estimated to be around 100m wide. This image can then be contrasted to the photograph of Barreta Island taken early on the 19th February 2003 shown in Figure 8.2.3 in which there is virtually no vegetation and only a narrow strip of beach remaining of the barrier island. The barrier island was so narrow and of such low elevation that it was subject to overwash by large waves at high tide, hence the reason for the presence on the island of the author and a team from the University of Algarve to study these overwash processes during a wave event. Overwash processes such as these are thought to be a possible mechanism triggering the opening of a new inlet.

Figure 8.2.1 A mosaic of aerial photographs of the inlet at Faro following the 1999 INDIA campaign. The vegetated dunes on Barreta Island are clearly visible.

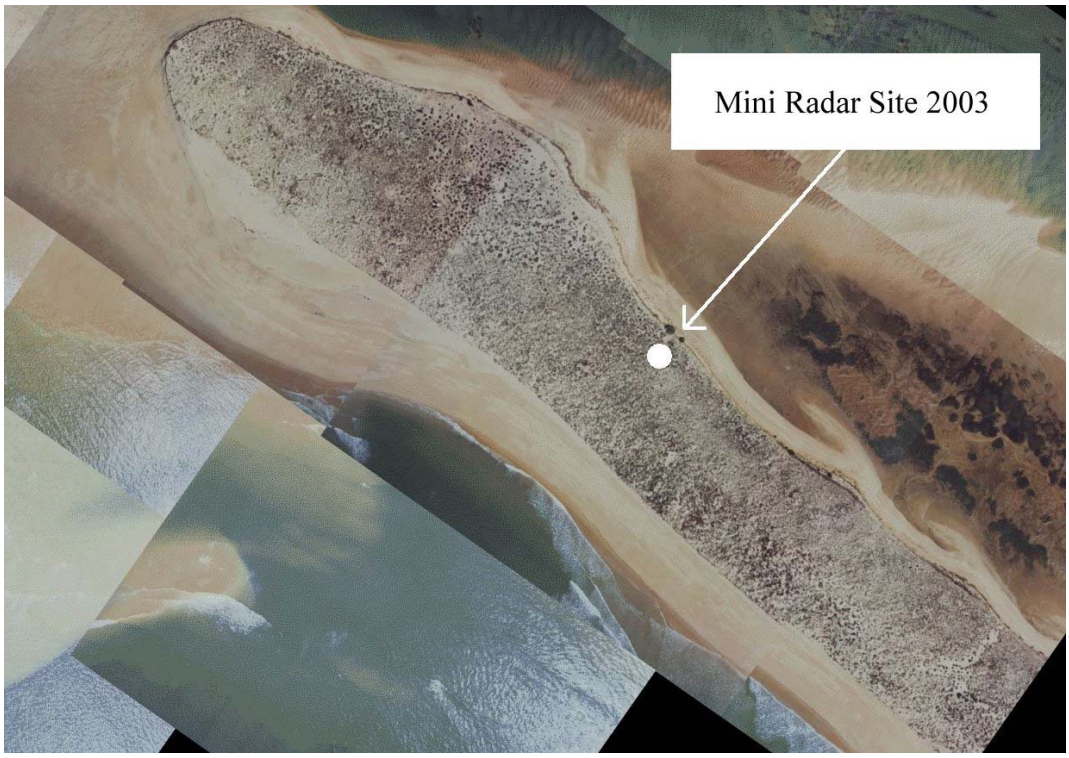

Figure 8.2.2 A close up of the vegetated dunes on Barreta Island in 1999. The approximate location of the mm wave radar during the 2003 overwash experiment is marked as the white dot.

Figure 8.2.3 A view from the remaining north-west end of Barreta Island looking south-east from the viewpoint marked on Figure 8.2.2 on the 19th February 2003 showing what remains of the barrier island as a narrow strip of sand with little or no vegetation remaining, and the beach subject to overwash by waves during high spring tides. The mm wave-radar is shown on the right of the image after being used to study overwash processes during the previous high tide.

The approximate location of the mm wave radar in 2003 and hence the viewpoint of the photograph in Figure 8.2.3 is shown as the white dot on the aerial photograph from 1999 shown in Figure 8.2.2.

8.3 Bathymetric Changes from 1999 to 2003

The change to the width of the island of Barreta illustrated in Figures 8.2.2 and 8.2.3 represents a significant level of erosion to take place in such a short period of time on what are thought to be relatively stable barrier islands (excluding inlet migration itself). Such a rate of erosion must have a cause, and this is almost certain to be related to the behaviour of the inlet. Clues to this may be sought within the radar derived bathymetries from the two years. To best exploit this data, it has been helpful to extract the bathymetric maps for as wide an area as possible in order to put any findings into context. With this aim in mind, radar data from both 1999 and 2003 were re-processed with a 64-pixel square maximum sub-image (480m square) to minimise errors and smooth the results at the furthest ranges. By enlarging the sub-image area, the bathymetries were effectively smoothed over the size of the sub-image, hence fine detail has been lost, but signals at the furthest ranges from the radar where the signals were weak have been optimised.

The bathymetries calculated in this way are shown in Figure 8.3.1 and 8.3.2 and are essentially smoothed versions of Figures 8.1.1 and 8.1.2. Besides the obvious migration of the inlet, these bathymetric maps show marked differences downdrift of the inlet. Comparing figures 8.3.1 and 8.3.2, the 5m contour appears in exactly the same place to the northwest (updrift) of the inlet. However, downdrift of the inlet to the south-east, the 5m contour in 2003 appears 150-200m closer to the shore than in 1999. If just the inlet had moved only a specific pattern of erosion and deposition could be expected – with erosion on the north-western flank of the ebb delta and deposition on the south-eastern flank.

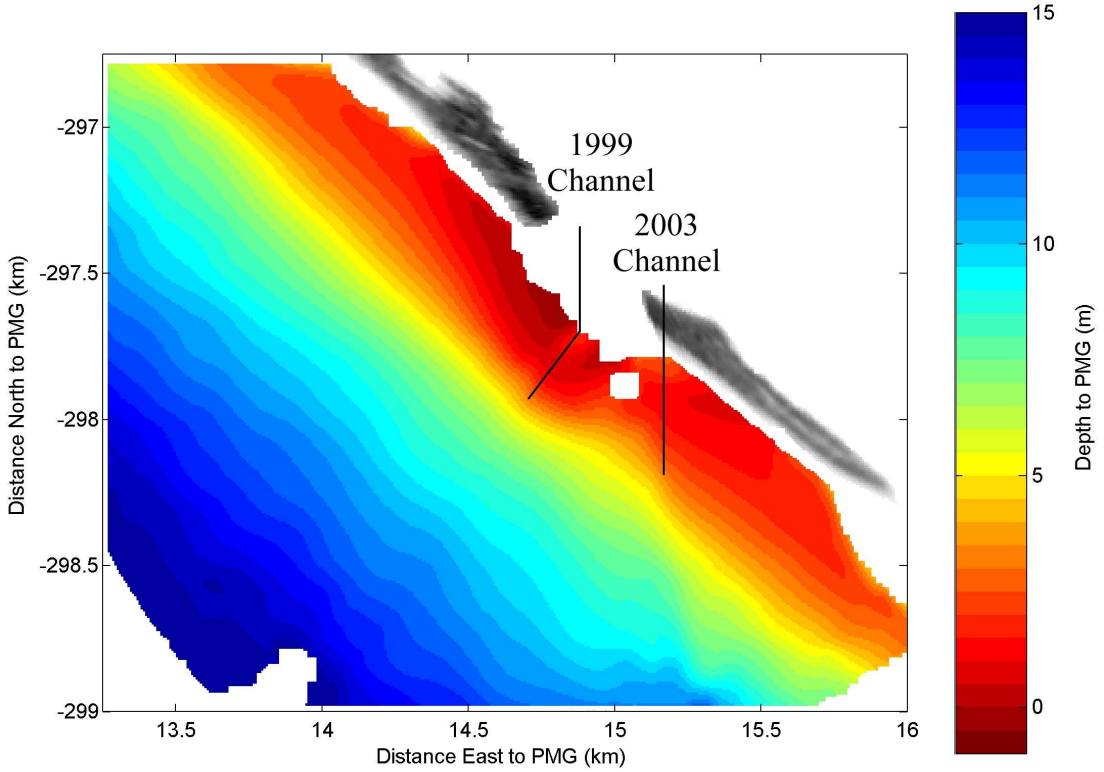

Figure 8.3.1 Radar derived 1999 bathymetry, re-processed to optimise the range of the bathymetry rather than fine detail.

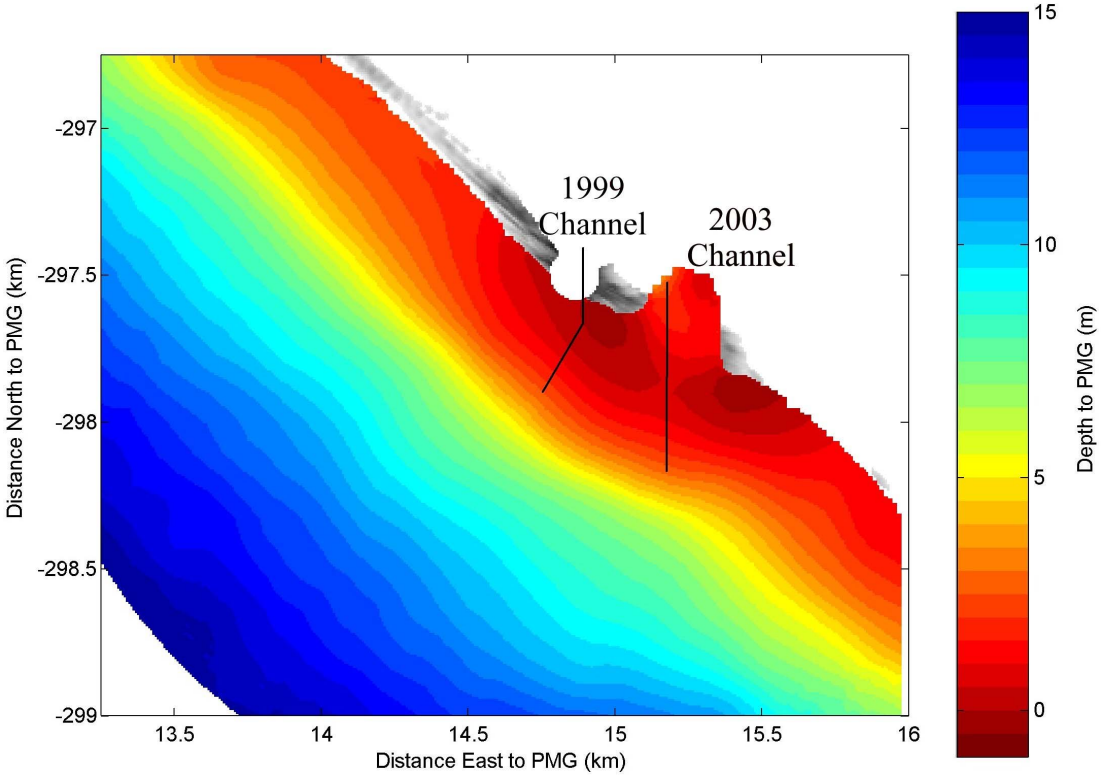

Figure 8.3.2 Radar derived 2003 bathymetry, re-processed to optimise the range of the bathymetry rather than fine detail.

These changes can be examined in more detail plotting the difference between the two bathymetries, illustrated in Figure 8.3.3. In this plot, height differences of less than +/-0.3m

have been ignored, as have any changes in water deeper than 12m – considered to be an artifact of the relatively poor quality of the data from 1999. The areas of erosion and deposition around the inlet itself in zone A are as might be expected with the inlet having migrated to the south-east. The associated movement of the ebb delta shows up as erosion to the northwest of the inlet, and deposition to the southeast. However, the extent of the ebb delta also appears have increased since 1999, with noticeable deposition on the ebb delta in zone B considerably seaward of zone A. This sediment would have been deposited by the jet of the ebb tide carrying a plume of sediment with it.

These ebb plumes often show up on the radar images as a pattern of roughened water, also visible by eye. An example of this is shown in the time averaged radar images shown in Figure 8.3.4, recorded during the INDIA project. Figure 8.3.4a was recorded during relatively slack water. In contrast, Figure 8.3.4b recorded only one hour later shows a strong sea surface roughness signature associated with the ebb tide plume. This plume can be seen to extend in excess of 1km from the inlet, the turbulence associated with this plume no doubt carrying significant quantities of sediment with it.

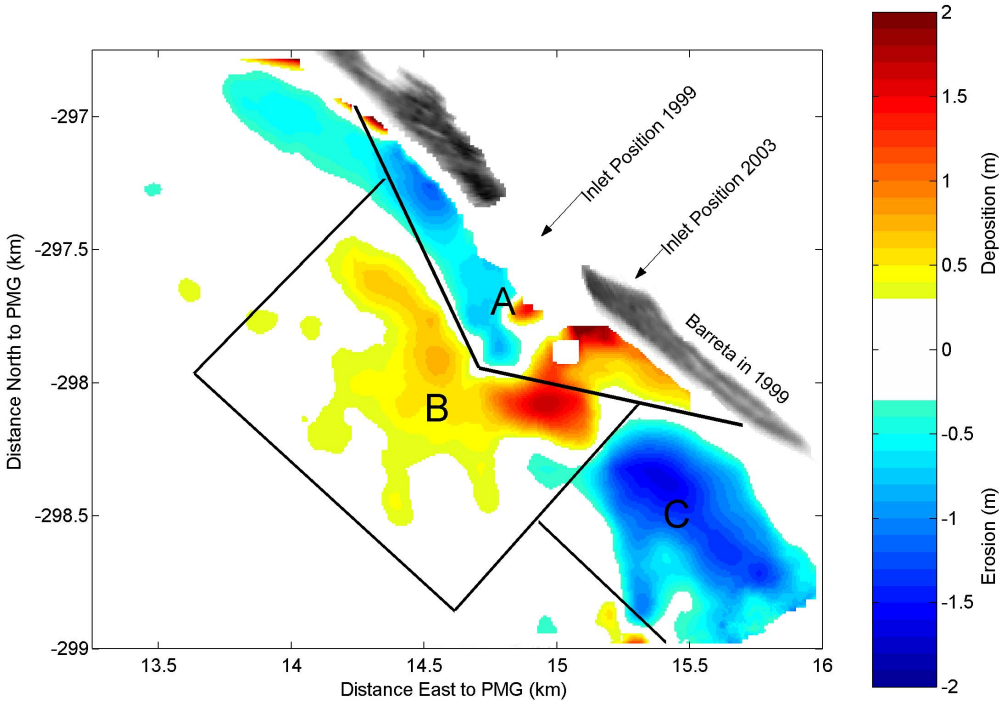

Figure 8.3.3 The difference between the radar derived bathymetries from 1999 and 2003 in the vicinity of the Ancao Inlet. The radar image of the dunes in 1999 is shown in greyscale. Zone A denotes the flanks of the ebb delta, zone B denotes the outer ebb delta and zone C denotes the area down-drift of the inlet.

In the presence of a fixed supply of sediment originating via longshore drift from the north-west, this additional deposition on the ebb delta must be balanced by a deficit of sediment elsewhere in the system – particularly if the deposition on the ebb delta is matched by deposition on the flood delta, out of view of the radar.

This sequestering of sediment to zone B of the ebb delta rather than the normal longshore drift is likely to be the cause of the large area of erosion in zone C extending approximately 600m offshore to the southeast of the inlet. Longshore drift has continued on the beaches of Barreta, but without the replenishing sand from the beaches to the north-west the net result has been the erosion of the beaches and regions directly offshore of the island. This loss of the beaches has allowed wave action and high tides to erode the dunes on Barreta with the results being clearly illustrated in the photograph of the island in Figure 8.2.3.

A rough estimate of the change in the volumes of sand involved may be determined by integrating the volumes changes contained in the three zones:

Zone A ~ -5000m^3

Zone B ~ +310,000m^3

Zone C ~ -450,000m^3

The amount of sand lost from zone C is likely to be an underestimate as the bathymetry calculated for 1999 does not extend as far shoreward as the 2003 bathymetry due to the narrowing of the island of Barreta in the intervening period.

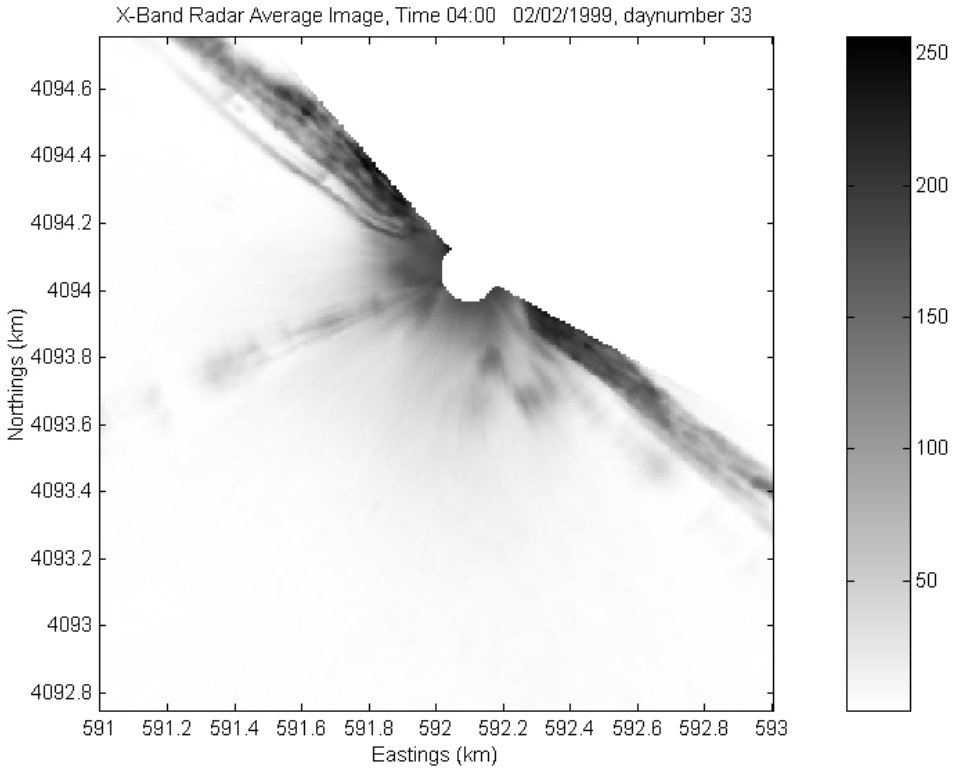

Figure 8.3.4a A time-averaged radar image of the Ancao inlet during the INDIA experiment just before the ebb tide early on the 2nd February 1999.

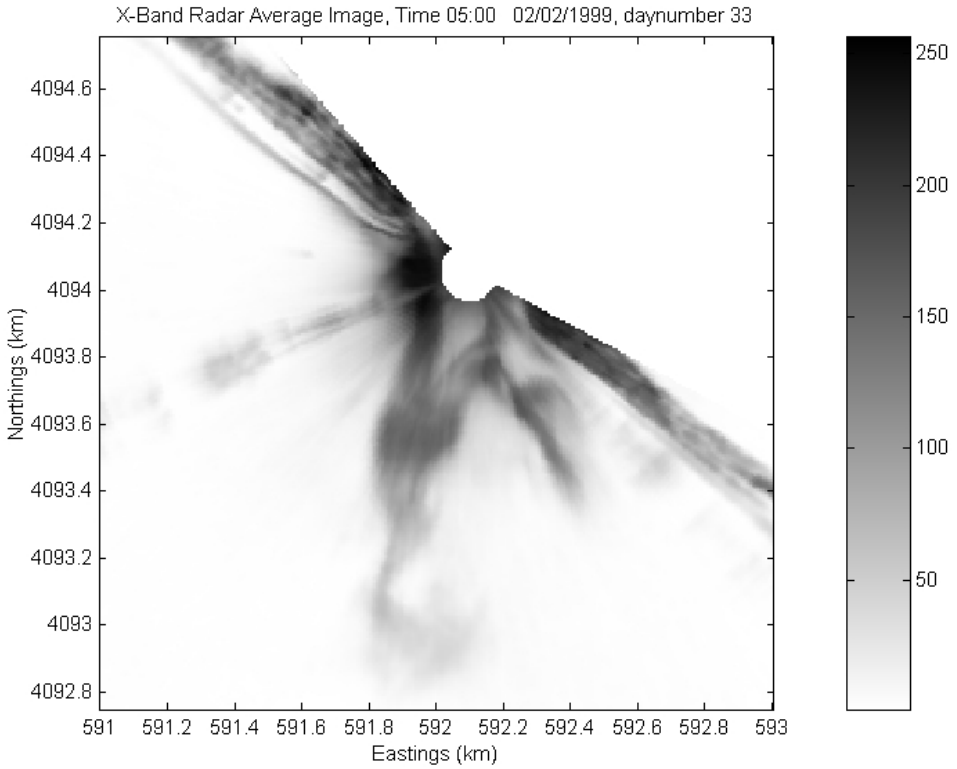

Figure 8.3.4b A time-averaged radar image of the Ancao inlet during the INDIA experiment during the peak of the ebb tide early on the 2nd February 1999, showing a strong sea surface roughness signature of the tidal plume extending more than 1km from the inlet.

While these figures must be treated with some caution, the overall pattern confirms that the triangular form of the main part of the ebb delta in zone A was largely sediment neutral as it migrated between 1999 and 2003, showing only a slight erosion of 5000m^3, a figure easily within the error level of this rough calculation. The erosion down-drift of the inlet in zone C of 450,000m^3 of sediment is not quite balanced by the deposition in zone B of 310,000m^3. However, if the deposition offshore in zone B is mirrored to a limited extent by deposition on the landward side of the inlet in the flood delta which was out of view of the radar, the total sediment budget would approximately balance. Researchers at the University of Algarve have commented that there is a significant and growing accumulation of sediment on the landward side of the inlet on the flood delta, but it is an area that is extremely difficult to survey due to the risk of beaching the survey boat.

It is possible to evaluate how reasonable these estimates are by comparing them to the net yearly input of sand to the inlet from longshore drift. Balouin & Howa (2002) used sediment tracer studies during the INDIA project to estimate the longshore drift of sand entering the inlet system from the north-west during the period of the experiment. The yearly longshore sediment transport was estimated to be 130,000m^3 based on those results. If this figure is multiplied by 4, it indicates a total longshore transport of sediment between 1999 and 2003 of 520,000m^3 in that time.

If the longshore drift estimate of Balouin & Howa is correct, the radar derived bathymetric changes suggest that the loss of 450,000m^3 of sediment from zone C represents in excess of 85% of the sediment entering the inlet system by longshore drift. The volume sequestered offshore of the ebb delta in zone B alone represents approximately 60% of the overall longshore drift during those 4 years.

These results demonstrate the efficiency with which this inlet has diverted sediment from the normal pattern of longshore drift. They also demonstrates the inevitability of the erosion of the island of Barreta, downdrift of the inlet, with a maximum of only 15% of the normal quantities of sediment arriving on Barreta to replenish the longshore drift taking sediment downdrift to the south-east. It is only a matter of time before the island is eroded enough to be breached, and the inlet position may not just migrate, but actually jump to a new position on this heavily eroded stretch of coast.

The erosion of the island of Barreta as a result of its location downdrift of the Ancao Inlet is not without precedent. The erosion of beaches downdrift of inlets is common around the world, an extreme case of which is illustrated by Shinnecock Inlet in the USA shown in Figure 8.3.5, in which the rock armouring of a tidal inlet has effectively stopped both the migration of the inlet and also the natural westerly flow of sediment down the coast, leading to severe erosion of the beach to the west of the inlet.

Figure 8.3.5 A photograph of Shinnecock Inlet in the USA in which the erosion of the beach downdrift (left) of the inlet is clear.

8.4 Relating Bathymetric Changes to Historical Inlet Behaviour

The erosion of Barreta and its offshore areas due to the sequestering of so much sediment by the inlet may help to explain the historical behaviour of similar previous inlets on this stretch of coast. Vila et al. (2002) showed that inlets on this particular stretch of coastline exhibit a very particular pattern of behaviour. Following the initial opening of an inlet there is a period of relative stability in which the inlets remains in approximately the same place for a few years. During this relatively stable period the inlet channel reaches dynamic equilibrium and the flood and ebb deltas develop. After this, the inlet has reached its mature stage and begins migrating east down the coast, accelerating as it goes. The period of initial stability coincides with the inlet being confined by what is initially the relatively wide expanse of Barreta Island. However, as sediment is gradually diverted away from its natural progression down the coast in favour of sequestration in the ebb (and possibly flood) delta, Barreta is gradually eroded away. The thinner that Barreta becomes, the less resistance it provides to the migration of the inlet, and so the migration of the inlet accelerates. Figure 8.4.1 illustrates the migration of the present and previous two inlets occupying this stretch of coast.

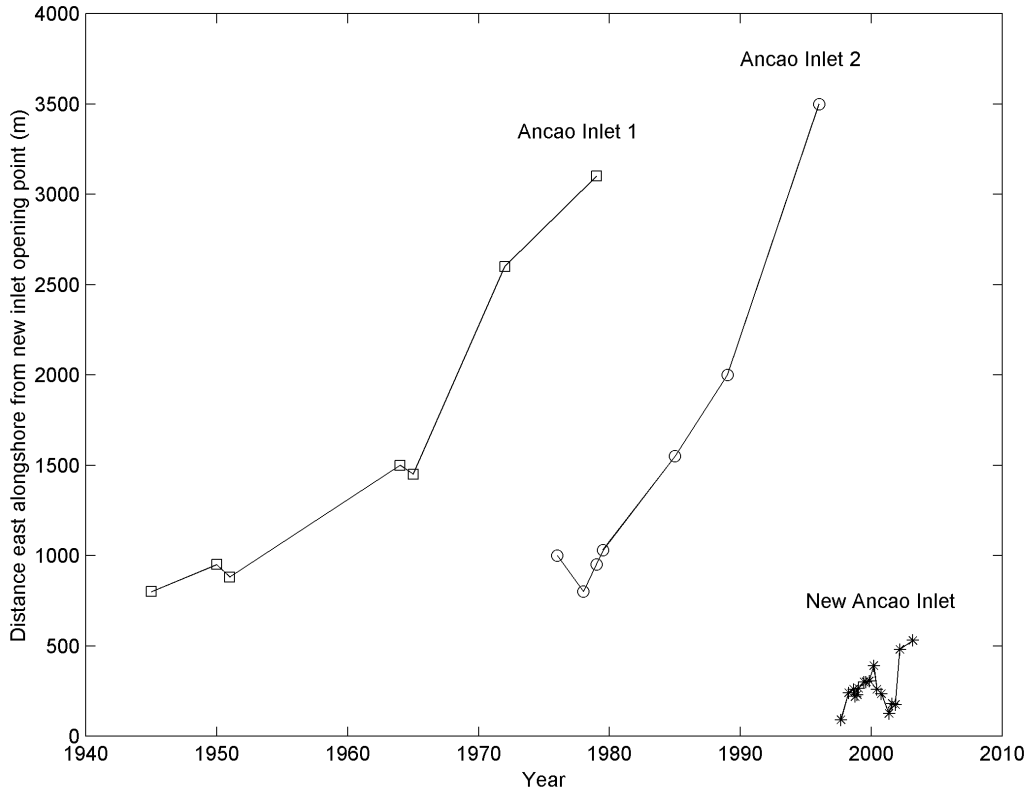

Figure 8.4.1 Historical inlet positions of the present and previous two Ancao inlets (based on plots in Vila et al., 2002 & 2003).

The present inlet was opened artificially in 1997 in a region of relatively high dunes for that part of the Ancao peninsula. This starting point for the new inlet lies approximately 800m west of the opening point of the previous two naturally opened inlets, implying that this part of the Ancao peninsula had experienced at least 50 years of dune growth without being disturbed and re-worked by the passage of successive inlets. The stability of the barrier island at this point may have contributed to the inlet having migrated only about 300m east since its opening in 1997. These relatively high dunes are still being eroded away but much of the older area of dunes comprising the westernmost tip of Barreta have now gone. By the time of the experiment in 2003, the inlet had less than 200m of the old dunes to erode before the lower elevation region shown in Figure 8.2.3 would be reached. This area is actually the start of the track of the previous two inlets, and what vegetation was visible in the 1999 photograph in Figure 8.2.2 had disappeared along with most of the width of the island, as described already. Once the inlet has reached this part of Barreta, it could be expected that the inlet migration would accelerate considerably, the thin strip of sand remaining by 2003 presenting little in the way of resistance to the progress of the inlet.

This would be an excellent time for a further visit to the site with the X-band radar system to observe the anticipated rapid migration phase.

Chapter 9: Conclusions

9.1 Summary & Discussion

It has been demonstrated that given sufficient knowledge of the behaviour of surface waves in shallow coastal regions using remotely sensed radar data, it is possible to map the underlying water depth. The study used two types of radar: X-band (9.8 GHz); and mm wave (77 GHz), to produce image sequences of waves at two different resolutions. X-band radar can image both breaking and non-breaking waves up to 5 km from the radar, and the recording system digitised these images with a radial resolution of 7.5 m to a range of 2 km from the radar. The mm wave radar operates at a much higher frequency and images only steep or breaking waves. The recording system for that radar was able to digitise with a radial resolution of 0.5 m to a range of 230 m from the radar. The X-band radar cannot produce images of waves in low wave conditions and so its use is limited to wave events for this application. However, this should not be viewed as a restriction, since changes in beach morphology and offshore bathymetry are often imperceptible in low wave conditions. The mm wave radar has been observed in the field to detect return signals only from breaking or near breaking waves, so its use is limited to the surf and swash zone.

The raw image sequences recorded by these radars take the form of a plan view movie of the sea surface. Initially a cross correlation technique was developed to track the motion of small sub-sections of the wave patterns in X-band radar image sequences recorded at Holderness in 1995 and hence determine average wave celerity maps. The spectral peak of the image spectrum was used to estimate the wave period and a depth inversion based on linear wave theory yielded an estimated bathymetric map of the Holderness study area. Unfortunately, the absence of a corresponding bathymetric survey meant that the accuracy of the radar derived bathymetric map could not be verified at that site. However, variations in the radar derived water depths along a line of pixels located 300 m offshore showed a tidal signal of approximately the correct magnitude and phase, lending confidence to the absolute depth estimates.

The uncertainty in exactly what wave celerity and period was derived from images containing a whole spectrum of waves led to the development of algorithms to work with individual wave frequencies. By applying a Fast Fourier Transform (FFT) to each pixel time series in a radar image sequence, it is possible to isolate individual wave frequencies and plot

plan views of the waves at those frequencies from the complex Fourier coefficients, provided there are waves present at that frequency. A number of techniques were developed to map the wavelengths in these single frequency 'Fourier layers'.

A technique using the radon transform was developed which identified the wave direction of small sub-sections of the single frequency wave images, typically of sizes 240 m x 240 m. This reduced the problem of identifying a 2D waveform to one of identifying a 1D waveform. This was later replaced by a more computationally efficient algorithm that uses a 2D FFT on the single frequency image sub-sections to identify the approximately spectral peak, and then converges on the exact spectral peak, yielding the wavelength, direction and phase of the strongest wave signal in the image subsection. This new algorithm proved almost 100 times faster than the radon transform algorithm; 1000 cycles took approximately 10 seconds to identify a complex 2D sinusoidal waveform in a 16 x 16 pixel matrix to an accuracy of 0.001 pixels. For comparison, to achieve ~0.05 pixel accuracy by zero padding the 16 x 16 pixel data to 2048 x 2048 and applying a 2D FFT would take almost 2 hours to execute 1000 times on the same machine.

Using this algorithm to identify the wavelengths in the 2D image sub-sections at a range of wave frequencies yields a series of wavelength estimates against wave frequency to which a water depth can be fitted to the data in a least squares sense. This process is repeated at intervals across the area covered by the radar data, hence building up a map of water depths.

In order to relate the wavelengths, wave frequencies and wave heights to water depth a range of wave dispersion equations were tested against predictions from Fenton's stream functions, which are numerically derived solutions to the wave equations for monochromatic waves involving high order Fourier series and are considered as the best approach to use where accuracy is the principal requirement. Linear wave theory, which neglects amplitude dispersion of waves, was shown to significantly under predict the wavelength in shallow water compared to the stream function predictions. Amongst the equations tested were a number of engineering approximations to the analytically derived non-linear wave theories which do account for amplitude dispersion. These approximate equations are significantly easier to use than the theories on which they are based and hence are implemented in many wave models. One of the simplest of these is an equation described by Hedges' (1976) (equation 2.6.1) which uses a correction to linear theory based on a function (Z) of the waveheight. It was shown in section 6.2 that using $Z = 0.5H$ gave a good approximation to

Fenton's stream function predictions for monochromatic waves. This approach assumes that the waves are homogeneous within the individual image sub-sections used to determine the wavelength, which is almost certainly not the case in coastal waters. However, provided the bathymetry is smoothly varying within the image sub-sections, the mean value of water depth generated for that subsection should be an acceptable measure for the depth. Situations which will cause a problem to the analysis would be characterized by rapidly changing bathymetry such as sandbanks with dimensions less than the size of the analysis sub-image areas. In such cases the average water depth calculated for the sub-image area would not adequately resolve the bathymetric features. A potential source of error that has been neglected in this work is the influence of currents on the waves, which would introduce a Doppler shift to the waves and hence cause errors in the calculated water depths. In order to minimize the impact of tidal currents in this respect, the results from a series of radar records at different stages of the tide were averaged in each case.

A set of radar data recorded in Faro, Portugal in 2002 during a storm, using both radars operating simultaneously, were processed using the Fourier transform based technique together with Hedges' dispersion equation to produce a set of water depth maps at different stages of the tide. The study area was characterized by a long straight beach with smooth shore-parallel isobaths. The mm wave radar data were processed using image subsection sizes of 32 m square and values of $Z = 0.5H_S$, $Z = 0.4H_S$ and $Z = 0$ in the dispersion equation. The offshore significant waveheight measured by a Waverider buoy during this experiment was approximately 2 m. These results were compared with a set of closely spaced cross shore transects surveyed using conventional techniques. The survey transects ran from the beach out to a distance of 1.5 km from the shore to around the 14 m depth contour. Linear theory, i.e. $Z = 0$, led to an over prediction of water depth, particularly noticeable in the shallowest regions by a mean offset of 0.8 m. Setting $Z = 0.5H_S$ led to an under prediction of approximately 0.2 m, while $Z = 0.4H_S$ reduced this offset to a slight under prediction of the water depth by 0.06 m. The standard deviation of the scatter about the mean offset was an average of 0.19 m, and this scatter was only slightly changed by the varying Z parameter.

The X-band radar from the same experiment was then processed using a similar analysis but with a larger image subsection size of 240 m square due to the lower resolution of that radar and to allow at least one wavelength of the longer waves found further offshore to be encompassed by the image sub-sections. The mean offset produced by the depth inversion

based on linear wave theory gave an over prediction in water depth of 0.62 m, and an average standard deviation of 0.39 m. The non-linear inversion using $Z = 0.4H_S$ reduced this offset on average to a slight under prediction of the water depth by 0.1 m. The standard deviation about the mean was reduced on average to 0.3 m.

These results compare well with work by Holland (2001) using video image sequences of waves in the breaker zone which suggested that for real world spectral waves in the shallow water limit at that particular site, setting $Z = 0.4H_S$ yielded an accurate relationship between wave period, length, significant wave height and water depth.

The analysis was also tested on data collected during the 1999 COAST3D project at Teignmouth on the south west coast of England. The area chosen for the comparisons was again characterized by smoothly varying bathymetry. The problem of rapidly changing bathymetry will be a topic for future work. A series of 11 hourly X-band radar records from a wave event were processed using the same technique and the results compared to a survey that extended 1km from the shore to a maximum water depth of 7 m to chart datum. The significant wave height in this case varied between 1.25 m and 1.5 m during the wave event and was recorded within the survey area rather than from an offshore site as was the case in the Faro experiment. Linear wave theory yielded an over prediction of the water depths by a mean offset of 0.5 m. However, the use of $Z = 0.4H_S$ generated an over-correction of the water depth, leading to an under prediction of the water depth. As a result, the Z parameter was adjusted to $Z = 0.3H_S$ which reduced the mean offset a slight under prediction of 0.07 m. The average standard deviation of the scatter for the individual records was 0.32 m and 0.23 m for linear and non-linear equations respectively.

When a number of the individual Teignmouth water depth maps calculated in this manner had the tide level removed and were averaged, the resulting bathymetric map had a mean offset of -0.07 m, i.e. a slight under prediction of the water depth, and the standard deviation of the scatter was 0.21 m.

The need to reduce the influence of the waveheight parameter when processing the Teignmouth data is a cause of some concern, but may be due to the location of the wave measurement used. The significant waveheight used for the Faro data was recorded several kilometers offshore in 20-25 m of water. At Teignmouth the significant waveheight was recorded in much shallower water of no more than 7 m and within 1 km of the shore. Even

with setting $Z = 0.4H_S$, the water depths recorded at Faro show a slight over correction by the non-linear equation, suggesting that the Z parameter should be slightly smaller again. The theoretical comparisons of Equation 2.6.1 in section 2.6 assumed monochromatic waves. However, the significant waveheight of spectral seas represents a somewhat larger waveheight than this. The significant waveheight is related to the root mean square (RMS) water surface profile by the equation: $H_S = 4\eta_{RMS}$. This implies that the significant waveheight can be related to the equivalent monochromatic waveheight corresponding to the RMS water surface profile by:

$$H_{monochromatic} = \frac{2H_S}{4}\sqrt{2} = \frac{H_S}{\sqrt{2}}$$

Hence it might be expected that the Z parameter in Hedges equation when applied to spectral waves should actually be $Z = 0.5H_{monochromatic} = 0.35H_S$.

The spatial averaging due to the finite size of the sub-image areas used to determine the wavelengths will inevitably lead to a certain level of scatter in the data when compared to conventional surveys performed at higher spatial resolutions. However, this spatial averaging should not affect the ability of the technique to determine overall volume changes in areas of changing bathymetry.

The Faro series of deployments of the radars provided the raw data needed to quantify the previously unrecorded large scale bathymetric changes contributing to the natural migration of a tidal inlet through the barrier islands of the Ria Formosa region of the Algarve in Portugal. The sequestration of sediment on the ebb delta and the consequent deficit of sediment that developed down drift of the inlet following its opening in 1997 allowed the down drift barrier island of Barreta to be gradually eroded in the 4 years between the 1999 INDIA experiment and the 2003 return visit. This is backed up by photographic evidence of the substantial loss in width of Barreta, and also helps to explain the results of Vila et al. (2003), which indicated that the migration of previous inlets on that stretch of coast tended to accelerate following an initial period of relative stability. The erosion of Barreta Island to a thin strip of sand must present little resistance to the migration of the inlet, and hence as more of the width of the island is eroded, the faster the inlet is likely to migrate. An estimate of the annual longshore drift rate, determined from sediment tracer studies during the INDIA project, combined with the bathymetric maps generated using radar data suggest that in excess of 85% of the longshore sand transport has been diverted to the flood and ebb deltas, and explains the observed dramatic erosion of Barreta.

The observation of the erosion of the beaches downdrift from the eroding tip of the island of Barreta has not been documented in any prior work due to its inaccessibility and the difficult conditions for conventional surveying, and was only possibly in this study due to the ability of the radar to produce remote images of the sea surface from safer, more accessible locations. This advantage of radar will continue to be exploited in a range of future studies. It is noted also that the all-weather, day and night operational capability of radar systems gives them certain advantages over visual techniques currently used by the coastal research community.

The development of this technique has provided the means to observe bathymetric changes at relatively low cost and effort over a wide area by carrying out repeat deployments of the radar over a number of years. At the time of writing, a new marine radar can be purchased for around £9k and somewhat cheaper if bought second hand. A low cost recording system has now been developed that costs approximately £5k for the hardware involved. A typical single survey of a similar area to that viewable by marine radar could be expected to cost at least this amount and probably more.

9.2 Further Work

During this study a great deal has been learned about how to get the best out of radar systems. Following almost 12 years of deployments in harsh environments the X-band radar recording system is no longer sufficiently reliable for use due to its age. A new radar recorder has now been developed by the author for future experiments, and will allow long time-series of radar images to be collected at longer ranges than the old system. While commercially available systems exist, their cost is prohibitive. The new recorder has been developed using off-the-shelf components at a cost that will make the use of radar accessible to interested research group.

With the ability to collect data without the various uncertainties of the old recording system, several areas of work immediately suggest themselves:

It was noted that the correction for wave height in the wave dispersion equation used for the depth inversions appears to vary, probably depending on wave conditions and the location of the wave recorder. The data from the mini-radar may already be sufficient to study the

possible frequency dependence of the wave height correction in breaking waves, while the collection of longer time series of X-band radar images from a number of sites should provide more insight into the performance of the various wave dispersion equations across the range of wave frequencies for non-breaking waves in slightly deeper water. The use of a single value of the significant wave height is possibly also over simplistic, but has been shown here to be sufficient for most purposes. It would be interesting to investigate the use of the individual spectral amplitudes on each wave frequency to see if more accurate water depths inversions resulted.

It is also known that the Doppler shift of the waves under the influence of currents can be picked up on the radar. The accuracy and resolution possible in determining these currents requires further study, but should provide further insights into nearshore processes, particularly in the region of tidal inlets, and, in the case of the mini-radar, rip cells.

Once confidence has been gained in the wave and current measurements obtained using these systems, it may be possible to use them to 'drive' sediment around the area viewed by the radar, providing real forcing to sediment transport models.

Another feature that may be observed in the frequency breakdowns of radar image sequences are the sea surface signatures of edge waves and/or infragravity waves – long period waves bound to the coast and related to wave groups. The small variations in water level generated by these long period waves would manifest themselves in the radar data as a modulation in the onset of wave breaking close to the shore, hence small variations in water depth caused by the edge waves could lead to a large and measurable signal in the radar data at the period of the long waves. There is some indication of large scale coherent signals that match this description in the longer period parts of the radar image breakdowns of some radar datasets such as can be seen close to the shore in the longest period single frequency images in Figure 5.2.1a. However, the duration of these early radar records is relatively short compared to the expected period of these long period waves and so these observations are tentative at present. The new generation of radar recorders will be able to collect the longer time series required to adequately resolve the radar signatures of long period infragravity waves if they are present. It would also be interesting to deploy systems to monitor the levels of suspended sediment in locations where these edge waves were observed on the radar data and measure any effects caused by the variation in wave breaking.

Another goal will be to try and improve the resolution of the techniques developed here to allow the detection of rapid local variations in water depth, without the large spatial averaging that is currently involved. However, as was discussed in section 5.4, the author is of the opinion that the ultimate limit of resolution of this bathymetric inversion technique is related to the wavelength of the waves whose interactions with the sea bed are effectively 'illuminating' the topographic features of the bed.

At the time of writing, the new radar recording system developed by the author has been successfully deployed for several months at Cassino Beach in southern Brazil, and a 2 year deployment is planned for the forthcoming EPSRC funded LEACOAST2 project at Sea Palling in East Anglia in the UK to study the hydrodynamics of the waters around a series of offshore breakwaters. A radar station with a WAMOS recording system has also been set up on Hilbre Island in the Dee Estuary near the Proudman Oceanographic Laboratory to study the behaviour of the sandbanks around the mouth of the estuary. This station is expected to go online in late 2005.

Although the present study has achieved success in the remote measurement of bathymetry and in the understanding of some coastal processes, it is felt that there is a great deal of information still contained in radar images of waves. Further work is required to unlock this potential and to disseminate the technology to the marine and coastal research community.

References

Airy, G.B., 1845, "Tides and waves". Encyclopaedia Metropolitana.

Bacon, Sir R., 1932, "The concise story of the Dover Patrol". London.

Balouin, Y. & Howa, H., 2002, "Sediment transport pattern at the Barra Nova inlet, south Portugal: a conceptual model". Geo-Marine Letters 21, 226-235.

Barrick, D.E., Headrick, J.M., Bogle, R.W. & Crombie D.D., 1974, "Sea backscatter at HF: Interpretation and utilization of the echo". Proc. IEEE, 62, 673-680.

Bascom, W., 1959, "Ocean Waves". 45-55 in "Oceanography: readings from Scientific American", edited by J. Robert Moore, San Francisco, California, W H Freeman & Co. 1971.

Bascom, W., 1964, "Waves and beaches". Anchor Books Doubleday & Company, Inc. Garden City, New York. 267pp.

Bell, P.S., 1995, "Routine X-band monitoring of nearshore wave climate". Oceans '95 Proceedings: Challenges of our changing global environment, San Diego, California, October 9-11, Vol 1, 520-525.

Bell, P.S., Hardcastle, P.J., Harrison, A.J., Humphery, J.D., 1997, "Instrumentation at Holderness". 7th International Conference on Electronic Engineering in Oceanography, Southampton Oceanography Centre, 23-25 June 1997,

Bell P.S., 1998, "Bathymetry derived from an analysis of X-band marine radar images of waves". Oceanology International 98: The global ocean, held 10-13 March 1998, Brighton, U.K., Vol. 3, 535-543.

Bell, P.S., 1999, Shallow water bathymetry derived from an analysis of X-band marine radar images of waves, Coastal Engineering, 37, 3-4, 513-527.

Bell, P.S., 2001, "Determination of bathymetry using marine radar images of waves". Proceedings of The Fourth International Symposium on Ocean Wave Measurement and Analysis, September 2-6, 2001, San Francisco, California.

Bell, P. S., Williams, J. J., Clark, S., Morris, B. D. & Vila Concejo, A., 2005, "Nested radar systems for remote coastal observations". Journal of Coastal Research, SI 39, and presented at the International Coastal Symposium, Brazil, 2004, (in press).

Booij, N., 1981, "Gravity waves on water with non-uniform depth and current". Rep. No.81-1, Dept. Civ. Eng., Delft University of Technology.

Borgman, L.E. & Petrakos, M., 1986, "The DSFWAV software package". The University of Wyoming website, Laramie, Wyoming, http://faculty.gg.uwyo.edu/borgman/DSF/

Boussinesq, J. 1871, "Theorie de L'intumescence Liquide Appelee Onde Solitaire ou de Translation se Propageant dans un Canal Rectangulaire," *Comptes Rendus Acad. Sci. Paris,* Vol 72, pp 755-759.

Carr, A.P., Hardcastle, P.J. & Blackley, M.W.L., 1977, "Swansea Bay (Sker) Project. Progress report for the period August 1976 to July 1977". Institute of Oceanographic Sciences, Taunton, Rep. No. 48/77, 32pp.

Chaplin, J.R., 1980, "Development of stream function wave theory". Coastal Eng., 3, 179-205.

Chappelear, J.E., 1961, "Direct numerical calculation of wave properties". J. Geophys. Res., 66, 501-508.

Copeland, A.C., Ravichandran, G & Trivedi, M.M., 1995, "Localized radon transform-based detection of ship wakes in SAR images". IEEE Transactions on Geoscience and Remote Sensing, 33, 1, 35-45.

Crombie, D.D., 1955, "Doppler spectrum of sea echo at 13.56MC/s". Nature, 175, 681-682.

Dean, R.G., 1965, "Stream function representation of nonlinear ocean waves". J. Geophys. Res., 70, 4561-4572.

Dingemans, M.W., 1997, "Water wave propagation over uneven bottoms". World Scientific Publishing Co. Pte. Ltd., 967pp.

Dugan, J.P., Fetzer, G.J., Bowden, J., Farrugia, G.J., Williams, J.Z., Piotrowski, C.C., Vierra, K., Campion, D. & Sitter, D.N., 2001a, "Airborne optical system for remote sensing of ocean waves". American Meteorological Society, July, 1267-1276.

Dugan, J.P., Piotrowski, C.C. & Williams, J.Z., 2001b, "Water depth and surface current retrievals from airborne optical measurements of surface gravity wave dispersion". J. Geophys. Res., 106, C8, 16903-16915.

Dugan, J.P. & Piotrowski, C.C., 2003. "Surface current measurements using airborne visible image time series". Remote Sensing of Environment, 84, 309-319.

Ebersole, B.A., 1987, "Measurement and prediction of wave height decay in the surf zone". Proceedings of Coastal Hydrodynamics, American Society of Civil Engineers, 1-16.

Eckart, C., 1952, "The propagation of gravity waves from deep to shallow water". Natl. Bur. Standards, Circular 521, Washington, D.C., 165-173.

Fenton, J.D. 1979, "A high-order cnoidal wave theory". J. Fluid Mech., 94, 129-161.

Fenton, J.D. & Gardiner-Garden, R.S., 1982, "Rapidly-convergent methods for evaluating elliptic integrals and theta and elliptic functions". J. Austral. Math. Soc. B, 24, 47-58.

Fenton, J.D., 1985, "A fifth-order Stokes theory for steady waves". J. Waterw. Ports Coastal Ocean Eng. ASCE, 111, 216-234.

Fenton, J.D., 1988, "The numerical solution of steady water wave problems". Computers and Geosciences, 14, 357-368.

Fenton, J.D. & McKee W.D., 1990, "On calculating the lengths of water waves". Coastal Eng., 14, 499-513.

Fenton, J.D., 1990, "Nonlinear wave theories". In: B. Le Mehaute and D.M.Hanes (Editors), The Sea, Vol 9, Ocean Engineering Science, Wiley, New York, N.Y.

Guinard, N.W., Ransone Jr, J.T., and Daley, J.C. 1971, "Variation of NRCS of the sea with increasing roughness". J.Geophys. Res, 76, 1525-1538.

Hart, C.A. and Miskin, E.A., 1945, "Developments in the method of determination of beach gradients by wave velocities". Air survey research paper no. 15, Directorate of Military Survey, UK War Office. (N.B. an original copy of this may be found at the British Library)

Heathershaw, A.D., Blackley, M.W.L. & Hardcastle, P.J., 1980, "Wave direction estimates in coastal waters using radar". Coastal Engineering, 3, 249-267.

Hedges, T.S., 1976, "An empirical modification to linear wave theory". Proc. Inst. Civ. Eng., 61, 575-579.

Hedges, T.S., 1987, "Discussion: An approximate model for nonlinear dispersion in monochromatic wave propagation models, by J.T.Kirby and R.A.Dalrymple", Coastal Eng, 11, 87-89.

Hessner, K., Reichert, K. and Rosenthal, W., 1999, Mapping of sea bottom topography in shallow seas by using a nautical radar. 2nd Symposium on Operationalization of Remote Sensing, ITC, Enschede, Netherlands, 16-20 August 1999.

Holland, T.K., Holman, R.A., Lippmann, T.C., Stanley, J. & Plant, N., 1997, "Practical use of video imagery in nearshore oceanographic field studies". IEEE J. Oceanic Eng. 22, 81-92.

Holland, T.K., 2001, "Application of the linear dispersion relation with respect to depth inversion and remotely sensed imagery". IEEE Trans. Geos. & Remote Sensing, 39, 2060-2072.

Hollmann, H. E., 1935, "Modulation-controlled magnetron oscillation". US Patent number 2090571.

Hoogeboom, P. & Rosenthal, W., 1982, "Directional wave spectra in radar images". Proceedings of IGARSS 82 International Geoscience and Remote Sensing Symposium, Munich, 1-4 June 1982, IEEE New York, Vol. 2, 5.1-5.3.

Hoogeboom, P., Kleijweg, J.C.M. & van Halsema, D., 1986, "Seawave measurement using a ship's radar". Proc. IGARSS '86 Symposium, Zurich, 819-823.

HR Wallingford, 2000, "Wave recording at Teignmouth. Report covering period 28 October to 22 November 1999". HR Wallingford Report EX 4132.

Hunt, J.N., 1979, "Direct solution of wave dispersion equation". J. Waterw. Ports Coastal Ocean Eng. Div., ASCE, 105, 457-459.

Hunter, J.K., and Vanden-Broeck, J.-M., 1983, "Accurate computations for steep solitary waves". J.Fluid Mech., 136, 63-71.

Janssen, P., 2004, "The interaction of ocean waves and wind". Cambridge University Press, 300pp.

Kalmykov, A.I. and Pustovoytenko, V.V., 1976, "On polarisation features of radar signals scattered from the sea surface at small grazing angles". J. Geophys. Res., 81, 12, 1960-1964.

Keller, W.C., Jessup, A.T., Melville, W.K., 1990, Measurements of Sea Spikes in Microwave Backscatter at Moderate Incidence. J. Geophys. Res., 90 (C6), 9679-9688.

Kenyon, K.E., 1998, "Capillary waves understood by an elementary method". Journal of Oceanography, 54, 384-346.

Khandekar, M.L. 1989, "Operational analysis and prediction of ocean wind waves". Springer-Verlag, 214pp.

Kirby, J.T. & Dalrymple, R.A., 1986, "An approximate model for nonlinear dispersion in monochromatic wave propagation models". Coastal Eng., 9, 545-561.

Kirby, J.T. & Dalrymple, R.A., 1987, "Discussion reply: An approximate model for nonlinear dispersion in monochromatic wave propagation models". Coastal Eng., 11, 89-92.

Korteweg, D.J. & De Vries, G., 1895, "On the change in form of long waves advancing in a rectangular canal, and on a new type of long stationary wave". Phil. Mag. 5th Series, 39, 422-443.

Krogstad, H.E., 2005, "The directional wave spectrum". Part of "Measuring and analysing the directional spectrum of ocean waves", edited by Daniele Hauser, Kimmo Kahma, Harold E. Krogstad, Susanne Lehner, Jaak A.J.Monbaliu & Lucy R. Wyatt, European COST Action 714, 15-54.

Lee, P.H.Y., 1977, "Doppler measurements of the effects of gravity waves on wind-generated ripples". J.Fluid Mech., 8(2) 255-240.

Lenau, C.W., 1966, "The solitary wave of maximum amplitude". J. Fluid Mech., 26, 309-320.

Lippmann, T.C. & Holman R.A., 1989, "Quantification of sand bar morphology: a video technique based on wave dissipation". J. Geophys. Res., 94, C1, 995-1011.

Lippmann, T.C. & Holman R.A., 1990, "The spatial and temporal variability of sand bar morphology". J. Geophys. Res., 95, C7, 11575-11590.

Mason, M.A. & Hall, W.C, 1941, "A study of progressive waves". Technical Report No.1, Beach erosion Board, U.S. Army Corps of Engineers, Washington, 39pp.

McLaughlin, D.J., Allan, N., Twarog, E.M., Trizna, D.B., 1995, High Resolution Polarimetric Radar Scattering Measurements of Low Grazing Angle Sea Clutter. IEEE J. of Oceanic Engineering, 20, 3, 166-178.

Miche, M., 1951, "Le Pouvoir Reflechissant des Ouvrages Maritimes Exposes a l' Action de la Houle". Annals des Ponts et Chaussess, 121, 285-319.

Miles, J.W., 1957, "On the generation of surface waves by shear flows". Journal of Fluid Mechanics, 3, 185-204.

Morris, B.D., Davidson M.A. & Huntley D.A., 2001, "Measurements of the response of a coastal inlet using video monitoring techniques". Marine Geology 175, 251-272.

Morris, B.D., Davidson M.A. & Huntley D.A., 2004, "Estimates of the seasonal morphological evolution of the Barra Nova Inlet using video techniques". Continental Shelf Research 24, 263-278.

Munk, W.H., Miller, G.R., Snodgrass, F.E., and Barber, N.F., 1963, "Directional recording of swell from distant storms." Philosophical Transactions Royal Society of London 255 (1062): 505-584.

Nieto Borge, J.C. & Reichert, K., 2005, "The marine radar". Part of "Measuring and analysing the directional spectrum of ocean waves", edited by Daniele Hauser, Kimmo Kahma, Harold E. Krogstad, Susanne Lehner, Jaak A.J.Monbaliu & Lucy R. Wyatt, European COST Action 714, 128-137.

Nwogu, O, 1993, "Alternative form of Boussinesq equations for nearshore wave propagation". J. Waterw. Ports Coastal Ocean Eng. Div., ASCE, 119, 6, 618-638.

Oudshoorn, H.M., 1961, "The use of radar in hydrodynamic surveying". Proc. 7th Conf. Coastal Eng., The Hague, Netherlands, 59-76.

Peregrine, D.H., 1976, "Interaction of water waves and currents". Advances in Applied Mechanics, 16, 9-117.

Phillips, O.M., 1957, "On the generation of waves by turbulent wind", Journal of Fluid Mechanics, 2, 417-445.

Pilkey Jr, O.H., Neal, W.J., Monteiro, J.H., & Dias, J.A., 1989, Algarve barrier islands: a non coastal plain system in portugal. Journal of Coastal Research, 5(2), 239-261.

Piotrowski, C.C. & Dugan, J.P., 2002, "Accuracy of bathymetry and current retrievals from airborne optical time-series imaging of shoaling waves". IEEE Trans. On Geoscience & Remote Sensing, 40, 12, 2606-2618.

Prandle, D., Ballard, G., Banaszek, A.D., Bell, P., Flatt, D., Hardcastle, P.J., Harrison, A., Humphery, J. D., Holdaway, G., Lane, A., Player, Rose J., Williams, J. J., Wolf, J., 1996, "The Holderness coastal experiment '93-'96". Proudman Oceanographic Laboratory, Report 44, 48pp.

Press, W.H., Teukolsky, S.A., Vetterling, W.T. & Flannery, B.P., 1992, "Numerical Recipes in C – The Art of Scientific Computing". Second edition, Cambridge University Press, 994pp.

Proctor, R. & Wolf, J. 1990, "Surface wave measurements using a ship's radar in the southern North Sea". Abstract of paper presented at 15th General Assembly of the European Geophysical Society, Copenhagen, 1990, Ann. Geophysicae, 8, 195.

Reichert, K., Borge, J.C.N., & Dittmer, J., 1998, "WaMoS II: An operational wave monitoring system". Proceedings of Oceanology International 98: The Global Ocean, 10-13 March 1998, Brighton, UK, 3, 455-462.

Reineker, M.M. & Fenton, J.D., 1981, "A Fourier approximation method for steady water waves". J. Fluid Mech., 104, 119-137.

Russell, J. S. 1844, "Report on Waves". 14th Meeting Brit. Assoc. Adv. Sci., 311-390.

Seeman, J., Ziemer, F. & Senet, C.M. 1997, "A method for computing calibrated ocean wave spectra from measurements with a nautical X-band radar". Oceans '97: MTS/IEEE conference proceedings, 6-9 October 1997, World Trade and Convention Centre, Halifax, Nova Scotia, 2, 1148-1154.

Senet, C.M., Seemann, J. & Ziemer, F. 1997, "An iterative technique to determine the near surface current velocity from time series of sea surface images". Oceans '97: MTS/IEEE conference proceedings, 6-9 October 1997, World Trade and Convention Centre, Halifax, Nova Scotia, 1, 66-72.

Skolnick M.I., 1981, "Introduction to radar systems". Mcgraw-Hill Book Co, Singapore.

Soulsby, R.L., 1998, "Coastal sediment transport: the COAST3D project". Proc. 26th International Conference on Coastal Engineering, Copenhagen, June 1998, ASCE, 2548-2558.

Srinivasa, N., Ramakrishnan, K.R., & Rajgopal, K., 1987, "Two-dimensional spectral estimation: a radon transform approach". IEEE Journal of Oceanic Engineering, OE-12, 1, 90-96.

Stokes, Sir George, 1847, "On the theory of oscillatory waves". Trans. Cambridge Phil. Soc., 8, 441-455.

Struik, D.J., 1926, "Determination rigoureuse des ondes permantes d'ampleyr finie". Math. Amer., 43, 595-634.

Thornton, E.B. & Guza, R.T. 1982, "Energy saturation and phase speeds measured on a natural beach". J. Geophys. Res., 87, C12, 9499-9508.

Ursell, F., 1953, "The long-wave paradox in the theory of gravity waves". Proceedings, Cambridge Philosophical Society, 49, 685-694.

U. S. Army Corps of Engineers, 2002, "Coastal Engineering Manual". U. S. Army Corps of Engineers manual No. 1110-2-1100, Washington, DC.

Vila-Concejo, A., Matias, A., Ferreira, Ó, Duarte, C., Dias, J.M.A., 2002, "Recent evolution of the natural inlets of a barrier island system in Southern Portugal". J. Coast.Res., (SI)36, 741-752.

Vila-Concejo, A., Ferreira, Ó., Matias, A., Dias, J.M.A., 2003a, "The first two years of an inlet: sedimentary dynamics". Cont. Shelf Res. 23, 1425-1445.

Vila-Concejo, A., Ferreira, Ó., Matius, A., & Dias, J.A., 2003b, "Inlet relocation as a coastal management tool". In: Vilas, F., Rubio, B., Diez, J.B., Frances, G., Bernabeu, M.A., Fernandez, E., Rey, D. e Rosón, G., eds. Special Volume on the 4th Symposium on the Atlantic Iberian Continental Margin, Thalassas, 19(2b):218-219.

Walker, J.R., 1976, "Refraction of finite-height and breaking waves". Proc. 15th international conference on Coastal Engineering, Honolulu, Hawaii, A.S.C.E. New York 1977, 507-524.

Wiegel, R.L., 1960, "A presentation of cnoidal wave theory for practical application". J. Fluid. Mech., 7, 273-286.

Williams, J.J., O'Connor, B.A., Arens, S.M., Abadie, S., Bell, P., Balouin, Y., Van Boxel, J.H., Do Carmo, A.J., Davidson, M., Ferreira, O., Heron, M., Howa, H., Hughes, Z., Kaczmarek, L.M., Kim, H., Morris, B., Nicholson, J., Pan, S., Salles, P., Silva, A., Smith, J., Soares, C. and Vila-Concejo, A., 2003a, "Tidal inlet function: field evidence and numerical simulation in the INDIA Project". Journal of Coastal Research, 19 (1), 189-211.

Williams, J.J., Bell, P.S., Humphery, J.D., Hardcastle P.J. & Thorne, P.D., 2003b, "New approach to measurement of sediment processes in a tidal inlet". Continental Shelf Research, 23, 1239-1254.

Williams, J.M., 1981, "Limiting gravity waves in water of finite depth". Phil Trans. Roy. Soc. London A, 302, 139-188.

Williams, W.W., 1946, "The determination of gradients on enemy-held beaches". Geogr. J. XIC, 76-93.

Witting, J.M., 1984, "A unified model for the evolution of nonlinear water waves". J. Computational Physics, 56, 203-236.

Wolf, J. & Bell P.S. 2001, "Waves at Holderness from X-band radar". Coastal Eng., 43, 247-263.

Wyatt, L.R., Thompson, S.P. & Burton, R.R., 1999, "Evaluation of HF radar wave measurement". Coastal Engineering, 37, 259-282.

Young, I.R., Rosenthal, W. and Ziemer, F., 1985, "A three-dimensional analysis of marine radar images for the determination of ocean wave directionality and surface currents". J. Geophysical Research, 90, C1, 1049–1059.

Young, J.D. & Moore, R.K., 1977, "Active microwave measurement from space of sea-surface winds". IEEE Journal of Oceanic Engineering, OE-2, 4, 309-317.

Technical Appendix – Matlab Scripts

The Matlab routines used to solve the various wave theories described in chapter 2 are supplied on the accompanying CD. They have been grouped in directories according to the type of wave theory. These routines and their various helper functions are supplied as a research tool only and are not guaranteed in any way by the author.

Stream Function Theories

Fenton's Stream Functions

This set of Matlab programs are a translation of the Fortran listings given in Fenton (1988) and were translated by the author primarily to obtain wavelength estimates and waveform shapes. The routines solve the wave equations numerically, yielding a user specified number *n* of Fourier components supplied as one of the inputs to `init.m`. The routines also allow the inclusion of currents, but either the author has misinterpreted the meaning of the parameters, or there is a bug or mistranslation in that part of the program because the effects on the wavelength of including a current on the waves did not seem sensible. The plots in Chapter 2 have all been generated by assuming zero current.

An example of the use of this set of Matlab scripts is the routine used to calculate wave lengths in Chapter 2:

```
[L,X,Y] = fentonstream_wavelength(T,d,H,plotflag)
```

where the inputs are:

`T` : wave period (s)

`d` : water depth (m)

`H`: wave height (m)

`plotflag` : set to 1 to generate and plot the shape of the waveform, zero otherwise.

The outputs are:

`L` : wave length (m)

`X` : if plotflag is set to 1, the x co-ordinate of the wave profile (m)

`Y` : if plotflag is set to 1, the y co-ordinate of the wave profile (m)

Dean's Stream Functions

The DSFWAV toolbox is included as found at the University of Wyoming web site (Borgman & Petrakos, 1986). These routines interpolate across look-up tables generated by Dean's streamfunctions to produce solutions for most wave conditions.

The author has modified the `wavtest.m` program to display the horizontal and vertical components of the orbital velocity field beneath the wave.

Another example of the use of this set of Matlab scripts is the routine used to calculate wave lengths in Chapter 2:

```
[L,X,Y] = deanstreamfunction_wavelength(T,d,H,plotflag)
```

where the inputs are:

`T` : wave period (s)

`d` : water depth (m)

`H`: wave height (m)

`plotflag` : set to 1 to generate and plot the shape of the waveform, zero otherwise.

The outputs are:

`L` : wave length (m)

`X` : if plotflag is set to 1, the x co-ordinate of the wave profile (m)

`Y` : if plotflag is set to 1, the y co-ordinate of the wave profile (m)

Linear Theory

Matlab routine to determine wave length from linear wave theory.

```
L = linear_wavelength(T,d)
```

where the inputs are:

`T` : wave period (s)

`d` : water depth (m)

The output is:

`L` : wave length (m)

Linear wave length including a mean current

```
L=linearpluscurrent_wavelength(T,d,u)
```

where the inputs are:

`T` : wave period (s)

`d` : water depth (m)

`u:` mean current (m/s)

The output is:

`L` : wave length (m)

Approximations to linear wave theory

These are approximations to linear wave theory that do not require iterative procedures to calculate the wave length of the waves.

```
[L_Eckart1952,L_Fenton1990,L_Hunt1979] = direct_linear_approx(T,d)
```

where the inputs are:

`T` : wave period (s)

`d` : water depth (m)

The outputs are:

`L_Eckart1952` : wave length (m) based on Eckart (1952)

`L_Fenton1990` : wave length (m) based on Fenton (1990)

`L_Hunt1979` : wave length (m) based on Hunt (1979)

Stokes Type Equations

There are a number of these listed in Chapter 2, and the Matlab routines to calculate the wavelengths are given below.

Stokes (1847) 3rd order

Stokes third order solution for the wave length:

```
L = Stokes3_wavelength(T,d,H)
```

where the inputs are:

`T` : wave period (s)

`d` : water depth (m)

`H`: wave height (m)

The output is:

`L` : wave length (m)

Struik (1926) 3rd order

Struik's third order solution for the wave length and wave profile based on Mason & Hall (1941):

```
[L,X,Y] = StokesStruik3_wavelength(T,d,H)
```

where the inputs are:

`T` : wave period (s)

`d` : water depth (m)

`H`: wave height (m)

The outputs are:

`L` : wave length (m)

`X` : if plotflag is set to 1, the x co-ordinate of the wave profile (m)

`Y` : if plotflag is set to 1, the y co-ordinate of the wave profile (m)

Brink-Kjaer (1974) 3rd order

Brink-Kjaer's third order solution for wave length in a closed channel:

```
L = BrinkKjaer_wavelength(T,d,H)
```

where the inputs are:

`T` : wave period (s)

`d` : water depth (m)

`H`: wave height (m)

The output is:

`L` : wave length (m)

Fenton (1985) 5th order

The typos in the 1985 paper and the 1987 errata have been fixed.

```
[L,X,Y] = FentonStokes5_wavelength(T,d,H,plotflag)
```

where the inputs are:

`T` : wave period (s)

`d` : water depth (m)

`H`: wave height (m)

`plotflag` : set to 1 to generate and plot the shape of the waveform, zero otherwise.

The outputs are:

`L` : wave length (m)

`X` : if plotflag is set to 1, the x co-ordinate of the wave profile (m)

`Y` : if plotflag is set to 1, the y co-ordinate of the wave profile (m)

Cnoidal Type Equations

Elliptic Integrals

Approximations to allow calculation of elliptic integrals, based on Gardiner-Garden & Fenton (1982). Please refer to the original paper for details.

```
[K,e,Tau,hod,alpha] = Cnoidal_elliptic_integrals(m,H,d)
```

The need for this routine was eliminated by using Matlab's built-in functions for calculating elliptic integrals, but the routine has been included for reference.

Maximum theoretical wave height

A helper function to calculate the maximum theoretical ratio of breaker height over breaker depth based on Fenton (1990).

```
Breakerhod = findbreakhod(L,d)
```

Where the inputs are:

`L` : wave length (m)

`d` : water depth (m)

and the output is:

`Breakerhod :` `ratio of breaker height to breaker water depth`

Wiegel (1960) 1st order

Wiegel's first order solution for wave length and wave profile:

```
[L,X,Y] = CnoidalWiegel_wavelength(T,d,H,plotflag)
```

where the inputs are:

`T` : wave period (s)

`d` : water depth (m)

`H`: wave height (m)

`plotflag` : set to 1 to generate and plot the shape of the waveform, zero otherwise.

The outputs are:

L : wave length (m)

X : if plotflag is set to 1, the x co-ordinate of the wave profile (m)

Y : if plotflag is set to 1, the y co-ordinate of the wave profile (m)

Fenton (1979) 1st order

Fenton's first order solution for wave length and wave profile:

[L,X,Y] = Cnoidalfenton1_wavelength(T,d,H, plotflag)

where the inputs are:

T : wave period (s)

d : water depth (m)

H: wave height (m)

plotflag : set to 1 to generate and plot the shape of the waveform, zero otherwise.

The outputs are:

L : wave length (m)

X : x co-ordinate of the wave profile (m)

Y : y co-ordinate of the wave profile (m)

Fenton (1979) 5th order

Fenton's 5th order solution for wave length and wave profile:

[L,X,Y] = Cnoidalfenton1_wavelength(T,d,H, plotflag)

where the inputs are:

T : wave period (s)

d : water depth (m)

H: wave height (m)

plotflag : set to 1 to generate and plot the shape of the waveform, zero otherwise.

The outputs are:

L : wave length (m)

X : if plotflag is set to 1, the x co-ordinate of the wave profile (m)

Y : if plotflag is set to 1, the y co-ordinate of the wave profile (m)

Composite Approximations

These approximate higher order wave theories to some extent to account for non-linear behaviour due to amplitude dispersion.

Hedges (1976)

This uses the equation from Hedges (1976) but with $Z = H/2$ as suggested by Booij (1981).

```
L = Hedges1976_wavelength(T,d,H)
```

where the inputs are:

`T` : wave period (s)

`d` : water depth (m)

`H`: wave height (m)

The output is:

`L` : wave length (m)

Kirby & Dalrymple (1986)

```
L = Kirby_Dalrymple1986_wavelength(T,d,H)
```

where the inputs are:

`T` : wave period (s)

`d` : water depth (m)

`H`: wave height (m)

The output is:

`L` : wave length (m)

Hedges (1987)

```
L = Hedges1987_wavelength(T,d,H)
```

where the inputs are:

`T` : wave period (s)

`d` : water depth (m)

`H`: wave height (m)

The output is:

`L` : wave length (m)

Kirby & Dalrymple (1987)

```
L = Kirby_Dalrymple1987_wavelength(T,d,H)
```

where the inputs are:

`T` : wave period (s)

`d` : water depth (m)

`H`: wave height (m)

The output is:

`L` : wave length (m)

Bell

Calculated wavelength based on the equations suggested in section 2.7.

```
L = Bell_wavelength(T,d,H)
```

where the inputs are:

`T` : wave period (s)

`d` : water depth (m)

`H`: wave height (m)

The output is:

`L` : wave length (m)